





VICTORIA UNIVERSITY OF TECHNOLOGY

**A STUDY OF BRUISE DAMAGE IN  
HORTICULTURAL PRODUCTS**

by

Taiwai David Ip



A thesis submitted to Victoria University of Technology for the degree of  
Doctor of Philosophy in Mechanical Engineering

School of Built Environment  
Faculty of Science and Engineering  
Victoria University of Technology  
Ballarat Road, Footscray, Victoria 3011, Australia

June 2001

FTS THESIS  
635.0460994 IP  
30001007742002  
Ip, Taiwai David  
A study of bruise damage in  
horticultural products

# TABLE OF CONTENTS

---

<b>ABSTRACT</b>	iii
<b>ACKNOWLEDGEMENTS</b>	iv
<b>NOTATIONS</b>	vi
<b>CHAPTER 1. Introduction</b>	<b>1</b>
1.1 Background	1
1.2 Physical Damage to Horticultural Produce	5
1.3 Review of the Characterization of Horticultural Materials	7
1.4 The Problem	14
1.5 Aim	15
1.6 Preview of the Thesis	15
<b>CHAPTER 2. Experimental Methods and Theoretical Considerations</b>	<b>17</b>
2.1 Experimental Methods	17
2.1.1 Introduction	17
2.1.2 Selection of Methods	18
2.1.2.1 Laser Displacement	18
2.1.2.2 Impact Force Analysis (IFA)	19
2.1.2.3 Shock Test	20
2.2.2.4 Dynamic Mechanical Analysis	21
2.1.3 Experimental Design	22
2.1.3.1 Impact Tests using Laser Displacement Sensing	22
2.1.3.2 IFA Tests	26
2.1.3.3 Shock Test	29
2.1.3.4 Dynamic Mechanical Analysis	32
2.2 Theoretical Considerations	35
2.2.1 Introduction	35
2.2.2 Postharvest Horticultural Materials	36
2.2.3 Characteristics of Deformation in Horticultural Materials	41
2.2.4 Characteristics of Instabilities in Horticultural Materials due to Damage	49
2.2.4.1 Damage Mechanics	52
2.2.4.2 Strain Softening Process	55
2.2.5 Cushioning Effect of Produce Skins against Bruise Damage during Impact	65
2.2.6 The Significance of Increasing the Duration of Impact for Damage Protection	71
2.2.7 Internal Energy Dissipation in Produce	74
2.2.8 Characteristics of Shock Pulses	81
2.2.9 Wave Effects in Dynamic Deformation of Horticultural Materials	85
2.2.9 Summary	100
<b>CHAPTER 3. Results and Discussion</b>	<b>102</b>
3.1 Introduction	102

3.2 Impact Force Analysis Results	103
3.2.1 Duration of Impact	103
3.2.2 Validation of the IFA Method	104
3.2.3 Coefficient of Restitution	106
3.3 Shock Tests	111
3.3.1 Relationship between Bruise Volume and Drop Height	111
3.3.2 Validation of the Shock Test Method	115
3.3.3 Shock Test Method	118
3.4 Laser Displacement Tests	121
3.4.1 Validation of the Laser Displacement Method	121
3.4.2 Soft Horticultural Materials	124
3.4.2.1 Viscoplastic Deformation	124
3.4.2.2 Skin Protection for Soft Produce	127
3.4.2.3 Plastic Deformation	129
3.4.2.4 Plastic/Viscoplastic Deformation coupled with Heat Diffusion	131
3.4.2.5 Consistency of Dynamic Deformation Characteristics in Soft Produce	134
3.4.3 Moderately-Crisp Horticultural Materials	140
3.4.4 Crisp Horticultural Materials	144
3.4.4.1 Strain-Rate Dependency	145
3.4.4.2 Pre-Peak cracking and Peak Transition	146
3.4.4.3 Dynamic Response of Aged and Market-fresh Crisp Produce	147
3.4.4.4 Natural Protection by Produce Skin	153
3.5 Dynamic Mechanical Analysis	156
3.5.1 Rheological State	156
3.5.2 Dynamic Poisson's Ratio	159
3.6 Characteristics of Dynamic Deformation in Horticultural Materials	165
3.6.1 Wave Propagation and Heat Diffusion in Soft Horticultural Materials	165
3.6.2 The Onset to Plastic Instabilities in Soft and Moderately-Crisp Horticultural Materials	183
3.7 Dynamic Instabilities due to Damage in Horticultural Materials	192
3.7.1 Introduction: Crack Growth in Horticultural Materials	192
3.7.2 Dynamic Instabilities due to Fibrillar Slippage	194
3.7.3 Micro-Crack to Meso-Crack Transition in Horticultural Materials	200
3.7.4 Meso-Cracking and Macro-Cracking Characteristics	208
3.7.5 Dynamic Effective Modulus of Horticultural Materials	224
3.7.5.1 Introduction	224
3.7.5.2 Application of the Strain Energy Density Method	225
3.7.6 Bio-Yield Point and S-shaped Sigmoidal Curve in Dynamic Response of Produce and their Relationship with Fibrillar Slippage	233
3.8 Summary	240
<b>CHAPTER 4. Conclusions</b>	<b>246</b>
<b>REFERENCES</b>	<b>248</b>
<b>APPENDICES</b>	<b>267</b>
Appendix A: Drop Test Results of Run ST-21-B	267
Appendix B: Sample Calculations of Peak Accelerations, Velocity Change and Coefficient of Restitution (Run ST-21-B)	269

## ABSTRACT

This thesis presents the results of a study of the properties of horticultural materials, in particular, it aims to identify the different physical processes associated with the dynamic loading conditions responsible for causing bruise damage to certain horticultural produce. The primary mechanisms identified as causing bruise damage include plastic/viscoplastic deformation, predominantly in soft produce, and damage instabilities associated with crisp and moderately-crisp produce.

A new laser based sensor used to obtain precise displacement measurements of material deformation during impact tests on selected produce is described. Drop tests on whole fruit were conducted and bruise damage was correlated with bruise volume by using the impact force analysis techniques. The duration time of impact in drop tests was measured with an instrumented shock testing machine, and a computer controlled dynamic mechanical analyzer was used to study the dynamic viscoelastic properties of produce material.

Wave effects on the material behaviour and properties of produce were analyzed and explained in terms of viscoelastic and plastic deformation and in terms of the extreme conditions of solid-like or liquid-like behaviour. The phenomenon of dynamic crack growth in horticultural materials at both microscopic and macroscopic levels has been investigated in relation to the experimental data.

The principal mechanisms identified as causing bruising in horticultural materials were plastic deformation, viscoplastic deformation and pre-critical instabilities such as micro-scale fibrillar slippage and debonding between cell walls. Produce with soft textures bruises under plastic and viscoplastic deformation but bruising is minimized by the initiation of shear banding instabilities, or heat diffusion which accompanies the decay and disappearance of the wave pulses. Produce with crisp textures bruises due to instabilities that include micro-scale fibrillar slippage, cell-to-cell debonding, plastic jumps associated with serrated features and meso-cracking. It manifests itself in the form of prematurely 'truncated' dynamic stress-strain curves. Crisp produce minimizes the extent of bruising by the various cracking processes in the textures.

For both crisp and soft produce the bio-yield point was identified as the first appearance of micro-scale instabilities.

## ACKNOWLEDGEMENT

The author wishes to thank my principal supervisor, Professor Geoffrey Lleonart, Honorary Professor of Engineering and former Department Head of Mechanical Engineering at Victoria University of Technology, with deep gratitude for his kind support and invaluable guidance throughout the completion of this work. His dedication and professionalism helped me develop both as researcher and academic. His patience and friendship and his willingness to supervise me in his retirement years have been a source of great strength and inspiration for me during the task of completing this thesis. His cheerful help and his sheer amount of energy spent on my work will be remembered. My sincere thanks to Dr. Bernd Wendlandt, senior research scientist of the Aeronautical and Maritime Laboratories of the Defense Science and Technology Organization (DSTO), Department of Defense Australia. He has been my research co-supervisor and also mentor in the area of wave propagation in viscoelastic materials. My gratitude is also expressed to my former supervisor, Dr. Jorge Marcondes, now with San Jose State University, for the many illuminating discussions during the initial part of the work.

Thanks also to Victoria University of Technology for the financial support through a University scholarship and for the happy times spent there. Thanks also to Associate Professor Kevin Duke, former Associate Dean of Engineering, and Associate Professor Michael Sek, Head of the School of Built Environment, who provided me with opportunities to teach as a tutor in the School. Thanks to Secomb Travelling Fund Committee to assist me financially in attending conferences in Tasmania and Singapore. The proof-reading of this work was made by Mrs. Angela Rojter, Language Consultant at the Student Learning Unit of Victoria University. Her careful work is gratefully appreciated. Thanks to Denise Colledge, Marlene Schutt and all other teaching staff of the School. Thanks to the staff at the Workshop who has been supportive of my experimental work. Thanks to my fellow research students for our warm companionship and sharing. My sincere gratitude to Vincent Rouillard, Research Manager of our School, who first introduced me to the application of lasers, which have proven pivotal in the outcome of this project.

To My Parents –  
For their love and support throughout the years

# NOTATION

The following is a list of the principal notation used in this thesis. Notation that does not appear here is defined in the text.

## ROMAN SYMBOLS

$a$	Contact bruise diameter of fruit
$a$	Acceleration
$a(t)$	Time-dependent wave amplitude
$a_m$	Maximum acceleration
$A$	Bottom surface area of impact load
$A_c$	Effective cushion (skin) area under compression
$A_{CR}$	Crack surface area
$A_0$	Original cross-sectional area of test specimens
$A(\varepsilon)$	New effective cross-sectional area of test specimens
$c$	Wave front phase velocity of propagation
$c'$	Plastic/viscoplastic wave front speed
$c_g$	Group velocity of wave propagation
$c_o$	Elastic propagating speed
$C_p$	Dilatational wave velocity
$C_s$	Shear wave velocity
$C_v$	Volumetric specific heat
$d$	Average diameter of bruise on fruit surface under whole-fruit drop tests
$D$	Diameter of cylindrical specimens
$D$	Strain energy density, or stored energy per unit volume in skin (cushion)
$D_m$	Modified damage parameter
$e$	Exponential
$e$	Coefficient of restitution
$E_0$	Young's modulus
$E$	Effective modulus
$E_S$	Instantaneous secant modulus
$E_t$	Instantaneous tangent modulus
$E_u$	Effective modulus under strain softening
$E^*(\omega), E(i\omega)$	Complex Young's modulus

$E'(\omega)$	Storage Young's modulus
$E''(\omega)$	Loss Young's modulus
$\bar{E}$	Effective modulus within the fracture process zone
$\bar{E}(R)$	Effective modulus of the fracture process zone of radius $R$
$\bar{E}_S$	Effective modulus of the plastic zone of radius $R_S$
$F$	Applied force that can be constant or sinusoidal
$f_i$	Acting body (internal) force per unit volume of viscoelastic medium
$G$	Energy release rate
$G_C$	Critical energy release rate
$G_R$	Crack growth resistance
$G_i$	Instantaneous complex shear modulus of the impactor.
$g$	Gravitational acceleration
$G(t)$	Time-dependent shear modulus
$G^*(\omega), G(i\omega)$	Complex shear modulus
$G'(\omega)$	Storage shear modulus
$G''(\omega), G''(j\omega)$	Loss shear modulus
$g_{max} (G_m)$	Peak-g or peak acceleration, a terminology widely used in the packaging industry
$g_{maxavg}$	Average peak acceleration in Kornhauser plot
$h$	Maximum bruise depth of fruit from whole-fruit drop tests
$h$	Instantaneous height
$h_0$	Initial drop height
$h_{0C}$	Critical drop height
$-h$	Strain softening modulus
$H(\tau)$	Relaxation spectrum
$J$	Cushion factor
$k$	Stiffness constant ( $k_1, k_2, \dots$ represent the stiffness constant of Materials 1, 2, ... etc.)
$k_c$	Critical wave number
$K$	Stress intensity factor
$K_C$	Fracture toughness
$L$	Length of test specimens
$m$	Mass
$mL$	millilitre denoting bruise volume
$M$	Mass of the impact load
$N$	Crack density

$n$	Strain hardening exponent
$P$	Perimeter length of crack
$P^0$	Micro-crack distribution tensor of zeroth order
PSI	Pound per square inches
$Q$	Heat content
$R$	Radius of a fruit at the point of impact under whole-fruit drop tests
$R$	Radius of curvature of the impact object
$R_E$	Ratio of energy stored as shear to longitudinal
$R_{shear}$	Percentage of total energy which is shear energy
$S$	Overall (effective) compliance tensor
SD	Statistic deviation
$t$	Lapsed time of an event
$t^*$	Relaxation time
$T$	Temperature
$T_c$	Cushion (skin) thickness
$u$	Velocity
$u$	Displacement normal to the direction of wave propagation
$U_A$	Acceleration wave velocity
$U_S$	Shock wave velocity
$V$	Volume of interest
$V$	Instantaneous velocity
$V_1$	Maximum impact velocity
$V_2$	Rebound velocity
$V_{crack}$	Crack velocity
$V_{soliton}$	Propagation velocity of crack tip as a soliton
$W$	Work done
$W$	Strain energy
$W_{Di}$	Potential strain energy density
$\overline{W}_r$	Unloading modulus under strain softening
$x(t)$	Time-dependent displacement in $x$ -direction
$x$	Displacement in $x$ -direction
$\ddot{x}$	Acceleration
$Y$	Yield stress
$y$	Vertical displacement under loading

## GREEK SYMBOLS

$\alpha$	Coefficient of linear heat coefficient
$\alpha_0$	Initial crack size
$\alpha_c$	Critical crack size
$\gamma$	Attenuation coefficient of wave front
$\gamma_c$	Critical shear strain
$\delta$	Phase angle usually associated with ( $\tan \delta$ ) or shear band thickness
$\delta'$	Kronecker delta
$\varepsilon$	Strain
$\varepsilon_F$	Final strain (when stress, $\sigma = 0$ )
$\varepsilon_U$	Strain at ultimate stress, $\sigma_U$
$\varepsilon_m$	Maximum strain of cushion under compression
$\varepsilon_c$ or $\varepsilon_{cr}$	Critical strain
$\varepsilon_e$	Elastic strain or instant elastic strain
$\varepsilon_{in}$	Inelastic strain
$\varepsilon_p$	Plastic strain or instantaneous plastic strain
$\varepsilon_{vp}$	Viscoplastic strain
$\varepsilon_c(t)$	Time-dependent creep strain
$\varepsilon_i$	Inertia strain
$\dot{\varepsilon}$	Strain rate of deformation
$\dot{\varepsilon}_{cr}$	Critical strain rate of deformation (for horticultural materials)
$\dot{\varepsilon}_{vp}$	Viscoplastic strain rate
$\bar{\varepsilon}$	Isothermal coupling constant
$\varepsilon_f$	Rupture strain where macro-cracking initiates
$\kappa$	Thermal diffusion coefficient
$\kappa'$	Instantaneous bulk modulus
$\lambda$	Lame parameter
$\mu$	Lame parameter
$\eta$	Viscosity coefficient
$\eta$	Damping coefficient

$\eta'$	Inverse relaxation time of a viscoelastic impactor.
$\eta^*$	Specific entropy
$\theta$	Temperature
$\sigma$	Stress
$\sigma_m$	Maximum stress experienced by cushion under compression
$\sigma_s$	Static stress of the skin cushion
$\sigma_Y$ or $\sigma_y$	Yield stress
$\sigma_i$	Internal stress
$\sigma_f$	Effective stress (sometimes called net stress)
$\sigma_v$	Viscous stress
$\sigma_{cr}$	Critical stress, failure stress or fracture stress
$\sigma_c$	Rupture stress where macro-cracking initiates
$\sigma_o$	Engineering (nominal) stress or constant applied stress
$\sigma_0$	Initial (fictitious normal) stress
$\sigma_{sy}$	Static yield stress of material that deforms in a perfectly-plastic or liquid-like manner
$\sigma_{True}$	True (Cauchy) stress
$\sigma_U$	Ultimate stress
$\tau$	Time duration of impact
$\tau'$	Particular time of interest during material deformation
$\tau_o$	Elastic impact duration
$\tau$	Shear stress
$\tau'$	A particular time of interest
$\nu$	Poisson's ratio
$\bar{\nu}$	Damaged Poisson's ratio
$\rho$	Material density
$\rho'$	Averaged density of micro-cracks over all possible orientations or vector directions
$\rho_0$	Material density in the unstrained (or initial) state
$\psi$	Range of material damage
$\psi(t)$	Rayleigh's dissipation function in cushion under compression
$\omega$	Radian angular frequency
$\omega'$	Damage parameter
$\Omega$	Equipotential yield surface

# CHAPTER 1

## INTRODUCTION

### 1.1 BACKGROUND

In recent years, the phasing out of tariffs and government subsidies is gathering pace in many countries. The horticultural industry in Australia and in other nations with developing horticulture exports such as Chile, New Zealand and South Africa has been challenged to become more internationally competitive against established exporters such as the United States. According to an Australian Federal Government report prepared by the Canberra Horticultural Task Force (1994), for instance, the fruit and vegetable industry in Australia alone could triple its exports of horticultural products to around US\$ 1.5 billions a year by 2000. The report also points out the many problems associated with the current practice of packaging and transport of horticultural produce, such as uncompetitive costs, unreliable delivery times and poor handling during distribution.

In Australia, horticulture is the largest agricultural plant-sector industry with an annual gross value of production of US\$ 2.5 billions and a total export value of US\$ 0.45 billion (1991-1992 figures), ahead of the export of grains and wool but behind that of the beef industry. Rapid export expansion has already allowed the horticultural industry to bring in nearly US\$ 1 billion from exports during 1993-94, according to Davis (1996). However, unlike grains, wool and livestock, horticultural products tend to suffer a higher degree of wastage during the course of transportation and handling. As pointed out by Peggie (1968), cited in Holt *et al.* (1981), the year-round average wastage in the fruit and vegetable industry in Australia has been around 8% to 10% of the crop. Most of this wastage has been due to bruising, O'Loughlin (1964). Such a level of waste, while diminishing through various pre-harvest

means of crop protection and advanced packaging and post-harvest technology, could be still further diminished and attention needs to be paid to this.

Until recently, the horticultural industry in countries such as Australia has been largely protected by governments from competition by quarantine and perhaps also by distance. This situation has made the horticultural industries in these countries orientate only towards their generally profitable domestic markets. However, apart from some strategic grain industries such as rice in Japan, Korea and Taiwan, this protection practice is widely believed to be illogical and is thus deemed 'unacceptable' to competitive exporting countries. Also, a direct and generally expected outcome of this protection practice is that the horticultural industry cannot be developed with a strong export culture.

The agricultural export business has been historically quite risky, requiring much pre-profit financial commitment, marketing efforts, perseverance and technical input from the growers in establishing firm overseas markets. This is particularly so for the horticultural export sector, as the wastage stemming from their activities always tends to be on the high side. Technically, the horticultural exporters need to select, by experience directly gained from expensive trial shipments, the best means for the protection of horticultural products during the extended shipping periods to overseas destinations, where higher demand for the marketability of the produce is expected from the overseas buyers. This coincides with the much higher risk of damage to the produce during the shipment period. Here, the means of protection is complex because the protection cost varies substantially between different kinds of produce. Some are more susceptible to shocks, such as apples and pears, while others are susceptible to chilling, for example bananas and pineapples, and others to vibration, such as ripe peaches and soft fruits like strawberries, raspberries and currants, according to Vergano and Testin (1991), as well as quasi-static loading such as compression during storage. Most of the produce is sensitive to changes in relative humidity (RH) during shipment and the requirement for RH varies. Most fruits, such as apples and pears, keep best at a RH of 90% or higher, while leafy vegetables such as lettuce and broccoli are best stored at a RH close to 100%.

While much experience has been gained in the packaging and post-harvest technology used for the protection of a variety of horticultural produce, losses, both in terms of export opportunities and financial returns, can occur because of the inappropriate application of protection to particular types of produce. Due to the different dynamic responses of various types of produce under high loading during shipment, each requires different degrees of protection and thus the selection of the optimum package design involves a balance between packaging cost and protection requirement. Some of the different

packaging options used for the distribution of produce are illustrated below for cherries, papaya and mangoes.

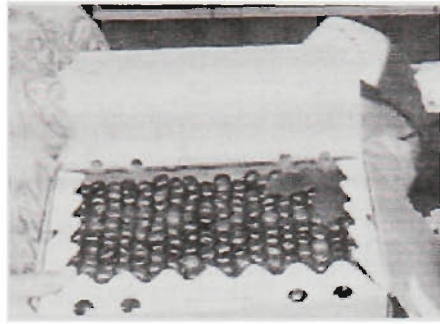


Figure 1.1 Packaging requirements for cherries on bubble-wrap cushion in a sturdy paper carton for air-freight shipment. From Domeney (1994).

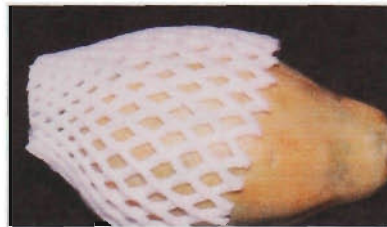


Figure 1.2 Packaging protection for papaya shipment with an expanding polystyrene sock.

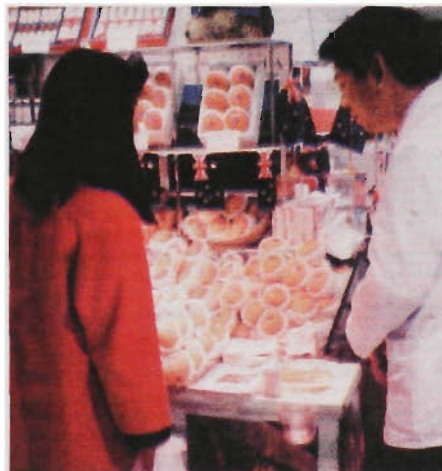


Figure 1.3 Mangoes from the State of Queensland, Australia, are shown here with expanding polystyrene sock protection at a supermarket in Japan. From Biggs (1995a).

Australia has been one of the major suppliers of fruits and vegetables in the Asia-Pacific Rim. The substantial annual exports of apples of approximately 100 tonnes a day or 12% of the total crop, according to Biggs (1995b), pears and many other major varieties like potatoes, tomatoes, mushrooms, onions, bananas, oranges and melons to regional markets are still expanding, as noted by Davis (1996). In particular, the export demand on some of the comparatively new produce such as nashi (or oriental pears), persimmon, lychee and carambola (starfruit) is currently growing at an even faster rate than in the 1980's, according to Biggs (1993). One example is the Asian food markets that have been substantially developed over the last decade. Opportunities have arisen for growers in the Southern Hemisphere to

supply high quality perishable horticultural products outside the normal Northern Hemisphere season. This is both an opportunity and a challenge particularly to Australasian producers due to their geographical vicinity to the Asian markets.

Demands for the comparatively new products from these emerging markets can be enormous. Total nashi production in Australia increased substantially from 2,460 tonnes in 1991 to 5,800 tonnes in 1993. In 1991, only 5.5% of the total production were exported. Of the total export tonnage, 125 tonnes was destined for the Hong Kong and Singapore markets. This export amount, incidentally, accounts for only 0.24% of the total annual consumption (51,500 tonnes) in these two markets in 1991, according to Biggs (1993). Another example can be drawn from the experience of exporting persimmons, a very soft and tasty fruit native to south China. Australia has 150,000 persimmon trees, according to Collins (1994). The bulk of the crop each year has been exported to a single market – Singapore. However, the export volumes still represent less than half the quantity the Singaporean importers want to buy. This has been due in part to problems associated with the perishable nature of persimmons during shipment and highlights the need for strict standards that can be applied to specific fruits during transit, Ito (1971). According to Collins (1994), the annual export potential of persimmons for the Japan and China markets alone is expected to be 200,000 and 400,000 tonnes, respectively. A more updated list of postharvest storage techniques for shipment of exotic fruits can be found in Taylor (1993).

Many horticultural products have a very limited market life. Most of them have to be transported overseas by air, regardless of the extra costs of shipment involved. These include most vegetables as well as many fruits such as strawberries, persimmons and mangoes. Many others, particularly those which can be picked while they are unripe, have a much longer market life, and can be exported by sea under the right post-harvest conditions during the period of shipment. Examples include bananas, papayas, kiwifruit, apples, pears, and oranges. Since produce is sensitive to temperature and humidity changes, an unexpected power failure of the refrigeration plant of the container may result in early ripening of the whole shipment. These undesirable outcomes have been alleviated by the introduction of various modified-atmosphere (MA) packaging such as the application of films impermeable to water, as shown in Figure 1.4. Fruits in general are more susceptible to bruising when their textures soften during ripening, as pointed out by Bourne (1979).

The chances of produce bruising are, contrary to general belief, quite low during harvest compared to post-harvest shipment and handling. All over the world most seasonal fruit pickers are experienced and are credited with limiting the amount of fruit bruising to a minimum during harvest.

Also, the expected probability of bruising along cushion-lined conveyors during the grading and packing processes is relatively small compared with that during the period of shipment. Besides, orchards are often designed to maximize irrigation efficiency and pollination, as well as to minimize chances of picking losses during harvest. Examples include V-shaped grids for easy handpicked harvesting.

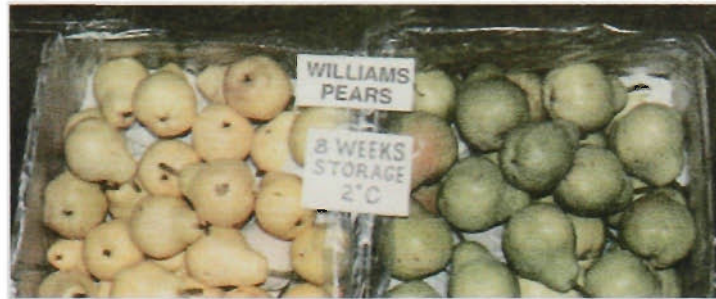


Figure 1.4 Australian Williams pears destined for Vancouver, Canada, which underwent accidental heat shocks resulted in early ripening (left), but not if effective MA film was applied. From Buckingham (1995).

The horticultural sector has been quite active in seeking to prevent bruise damage to their crops, from the orchard planning stage down to the packaging design and shipment stage, according to Biggs (1994). However, further advance in reducing bruise damage to particular crop varieties depends on deepening our understanding of the physical nature of the bruise process. A successful outcome to such research would have application in the design of appropriate protective measures for the produce concerned.

## 1.2 PHYSICAL DAMAGE TO HORTICULTURAL PRODUCE

Horticultural produce suffers various degrees of bruising during transportation and handling. The following distinctive types of damage due to physical causes has been identified by Mohsenin (1986):

- (1) Bruise damage – Rupture damage to the tissues (or individual cells) of produce under loading, causing the rupture of the cell walls and the release of cell sap into the intercellular space. This will change the physical properties of the bruised tissues, which may include browning and a change of taste.
- (2) Swelling damage – Cracking damage to the cell walls of the tissues due to a slight increase in the turgor pressure within the cells. This situation can be demonstrated in a skinless fruit by immersing it in salt water.

- (3) Puncture damage – Damage caused by pointed-stems or thorns, which penetrate the produce skins and the tissues underneath. Examples include some grapes (within a bundle) squeezed between pointed-stems during their normal growth cycle.
- (4) Cracking – This normally represents cracking on the skin and/or the tissues underneath due to impact or pressure loading. Here, cracking is denoted, after Glenn and Poovaiah (1990), as:
  - (a) cell rupture (crack-failures of individual cells) as in (1), or
  - (b) macro-scale (or global-scale) shearing fracture between (or debonding of) cells, but without rupturing the cells during the initial stage of cracking. However, as the crack propagates, (b) will eventually become (a).

Some researchers refer ‘cracking’ specifically to produce skin, and ‘splitting’ to cracks which extend into the interior of the produce flesh, Opara *et al.* (1997).

The final outcome of either (1) or (4) ends up as bruise damage. Both of these cases occur under high dynamic loading conditions, such as impact.

Factors which cause the bruising of horticultural produce are primarily the magnitude of the force acting on it within a very short time (generally in the order of milliseconds), and the characteristics of the transient interaction between the produce tissues and the impulsive load which propagates through the tissues. Some of these factors and dynamic characteristics of deformation of produce are as yet not fully known. Although many quasi-static and quasi-dynamic tests on the deformation characteristics of produce tissues have been performed and well documented in the past, few studies of the dynamic characterization of horticultural materials based on precision stress-strain measurements have been reported. This represents a critical gap in our knowledge of bruising due to dynamic effects. With the recent advent of reliable laser displacement sensors, however, accurate records of displacement under high strain rates for a wide range of highly deformable materials, including horticultural materials, can be acquired for analysis.

### 1.3 REVIEW OF THE CHARACTERIZATION OF HORTICULTURAL MATERIALS

The most extensively used method for testing postharvest horticultural materials has been the quasi-static Magness-Taylor firmness test over the past 60 years. The key operations involve a plunger that penetrates the fruit flesh and the maximum force level is recorded. However, firmness data obtained from different types of testers can only be compared among one another by including a weighting function to the different data sets. The test data normally show considerable variation when taken at different locations on any fruit. Queries were raised in the past as to what is really being measured in this type of test, and whether it is possible to define precisely what 'firmness' means in terms of the overall property of fruits. It has been pointed out that the test data result from a combination of shear and compressive stresses, Yang and Mohsenin (1974). Yang (1973) noted that the theoretical and experimental curves were not in detailed agreement. Only the trends were in good agreement, showing that the effects were due to a number of causes. Manual firmness tests suffer from the difficulty of controlling loading rate and it has been shown that the firmness of apple as measured by other quasi-dynamic tests were load rate sensitive, see Fletcher *et al.* (1965). Bourne (1965) tried to simulate fruit firmness tests by mounting a plunger onto a universal testing machine, but concluded that the relationship between the tester and fruit (apple in his case) was complex and could not be expressed in the form of a simple formula. Bourne (1980) further noted that a precise definition of 'fruit firmness' in general is probably impossible. Shapes of plunger tips can also be quite sensitive to measurements, according to Studman and Banks (1989a).

In the early 1960's, tests were carried out to investigate the transient mechanical properties of horticultural materials based on the quasi-dynamic material responses from large flat test specimens (with or without skin) using a pneumatic plunger developed by Mohsenin and Gohlich (1962). Later Fletcher *et al.* (1965) used a high-speed model with multi-speed functions. From these tests, force-deformation curves were produced. The force has also been interpreted as a measure of the flesh firmness. While such tests can register the initial peak, denoting the bio-yield point, and the maximum force, denoting the failure strength, of a test specimen, the cross-sectional area of the probe does not represent the true area of the tissues under loading, nor does the measured deformation, due to uncertainties which arise from the complex relationships between the tissues directly underneath the plunger tip and those in the vicinity of the plunger, as pointed out by Fridley (1976).

Force-deformation plots from these tests are typically very scattered but in most cases with a noticeable linear pattern, as observed by Fridley and Adrian (1966). This might have given researchers an indication that horticultural materials normally deform in a fairly random fashion, and the mechanical

properties of these materials could be confidently characterized only by averaged values of material properties from test data. Whether this has been a clear indication or just a misconception deserves to be verified by new dynamic tests on these materials.

Faced with these unresolved uncertainties, several investigators shifted their attention to an energy balance approach based on the principle of conservation of momentum, and tried to establish a direct relationship between bruise volumes and total impact energy in test specimens. Some used free-swinging pendulum drop tests, Zoerb and Hall (1960), Bittner *et al.* (1967), Finney and Massie (1975), and Jindal and Mohsenin (1976). Others used the free-fall drop test method incorporating an instrumented falling mass fixed on top of a guided platen which impacts on stationary whole fruit or small specimens placed on top of a load cell or force gauge, Hammerle and Mohsenin (1966), and Diener *et al.* (1979). The origin of this method can be traced to free-fall drop tests made during World War II by Bell Laboratories in the United States, see Lubin and Winans (1944). These better defined impact tests allow workers to study the effects of any cushioning materials placed between the impactor and the test specimens. These tests, however, are not entirely suitable for real whole-fruit drop simulation because two loading fronts are involved on the specimens. Nevertheless, this approach has opened up a new pathway of assessing the relationship between bruise damage and impact energy, and the impact parameters involved in the bruising process, such as drop height and coefficient of restitution.

As pointed out by Fluck and Ahmed (1973), contradictory experimental results of drop tests based on the evaluation of impact energy requirement for the yielding of produce textures have not been satisfactorily explained. Researchers found that the impact energy required to produce a certain strain in samples under drop tests was less than that under static (dead-load compression) or quasi-static loading conditions to achieve the same strain. This was contrary to the expected outcome for material testing on ductile metals. Results that showed this outcome included testing on peaches, pears, apricots and apples, Fridley and Adrian (1966); sweet potatoes, Wright and Splinter (1968); processed apples, Fletcher (1971), and many others. This discrepancy could be explained by the existence of dynamic effects such as cracking of produce tissues. Fridley and Adrian (1966) and Horsfield *et al.* (1972) found that a few impacts on fruits with severe energy in each impact could achieve the same level of bruises with multiple blows with slight impact energy per blow.

It has been pointed out by some workers such as Manor (1978) and Mohsenin (1986) that the measured impulse is almost certainly greater than that calculated from the theoretical rigid body momentum change,  $\Delta mV$ . Nelson and Mohsenin (1968) called this inequality of momentum change the 'absorbed momentum' but without further elaboration. It has been suggested that the difference may be

due to energy loss during the viscoelastic wave propagation. However, the amount of energy being carried through wave propagation, particularly viscoelastic or plastic waves, is normally quite small when compared with other losses such as internal friction energy dissipation, see Hunter (1957).

Significant progress was made by Holt and Schoorl as proponents of cracking theories in horticultural produce, see Hort and Schoorl (1977 and 1983), and Schoorl and Holt (1980). They attempted to prove and apply, through experimental means, the theory of fracture in biomaterials to horticultural materials from a new 'school of thought' elaborated by Gordon (1978), Andrews (1980), Jeronimidis (1980) and Vincent (1982). Holt and Schoorl (1982a and 1984) then raised the conjecture of dynamic effects and initiated concepts of applying damage mechanics to horticultural materials. Basically, this 'school' pointed out that biological materials under load frequently exhibit large deformations in which significant energy loss takes place during the material cracking process and consequently traditional engineering fracture theory such as the Griffith (1921) theory fails to provide a suitable framework. In particular, Gordon (1978) explained that a crack may exist in a material without leading to complete cleavage as long as it remains shorter than a critical size. In the sense of Krajcinovic (1996), these are micro-cracks that possess free-surfaces and/or free-volumes but they are isolated from one another, although they have a strong tendency to join up. Following this concept, Holt and Schoorl postulated that cell walls tend to fail by slippage (micro-cracking) as the strain rates of deformation increase, Holt and Schoorl (1982b). This complements the results from other experimental and numerical modelling work that cell wall rupture is a necessary condition for bruise damage, releasing cell sap which causes tissue softening and oxidation reaction (browning), as described by Diehl *et al.* (1979) and Pitt (1982). This reaction follows the oxidation of the phenolic compounds in horticultural materials by polyphenoloxidases to quinones that are unstable and easily polymerize as dark-colour melanic compounds, according to Vamos-Vigyazo (1981).

Recently, in his studies of produce tissue strength and the parenchyma (flesh) properties, Vincent (1990 and 1991a), pointed out the necessity of considering fracture for the bruising of the plant tissues. He noted that this area was one which experimental investigators had rarely looked into. Earlier, Studman and Banks (1989b) noted the necessity of damage evaluation in fruit bruising. While performing drop tests with nashi fruits, they encountered cracking problems within the fruits and suggested a more accountable estimation of the absorbed impact energy of the fruits by measuring the cracked free-surfaces inside the fruits. A comprehensive review on the cracking and splitting of fruit skin was provided by Opara *et al.* (1997). An equally comprehensive review on the fracture properties of agricultural materials was presented earlier by Vincent (1990).

Whereas pendulum and free-fall drop tests are used to reveal the sensitivity of produce firmness to variations in impact parameters, drop test methods have been further improved to perform whole-fruit drops. Recently developed tests show that impact force analysis (IFA), where whole fruits are dropped to impact a stationary force load-cell sensor, have become the preferred option in simulating real drops for round-shaped fruits and vegetables. This approach was first reported by Nahir *et al.* (1986) to simulate tomato grading. Recent IFA tests have also been reported. These include testing with peaches, Zhang *et al.* (1994); kiwifruits, Imou *et al.* (1993); and peas, Van der Burg (1993). This method, as well as other drop test approaches, is not suitable for dynamic material response analysis based on stress-strain behaviours.

Besides produce firmness, other impact parameters have also been extensively examined in the past, as recorded by Fluck and Ahmed (1973), Finney and Massie (1975), and Diener *et al.* (1979) and others. These include the primary parameters such as the duration of impact, momentum change, impact energy absorbed during impact, drop height, and bruise volume, as well as secondary parameters such as fruit size and weight, storage period, storage temperature, and water loss. Primary parameters also include any combinations of these parameters, such as the coefficient of restitution (the ratio of rebound to impact velocity) and the recently well-researched bruise susceptibility (or the impact energy absorbed per unit bruise volume). The popularity of the latter was probably inspired by results from Holt and Schoolt (1977) which hint at a linear relationship between the bruise volume and absorbed energy for some apples, see Klein (1987), Studman and Banks (1989b), Bruswitz and Bartsch (1989), and Hung and Prussia (1989). Holt and Schoolt coined this linear relationship as bruise resistance coefficient (BRC). Following the approach of Holt and Schoolt, researchers began to query the general applicability of this linear relationship to other fruits and spherical produce such as potatoes that have similar characteristics, Noble (1985). Blahovec *et al.* (1996) noted that, under quasi-static load tests, some horticultural materials such as cherries indicated a nonlinear relationship between bruise volume and absorbed energy. For higher deformation, the BRC is an increasing function of deformation up to the bio-yield point. Studman and Banks (1989b) pointed out the difficulty of the bruise susceptibility approach in the case of some fruits like nashi, see Figure 1.5. Under impact loading, the fruit sustains many cracks that may extend into the unbruised tissues. This is due to the unique size distribution of the parenchyma cells of pear and nashi. Unlike the relatively uniform cell-size distribution of apple tissues, see Lapsley *et al.* (1992), those of nashi or pear are extremely uneven. Under high loading, propagating cracks will initiate underneath the skins of nashi and pear and will pass through the larger cells, as shown in Figure 1.6. In apples, fracture planes are rarely found in whole-fruit drops except when the free-fall drop height exceeds about one metre. The bruise shape in almost all varieties of apples is predominantly hemispherical, as shown in Figure 1.7.

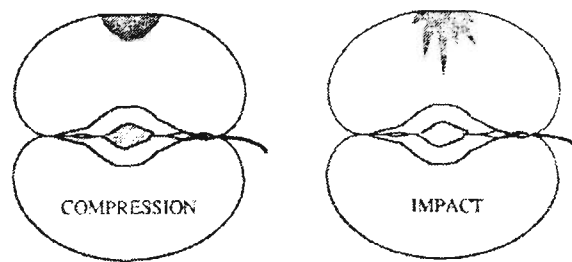


Figure 1.5 Bruise shapes on pear or nashi under (left) quasi-static compression and (right) impact, resulting in hemispherical and irregular crack-dominating shapes, respectively, showing fundamentally different modes of impact energy dissipation. From Chen *et al.* (1987).

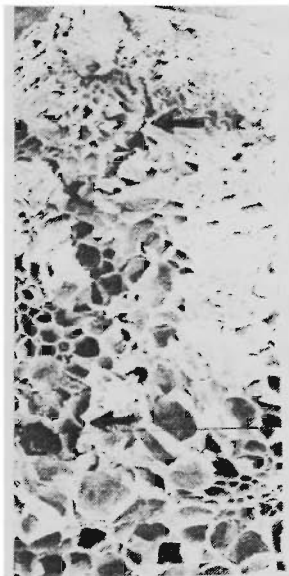


Figure 1.6 Fracture surfaces (black arrows) in bruised pear tissues which follow the larger parenchyma cells (X 60). From O'Brien *et al.* (1984).



Figure 1.7 Typical spherical bruise zone in apple tissues showing the impact energy dissipation and cell bruising primarily in the direction of wave propagation. From Holt and Schoorl (1977).

Under a typical drop-test impact mode, almost all the primary impact parameters, except the duration of impact, can be characterized by a shock pulse that is represented by the acceleration time history of the impact. The sum of the total area underneath this shock pulse provides insight into the momentum change during the impact, as well as a means of correlation between the bruise volume and the absorbed impact energy under a particular drop height. Despite past research work on impact parameters there appears to be no study that looks into the direct relationship between bruise volume and the time duration of whole-fruit impact, under similar impact energy levels. The establishment of such a

relationship would certainly enhance our understanding of how the duration time affects the packaging protection of the products under dynamic loading.

Regarding the shock pulse, some workers applied double integration of the accelerometer history data for the determination of the displacement values, Hammerle and Mohsenin (1966); Fluck and Ahmed (1973); Lichtensteiger *et al.* (1988). The acceleration data are usually obtained from instrumented impact tests on samples with uniform dimensions. Stress-strain curves can thus be constructed, see Oleson (1966). However, the accuracy of the stress-strain curves often becomes questionable for short-duration tests such as impacts, as the acceleration data often comprise abrupt changes during their time history. The accuracy deteriorates sharply when the acceleration data become noisier, with unrealistic drifts of resulting velocity and displacement, as pointed out by Pacifico (1981). Many efforts have been made to improve the processing of noisy acceleration data but displacement and strain values are only indirectly obtained.

Dynamic tests on cylindrical apple specimens based on direct force and displacement measurements were performed by Miles and Rehkugler (1973) using an experimental set-up which, though primitive compared to modern instruments, was able to provide independent force and displacement measurements. The force readings were measured with a load cell placed underneath a test specimen. Maximum deformation values could be measured from deflected angles of a long hinged light-weight cantilever beam with its free end resting on top of each test specimen. In this last regard the deformation history could only be assumed to be linear, as only the ultimate deformation values could be measured. Regardless of such limitations, these tests did provide a rough representation of the dynamic response of produce materials with independent force and deformation (and hence stress and strain) data for the first time.

The first truly direct displacement measurements of large deformations in horticultural materials were reported by Jarimopas *et al.* (1990), using a pendulum tester equipped with a piezoelectric force transducer and an electro-optical follower. The authors claimed to capture successfully the deformation history of whole-apple samples up to peak force levels at a relatively low sampling frequency of around 5 kHz. It is generally accepted that a sampling rate of at least 40 kHz to 50 kHz is required for a valid dynamic characterization of the transient behaviour of highly deformable materials, see Cheresch and McMichael (1987). Since the early 1990's, precision laser displacement sensors able to capture displacement data at rates up to 100 kHz have become available. A laser displacement sensor operating on an 'optical triangulation principle', as has been described by Ji and Leu (1989), can be used to advantage in point-by-point measurements of absolute distance, or when small sized test specimens are

used or a flexible operating range is required, or where small sensors are suitable for positioning in otherwise inaccessible locations, according to Hanke (1990). Ip *et al.* (1996a) illustrated this sensor system for stress-strain characterization of horticultural materials under transient loading.

Regarding dynamic rheological characterization, most of the research has been done on the time-dependent behaviour of viscoelastic food products like mayonnaise and salad dressing, using small amplitude oscillatory testers or rheometers, see Munoz and Sherman (1990). The main objective of these tests was to characterize the viscoelastic properties of the test materials and to determine the dynamic properties such as complex Young's modulus,  $E^*(\omega)$ , complex shear modulus,  $G^*(\omega)$ , phase angle,  $\delta$ , and the corresponding radian frequency,  $\omega$ . Hamann (1969) first applied this test method to horticultural materials (apple flesh) by investigating the dynamic relationship between  $E^*(\omega)$  and  $\omega$ . Rao *et al.* (1976) applied the same tests to sweet potato. Petrell *et al.* (1980) applied similar tests to apple samples in relation to sample location and ripening. Few other records based on this test method for horticultural materials have been reported. Test results obtained by using this method are vital for a realistic assessment of the phenomenological state of horticultural materials, and can be used to determine whether such materials are solid-like, liquid-like, or viscoelastic. This approach has been long applied to plastics, Lethersich (1950), for the evaluation of dynamic mechanical properties such as Poisson's ratio and energy partitions during energy dissipation in the materials under a pulse disturbance. Mohsenin (1970) noted that direct measurements of Poisson's ratio,  $\nu$ , for most horticultural materials in their natural state was extremely difficult, due to the fact that accurate techniques for the two-dimensional straining of horticultural materials have never been properly applied, as pointed out by Vincent (1992).

A test method was proposed some years ago for the determination of dynamic Poisson's ratios based on measured data such as  $E^*(\omega)$  and  $G^*(\omega)$ , see Sips (1951) and Rigbi (1967). Longitudinal and shear energy partitions (which are  $\nu$ -based) can also be determined, see Tillett (1954) and Dyson (1965). Early attempts at  $\nu$  measurements with primitive rheometers for horticultural materials were less successful. Chappell and Hamann (1968) found Poisson's ratio of Winesap apple specimens to be stress and time dependent during the initial stage of disturbance, but stabilizing in a range of 0.14 to 0.24. Finney (1969) gave a range of  $\nu$  for Rome Beauty apple with similar values. Other workers resorted to sonic pulses for  $\nu$  determinations. Garrett and Furry (1972) gave a  $\nu$  range of 0.26 to 0.39 for Rome Beauty. While these  $\nu$  values are more credible than the earlier results, such a large range was due to the scattering of velocity data from 100 to 180 metres per second passing through apple tissues of whole fruits which are in general predominantly anisotropic in nature, see Khan and Vincent (1990).

Hammerle and McClure (1971), using a new approach, estimated the Poisson's ratio of cylindrical specimens of sweet potato by direct measurements of the radial strains with a photomicrometer during the quasi-static compression of the specimens with a universal tester. The size of each specimen was 1 inch in diameter by 1.25 inches in length. They found that the  $\nu$  values of sweet potato specimens remain almost constant at  $0.32 \pm 0.02$  up to 4% strain. The  $\nu$  values creep slightly upwards to  $0.35 \pm 0.03$  at 8% strain (the maximum strain limit of their tests). All their test specimens were obtained as direct core into the cheek of each sweet potato. This might have given us a clear indication that the Poisson's ratio of horticultural materials may not be very scattered at each particular location with the same orientation of the loading direction in the produce. Whether this has been a clear indication deserves to be verified by new dynamic testers on these materials. In recent years precision oscillatory testers such as the dynamic mechanical analyzer (DMA) have been used for the dynamic rheological testing of elastomeric and polymeric materials such as polyethylene, Gill *et al.* (1984). However, little work based on the DMA tests on horticultural materials have been reported so far.

#### 1.4 THE PROBLEM

It is important to develop packaging systems that not only suit particular modes of transport, but also meet the specific protective needs of the produce. An essential requirement for improving packaging systems relies upon heightening our understanding of the physical processes associated with the bruise damage that occurs in produce under dynamic loading conditions. The research work proposed in this thesis involves conducting experimental and theoretical investigations concerned with the transient processes linked to bruising of certain horticultural products. A successful outcome to the research program would help the horticultural industry in this country by improving the quality of horticultural products through reduced wastage, increasing marketability, further developing export markets and enhancing economic benefits, as well as the provision of useful data for future studies of package protection optimization.

The scope of the present research program was limited to the study of bruise damage in produce tissues under transient deformation, since such bruising is a significant cause of physical damage to certain economically important horticultural produce during distribution. The thesis describes how the dynamic characterization of selected horticultural materials can be achieved and includes results obtained from theoretical and experimental investigations.

## **1.5 AIM**

The aim of this research program was to conduct theoretical and experimental studies, designed to identify the different physical processes associated with the dynamic loading conditions responsible for causing bruise damage to certain horticultural produce.

## **1.6 PREVIEW OF THE THESIS**

The thesis comprises four chapters. Chapter 1 is the introductory chapter. It provides the background of the present study and includes a review of literature that attempts to trace the chronology and evolution of research in the characterization of horticultural materials from quasi-static to dynamic tests. Chapter 1 also serves to define the objective and the scope of the present studies.

The experimental methods used in this study are presented in Chapter 2, the rationale behind the selection of the methods, and description of the experimental design based on the selected methods. The chapter also includes the theoretical basis required for the experimental studies.

The major outcome of the experimental program is given in Chapter 3 along with an analysis of the experimental data. Here, efforts were made to address various hypotheses so that knowledge could be established before moving on to discuss their implications in the following theoretical discussions later in the chapter.

Chapter 3 also serves to identify the various dynamic features associated with the bruising processes in horticultural materials with a theoretical analysis. In particular, it focuses on the dynamic plastic deformation characteristics of horticultural materials, as illustrated by experimental results. Based on the relevant constitutive equations from these models, an attempt was first made to present an account of the deformation in terms of wave pulse propagation in horticultural materials within the context of continuum mechanics predominantly represented by plastic deformation, but without the involvement of damage. It is followed by a treatment of how soft horticultural materials can be protected from the destructive effect of propagating plastic wave fronts. Chapter 3 includes a discussion on shear banding, a

form of dynamic material instability that is the sole consequence of severe plastic deformation. Features of shear banding are illustrated by experimental results.

Chapter 3 also presents a theoretical investigation of the dynamic instabilities caused by damage such as micro-scale and meso-scale cracking, macro-scale cracking (strain softening) and fracturing in horticultural materials. The chapter includes discussions of the features of instabilities such as pre-peak fibrillar slippage, cell debonding and others such as the S-shape sigmoidal curves, in the sense of Gordon (1978). This chapter includes a study of the micro-cracking to meso-cracking transition, as well as meso-/macro-cracking characteristics in horticultural materials. The chapter ends with a discussion on the bio-yield point and dynamic characteristics of some crisp produce such as the pre-peak serrated or staircase-like stress-strain characteristics in deformation.

The thesis is completed in Chapter 4 with general conclusions of the present work.

# CHAPTER 2

## EXPERIMENTAL METHODS AND THEORETICAL CONSIDERATIONS

### 2.1 EXPERIMENTAL METHODS

#### *2.1.1 Introduction*

Questions regarding the causes, processes and consequences of bruising in different types of produce have been raised in the past forty years and answered with various degrees of success using quasi-static and quasi-dynamic tests. The present study, based on modern materials science techniques, reflects an approach that focuses on the search for general features characteristic of damage caused to horticultural produce by dynamic loading processes. Equally important to the approach is a respect for the details and subtleties of specific phenomena, and an emphasis on understanding how damage due to dynamic processes differs in various contexts.

This study presents an account of dynamic characterization of horticultural produce based on precision stress-strain responses using a laser displacement sensor. Besides the dynamic stress-strain characteristics, other significant results such as peak accelerations, duration of impact and velocity changes during impact were established for selected cylindrical produce specimens. These results were then compared with those established by other impact tests of whole-fruit specimens, based on an improved drop test technique termed Impact Force Analysis (IFA), to investigate whether the dynamic responses from laser-based tests and actual drops are comparable. The IFA technique also serves to establish relationships between the coefficients of restitution and drop heights, and impact and rebound velocities for whole-fruit drop tests. Indications of damage in produce tissues from the

IFA and laser-based tests and from earlier crack damage postulates by other researchers provide us with an opportunity to investigate the produce bruising mechanisms successfully.

This study was followed by an investigation of the impact time duration, based on whole-fruit impact tests using a shock tester, which is capable of establishing accurate impact time duration for each test, so that a relationship between impact time duration and bruise size could be established. The viscoelastic properties of horticultural materials, which provide information about the deformation and energy states of the materials, were characterized under dynamic conditions using a dynamic mechanical analyzer. Notable parameters such as the Poisson's ratio of produce under dynamic conditions were established. These parameters were crucial for an accurate assessment of the energy partitioning due to the shear and longitudinal stresses. They are essential in any future numerical modelling studies, such as the finite element analysis, of the time history of the whole-fruit deformation during an impact and the evolution and decay characteristics of the stress wave front.

Theoretical considerations that are pertinent to this study are included in this chapter. These include an overview of postharvest horticultural materials, their inherent characteristics of deformation under dynamic conditions and the occurrence of instabilities as a result of damage, which includes an introduction to damage mechanics and strain softening process. In order to characterize the damage mechanisms of horticultural produce, a technique based on the strain energy density theory is introduced in the section on strain softening. This technique, which is capable of establishing an accurate relationship between the effective modulus of horticultural materials and the corresponding strain level under transient conditions, was developed in this study and will be presented in Chapter 3. This chapter is concluded with an introduction of the cushioning effect of produce skin, the significance of lengthening the impact duration and the internal energy dissipation in produce.

### ***2.1.2 Selection of Methods***

#### ***2.1.2.1 Laser Displacement***

An approach similar to the direct displacement measurements by Jarimopas *et al.* (1990) was adopted in this study for the evaluation of dynamic stress-strain characteristics. The system comprises a piezoelectric accelerometer and a laser displacement sensor. The advantage of the laser sensors is that displacement can be directly measured with high precision while the impacting hammer is in motion. Figure 2.1 shows the sensor arrangement, with a source beam from a laser diode focussed by

a transmission lens onto a moving object surface. The reflected beam, at an inclined angle to the incident beam, passes through a reception lens and the spot image is projected onto a position-sensitive photo-detector. The position of the spot depends on the distance between the sensor and the surface of the object. The model of the laser sensor chosen for the present studies was a Keyence High-Precision Model LB-12/72.

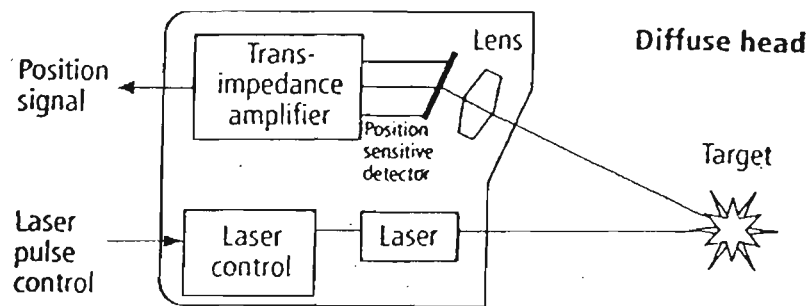


Figure 2.1 Laser displacement sensor layout. From Slazas (1996).

### 2.1.2.2 Impact Force Analysis

Drop tests under the IFA make use of a massive dynamic load-cell that has a relatively low natural frequency. The advantage of this method is its ability to simulate spherical-shaped produce in real drop situations with reliable assessment of the associated impact parameters. Its disadvantage is that test data tend to be inaccurate as the frequency response of the drop approaches the natural frequency of the load-cell. This method was adopted in the present study using a dynamic load-cell Model LU-200KE rated at 2 kN capacity manufactured by Kyowa Electronic Instruments Co. Ltd. as shown in Figure 2.2. The Kyowa load-cell was used in test runs with relatively high drop heights of 5 cm to 20 cm. A 100 N Sangamo load-cell, shown in Figure 2.2, was used in small drop heights ranging from 0.5 cm to 5 cm.

The company-certified frequency response of the load-cell was 328 Hz, or a minimum allowable time duration of impact of 3.05 milliseconds (ms), which was able to accommodate the expected lowest time duration for apple drops of about 4 ms as observed by Studman (1995b) using a high-speed video camera. The IFA method for whole-fruit drops is capable of correlating bruise damage in terms of bruise volume with most of the significant impact parameters such as momentum change, peak acceleration, absorbed impact energy assessment, drop height, fruit weight, storage period, storage temperature, water loss, coefficient of restitution and bruise susceptibility.



Figure 2.2 Kyowa 2 kN (centre), and Sangamo 100 N (right) dynamic load-cell.

### 2.1.2.3 Shock Test

The IFA method is capable of correlating bruise damage with most of the significant impact parameters, with one important exception, that is, the time duration of impact. Any attempt to establish a direct relationship between bruise volume,  $BV$ , and impact duration,  $\tau$ , for whole-fruits has to make use of free-fall shock test instruments or their equivalents. The main advantage of these shock test instruments is that some impact parameters can be pre-determined. In this regard, the duration of impact, drop height and the inherent shock-pulse shape for the case of horticultural produce, generally analogous to a haversine or bell-shaped pulse, can be pre-set. This control does not necessarily simulate actual drop situations. Rather, the main purpose is to attempt to establish a direct relationship between the duration of impact and the resulting  $BV$ .

The main disadvantage of the shock test is that two loading fronts may be involved in the fruit under test when the fruit is fixed onto the shock table by a jig or fixture. Any shock pulses due to the jig or fixture on fruits has to be mitigated through careful design of experiments. It has also been pointed out by Siyami *et al.* (1988) that the actual impact velocity experienced by the fruit under test may be the sum of the free-fall velocity and the maximum rebound velocity of the shock table. If such is the case, then the bruise volume due to the impact will be larger than expected. This undesirable situation can be avoided by allowing a lower coefficient of restitution for the shock table compared to the fruit under test. This condition needs to be established by experiment prior to any test program. A Lansmont shock tester, as shown in Figure 2.3, was used to perform shock tests.



Figure 2.3 A programmable Lansmont shock tester with control console showing blue-colour shock table with piston underneath and black-colour shock-absorbing rubber sleeve.

#### 2.1.2.4 Dynamic Mechanical Analysis

Dynamic Mechanical Analysis (DMA), sometimes referred to as dynamic mechanical spectrometry, is the study of mechanically dependent behaviour of materials. This includes those based on time, temperature, strain rate, stress and strain. In general, a test with an analyzer can be described as a DMA test if it provides measured quantities in terms of a three-part modulus comprising complex, storage and loss, respectively. The complex modulus describes the bulk viscoelastic material behaviour with combined elastic and viscous properties. It is given by the ratio of the maximum stress to the maximum strain. Older mechanical analysis tests do not separate the elastic properties from the viscous properties of the test materials, and are unable to report the material's ability to store mechanical energy, characterized by the storage modulus; or to dissipate mechanical energy, specified by the loss modulus. The ratio of the loss modulus to the storage modulus is termed tangent delta ( $\tan \delta$ ), which is an indicator of the state (or phase) of a material. Those with  $\tan \delta$  values close to zero exhibit a more elastic behaviour, with a relatively high storage modulus. Their behaviour is solid-like. Those with  $\tan \delta$  substantially higher than one are non-gel liquid-like, with a higher loss modulus. Those with  $\tan \delta$  greater than zero behave viscoelastically. Knowledge of the values of the moduli and  $\tan \delta$  over a range of frequencies are useful for characterizing the viscoelastic properties of materials.

Dynamic mechanical analyzers able to measure data with high oscillatory amplitudes and phase angles with high precision began to appear in recent years. These modern analyzers are able to perform with oscillatory amplitudes much smaller (in the order of microns) than those used by the ‘conventional’ reciprocal mechanical devices, Perkin-Elmer (1995), or the ‘new’ devices, Whorlow (1992), which use steady rotation of boundary surfaces to produce harmonic strains in the materials under tests. In this regard, these analyzers can be successfully applied to the testing of materials such as crisp produce tissues that have limited allowance for stretching. In the present study, a Perkin-Elmer 7-series analyzer, Figure 2.4, based on a 3-point bending test mode was used. The operating frequency range was from 1 to 50 Hz, which is considered adequate in representing practical ranges for horticultural materials within which most of the energy dissipates. Typical horticultural industry standards are between 1 and 15 Hz for practical packaging applications.



Figure 2.4 Perkin-Elmer 7-series desktop dynamic mechanical analyzer with PC-controlled Unix-based platform.

### *2.1.3 Experimental Design*

#### *2.1.3.1 Impact Tests using Laser Displacement Sensing*

The impact tests based on laser displacement sensing were designed to provide precision displacement measurements of the time history of material deformation. Figure 2.5 shows the set-up with a laser displacement sensor firmly secured with bolts onto the side of a 12 kg steel block. The laser beam was carefully adjusted to achieve a vertical beam source. The optical path points to the bottom of a free-fall steel platen, which was vertically guided by a pair of parallel piano wires tightly connected to the top cantilevers and floor fittings. The displacement data acquisition system was

automatically activated when the platen approached to within the 50-millimetres (mm) range. A maximum allowable specimen thickness of 15 mm was used.

An accelerometer and cylindrical steel weights of various sizes were mounted rigidly on top of the platen. The test set-up was designed to perform drops with drop heights from 15 to 1200 mm, with nominal strike weights of 500 grams (gms), 900 gms, 1,300 gms, 1,700 gms, or any two of these combinations. For the present series of studies, a drop-height range of 50 mm to 250 mm was adopted. The actual selections of strike weight, which includes a cylindrical weight, steel platen, connecting bolts, accelerometer and accelerating base plate, were 495.38 gms, 900.81 gms, 1,293.95 gms and 1,692.71 gms. This was a modified version of an earlier design based on a single square strike weight instead of cylindrical weights, Ip *et al.* (1996b). With a wide selection of drop heights and strike weight combinations, the set-up was capable of measuring a range of strain rates,  $\dot{\epsilon}$ . The maximum strain rate achieved was approximately 1,000/sec., under a drop height of 250 mm. The minimum strain rate, achieved with a drop height of 50 mm, was about 75/sec. The laser source beam always strikes at the same point underneath the platen, which could be identified by a white arrow marked on the side of the platen. Signals from the displacement sensor and the accelerometer were captured and processed by PC-based data acquisition software.

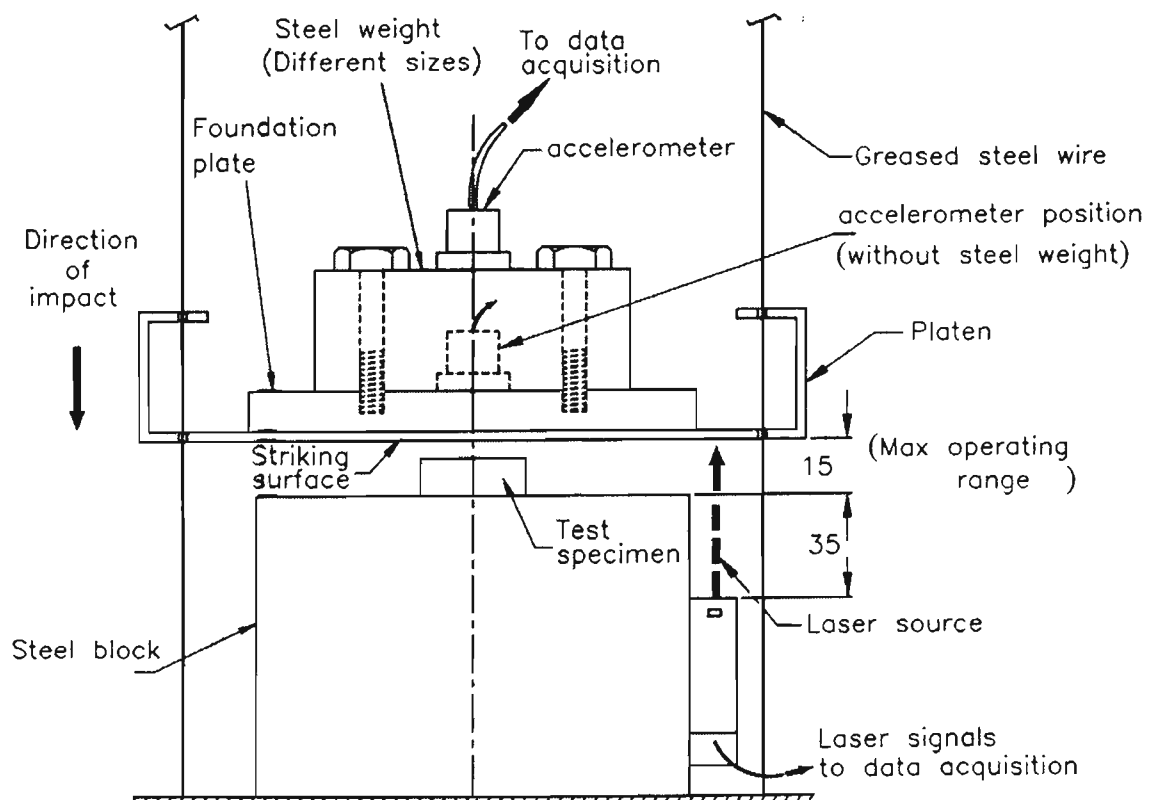


Figure 2.5 Arrangement of test sample and laser displacement sensor. Units in mm.

Before the preparation of test specimens, all produce was weighed and stored in zip-bags before being stored in an environmental chamber set at 4°C to 5°C and 100 % RH at least 36 hours before any tests. Cylindrical test specimens from all produce were always cut by forcing a sharp core borer on the face of the produce radially towards the stem-calyx centre line and trimming to a size of 10 mm in thickness and 26 mm in diameter. For all laser-based tests, only one produce test size was used. Typically, two specimens were cored from each piece of produce, facing in the opposite direction to each other, as shown in Figure 2.6. All cylindrical produce specimens were prepared with this radial orientation, in the sense of Khan and Vincent (1993). Specimens were prepared immediately before each set of test runs. After preparation, specimens were temporarily stored in plastic zip-bags.

A limited number of tests were performed to investigate the dynamic interaction between produce specimen and packaging materials such as corrugated fiberboard and packaging material such as bubble-wrap, with each produce specimen placed on top of the packaging specimen. For packaging specimens, they were cut to sizes of 50x100 mm and stored inside zip-bags in a separate environment chamber at 23°C and 50% humidity for months. Before any test run, they were taken out and marked for identification, and replaced in the chamber for at least 4 hours. Immediately before each test run, a specimen was placed on top of the 12 kg steel block. A steel platen served as the striking surface and, upon release, fell from selected drop heights onto the test specimen. Two sets of data were independently captured in each test run: time histories of acceleration and displacement. Each set comprised 1,024 data points. For all impact tests that involved packaging materials such as bubble-wraps, a time window of 10 ms was used; for produce, a time window of 20 ms was used. This corresponds to a sampling frequency of about 100,000 Hz and 50,000 Hz, respectively.

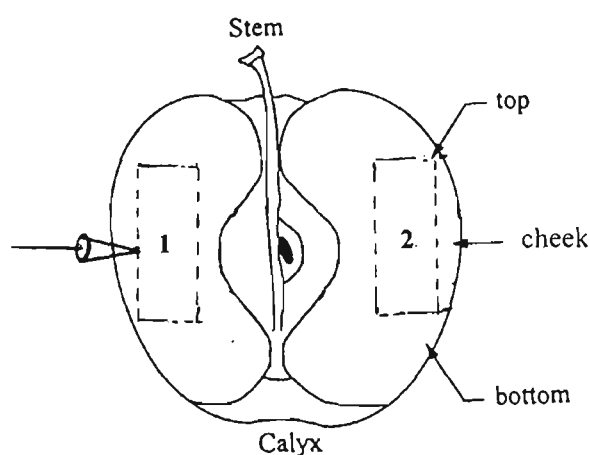


Figure 2.6 Orientation of the 2 cored cylindrical specimens of produce in radial direction. All cylindrical produce specimens were prepared with this radial orientation, in the sense of Khan and Vincent (1993).

Throughout the test series, nominal (engineering) stresses,  $\sigma_o$ , and strains were used in the analysis. The advantage of keeping the stress in nominal units and not converting to Cauchy (true) stress,  $\sigma_{True}$ , is that the strain softening processes of the test specimens can be clearly seen on the nominal stress-strain curves, Ashby and Jones (1996). For all tests carried out, a fixed length to diameter (L/D) ratio of 0.385 was used. Materials which are brittle and structurally weak, such as crisp produce, are susceptible to damage under loading due to the initiation of micro-cracks. For test specimens with large L/D ratios, any decrease in the cross-sectional area due to crack formation could significantly affect the stability of the specimens. Specimens with low L/D ratios are stable and have nominal stress levels close to those of the true stress, as illustrated in Figure 2.7.

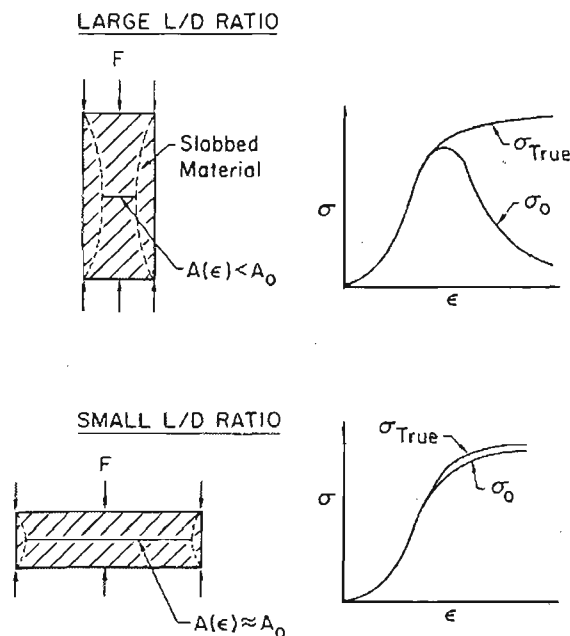


Figure 2.7 Effect of length/diameter ratio on the difference between true and engineering stress-strain curves. ( $A_0$  = original area;  $A(\epsilon)$  = new effective area). From Read and Hegemier (1984).

In this study, for all crisp produce specimens such as apple and nashi, each drop was repeated 5 to 10 times. For all other soft or less-crisp produce specimens, 3 to 5 times of drops were found to be adequate. For other laser-based drop tests which involved packaging materials, it was found that three repeated drops were adequate. Due to the possible occurrence of instabilities such as micro-cracking during the large material deformation, particularly in crisp materials, the dynamic stress-strain data obtained from the several runs for each set of tests were not averaged.

Each test for soft horticultural materials such as papaya and kiwifruit specimens comprised two drop heights: 50 mm and 100 mm, with a strike weight of 0.9 kg. Each test for crisp produce specimens such as apple and nashi comprised four drop heights: 50 mm, 100 mm, 150 mm and 200

mm. A few trial tests with nashi and Golden Delicious apple specimens involved drop heights of 250 mm. Each test series with a 250-mm drop height comprised two drops, for aged and fresh nashi and Golden Delicious apple specimens. For crisp produce specimens, strike weights of 0.5 kg, 0.9 kg, 1.3 kg and 1.7 kg were used. Some tests with fresh apple and nashi specimens with skins attached were performed to investigate the cohesive effects on the flesh due to attached skins.

Cylindrical produce specimens were aligned directly with the centre of the striking platen. Prepared specimens of all test materials were stored in labeled zip-bags and were taken out (with the zip-bags) from the environmental chamber at the same laboratory room immediately before each test run. The data of from each test was processed using a Microsoft Excel file for further analysis.

One series of laser-based tests involved packaging materials: bubble-wrap. The aim of these tests was to investigate the cushioning effects of bubble-wrap and its dynamic responses under impact conditions. The thickness of test samples of bubble wraps was 3.72 mm and was measured with a micrometer. Drop heights of 50 mm, 100 mm, 150 mm and 200 mm were adopted, with a single strike weight of 0.9 kg. The basic configuration of the bubble-wrap samples was rectangular in shape with a single size of 50x100 mm, to conform with the shape and size of the strike platen, so that the impact loading from the rectangular platen of comparable size could be more evenly distributed.

#### 2.1.3.2 IFA Tests

Golden Delicious apples were purchased batch fresh from wholesale distributors and were used for all IFA tests. The apples were market fresh and were purchased within 7 days after harvest at the Shepparton area in Victoria, Australia. After purchase, they were immediately sorted, weighed and stored in sandwich zip-bags at 5.5°C in a temperature-controlled refrigerator. The RH within some zip-bags was sampled and monitored by an environmental data recorder. Typically they rose from 55% to 100% RH within 12 hours and stayed at 100% RH throughout the storage period. After the tests, each apple was again stored in a zip-bag in the refrigerator at 5.5°C for 24 hours before bruise dimensions were measured. Bruise dimensions were measured using a radius of curvature meter that includes a dial indicator and is shown in Figure 2.8.

Bruise volumes were measured using the expression suggested by Schoorl and Holt (1980):

$$BV = \frac{\pi h}{24} (3d^2 + 4h^2) + \frac{\pi x}{24} (3d^2 + 4x^2) \quad (2-1)$$

where  $BV$  is bruise volume of the produce in milli-litres (or mL),  
 $h$  is the maximum bruise depth (cm),  
 $d$  is the average diameter of bruise on fruit surface (cm),  
 $x = R - [R^2 - d^2/4]^{1/2}$  (cm),  
 $R$  is the radius of the fruit at the point of impact (cm).

It is necessary to measure the values of  $x$ , as illustrated in Figure 2.9, directly by means of the radius of curvature meter, because, according to Mohsenin (1986), the uncertainties arising from the estimation of the values of  $R$  can be eliminated.

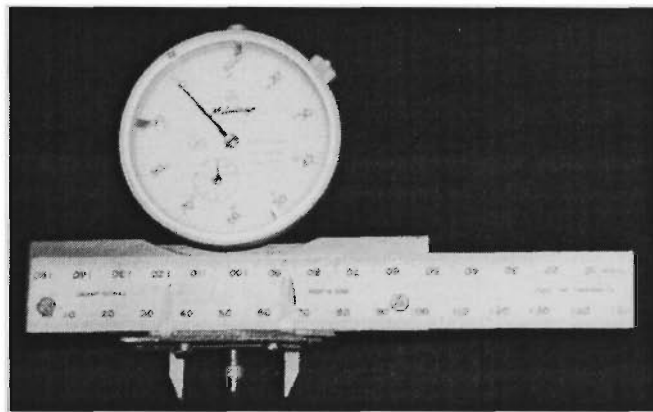


Figure 2.8 View of radius of curvature meter.

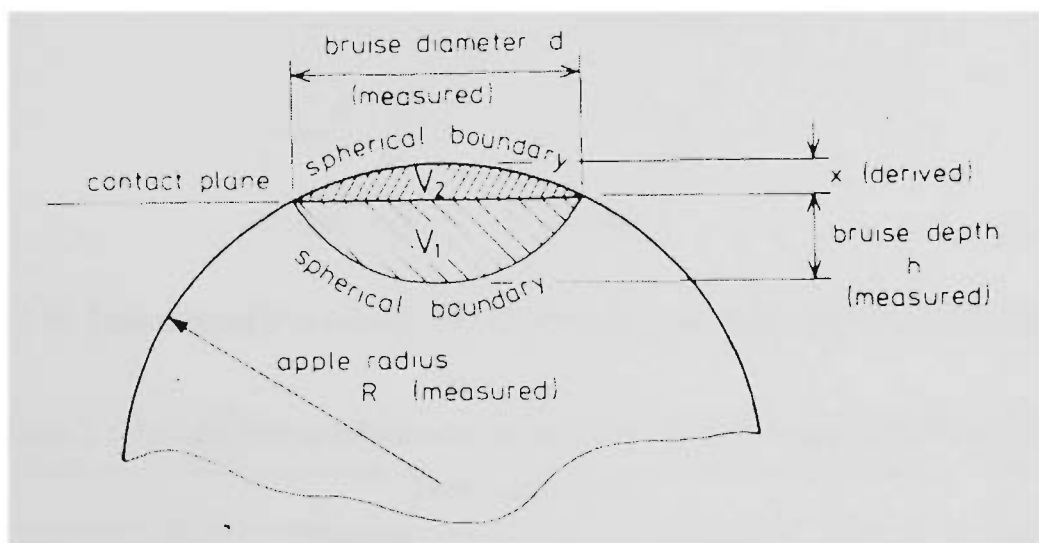


Figure 2.9 Assumed shape of the spherical bruise volume showing measured parameters.  
 From Schoorl and Holt (1980).

The IFA setup with a 2 kN load cell sensor, Figure 2.10, was used to perform a series of free-fall whole-fruit drop tests. The purpose of this series of tests was to compare the results obtained from these direct tests with those from the other test series using a shock tester under similar sets of drop heights.

The voltage representing the force was amplified before being processed by data acquisition software. Shock levels in terms of gravitational acceleration,  $g$ , were calculated using the voltage data (see Appendix B for sample calculations). The signals were not filtered. Coefficients of restitution were determined using calculated impacting velocities from known drop heights and rebounding velocity from known velocity change,  $\Delta V$ . The Golden Delicious apples used for this series of IFA tests were taken from the same batch used for shock tests. Each data point was the average result based on five drops. As five apples were involved in each drop height, they were so arranged that the deviation in weights was minimized. Table 2.1 is an example of the arrangement of apples for each test based on their weights.

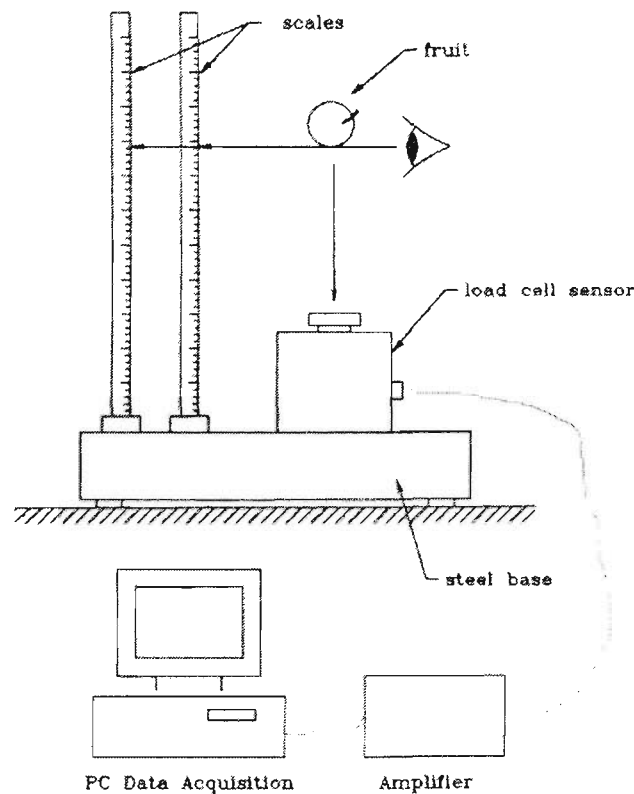


Figure 2.10 Experimental IFA setup of free-fall drop tests for whole-apples on a 2 kN load-cell.

Table 2.1 Weight distributions among fresh Golden Delicious apples for Run ST-25

Drop Height (mm)			
50 mm	100 mm	150 mm	200 mm
135.06 gm	144.52 gm	146.63 gm	150.83 gm
139.49 gm	145.02 gm	147.18 gm	152.15 gm
142.34 gm	145.33 gm	147.57 gm	153.23 gm
142.97 gm	145.76 gm	148.17 gm	153.83 gm
143.33 gm	146.24 gm	149.36 gm	154.32 gm

Rather than performing direct comparisons with shock tests, other series of IFA tests were performed at various drop heights using Golden Delicious apples of various degrees of maturity. The purpose of these tests was to investigate any change in the duration of impact due to effects of frictional contacts when the apples softened during aging. In one case, whole-apple specimens were frozen to  $-4^{\circ}\text{C}$  so as to achieve rigid skin boundaries, for the purpose of simulating impacts with rigid boundaries. Test data were compared based on their coefficients of restitution,  $e$ , at various drop heights. These data were further compared to data from whole-fruit drop tests under market-fresh and two- to three-week stored Golden Delicious apple-to-rigid-surface impacts.

### 2.1.3.3 Shock Test

During an impact, the time duration of contact,  $\tau$ , between an impactor and a surface is the time between first contact and the moment the impacting object leaves the surface during the rebound cycle. At comparable drop heights, say 10 cm and 20 cm,  $\tau$  has been found to be virtually invariant, based on past experience, if the material properties of the impactor and the contact surface remain unchanged. Therefore it is not possible using conventional free-fall or pendulum drop tests to perform tests with controllable  $\tau$ , with any particularly chosen drop heights. Instead, a shock tester that is used for package damage susceptibility tests may be used. A shock tester was used to study the direct relationships between bruise volumes and impact duration under several fixed drop heights (and hence fixed amount of impact energy) by changing the material properties of the impact surface. This was achieved by changing the number of rubber pads on top of the shock tester damper, Figure 2.11.

The desired level of duration of impact was achieved by trial and error by choosing different numbers of ring pads. For most cases, pieces of plain cloth were placed on top of the rubber rings to fine-tune the  $\tau$  values to the desired level. Tests were performed for impact duration of 2 ms, 4 ms, 6 ms, 8 ms and 10 ms, under drop heights of 5 cm, 10 cm, 15 cm and 20 cm, using market-fresh Golden Delicious apples. Drop heights for whole-fruit tests were pre-set accurately with the tester control console. When a selected  $\tau$  value was achieved, an apple was fixed onto the centre of the shock tester platform with a piece of softwood using long bolts and nuts. A thick piece of rubber padding was carefully placed between the apple and the softwood jig to eliminate any loading front on the apple due to the softwood jig, see Figure 2.11. Shock levels in terms of 'g', the gravitational acceleration, were captured by an accelerometer fixed on the shock table beside the apple. Captured signals passed through a charge amplifier before being processed with PC-based data acquisition software. Each data point represents the average result based on five drops. The preparation and sorting schemes for

the apples and bruise measurements in this test series were similar to those applied to the IFA tests. All shock tests were carried out with the fruit and accelerometer fixed at the centre of the 600 x 800 shock table, as illustrated in Figure 2.12.

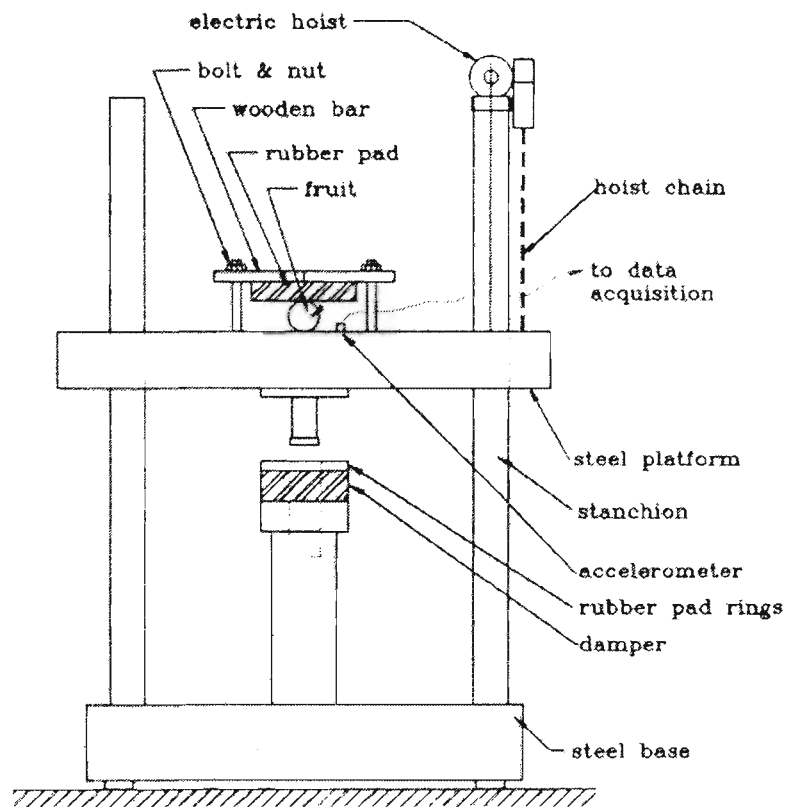


Figure 2.11 Experimental set-up of shock tests for establishing a direct relationship between duration of impact ( $\tau$ ) and produce bruise volumes ( $BV$ ).

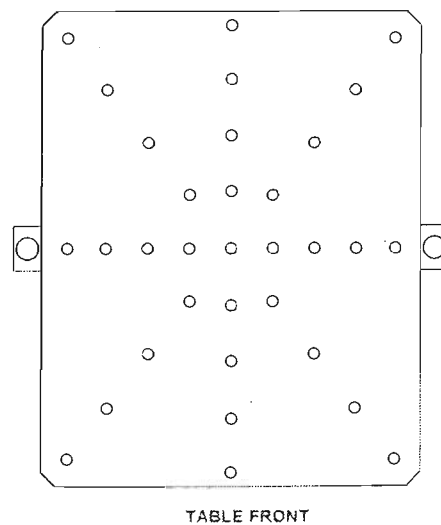


Figure 2.12 Top-view of the shock table showing dimension of 600 x 800 mm and 33 locations as shown by circles "o" of accelerometers for dynamic response testing.

It is necessary to know whether the shock table response will vary according to the location of an impact, so that the fruit can be fixed at any spot on the shock table. Three accelerometers were

fixed in turns onto 33 different locations in 13 different scenarios, see Figure 2.12, and the table was dropped using various drop heights. The first scenario was chosen with all three accelerometers located at the centre of the table, to make sure they would produce the same readings. Other scenarios include locations at the middle three spots of the diagonals or boundaries of a quarter square on the table. A 3-dimensional dynamic response graph is illustrated in Figure 2.13. It was found that the dynamic response of the table in terms of  $g$  values varied with the position of the impact. This can be clearly seen for the cases of 5 cm as shown in Figure 2.13 and 30 cm drop height in Figure 2.14 as 2-dimensional contours, as noted by Marcondes and Ip (1994). There was a unique response shape for each drop height.

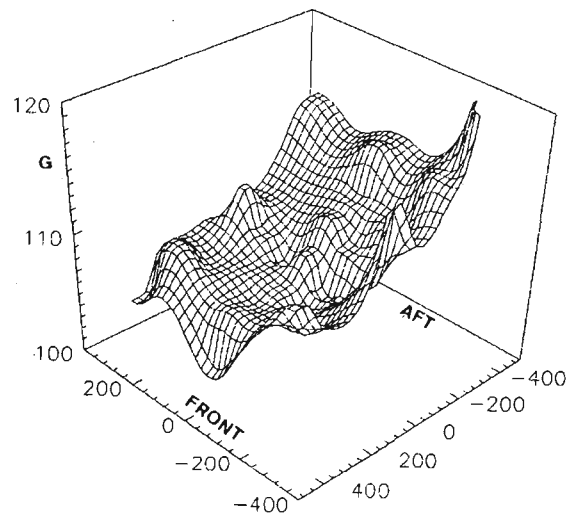


Figure 2.13 Three-dimensional acceleration contours on top of the shock table during an impact from a drop height of 5 cm. (Here the vertical unit,  $G = g$ , the gravitational acceleration). (Run ST-14).

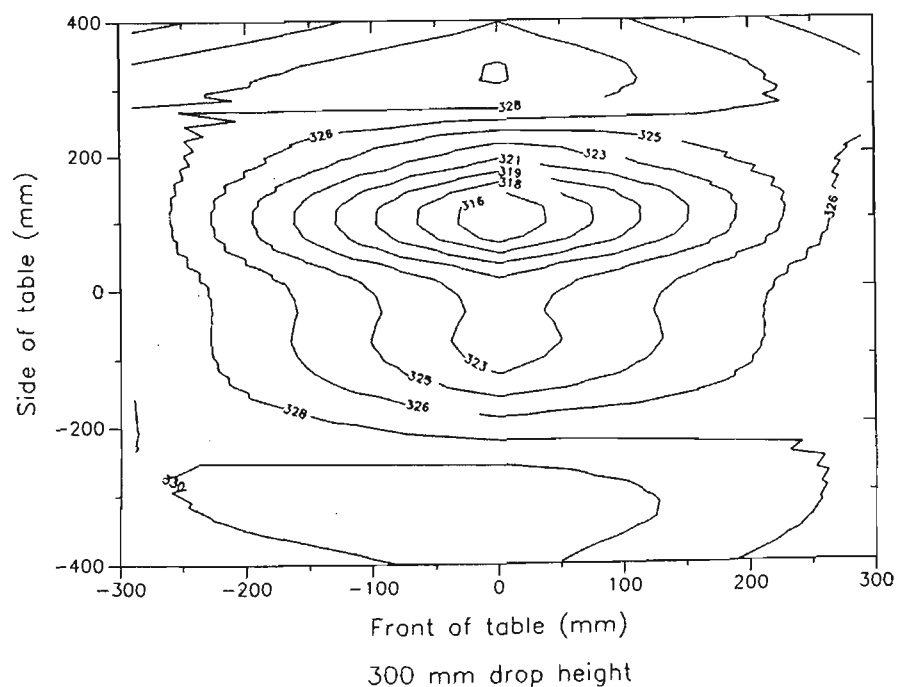


Figure 2.14 Acceleration contours on top of the shock table. Drop height is 30 cm. (Run ST-18).

It was found that the centre point of the shock table was the best spot for locating the accelerometer for all shock tests, as the centre spot of the shock table is where the statistic median of the acceleration response is by and large located. In Figure 2.13, the median is  $110 \pm 7 g$  for 5 cm drops, while, in Figure 2.14,  $322 \pm 9 g$  is the median for 30 cm drops. For a 20 cm drop, the median is  $275 \pm 15 g$  (diagram not shown). The medians are all located at the centre of the table.

#### 2.1.3.4 Dynamic Mechanical Analysis

If horticultural materials are subjected to a time-dependent input stress,  $\sigma(t)$ , they can be deemed viscoelastic in nature if their resulting strain is a functional of  $\sigma(t)$ , in the form:

$$\varepsilon(t) = f\{\sigma(t, \tau'), \sigma(t)\} \quad (2-2)$$

where  $\tau'$  and  $t$  are time parameters, and  $\tau'$  is smaller or equal to  $t$ . Their viscoelastic material behaviour is defined as linear if and only if it satisfies the following criteria, Haddad (1988):

- (i) it is homogeneous, with the form:

$$f\{C \sigma(t)\} = C f\{\sigma(t)\} \quad (2-3)$$

where  $C$  is a constant, and

- (ii) it conforms to the principle of superposition, with the form:

$$f\{\sigma_1(t_1), \dots, \sigma_n(t_n)\} = f\{\sigma_1(t_1)\} + \dots + f\{\sigma_n(t_n)\} \quad (2-4)$$

where  $n = 1, 2, 3, \dots, n$ .

Under a one-dimensional stress state, linear viscoelasticity allows the relation between stress and strain to be expressed as, Christensen (1982):

$$\sigma(t) = \varepsilon(0)G(t) + \int_0^t G(t-\tau')\varepsilon(\tau')d\tau \quad (2-5)$$

where  $\sigma(t)$  is the shear stress at time  $t$ ,

$\varepsilon(t)$  is the shear strain in the material at time  $t$ , and

$G(t)$  is the shear modulus, or the stiffness of the produce material, whose value depends upon the particular material of interest. Here,  $G(t)$  is the simplest form of  $G(i\omega)$ , the complex shear modulus.

Because of the viscoelastic nature of the material, the phase difference between the input stress and response has to be accounted for, in the form:

$$G(i\omega) = G'(\omega) + G''(j\omega) \quad (2-6)$$

where  $G(i\omega)$  is the complex shear modulus, or simply  $G^*(\omega)$ ,

$G'(\omega)$  is the real storage shear modulus,

$G''(j\omega)$  is the imaginary loss shear modulus, or simply,  $G''(\omega)$ , and

$\omega$  is the radian frequency.

The storage shear modulus,  $G'(\omega)$ , can be defined as the stress in phase with the strain in a sinusoidal shear deformation divided by the strain. It is a measure of the energy stored and recovered per cycle, when different systems are compared at the same strain amplitude. The loss shear modulus,  $G''(\omega)$ , can be defined as the stress  $90^\circ$  out of phase with the strain divided by the strain. It is a measure of the energy dissipated or lost as heat per cycle of sinusoidal deformation, when different systems are compared at the same strain amplitude. In the sense of Equation (2-6), the same expression can be applied to complex Young's modulus,  $E^*(\omega)$ , storage Young's modulus,  $G'(\omega)$  and loss Young's modulus,  $G''(\omega)$ .

The complex shear modulus,  $G^*(\omega)$ , can be accurately obtained by setting up a steady state oscillating system with control options on frequency, Ferry (1980), or by using a dynamic mechanical analyzer used in conjunction with a thermal system. The DMA is able to estimate accurately the normal stress at any time within the material over a range of testing temperatures. In the present studies, all tests were carried out at ambient temperature of approximately  $18^\circ\text{C}$ . The dynamic tests are suitable for determining viscoelastic characteristics as a function of frequency. A constant sinusoidally applied force normally loaded the test sample with a 3-point bending mode in the present series of tests, as shown in Figure 2.15. The relationship between force and deformation can be measured. Significant improvements in the capability and ease of operation of the DMA in the late 1980s provide a superior option in the characterization of viscoelastic materials than the traditional oscillatory testing methods. DMA can also be used to analyze both very stiff and very soft materials.

A viscoelastic horticultural material can be defined as nonlinear if it does not obey either Equation (2-3) or (2-4). In particular, for two-phase solid-fluid composite materials such as produce tissues, micro-structural damage is often considered to be the most important source of nonlinear behaviour of such materials, Haddad (1988). These materials are most likely to behave nonlinearly and are often called strain rate-sensitive materials. To account for nonlinearity it is necessary to modify  $G(t)$

in Equation (2-5) to depend not only on time but also on the magnitude of strain  $\varepsilon(t)$ . Thus, a nonlinear form for Equation (2-5) can be expressed as:

$$\sigma(\varepsilon, t) = \varepsilon(0)G(\varepsilon, t) + \int_0^t G(\varepsilon, t - \tau)\varepsilon(\tau)d\tau \quad (2-7)$$

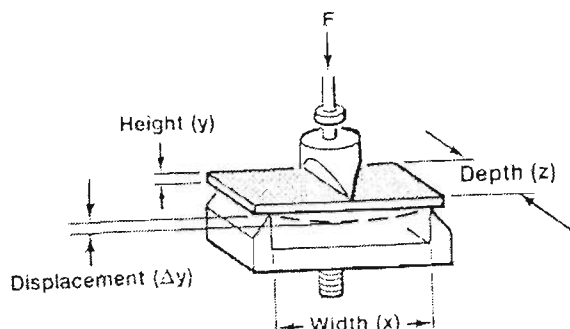


Figure 2.15 A 3-point bending testing mode on test sample by a sinusoidally applied force  $F$  using the dynamic mechanical analyzer. The width ( $x$ ) is 15 mm fixed. From Perkin-Elmer (1995).

As long as the material deformation remains microscopic, Equation (2-7) is valid, owing to the fact that micro-cracks created as a result of deformation are independent of each other and are not linked. Using the DMA, deflections and phase angles under an oscillatory constant applied force can be measured with high precision at corresponding time and frequency of oscillations. Thus, based on calculated values of  $\sigma(\varepsilon, t)$  and  $\varepsilon(\tau)$  in Equation (2-7), an accurate assessment of the values of  $G^*(\omega)$ ,  $G'(\omega)$ ,  $G''(\omega)$ ,  $E^*(\omega)$ ,  $E'(\omega)$ ,  $E''(\omega)$  and  $\tan \delta$  can be achieved. The deflections of the test specimen under the DMA tests are so small (in order of microns) that any initiation of damage due to material instabilities tends to be avoided.

All produce specimens under the DMA frequency test mode were prepared with the same orientation and size of 25 mm width, 10 mm depth and nominal thickness of 4 mm, as in Figure 2.15. Precision thickness DMA readings indicate a roughly  $\pm 0.15$  mm difference in the specimen thickness, owing to the limitation of preparation technique. For example, the thickness for the market-fresh Golden Delicious apple specimens for Runs F02-AP-12-4 and F03-AP-12-4 are actually 4.138 mm and 3.883 mm, respectively. Due to the good repeatability, only one extra test run was performed for each test. All tests were run through the whole operating frequency range sweeping from 1 Hz to 50 Hz. Typically, a set of tests comprises two applied force levels, each level requiring two test runs or two specimens, or a total of four specimens for each set of tests. All these four specimens were prepared from a single fruit, as shown in Figure 2.16, in radial direction. All specimens for DMA tests were prepared with this radial orientation, in the sense of Khan and Vincent (1993).

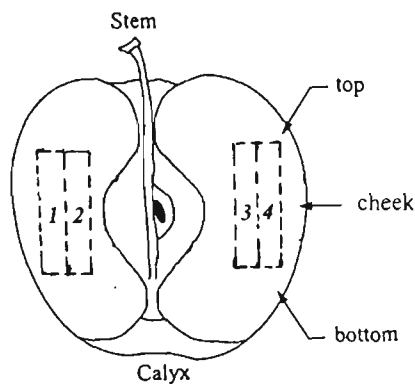


Figure 2.16 Orientation of the 4 cored rectangular produce specimens (25x4 mm) in radial direction. All rectangular produce specimens were prepared with this radial orientation, in the sense of Khan and Vincent (1993).

The timing of all tests was set at 20 minutes for a complete frequency sweep through the operating range. All specimens for each set of tests (with 4 runs) were prepared immediately before the test and sealed in a plastic zip-bag to prevent evaporation and drying.

## 2.2 THEORETICAL CONSIDERATIONS

### 2.2.1 Introduction

Theoretical background that is pertinent to the present study is presented in Section 2.2. It includes an introduction in Section 2.2.2 to postharvest horticultural materials, focusing on the mechanical and structural characteristics of individual cells, particularly those in regions comprising the complex protective skin and the parenchymatous cells immediately underneath.

The deformation characteristics of the horticultural materials under loading are introduced in Section 2.2.3 in terms of the microscopic cell-wall structures and the phenomenological states of these materials such as their solid-like, viscoelastic and liquid-like attributes. These attributes are introduced in terms of the deformation behaviours of the materials within the ‘classical’ context of materials science laws such as elasticity, viscoelasticity, plasticity, viscoplasticity and a combination of any of these.

The characteristics of instabilities in horticultural materials due to damage are presented in Section 2.2.4, focusing on the characteristics of the materials in terms of damage mechanics and the strain softening process. In this last regard, a detailed description is included for the strain energy

density method. This method, based on the effective modulus of the materials, quantifies accurately the state of damage of the horticultural materials.

An introduction is presented in Section 2.2.5 of the cushioning effect of produce skin during impact, based on cushioning theories. In particular, this section attempts to highlight the significance of the relationship between the initial strain rate of deformation and the drop height/skin thickness of the produce. This is followed by an elaboration in Section 2.2.6 to the significance of increasing the impact duration for damage protection of the produce.

An introduction to the internal energy dissipation in produce materials is included in Section 2.2.7. Here, the difference between the processes of energy attenuation or dissipation and energy dispersion is clarified. The significance of the dynamic Poisson's ratio that governs the relationship between shear and longitudinal energies is also included.

The theoretical background concludes with a description of the characteristics of shock pulses generated from real drops of whole-fruits, the wave pulse propagation and dispersion characteristics. In this last regard, the wave pulse can be transformed into other forms of energies.

## **2.2.2 Postharvest Horticultural Materials**

Harvested fruit and vegetables are living structures that continue to perform metabolic reactions and maintain their physiological systems. Respiration and transpiration continue after harvest, and the produce depends entirely on its own food reserves and moisture content. Losses of respirable substrates and moisture are not made up and deterioration, or senescence, commences. This is a degradative catabolic process that leads to progressive disorganization of the metabolic apparatus of the cells and finally death of the tissue. Most of the solid matter of fruit and vegetables is made up of carbohydrates such as sugar and starch, along with smaller amounts of protein and fat. Included in these groups are the constituents which build up the main structural features of horticultural tissues, including the cell walls, which are layers of living cytoplasm with storage starch, and cell sap, as shown in Figure 2.17. For the purpose of physical analysis, a simple model as shown in Figure 2.18 can represent a typical turgid cell of fruits and vegetables. The cell comprises an osmotic solutes in the cell sap which is surrounded by a cell membrane called plasmalemma that separates the outer cell wall and the inner cytoplasm and moisture content in cell sap, see Wills *et al.* (1981). This membrane, which is highly viscoelastic and exerts very little or no resistance to deformation, is

permeable to water but is impermeable to osmotically active solutes. The properties of the cell wall, together with the osmotic forces exerted by the cell, determine the extent and rate of normal cell expansion that is crucial during the process of bruising and impact damage.

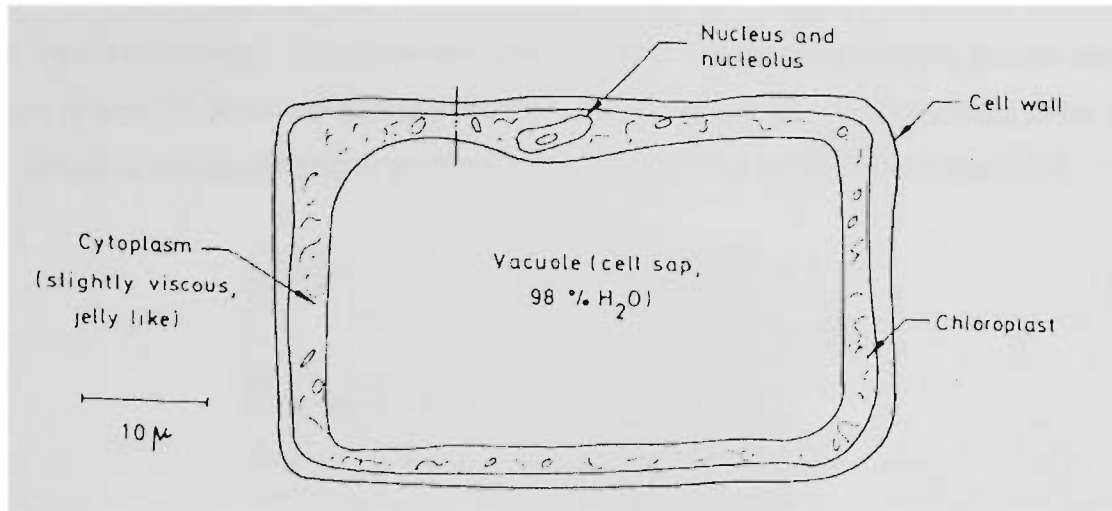


Figure 2.17 Typical plant cell of fruits and vegetables. From Akyurt *et al.* (1972).

The mechanical properties of the cell are regulated by the metabolic activities of the cell, and keep changing during the postharvest lifetime of the produce. The rate and extent of such changes depend on the physiological role and stages of maturity of the produce. These properties are highly dependent on the moisture stored in the cell sap. The most abundant constituent of fruit and vegetables is water. This water content, which often exceeds 98% of the volume of cell sap within a cell, assumes a characteristic maximum value that is associated with a state of complete turgor, or turgidity, of the cell. The turgor pressure of the cell sometimes exceeds 9 atmospheres, see Duckworth (1966). This characteristic condition is reached when the inward pressure of the fully extended cellulose cell wall exactly balances the turgor pressure, developed as a result of osmotic forces. This is the condition in which the tissue is physically incapable of absorbing any more water through osmosis.

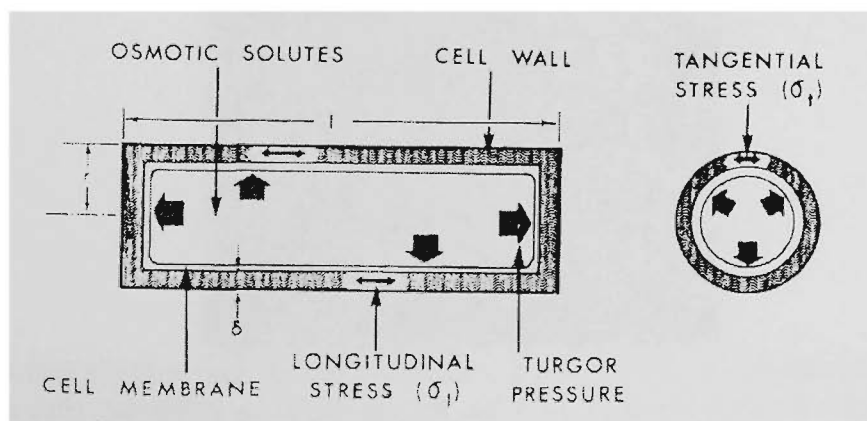


Figure 2.18 Diagrammatic representation of a model turgid cell. From Lockhart (1965).

In general, it is desirable to harvest produce when this maximum possible water content is present. However, it is under this condition that the produce is most susceptible to bruise damage, as the cell walls are stretched to the limit. The extent of bruise damage depends on the structure and thickness of cells, particularly those of the epidermis, or skin, where the highest loading due to impact is expected to occur. The epidermis comprises the outermost cell-layers that are structurally modified to protect the structural integrity of the surface section of the produce. Some of the skins are hard and complex, such as the highly protective seed coat of peas as shown in Figure 2.19.

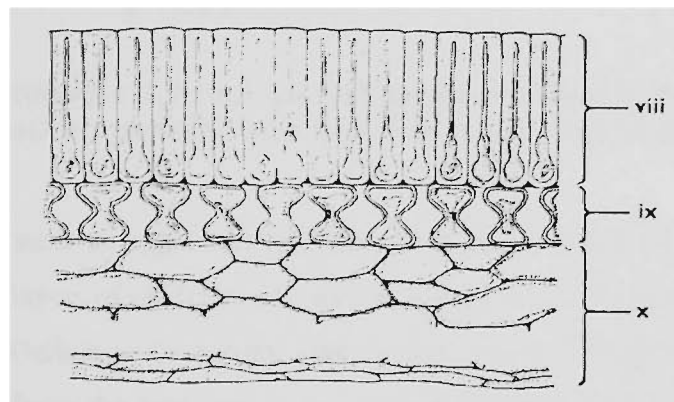


Figure 2.19 Typical complex skin or seed coat of a pea: Layers *viii* (sclerenchyma) and *ix* (collenchyma) are separate structures of the skin. From Duckworth (1966). (Not to scale)

Most vegetables have well-structured protective cushion layers of epidemic cells which can minimize bruise damage by acting as a damper against impacts. Examples are cucumber in Figure 2.20, and potato in Figure 2.21. The strongly cohesive skin helps to prevent skin fracture or cracking under dynamic loading.

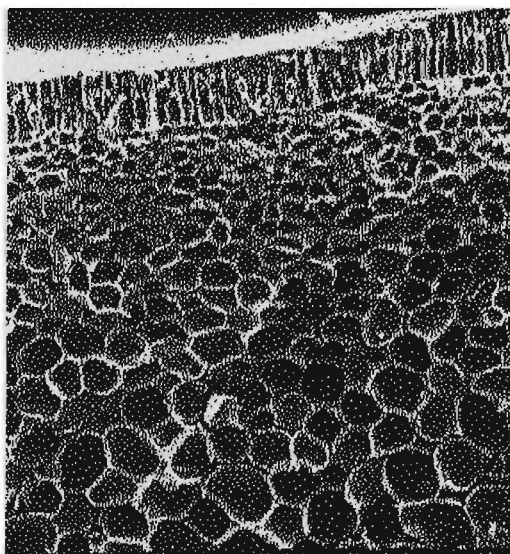


Figure 2.20 Scanning electron micrograph (SEM) of a cross-section of cucumber fruit, showing the parenchymatous cells increasing in size at greater distances from the strongly cohesive epidermic cells of the skin (X160). From Smith (1978).

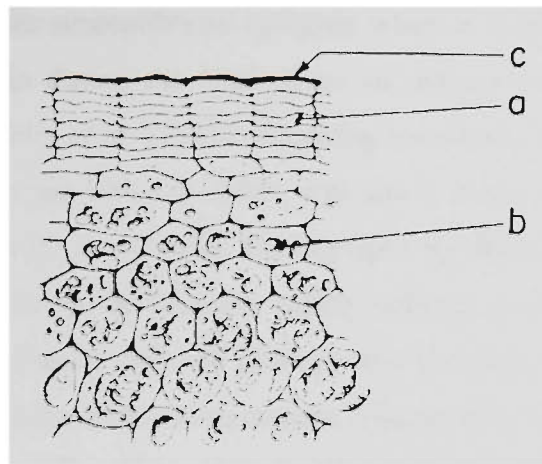


Figure 2.21 Complex protective skin of potato with layers of **c** - cuticle; **a** – cork or epidemic section called collenchyma; and **b** – parenchyma or flesh with starch. From Muller (1948). (Not to scale)

Other produce such as apple has relatively thin single layers of water-insoluble protective cuticle on top of single layers of epidermis, as shown in Figure 2.22. Some produce has a thin layer of cuticle on the surface. Cuticle is the natural coating that acts as a major barrier to water loss in the form of water vapour from the produce. It consists of saturated hydrocarbon or natural wax and hydroxyl acids. Cuticle does not provide material strength to the produce. On the other hand, the single- or multi-layer epidermal cells (called collenchyma) shown in Figure 2.22 provide a structural protective ‘membrane’ which can prevent the occurrence of fracture under shear stresses during dynamic loading. Another example of ingenious protective structures can be found in grape berries, each of which is enclosed by a spherical grid called dorsal bundle network embedded in the cuticle, see Coombe (1987). The grid causes any heavy loading to be spreaded out quickly and evenly, thus minimizing chances of bruising.

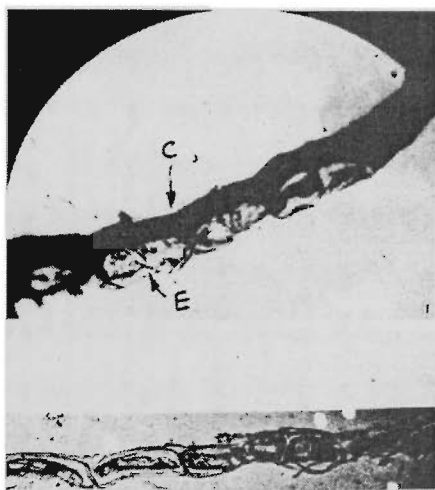


Figure 2.22 Cross-sectional view of skin structures of Granny Smith apple: (top) cuticle-**C** and epidermis-**E** (X 480) and (bottom) epidermic cells (X 520). From Huelin and Gallop (1951).

Produce flesh is more susceptible to splitting when it starts to ripen. Produce ripening is generally considered to begin during the final stages of maturation and to be the initial stage of senescence, according to Willis *et al.* (1981). Ripening transforms produce from a physiologically mature but inedible state into one which is edible, with much starch in the produce tissues converted into sugar during the process for many fruits. During ripening, textures that normally become softer are associated with a reduction in the firmness widely believed to be due to changes of the pectic substances of the produce. Fleshy cells of produce are primarily held together by these pectic substances (called pectinic acid) which acts as cement. The pectin composition largely determines the firmness with which adjacent cells adhere to each other, which in turn has important bearing on the overall textural characteristics of the produce, according to Duckworth (1966).

During ripening, however, pectic substances undergo qualitative changes resulting in progressive solubilization and depolymerization of these substances, see Duckworth (1966). This is arguably the most significant change associated with the overall mechanical properties of produce, as demonstrated by the softening of texture commonly found in ripening fruits such as apples. During ripening, the insoluble pectic substances become gradually soluble, believed to be triggered by enzyme actions, see Dilley (1970). More recent works can be referred to Jarvis (1984) and Tucker (1993). The pectic substances change through depolymerization, as recently demonstrated as a fenestration process of the substances by Glenn and Poovaiah (1990). Like in apples, softening is also associated with the dissolution of the middle lamella in pears, and in addition a gradual disintegration of fibrillar material throughout cell walls as well, see Ben-Arie *et al.* (1979).

One of the natural substance that triggers the ripening process of most fruits is ethylene, see McGlasson (1970) and Jobling (1993). The rapid increase in ethylene production in produce which signifies the beginning of ripening seems to be associated with detached fruits and the disappearance of some natural constraints to ripening. Earlier reports of the presence of the endo-polygalacturonase enzyme, which has been speculated to be a trigger of fruit ripening, see Jarvis (1984), has not been consistently substantiated by recent workers, see, for instance, Abeles and Takeda (1990). A lot of research has been focused on controlled atmosphere storage and packaging in order to retard ripening in terms of temperature, humidity, oxygen supply and other controlling factors, Spencer (1965). As has been a commonly accepted practice, it is significant to farmers in harvesting fruits at the right time according to the optimum conditions of the fruits based on their fruit firmness determined by a fruit pressure tester such as the Magness-Taylor tester.

### 2.2.3 Characteristics of Deformation in Horticultural Materials

The response of horticultural materials such as apples to external quasi-static loads, often called creep, is illustrated in Figure 2.23. It shows a typical deformation-time history of a whole Rome Beauty apple under a constant stress, which can either be dead load or step stress. Immediately upon loading, an instant elastic strain,  $\epsilon_e$ , occurs in a very short time interval. This corresponds to a deformation up to point *A* in Figure 2.23. Then, the deformation trend follows a seemingly exponential curve towards a constant maximum strain value. When the external load is removed, this deformation is only partially recoverable. The recoverable part of the strain behaves viscoelastically, while the unrecoverable strain is plastic deformation. The overall strain caused by this time-dependent viscoelastic/plastic deformation is commonly referred to as creep strain,  $\epsilon_c(t)$ , with  $t$  denoting the time lapsed. The strain response curve in Figure 2.23 is the result under quasi-static conditions only. If transient loading causes the deformation, there will be two more instantaneous strains as a result of the dynamic effects. They are often called the instantaneous plastic strain,  $\epsilon_p$ , and the strain due to inertia effects,  $\epsilon_i$ , or simply inertia strain. Within the recoverable portion of strain, the inherent viscoelastic character of most horticultural materials can be illustrated as shown in Figure 2.24. Viscoelastic materials possess memory effect that distinguishes them from perfectly elastic materials.

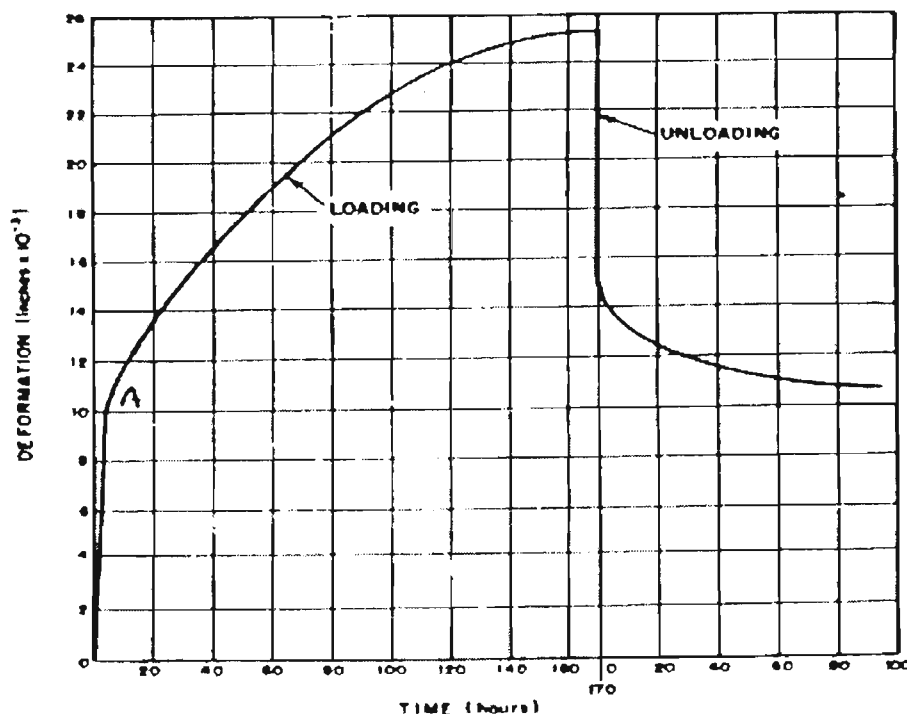


Figure 2.23 Creep test showing deformation time history of a whole Rome Beauty apple. Units in  $\times 10^{-3}$  inches of deformation versus time in hours. From Mohsenin *et al.* (1962).

Some horticultural materials are characterized within their fully recoverable portion of strain by viscoelastic deformation that varies with time, or time-dependent with changing deformation gradients.

In this case the applied stress depends not only on the instantaneous value of the deformation gradients, but also on the complete previous histories of the deformation gradients. New deformation gradients ‘memorize’ all previous gradients and superpose themselves onto the previous ones, as shown by the additional creep in Figure 2.24. However, past deformations have less influence the longer the lapse of time. This is normally recognized as the phenomenon of fading memory or the ‘principle of superposition’ proposed by Ludwig Boltzmann in 1874. In Figure 2.23, the unbruised portion of the apple under the applied load still retains all the inherent viscoelastic characteristics of the fruit material. After the removal of the applied load, all viscoelastic strains as a result of the applied load dissipate exponentially towards the original state as they ‘memorize’ their initial values. This is valid for viscoelastic materials that are classified as solids or liquids. To be exact, the solids here include solid-like, or arrheodictic materials, which besides solids, also comprises viscous elements, but show no evidence of viscous flow, in the sense of steady-state fluid-flow under an applied load.

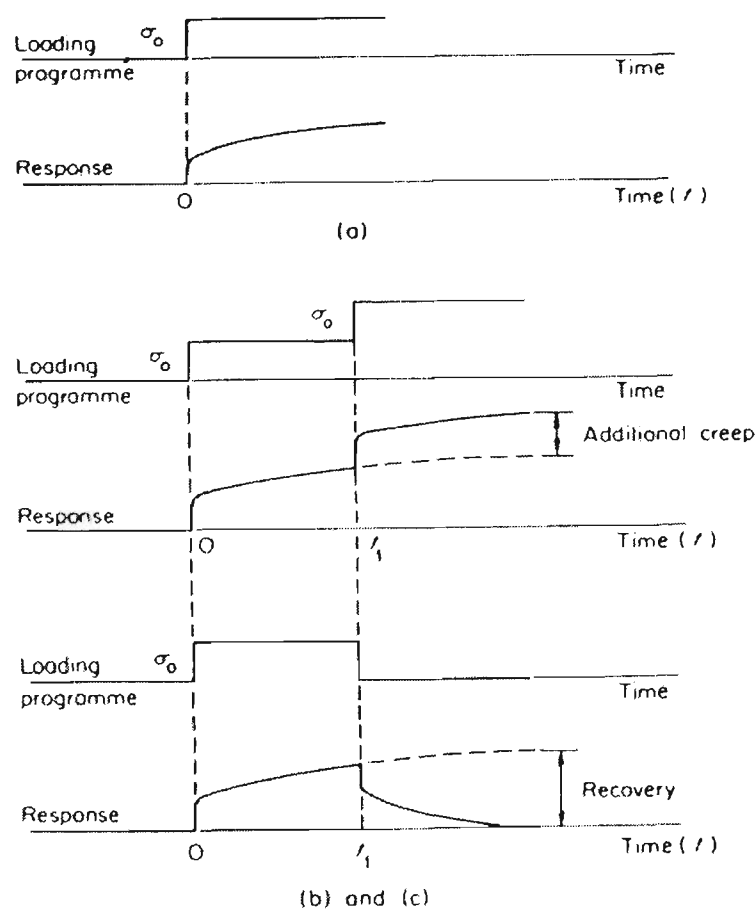


Figure 2.24 Viscoelastic time ( $t$ ) response of strain ( $\epsilon$ ) of materials under constant stress ( $\sigma_0$ ).  
From Ward (1990).

Solid-like horticultural materials are in general structurally closed-cell fluid-solid composites. The contents of one of their cells consist primarily of water in the form of a continuous jelly-like liquid phase called cell sap, Scott Blair (1974). It is protected by the fibrous cell wall, which acts as the main

structural constituent of the cell. The cell-wall structure is mainly composed of cellulose, which are  $\beta$ -glucose polymeric micro-fibrils called  $\beta$ -1-4-linked glucans, Brett and Waldron (1996). Plant cells and natural fibres, being polymeric in nature, cannot be digested by humans. The cellulose micro-fibrils on the cell walls are held together by strong hydrogen bonds, see Bacic *et al.* (1988) and Tucker (1993). The micro-fibrils are embedded in and extensively linked to the pectin matrix on the cell wall through non-covalent bonds, Jarvis *et al.* (1981). These links are much weaker than the hydrogen bonds that bind the fibrils, allowing debonding activities to occur between the fibrils and their matrix under sliding friction when the cell walls are under dynamic loading. The debonding activities result in fibrillar slippage that has been postulated since Hort and Schoorl (1982b) but few experimental studies have been reported to confirm these activities.

Common elastic and viscoelastic solids include many polycrystalline materials such as metals, rock, ceramics, and ice and, in some cases, crystalline polymers, Tobolsky (1958). Polymers can exist in amorphous form, Figure 2.25a. In most cases, they are semi-crystalline in either disoriented, Figure 2.25b, or in oriented form, Figure 2.25c, according to Alfrey (1948). The latter is particularly significant in the studies of produce cell walls because in most cases they appear in this form. As for the amorphous polymeric materials shown in Figure 2.25a, examples abound in many fibre-reinforced composite (FRC) materials such as particleboard composites. Many relatively inexpensive FRC materials are amorphous in nature. Only in high-technology fields do we expect to use highly oriented high-tensile fibre composite structures. However, the multi-layered, well-oriented cell wall structures of horticultural materials are arguably more sophisticated in design than the most expensive carbon-fibre aerospace composites available. The high degree of structural complexity of the fibrillar cell walls had been suspected but not clearly demonstrated until by the defining work of Roland and Vian (1979). Captured images of the multi-layered sheath characteristics of the cellulose micro-fibrils are illustrated for onion in Figure 2.26.

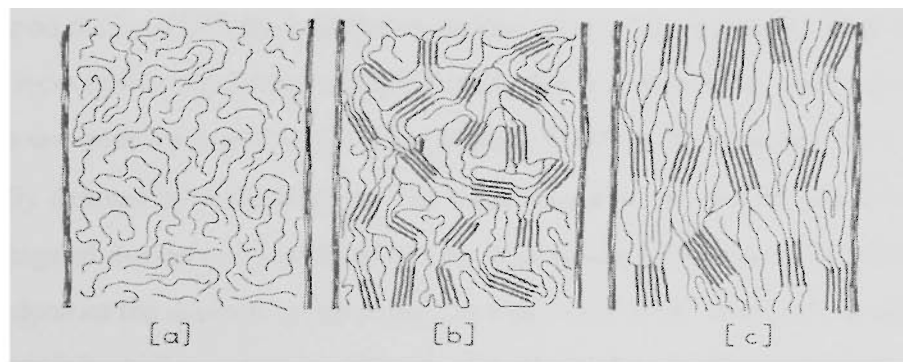


Figure 2.25 Schematic diagrams showing structures of (a) amorphous polymer (thermoplastics or thermosets), (b) disoriented semi-crystalline polymer (thermoplastics), and (c) oriented semi-crystalline polymer (thermoplastics). From Alfrey (1948).

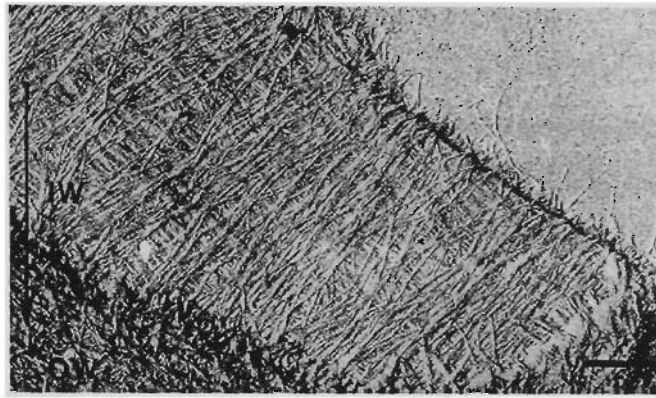


Figure 2.26 Transmission electron micrograph (TEM) of fractured onion root-hair cell wall. The micro-fibrils of the inner part of the wall (IW) are  $45^{\circ}$  to the long axis (long arrow), and successive layers appear to be at  $90^{\circ}$  to each other. The (darker colour) micro-fibrils of the outer wall (OW) appear to have a random, or amorphous, texture. (X 10,500) From Giddings and Staehelin (1991).

Rheodictic (liquid-like) materials include pure liquids, viscoelastic liquids such as polymer melts, as well as some soft horticultural materials. Examples include persimmon fruit tissues that exhibit steady-state fluid flow under intensive loading. Flow within these materials under transient deformation is sustained unless the load is removed. In such extreme conditions of material flow, materials do not have a preferred configuration but tend to be liquid-like. At the instant when they totally lose their ability to resist shear deformation, they can no longer be characterized by their dynamic stress-strain responses. At this stage, they are totally in a fluid-state and they are best characterized in terms of their thermodynamic state such as the equations of state as illustrated by pressure-volume diagrams.

Phenomenologically, the dynamic deformation characteristics such as displacement of the liquid-like materials differ sharply from elastic/viscoelastic displacement of the solid-like materials. Here, 'flow' is a more appropriate word than 'displacement'. For solid-like materials, there will be no flow if an equilibrium state of deformation is achieved. Work is done upon the material by the stress only in the transient period during which the equilibrium deformation is being attained. This work is stored up in the material as recoverable free energy of deformation. On the other hand, during the flow of liquid-like materials, a non-equilibrium state will be established, which is characterized by a constant rate of deformation usually denoted by a constant  $\dot{\epsilon}$ . The significance of the almost invariant  $\dot{\epsilon}$  for produce during the early stage of dynamic deformation can be illustrated by their pre-critical displacement time histories. Work is done on the material continuously, as long as the shear stress acts on the material under predominantly shear deformation. It flows under any distortional stress, however small.

Solid-like materials flow only if their yield stress is reached or exceeded. Apart from this ‘restriction to flow’ (or yield stress) for solid-like materials, the fundamental flow characteristics of both the solid-like and liquid-like materials in terms of their stress and strain rate are basically invariant only if the flow in both materials are under steady-state flow. This is illustrated in Figure 2.27. Even for solid-like horticultural materials, the bulk of the material is liquid-based cell sap as denoted by the 90%-plus of total weight of water in a cell. The primary barrier to flow is due to the yield strength of the cell wall. Once the flow barrier is removed, a steady-state flow can be established when the bruised tissues are transformed into liquid-like forms. For crystalline solids such as metals, the flow barrier is also due to other features such as drag mechanisms of the dislocation process of materials under plastic deformation, Meyers (1994). But, regardless of the existence of any extra features, a steady-state flow can always be achieved if the materials, be it metals, plastics, solid-like or liquid-like horticultural materials, are totally in a liquid state.

Based on experimental results solid-like horticultural materials may be classified according to their pre-critical dynamic characteristics. If the produce cell walls are structurally homogeneous, their deformation is primarily under viscoelastic, elastic/perfectly-plastic or viscoplastic processes. In other words, their deformation behaviour can be described under the broad context of the material science laws of elasticity, viscoelasticity, plasticity and viscoplasticity. The most common characteristics are as follows:

- (i) Viscoelastic-then plastic-then perfectly-plastic:
  - is described by a continuous viscoelastic-then-plastic stress-strain curve up to the ultimate strength of the material. A horizontal curve denotes a perfectly-plastic deformation. One example for this kind of deformation is shown by the horizontal stress-strain curve under a strain rate of 1% per minute in Figure 2.27. By multiplying the relaxation time (of 1 minute) with the strain rate of 1% per minute, a strain of 1% can be achieved at which the yield stress occurs. This is the stress level where the shift of viscoelastic-to-plastic deformation occurs. This fundamental shift from the viscoelastic to perfectly-plastic process denotes a transformation of the material from an arrheodictic (solid-like) state to a rheodictic (liquid-like) state.
  
- (ii) Elastic-then plastic-then perfectly-plastic:
  - is described by the same processes as in (i) except that the initial loading curve is denoted by an elastic deformation instead of a viscoelastic one. Thereafter it follows a horizontal perfectly-plastic curve similar to the situation in (i).

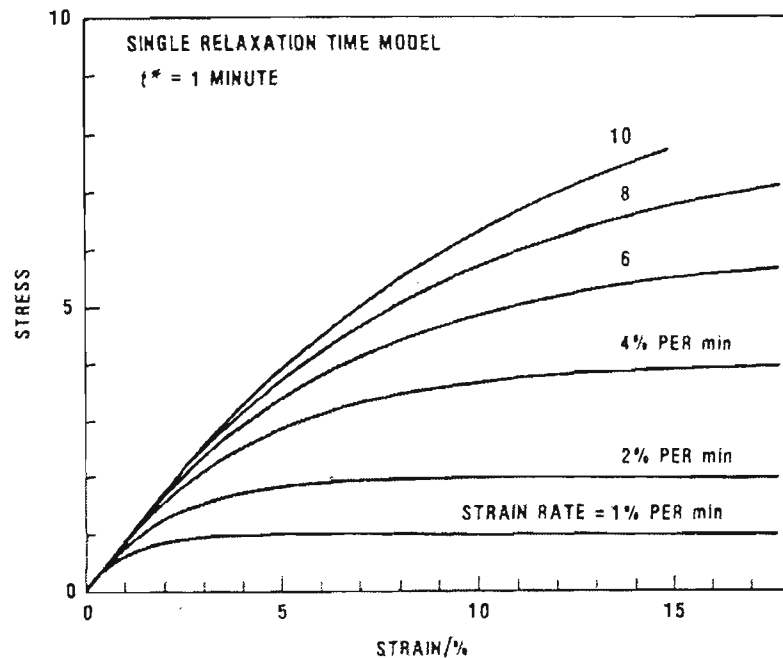


Figure 2.27 Stress-strain curves produced by a material model with only a single relaxation time under elastic/viscoelastic, plastic or viscoplastic deformation as denoted by their curve shapes and strain rates. From Matsuoka (1986).

(iii) Viscoplastic:

- is characterized by some of the stress-strain curves in Figure 2.27 under relatively high strain rates, for instance, those with  $\dot{\epsilon}$  of 8% and 10% per minute. These curves are characterized by their high dependency to strain rates, or rate-sensitivity. Under a genuine viscoplastic deformation, each curve is a unique stress-strain record with respect to a particular strain rate. Another important aspect of viscoplastic deformation is the absence of a distinct yield-point. This is illustrated in Figure 2.28.

The elastic and viscoplastic regime is denoted by the equipotential yield surface,  $\Omega$ , with  $\Omega$  greater than 0. Unlike the plastic case, where  $\Omega$  equals 0, in the case of viscoplastic deformation the yield surface is denoted by the rings which change in shape according to the applied strain rate, with  $\Omega$  varying from slightly greater than zero to infinity. This corresponds to strain rates of slightly greater than zero to infinity. For horticultural materials, a distinctive yield-point, no matter how small, is believed to exist in most cases. This can be illustrated with an imaginary solid-phase equipotential cylinder shown in Figure 2.28 with an extremely small diameter. In this sense, the yield-point is a genuine material property. This is not to be confused with the 'bio-yield point' which is a direct result of material instabilities such as cracking, fracturing, bifurcation or the formation of shear bands in the

materials. However, both the material deformation and instabilities can co-exist under dynamic loading and the processes are complex.

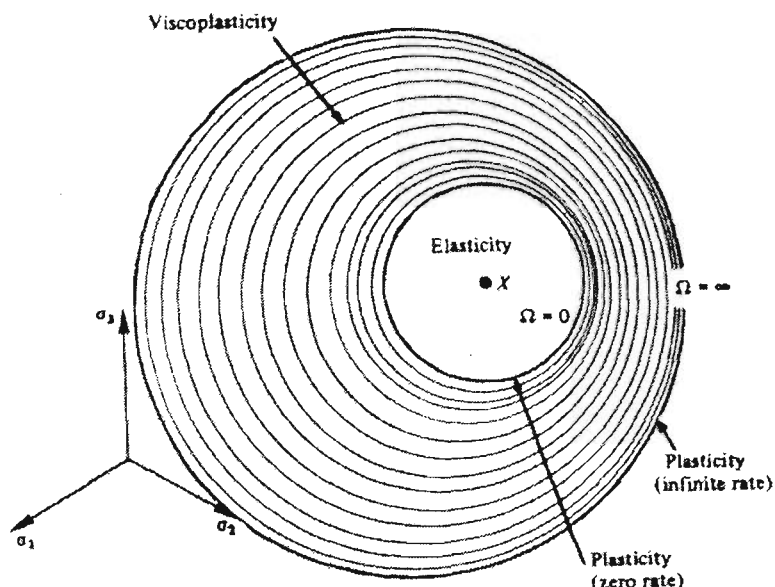


Figure 2.28 Schematic diagram showing equipotential yield surface ( $\Omega = 0$ ) and flow surface ( $\Omega \neq 0$ ) by looking from the centre  $x$  toward the origin of the  $\pi$ -plane. The 'rate' in this Figure denotes 'strain rate'. From Lemaitre and Chaboche (1990).

Ludwik (1909) was probably the first person who observed that, during the deformation of many materials, higher stresses would produce higher strain rates for a fixed plastic strain, as shown in Figure 2.27. Based on the simplest linear viscoelastic theory, Figure 2.27 has been modified by Matsuoka (1986) to accommodate changes of strain rates by the following expression:

$$\sigma(\dot{\epsilon}) = E_0 \dot{\epsilon} t^* \left( 1 - e^{-\frac{\epsilon}{\dot{\epsilon} t^*}} \right) \quad (2-8)$$

where  $E_0$  is Young's (unrelaxed) modulus,  $t^*$  the relaxation time, and  $\dot{\epsilon}$  the strain rate. Figure 2.27 was actually plotted using Equation (2-8) with different values of  $\dot{\epsilon}$ . The stress-strain curve has an initial slope  $E_0$ . The slope decreases conspicuously at a strain  $\epsilon = \dot{\epsilon} t^*$ . In this Figure, we note that, at low strain rates, the dynamic curve approaches the elastic/perfectly-plastic mode. However, in the case of deformation similar to some of the soft produce characterized with perfectly-plastic deformation, strain rates have no effect on the dynamic curve. This is because the strain will be insensitive to any stress increment on the horizontal region of the dynamic stress-strain curve. This perhaps can illustrate the inadequacy of using only the viscoelastic theories, instead of plastic and viscoplastic theories for a full description of the deformation of soft produce. Based on plasticity and viscoplasticity theories, when the strain rates are non-zero, the deformation process for soft produce becomes viscoplastic. This can be shown in Figure 2.29.

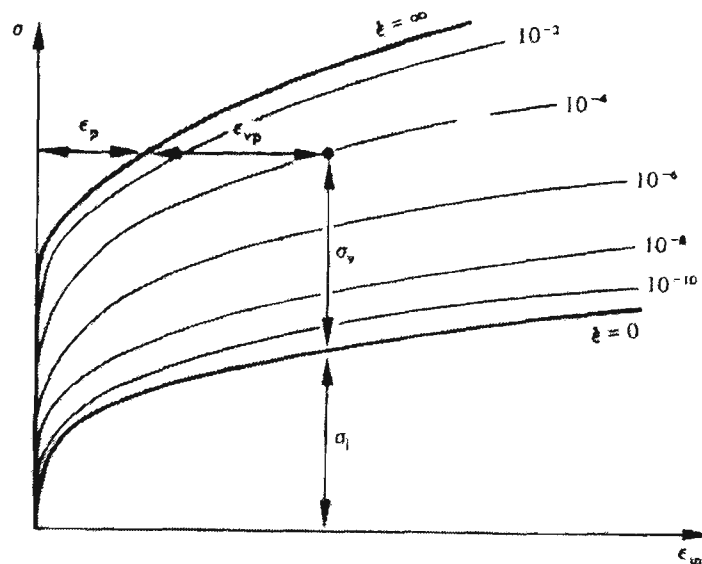


Figure 2.29 Schematic diagram showing stress-(inelastic) strain curve of the superposition of both the plasticity ( $\dot{\epsilon} = 0$ ) and viscoplasticity ( $\dot{\epsilon} \neq 0$ ) theories. From Lemaitre and Chaboche (1990).

In this case, the total stress can be subdivided into two components:

- (a) internal stress,  $\sigma_i$ , which is inside the domain of elastic/viscoelastic deformation and rate-independent; that is, viscoplastic dissipation potential,  $\Omega = 0$ , and
- (b) viscous stress,  $\sigma_v$ , which is inside the domain of plastic/viscoplastic deformation and rate-dependent; that is,  $\Omega \neq 0$ .

The total strain can be subdivided into two components:

- (a) elastic strain,  $\epsilon_e$ , and
- (b) inelastic strain,  $\epsilon_{in}$ , which comprises plastic strain,  $\epsilon_p$ , and viscoplastic strain,  $\epsilon_{vp}$ .

This was shown in Figure 2.28 in terms of yield and flow surfaces.

From Figure 2.28, for that produce with very soft textures, the central solid cylinder would be negligibly small. For the more crisp ones, their cylinders are larger, and they are comfortably accommodated by Von Mises yield criterion, as shown in Figure 2.30. For those cases with high fracturing tendencies, Tresca criterion is more appropriate, see Figure 2.30. Except perhaps for plastics and some biomaterials, the modelling of dynamic viscoplasticity and plastic yielding lags behind comparable studies in metals and solids. This is certainly true in the case of research in horticultural materials. A 'unified' theoretical description of the dynamic behaviour of biomaterials in general and agricultural materials in particular is yet to be achieved. Crisp produce textures are in general more susceptible to pre-peak and peak instabilities as well as post-peak macro-cracks which will have profound consequence to the post-peak dynamic stress-strain characteristics.

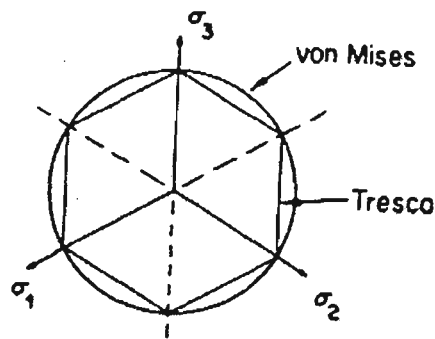


Figure 2.30 Schematic diagram showing Von Mises and Tresca yield surfaces toward the origin of the  $\pi$ -plane.

#### 2.2.4 Characteristics of Instabilities in Horticultural Materials due to Damage

The occurrence of instabilities like skin cracking and flesh splitting during the deformation of horticultural materials has been widely observed. In order to distinguish the different causes of these instabilities in horticultural materials, one would begin to question the state of structural integrity of the produce cell walls during deformation, particularly under high loading conditions. With these cell walls being polymer-based natural composite materials, one may ask whether the long-established failure mechanisms in resin-based fibre-reinforced composites (FRC), namely fibre-breaking, matrix cracking, and debonding, also act in a similar way in horticultural materials.

Unlike the FRCs, the situation in the case of horticultural materials is believed to be more complex. This is because the size factor in the case of horticultural materials would play a decisive role during the inducement of instabilities in these materials. This fact is not difficult to recognize since the matrix and the imbedded micro-fibrils that make up the cell walls can only be described microscopically. In other words, in the sense of the FRC failure mechanisms in horticultural materials, the micro-cracking of the cell walls by the breaking up of micro-fibrils, matrix micro-cracking and/or micro-fibril slippage would be sensitive to the size effects. The direct effect of this sensitivity is that the progress of and the consequence due to the instabilities in horticultural materials will be different under microscopic, mesoscopic or macroscopic events.

In the sense of stress-strain characterization, we can define the occurrence of the material failure as the critical, or peak, stage at which the ultimate strength of the horticultural materials is reached. As in

the case of FRCs, this is the critical point at which the bulk of the micro-fibrils snap or debond. Before reaching this critical stage, the primary failure mechanism can only be the debonding or slippage of the micro-fibrils. Unlike FRCs, the matrix cracking mechanism in the produce cell walls is not as well defined. The covalent and non-covalent cross-links between the micro-fibrils and the glucan matrix are extremely complicated and are not yet fully recognized, Brett and Waldron (1996). Both the micro-fibrils and the glucan matrix are long-chain polymers, intermingled with cross-links, Fry (1989). Thus, it is accurate to describe the pre-peak mechanism as a ‘generalized’ micro-cracking phenomenon, rather than in separate matrix cracking and micro-fibril slippage processes, as these processes are indistinguishable.

All of these three failure mechanisms cause ‘permanent’ damage to the material. This has to be distinguished from the permanent plastic deformation in the materials. Massive plastic deformation of horticultural materials is possible only in the macroscopic debonding between two adjacent cells at their common middle lamella, a plastic pectin cement which glues produce cells together, see the comprehensive review by Jarvis (1984). Both phenomena can occur in horticultural materials, as can be seen for the case of apple cells in Figure 2.31. Many fruits and vegetables tend to be mealy and become soft when aged. They become more plastic with massive cell-to-cell debonding tendency under loading, as the middle lamella glue gradually dissolves during the fruit maturation, Ben-Arie *et al.* (1979). A TEM of a cross-section between apple cells is illustrated in Figure 2.32, showing the presence of the middle lamella bonding two adjacent cells.

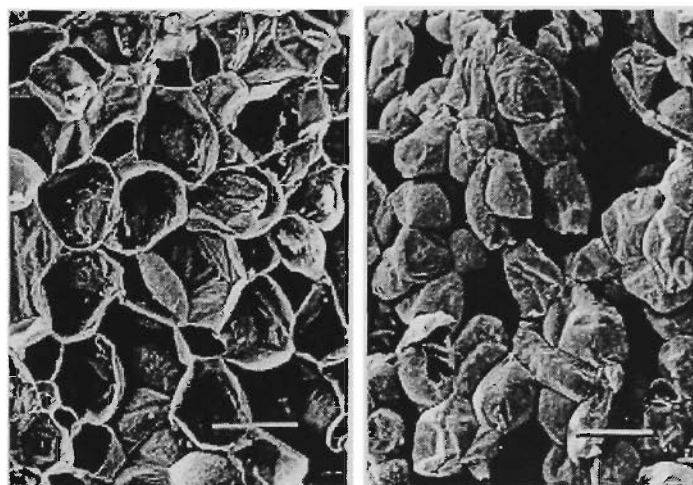


Figure 2.31 Scanning electron micrograph (SEM) of fracture surfaces in apples. (a) A crisp Granny Smith apple: most parenchyma cells have been broken open, releasing juice. (b) A mealy Cox Orange Pippin apple: most parenchyma cells remained intact, thereby retaining juice and giving a dry mouth-feel. (X400) Bars, 200  $\mu\text{m}$ . From Brett and Waldron (1996).

During the pre-critical stage, both plastic deformation and damage of the cell walls may co-exist, Figure 2.33c, but they are independent processes. The former one is governed by plasticity theories, the latter by theories of damage mechanics. There will be no change to the Young’s modulus,  $E_0$ , of the

materials under plastic deformation, Figure 2.33b. Under damage processes, however, their modulus, commonly called effective modulus,  $E$ , will decrease, Figures 2.33a and 2.33c.  $E$  will degrade gradually as the level of damage intensifies. The instantaneous value of the gradually diminishing  $E$  can effectively serve as a measure of the extent of damage in the material.

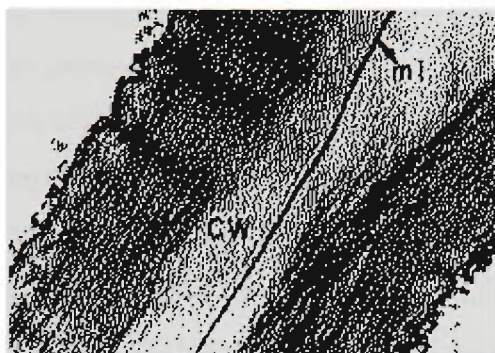


Figure 2.32 TEM showing cell wall (CW) and oriented micro-fibrillar network and the presence of the middle lamella (ml) at transverse section of parenchyma cells from Granny Smith apple specimen. (X 10,260) From Rodriguez *et al.* (1990).

Horticultural materials are more susceptible to damage than metallic solids. Size and shape factors may lead to buckling and other instabilities, Chu and Peleg (1985). Loading conditions may initiate micro-crack formation, leading to catastrophic fracture. Worse still, these damage factors are often interrelated. For instance, a meso-crack is an interim slit of micro-cracks in the processes of linking together, but before appearing as a primary and catastrophic macro-crack. For a produce test specimen under an applied load, if the material-to-slit size ratio (MSR) is large, the damage potential to the specimen is negligible. This is because the loading process can be regarded as a global phenomenon with minimum adverse effect from the stress-concentration around the meso-crack. On the other hand, if the MSR is small, the whole specimen will be affected by the stress-concentration around the meso-crack. The loading process now becomes a local process and the damage potential can suddenly increase significantly.

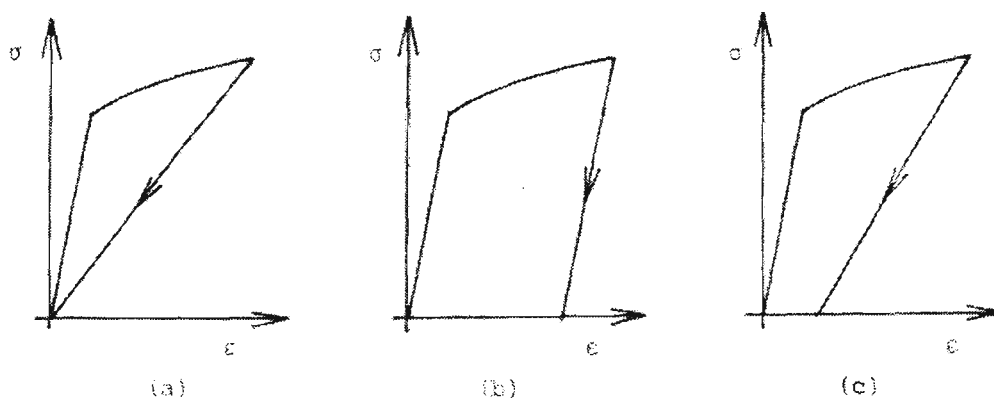


Figure 2.33 Schematic stress-strain diagrams showing unloading paths as a result of: (a) pure damage; (b) pure plastic deformation; (c) coupling of the two processes. From Hult (1988).

It seems there has been some confusion in distinguishing the processes of plastic deformation and damage within the context of the mechanical responses of produce. The current concept of regarding the onset of plastic deformation is that permanent damage occurs as the impact pressures, or stresses, exceed a so-called 'dynamic yield pressure' (DYP) of the tissue, Mohsenin (1986). A recent query by Hyde (1997) regarding the validity of this concept shows that if this were true, then the DYP can serve as one of the critical impact damage parameters. In reality DYP can be the consequence of either one of these two processes, that is, plastic deformation and damage, or both. If the damage process dominates, an estimation of the damage parameter becomes necessary. Therefore, DYP is no more than the direct outcome of (i) instabilities due to damage such as micro-cracking, and/or (ii) instabilities due to plastic deformation such as shear banding. Research efforts should be more appropriately focused on the containment of instabilities, rather than attempting to quantify, uphold or reject the DYP or any other similar hypothetical variables.

#### 2.2.4.1 Damage Mechanics

An approach called damage mechanics has been proposed to quantify material damage in a seminal paper by Kachanov (1958). This approach, taking into account the degree of damage as a result of weakening of the materials strength due to micro-cracks and micro-cavities, is particularly suitable in the elaboration of some post-critical mechanical response of materials such as the strain softening process. The concept can be conveyed in terms of the range of material damage,  $\psi$ , such that  $\psi = 0$  corresponds to a virgin state with no damage, and  $\psi = 1$  corresponds to complete failure of the material with no remaining load-carrying capacity.

Kachanov (1958) initially postulated the concept that  $d\psi/dt = -C [\sigma / \psi]^v$ , where  $C$  and  $v$  are material constants and  $\sigma$  here denotes tensile stresses. He introduced the concept of material 'continuity' in terms of  $\psi$ . Later, a dimensionless, scalar quantity  $\omega'$  ( $= 1 - \psi$ ) which is often called the Rabotnov damage parameter has been used to denote the degree of material damage by relating the original cross-sectional area,  $A_0$ , of the material to its new cross-sectional area,  $A(\epsilon)$ , see Rabotnov (1969). The decreased new cross-sectional area is due to the formation of cavities and micro-cracks under an applied tensile load, in the form of  $\omega' = A(\epsilon)/A_0$ . The effective modulus,  $E$ , was defined by Lemaitre and Chaboche (1978) as:

$$E = \frac{\sigma_f}{\epsilon}, \text{ or, } \omega' = \frac{E}{E_0} \quad (2-9)$$

where  $\epsilon = \ln [A(\epsilon)/A_0] = \ln \omega'$ , is the strain,

- $\sigma_f$  =  $\sigma_0 \{e^\epsilon / (1-\omega')\}$  is the effective stress (sometimes called net stress),  
 $\sigma_0$  = initial (fictitious normal) stress, and  
 $E_0$  = Young's modulus.

The extent of complication for the new effective area,  $A(\epsilon)$ , will be heavily dependent on the porosity of the material. When a test specimen is under tensile loading, micro-elliptical cavities and, to a minor extent, sharp micro-cracks, as shown in Figure 2.34, will be formed within the material body, Hult (1988). If the loading is compressive, free volumes such as those shown in Figures 2.34 are not normally observable. However, free surfaces in the form of micro-cracks are formed and they provide a good measure of the extent of damage in terms of the effective area,  $A(\epsilon)$ .

With the many material parameters involved for the monitoring of material damage, it is always desirable to correlate all the parameters involved in the damage process in the simplest form possible. This can be achieved, for instance, with a characteristic damage parameter such as the crack length versus damage, if the material undergoes fracturing. For a selected parameter which is able to represent the damage, or, more specifically, to represent the effect of micro-defects on the elastic properties of an effective continuum, the parameter needs to be observable, identifiable and measurable in experiments, Krajcinovic (1996).

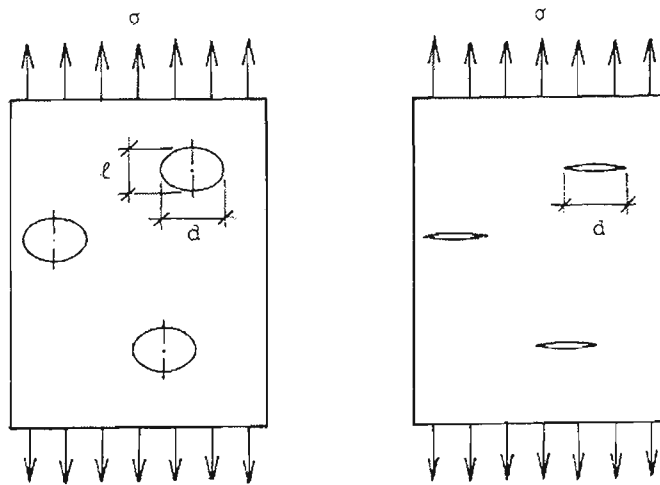


Figure 2.34 Formation of micro-elliptical cavities and sharp cracks under tensile load.

Budiansky and O'Connell proposed the damage parameter,  $\omega'$ , where  $\omega' = 2N/\pi \langle A_{CR}^2/P \rangle$ , see Budiansky and O'Connell (1976). The variables  $A_{CR}$  and  $P$  are the crack surface area and the perimeter length, respectively, of each elliptical penny-shaped micro-cracks. It is assumed that all micro-cracks have the same size. The parameter  $N$  represents the density of cracks, or the total number of micro-cracks per volume of  $V$ . The angular bracket stands for the statistical average over a

certain characteristic volume. This characteristic volume was defined earlier by Hill (1967) as the representative volume element (RVE) denoting the smallest possible volume with the minimum prescription for the size of the unit cell in the sense of Hill. Here the distribution of defects, material properties and the strain-strain fields are assumed to be statistically homogeneous. The proposed damage parameter,  $\omega'$ , while representing a reasonable possibility, cannot be measured directly and has limited practical use, Krajcinovic (1996). This parameter, together with that introduced by Kachanov (1958) and some other proposed volumetric damage measures, can be classified under the global-scale phenomenological continuum damage mechanics (CDM) models and was thoroughly reviewed by Krajcinovic (1985) and Hult (1985).

Lubarda and Krajcinovic (1993) made further progress in developing a more effective expression for the damage parameter. They defined  $P^0 = \omega' = 4\pi\rho'$ , where  $\rho'$  is the averaged density of micro-cracks over all possible orientations or vector directions, and  $P^0$  is the micro-crack distribution tensor of zeroth order, established using series expansions. Distribution tensors with higher orders are defined with micro-cracks embedded at different angles to the bedding plane. These are micro-mechanical expressions based on the Budiansky-O'Connell parameter for the description of the damage, expressed in terms of the effective stiffness or compliance tensors, and are a direct statement of the micro- to macro- (or local to global) transition, Krajcinovic and Mastilovic (1995). This is a departure, and an improvement, from the Kachanov damage parameter, which focuses only on the damage from a global point of view that, is based on continuum mechanics.

Upon release of the load in a tensile test, the unloading would result in closing of the cracks, without noticeable residual strain, as shown in Figure 2.33a. In this case, damage due to the formation of micro-cavities and micro-cracks can be shown by a decrease in Young's modulus, as shown by a gradual reduction in the effective modulus. This degradation can be observed in the case of a quasi-brittle material as shown in Figure 2.35 (right).

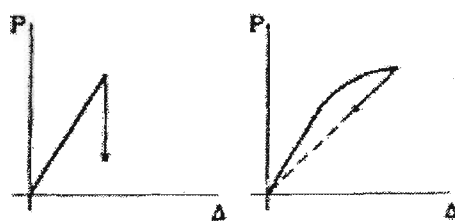


Figure 2.35 Force-displacement ( $P$ - $\Delta$ ) curve for a damaged specimen in uniaxial tension for (left) perfectly brittle and (right) quasi-brittle material.

This gradual degradation process is normally called strain softening. This contrasts with the case of a perfectly brittle material with the material strength dropping vertically as shown in Figure 2.35 (left), denoting the occurrence of a macro-crack or fracture. However, unloading from a state of pure plastic deformation can be observed with a distinctive invariant Young's modulus as shown in Figure 2.33b. In most practical cases, both the damage and plastic deformation processes can coexist, leading to an unloading path somewhere in between the first two cases as shown in Figure 2.33c.

By obtaining accurate measurements of the effective modulus during the post-critical unloading or strain softening, it is possible to evaluate the relative significance and the contribution of material deformation due to damage or plastic flow, or both, according to Lemaitre and Chaboche (1978 and 1990). In this sense, it is possible to study the deformation of horticultural materials, fibre-reinforced composites or any other materials that undergo strain softening, the process of which provides insights as to the contributions due to various modes of failure mechanisms and/or plastic deformation and their inherent deformation characteristics.

#### 2.2.4.2 Strain Softening Process

A large number of materials can be classified as softening, or strain softening materials, including some metals, most polymers, geomaterials such as soils and rocks, filled-rubber, wood, particle board composites, fibre-reinforced composites, fibre-reinforced concrete, ceramics and virtually all horticultural produce. These materials show a gradual reduction in their strength after reaching their ultimate strength, as a result of increasing localized deformational instabilities and damages. Localized plastic deformation is sometimes referred to as shear banding, particularly in metals, but also in plastics, soils and rocks. Damage includes fracture process zones in concrete. It also includes matrix cracking in the form of micro-cracks, meso-cracks or bridging zones, as well as macro-cracks, Figure 2.36, for the case of composites, horticultural produce, plastics, and many other materials. Strain softening will eventually cause a local failure through the occurrence of macro-cracks, most likely to be observed in fruits such as apples and pears with fairly crispy textures under high dynamic loading conditions.

Instead of cumulating into a single primary macro-crack, other fruits and vegetables that are comparatively softer in texture tend to form numerous micro-cracks under dynamic loading and to dissipate the energy into heat. The deformation of produce tissues tends to be plastic or viscoplastic, with minimum chance of occurrence of any pre-critical instability due to damage. This outcome tends to protect soft tissues from impact damage, since the material deformation can be limited by the

energy dissipation into heat. If the loading becomes large, the plastic deformation in the soft tissues tends to evolve into pre-critical plastic instabilities such as shear banding, thus limiting the extent of a bruise by ‘trapping’ the mechanical energies into a thin shear plane. In the post-critical state, strain softening may occur in both the crisp and soft produce textures.

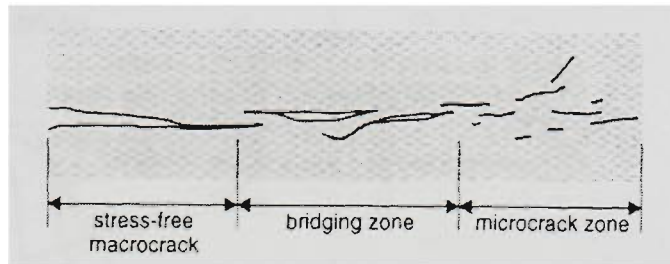


Figure 2.36 Schematic diagram showing micro-cracks, meso-cracks with propagating bridging zones, and macro-cracks leading to catastrophic fracturing. From van Mier *et al.* (1995).

A typical strain softening process is one which exhibits a decline of the uni-axial stress at increasing strain or, technically, a situation where the matrix of tangential elastic moduli,  $E_t$ , ceases to be positive-definite as shown in Figure 2.37.

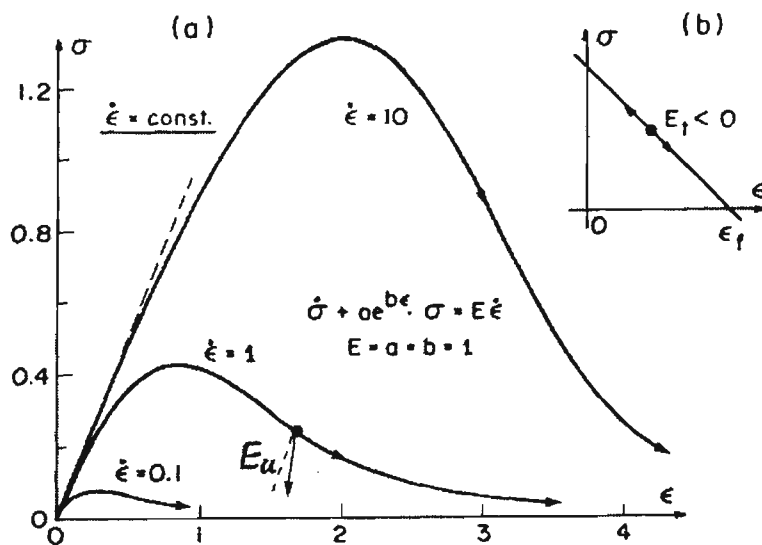


Figure 2.37 Stress-strain relationship showing strain softening process (a) with strain rate ( $\dot{\epsilon}$ ) effects; Effective modulus,  $E_u$ , is positive, (b) Negative tangent elastic modulus,  $E_t$ , along softening curve. From Bazant *et al.* (1984).

Strain softening occurs in material under tension, but also in compression and shear conditions, as pointed out by Read and Hegemier (1984). Until recently, strain softening has been incorrectly viewed as a true material property, according to Bazant (1976). In fact, strain softening is not a material property. The main cause of this process is the material heterogeneity, which initiates localized distortion, and the material brittleness, which initiates loss of inter-particle contacts and

bonding of the materials. It can be a strain rate-dependent as well as a rate-independent process, according to Kohn (1988). As materials start to deform under softening, effects due to the sizes and shapes will also cause various degrees of material instability, as shown in Figure 2.38.

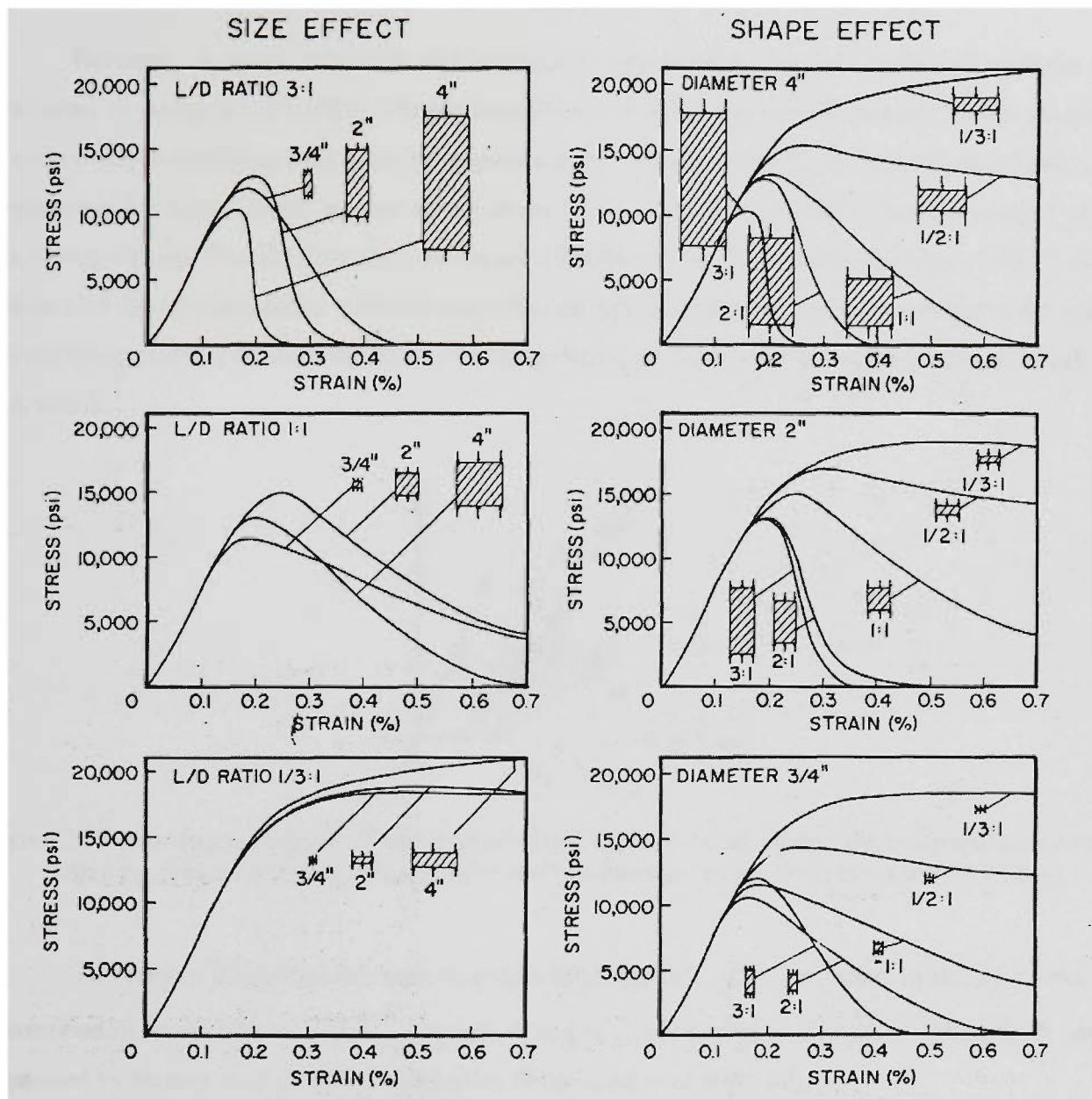


Figure 2.38 Influence of specimen size and shape on stress-strain curves for marble under uniaxial compression tests. From Hudson *et al.* (1971).

From Figure 2.36, material instability is shown to include the initiation of localized micro-cracks in the form of crack bands or singularities in the form of macro-fractures. These localized effects are outside the domain of the classical non-local or global continuum theories. Some of the most influential solid mechanists regarded softening process as inadmissible in continuum mechanics, see Thomas (1961), Hill (1962), Truesdell and Noll (1965), and Mandel (1966). In order to enable the softening process to be defined within the continuum concept, research workers have tried to emphasize the true stress of materials. They regard the gradual degradation of the total cross-sectional

area between the micro-cracks. This is the approach in the concept of damage mechanics. However, for most common and practical cases, a mathematical formulation with a variable resisting area approaching zero in a random way is necessary for accurate solutions.

Recently, a more practical and promising approach based on statistical analysis was developed by Bazant *et al.* (1984). The method allows the softening process to work within the global or macroscopic continuum context, by separating the stresses into local and non-local parts and considering the microscopic or true stress-strain fields to be Gaussian-distributed averages of the macroscopic fields. Results from their works are effective and here illustrated in Figure 2.39. It shows a sketch of stress-strain curve with the estimated energy dissipated (shown by hatched area) during the softening process, by the evaluation of damage based on the two effective (unloading) moduli,  $E_u$ , at A and B.

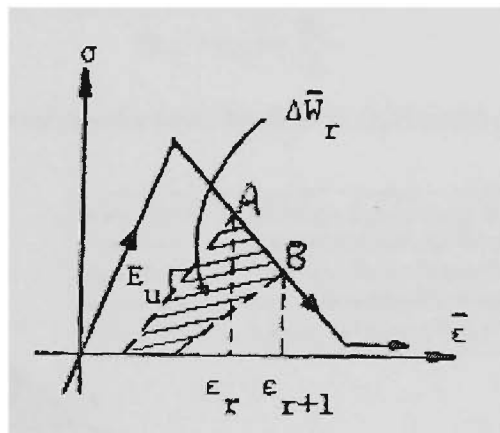


Figure 2.39 Schematic diagram of stress-strain characteristics showing energy dissipated under strain softening process between two effective moduli (hatched area). From Bazant *et al.* (1984).

The energy dissipated between two unloading moduli,  $\Delta \bar{W}_r$ , at strain values of  $\epsilon_r$  and  $\epsilon_{r+1}$  corresponding to stresses  $\sigma_r$  and  $\sigma_{r+1}$  at points A and B, respectively, as a result of softening. It can be expressed by Bazant *et al.* (1984), in the sense of the statistical approach, as:

$$\Delta \bar{W}_r = \frac{1}{2} (\sigma_r \Delta \bar{\epsilon} - \bar{\epsilon}_r \Delta \epsilon) \tag{2-10}$$

where  $\Delta \bar{\epsilon}$  is the weighted averaged (statistically determined) of strain between A and B,  $\bar{\epsilon}_r$  is the weighted averaged (statistically determined) of strain between O and A, and  $\Delta \epsilon$  is  $(\epsilon_{r+1} - \epsilon_r)$ , and here the effective modulus,  $E = E_u$  ( $E_u = \sigma / \epsilon$ ).

Equation (2-10) can be better illustrated in terms of the Strain Energy Density Theory developed by Sih (1973), and Sih and MacDonald (1974) by a simplified schematic diagram as shown in Figure 2.40. The essence of this approach is that it can account for both the damage and the

plastic deformation processes in a simple and accurate manner for both quasi-static and dynamic material characterization. Here, the stress and strain under softening conditions at A, for instance, can be expressed in terms of the stress and strain conditions at the damage conditions (at A), as well as the ultimate condition at U. We will make use of this strain energy density approach again in our estimation of the instantaneous effective modulus of materials during impact. In the present study, instead of referring to the ultimate conditions at U, we have characterized the rapid changes of the effective modulus based on the initial modulus, that is, the Young's modulus of slope OU from the experimental stress-strain curves.

From Figure 2.40, the following constitutive relationship was established by Sih (1973), Sih and MacDonald (1974), and Carpinteri and Bocca (1988) in the form of:

$$\sigma = E\varepsilon = \frac{\sigma_U \varepsilon_F}{(\varepsilon_F - \varepsilon_U) + \frac{\sigma_U}{E}} \tag{2-11}$$

where the subscripts *U* and *F* represents the conditions at *U* (ultimate) and *F* (final).

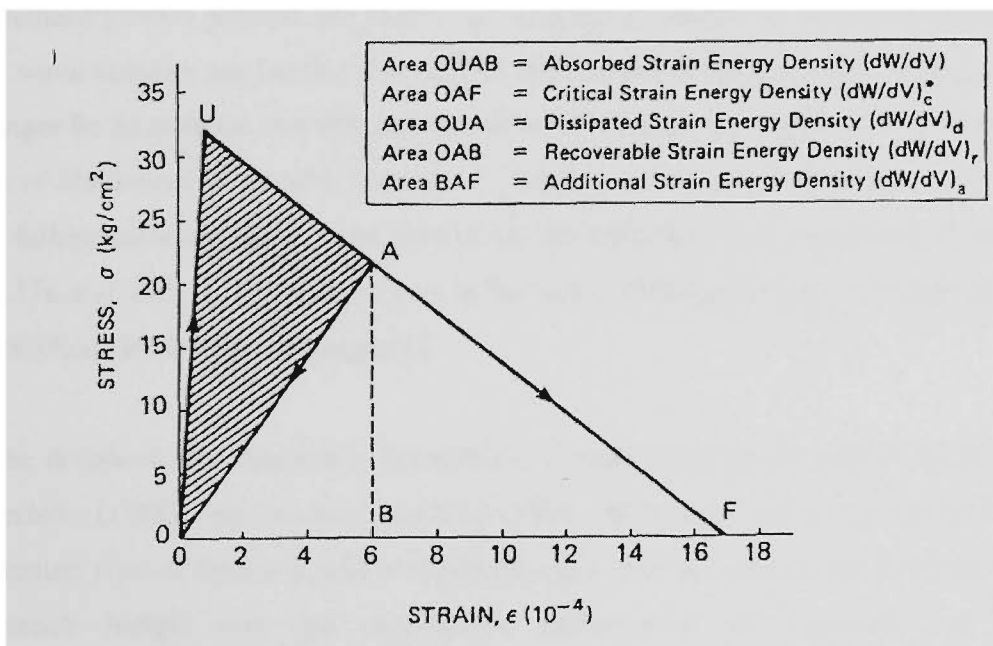


Figure 2.40 Simplified schematic strain softening stress-strain diagram as described by the Strain Energy Density approach using the ratio of instantaneous work to unit material volume (*dW/dV*). From Carpinteri and Bocca (1988).

Referring to Figure 2.40, the definitions for the various strain energy densities can be expressed, according to Carpinteri and Bocca (1988) as:

$$\left(\frac{dW}{dV}\right) = \frac{1}{2}(\sigma\varepsilon + \sigma_U\varepsilon - \sigma\varepsilon_U) = \text{Area OUAB} \tag{2-12}$$

$$\left(\frac{dW}{dV}\right)_r = \frac{1}{2}(\sigma\varepsilon) = \text{Area OAB} \quad (2-13)$$

$$\begin{aligned} \left(\frac{dW}{dV}\right)_d &= \left(\frac{dW}{dV}\right) - \left(\frac{dW}{dV}\right)_r = \frac{1}{2}(\sigma_U\varepsilon - \sigma\varepsilon_U) = \text{Area OUAB} - \text{Area OAB} \\ &= (\text{Hatched}) \text{ Area OUA} \end{aligned} \quad (2-14)$$

$$\begin{aligned} \left(\frac{dW}{dV}\right)_c &= \left(\frac{dW}{dV}\right)_c - \left(\frac{dW}{dV}\right)_d = \frac{1}{2}(\sigma_U\varepsilon_F - \sigma_U\varepsilon + \sigma\varepsilon_U) \\ &= \text{Area (OUF-OUA)} = \text{Area OAF}. \end{aligned} \quad (2-15)$$

Equation (2-15) represents the degraded critical value of strain energy density at any moment during the softening process, and is arguably the most significant term for dynamic material characterization with both damage and deformation processes.

There has been much debate on the theory and uniqueness of the strain softening process ever since Hadamard (1903) pointed out that if the tangent modulus,  $E_t$ , becomes negative, see Figure 2.37b, the wave velocity originating from a load impulse becomes imaginary. The equation of motion will no longer be hyperbolic, but elliptic. However, it has been pointed out by Bazant (1976) that the viewpoint of Hadamard is invalid. Instead of focusing on the tangent modulus,  $E_t$ , of materials in their post-failure softening regime, we should use the effective modulus,  $E$ , which is shown as  $E_u$  in Figures 2.37a and 2.39.  $E$  is positive even in the strain softening range. The minimum value of the effective modulus is zero, but not negative.

The debate on the theoretical foundation of strain softening continues up to the present, see Li and Duxbury (1989), and Duxbury and Kim (1991). Whether this process can be fully represented by a continuum type of theory is still being challenged. But because of the fact that this process can provide much insight into the post-failure deformation of materials and their damage/deformation/flow characteristics in this domain, to obtain effective moduli during softening by experiments obviously is one of the best approaches. More recently, fundamental studies of the effective moduli have attracted attention, see Kohn (1988), and of researchers with a statistical bent. For instance, Duxbury (1990) treated the failure threshold as a stochastic variable determined using the statistics of extremes. Recent trends in this approach seem to focus on the stochastic evaluation of material parameters under dynamic conditions, based on experimental data, see, for instance, Pan and Postle (1995) and Mishnaevsky (1995).

The effective modulus of a material describes its overall, macro-scale behaviour. It is usually defined based on the average stress and strain values of test specimen with sizes that are small enough compared with the length scale of the loads and boundary conditions, but are still large enough for the continuum theory to apply, see Hashin (1983). In the case of composites such as horticultural materials, a mixture of continua is applied, characterized by the anisotropic nature of these materials. If expressed in mathematical terms, the effective modulus depends analytically on the properties of all reinforced-fibre and matrix components, Kantor and Bergman (1984). The anisotropic nature of produce can be illustrated in Figure 2.41. A simplified physical model and failure mode is shown in Figure 2.42. The major failure modes commonly experienced by composite materials include fibre-breaking, slippage (debonding of fibre and matrix) and matrix cracking.



Figure 2.41 A high-resolution image of the cell-wall structure of a water chestnut fruit obtained by atomic force microscopy, showing the layering of the cellulose micro-fibrils (X 85,000). From Brett and Waldron (1996).

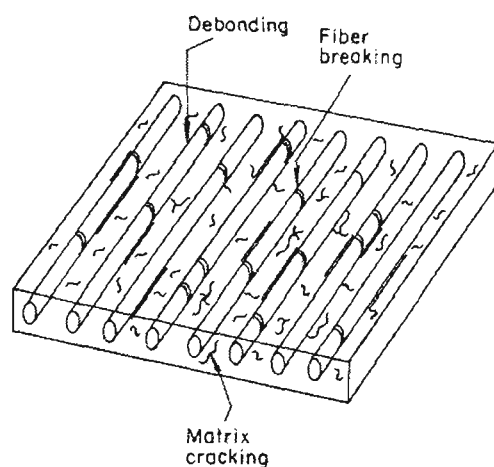


Figure 2.42 Simplified structure of fibre-reinforced composites showing their major failure modes. From Sih (1988).

For a wide range of materials such as construction, plastic, elastomeric and biomaterials, the progressive damage process of strain softening can be observed under programmed strain-controlled load cycles. The material damage is accurately revealed by monitoring the gradual reduction of the effective modulus, see Bieniawski (1971) for the softening characterization of hard rock (norite) and soft sandstone using uniaxial cyclic tension-compression tests as shown in Figure 2.43. From this Figure, it is most interesting to note that even after strength failure the rock exhibits a certain effective modulus. The fact that the loops as shown in Figure 2.43 are narrow permits the conclusion that these slopes represent the effective moduli of the materials at their corresponding strains. In fact, the difference in the effective moduli as shown in the stress-strain curve in loading and the unloading paths is an appropriate approach of the estimation of accumulated damage, as pointed out by Lemaitre and Chaboche (1978), cited in Krajcinovic and Sumarac (1987).

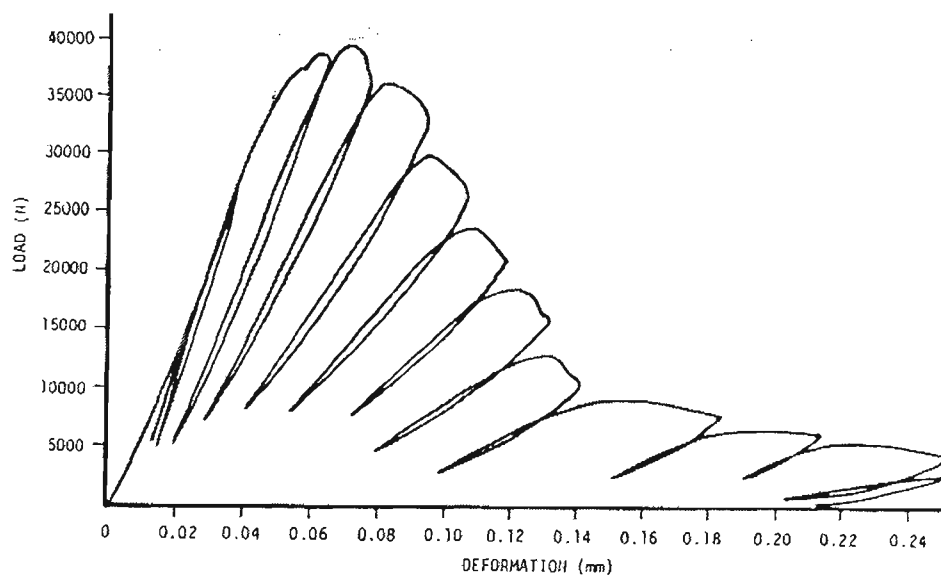


Figure 2.43 Deformational behaviour of sandstone under cyclic uniaxial compression load. From Bieniawski (1971).

The progressive damage process of strain softening can be illustrated in Figure 2.44. In Figure 2.44, quasi-static cyclic-load tests with programmable displacement-controlled capability were reported by Ip *et al.* (1997). Using natural-based banana fibres embedded in hybrid amino-phenolic resins, the specimens were tested with a servohydraulic tester using a cyclic straining program similar to Bieniawski (1971) and Vincent (1975). In this Figure, the Young's modulus, as denoted by AA', was maintained up to the peak strength of the material, showing only plastic deformation but with the absence of damage. After reaching the maximum material strength, damage dominates the degradation of the effective modulus, as denoted by the decrease of the slope of BB' to FF'. Earlier, a uniaxial tensile test machine was developed by Vincent (1992) that is capable of performing quasi-static cyclic-load tests with biomaterials as well as horticultural materials such as

potato flesh, see Hiller and Jeronimidis (1996). From the article by Hiller and Jeronimidis, it shows the progressive damage activity was more complex. A characteristic pre-peak degradation of the effective modulus of potato flesh was observed, showing the presence of pre-peak cracking damage as well as post-peak softening.

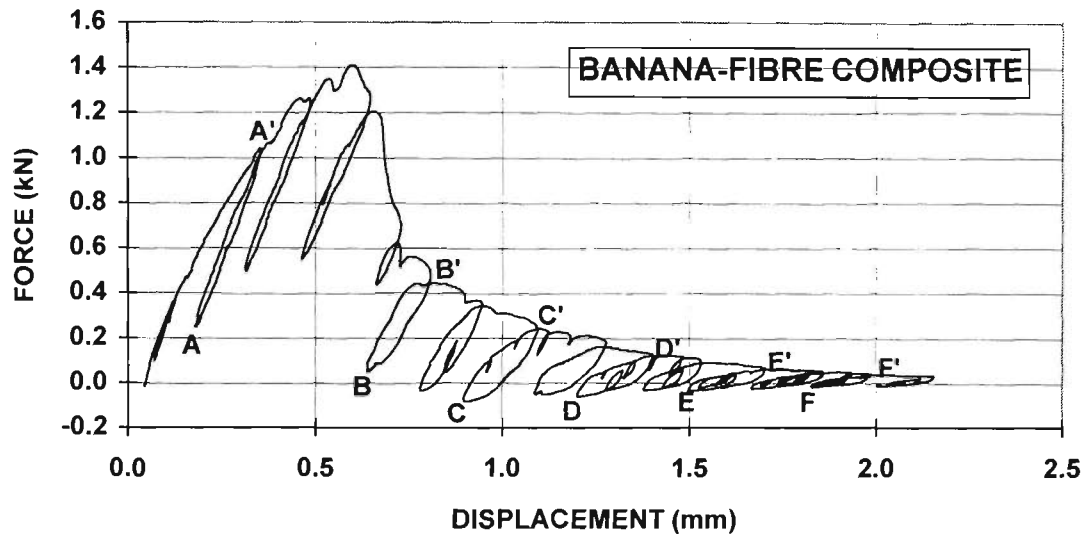


Figure 2.44 Progressive damage process of post-peak strain softening as revealed by a cyclic straining program on thin rectangular banana-fibre composite specimens. From Ip *et al.* (1997).

The quasi-static test methods as mentioned cannot be used to reveal material characteristics under dynamic processes. The dynamic deformation of horticultural materials normally exhibits characteristic post-peak strain softening patterns that cannot be modelled by equations such as Equation (2-8). Matsuoka (1986) modified the stress-strain characteristic curves based on Equation (2-8) by using constitutive equations in the form of a nonlinear viscoelastic expression, taking into account the strain softening phenomena as:

$$\sigma(\dot{\epsilon}) = E_o \epsilon e^{-C\epsilon} e^{-\left(\frac{\dot{\epsilon}}{\dot{\epsilon}^*}\right)^\beta} \quad (2-16)$$

where the first exponential factor with  $C\epsilon$  is invoked to describe yielding, and the second exponential factor provides the  $\dot{\epsilon}$  dominance of the yield stress;  $\beta$  is a temperature dependent material parameter obtained from experiments which is always less than one. Equation (2-16) is plotted in Figure 2.45, with different values of  $\dot{\epsilon}$  showing strain softening. However, the curves show only viscoelastic (but not viscoplastic) deformation, sharing the same Young's modulus,  $E_o$  (a typical viscoelastic phenomenon).

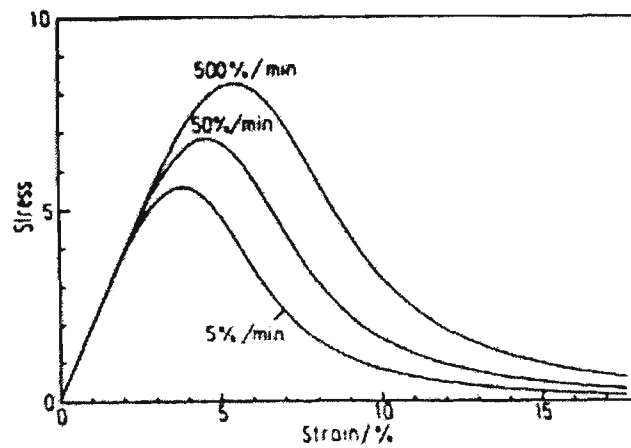


Figure 2.45 Nonlinear viscoelastic stress-strain curves showing strain softening and the effects due to strain rates of deformation. From Matsuoka (1986).

Recently Matsuoka (1992) developed a viscoelastic-viscoplastic model which is distinct from the linear and nonlinear viscoelastic models in that initial elastic/viscoelastic deformation would evolve into viscoplastic (viscous) flow after the relaxation time  $t^*$  is reached. He defined a critical strain,  $\epsilon_c$ , which corresponds to the yield stress,  $\sigma_y$ . The constitution equation can be expressed as:

$$\sigma_y = \frac{E_0}{e} (\epsilon_c)^{-\beta} (\dot{\epsilon} t^*)^\beta \quad (2-17)$$

The essence of Equation (2-17), which is initially elastic/viscoelastic but viscoplastic-evolving in nature, can be illustrated by Figure 2.46 which is initially elastic but viscoplastic-evolving. Although more simplistic than the relationship shown in Equation (2-17), Figure 2.46 illustrates the stress dependency of the strain as well as the strain rate. It is possible that, no matter how soft the produce texture is, the critical strain and the corresponding yield stress of produce materials may always exist, no matter how small the critical strain and its corresponding yield stress.

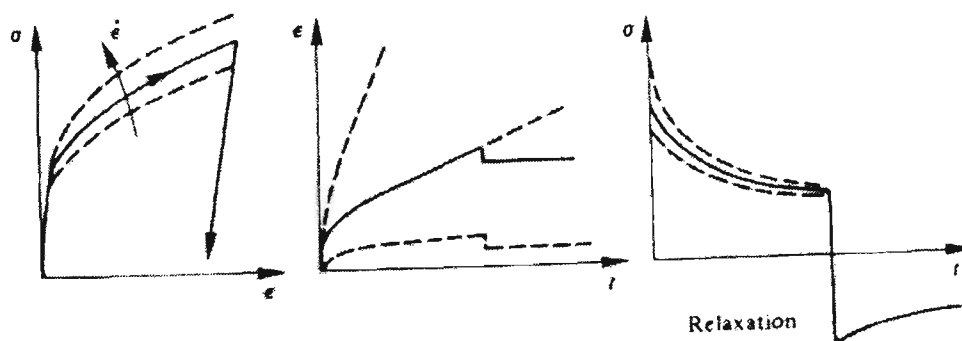


Figure 2.46 Schematic presentation of elasto-viscoplastic deformation of solid materials under different strain rates. From Lemaitre and Caboche (1990).

In Figure 2.46-centre, the strain rate  $\dot{\epsilon}$ , as denoted by straight slopes, can reach a maximum, as denoted by its maximum slope) when the critical strain is reached. Equation (2-17) is defined for the simplified case of uniaxial deformation, either in tension or compression. In order to solve the equation, a relaxation spectrum, or a spectrum of relaxation times,  $t^*$ , is required from experiments to observe how the yield stress depends on different strain rates (see the far-right sketch shown in Figure 2.46).

### 2.2.5 Cushioning Effect of Produce Skins against Bruise Damage during Impact

For vegetables such as tomatoes and fruits such as persimmons, their skin is the single most important component of their mechanical strength, according to Miles *et al.* (1969). Their well-structured epidermal cells effectively provide a structural protective layer that is able to deter fracture under shear stresses during dynamic loading. For other fruits such as oranges, shown in Figure 2.47, and many vegetables, their relatively thick skins act effectively as protective cushions in minimizing bruise damage during an impact, besides overcoming any shear stress loading.

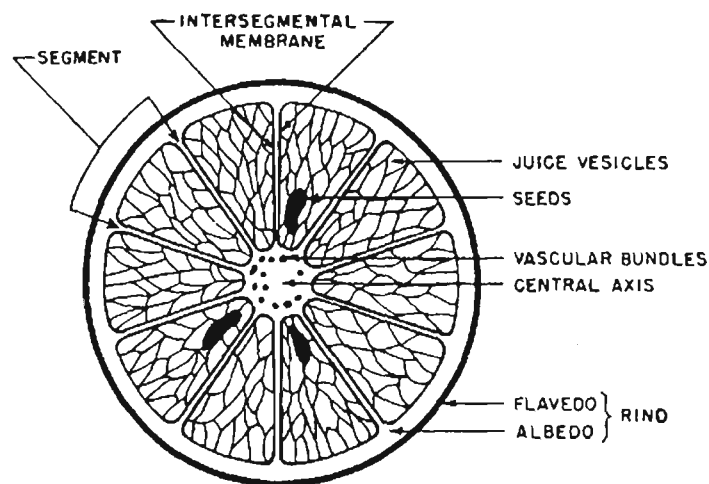


Figure 2.47 Cross-sectional view of a Florida Valencia orange with very thick protective skin of more than 5 mm. From Suole (1956).

The effectiveness of thick produce skins as cushions against impact damage is illustrated in Figure 2.48. Chuma *et al.* (1978) performed 38 drop tests on Satsuma oranges onto a rigid surface and confirmed that the skin thickness was linearly proportional to the fruit weight, which ranged from 75 grams to 225 grams. The corresponding skin thickness ranged from 2.0 mm to 4.2 mm. From Figure 2.48, Satsuma oranges of about 150 grams by weight, tested by dropping on a rigid surface, started rupturing at a drop height of about 100 cm. The fruits were examined under ultraviolet light to determine whether rupture had occurred. The cushioning effect of the Satsuma orange skin is much

superior to that of apples. Granny Smith apple skin, for instance, has a form of single-layered-cell cuticles and thin layers of epidermal cells as shown in Figure 2.49 with an averaged total thickness of less than 0.3 mm. In general, apples with comparable weights will start to bruise at a drop height of approximately 5 cm.

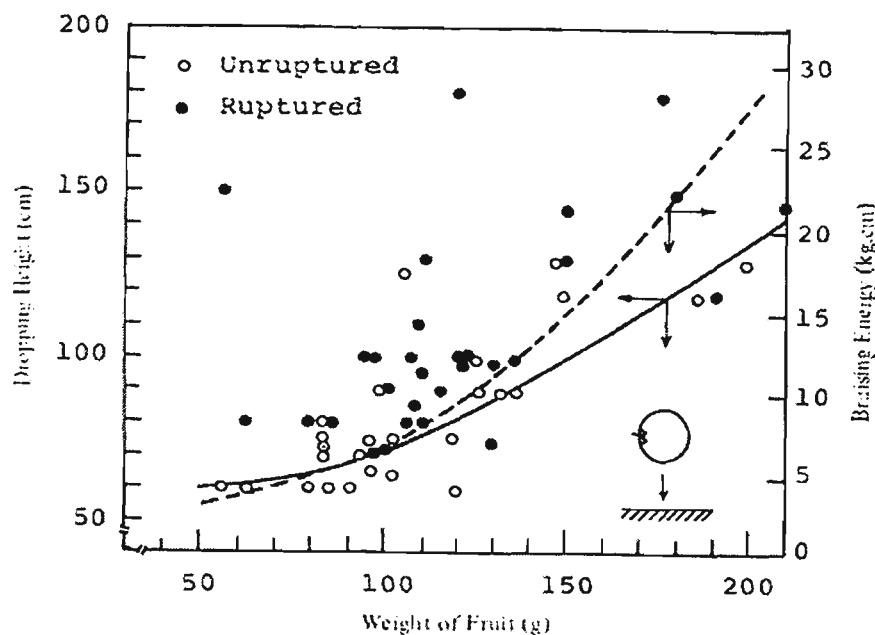


Figure 2.48 Relationship between orange weight and drop height or bruise energy. From Chuma *et al.* (1978).

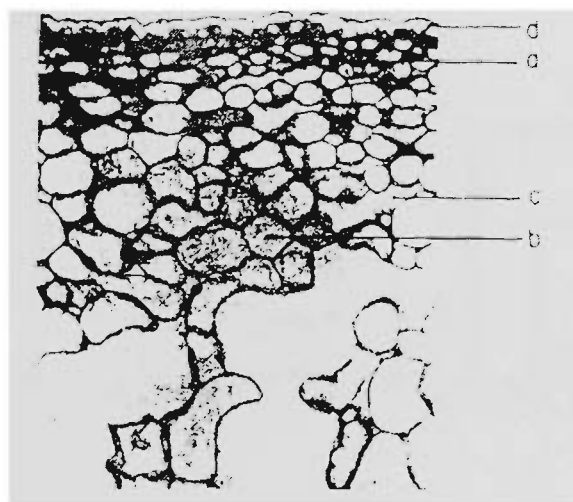


Figure 2.49 Cross section of Granny Smith apple, showing d: cuticle (skin); a: collenchyma (skin); c: intercellular space; and b: fleshy parenchyma cells. From Reeve (1953).

A more scientific approach to the study of cushioning effects of materials is credited to Mindlin (1945). For the case of produce skin, their function as cushions can be illustrated in Figure 2.50. Following the approach taken by Mindlin, we can consider a system as shown in Figure 2.50. Based on the law of conservation of energy, the sum of (i) the instantaneous kinetic energy, and (ii) the instantaneous energy stored in the skin cushion (in the form of an integral) should be equal to the potential energy of the produce at its instantaneous height  $h$  (as compared to its initial height,  $h_0$ ). The

instantaneous kinetic energy is  $0.5mV^2$  where  $m$  and  $V$  are the mass and instantaneous velocity of the produce, respectively. According to Mindlin, this relationship of energy conservation at the moment of first impact may be expressed as:

$$\frac{1}{2}mV^2 + A_c T_c \left[ \int_0^\epsilon f(\epsilon, t) d\epsilon + \psi(t) \right] = mg(h + T_c \epsilon) \quad (2-18)$$

where time  $t = 0$  is taken as the instant of first contact with the ground, with  $V = V_{max}$ , and  $h = h_o$ ,  $V_{max}$  and  $h_o$  being the maximum velocity and initial drop height, respectively. At this moment of first contact, the stored energy integral on the left-hand side of Equation (2-18) is zero, as well as the strain.  $A_c$  is the effective cushion (skin) area under compression,  $T_c$  is skin thickness, and the function  $\psi(t)$ , sometimes called the Rayleigh's dissipation function, is determined by the initial and boundary conditions. Here the strain,  $\epsilon$ , denotes the instantaneous strain of the skin cushion under compression. When the instantaneous strain reaches its maximum,  $\epsilon_m$ , all the kinetic energy is transformed into stored energy in the cushion and may be expressed as:

$$A_c T_c \left[ \int_0^{\epsilon_m} f(\epsilon, t) d\epsilon + \psi(t) \right] = mg(h_o + T_c \epsilon_m) \quad (2-19)$$

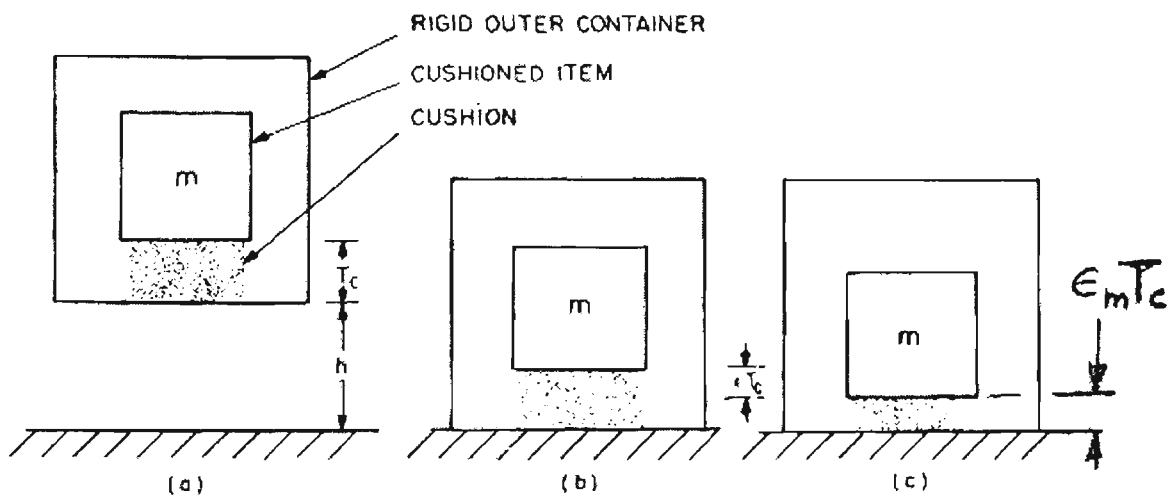


Figure 2.50 Impact of produce with skin as cushion: (a) at instant of release, (b) at instant of impact with ground surface, and (c) at time of maximum stress. From Mustin (1968).

The foregoing discussion was based on an implicit assumption of a system with one degree of freedom, with a drop direction normal to the uniformly stressed skin cushion. When the velocity becomes zero, it is clear that the stress on the skin cushion is at its maximum. The strain of the skin cushion due to compression is also at its maximum, if there is no time lag between maximum force (in the sense of maximum acceleration) and maximum displacement, which will be the case for linear and undamped responses of the cushion. If the cushion is viscoelastic, or plastic/viscoplastic with

permanent deformation during the loading, there will be a slight time lag between maximum stress,  $\sigma_m$ , and  $\epsilon_m$ , as shown in Figure 2.51.

The integral as shown in Equation (2-19) represents the stored energy per unit volume of skin cushion, and can be further expressed as:

$$\int_0^{\epsilon_m} f(\epsilon, t) d\epsilon + \psi(t) = \frac{mg}{A_c T_c} (h_o + T_c \epsilon_m) = \frac{mg}{A_c} \left[ \frac{h_o}{T_c} + \epsilon_m \right] = \sigma_s \left[ \frac{h_o}{T_c} + \epsilon_m \right] = D \quad (2-20)$$

where  $\sigma_s = \frac{mg}{A_c}$  is the static stress on the skin cushion. The term  $D$  has significant implications in the study of cushion protection and impact damage, and is normally called the strain energy density in terms of energy per unit volume. Since the maximum total force equals the sum of inertia force and the weight of the produce,  $mg$ , this can be written as:

$$\sigma_m = \sigma_s (g_{max} + 1) \quad \text{or} \quad g_{max} = \frac{\sigma_m}{\sigma_s} - 1 \quad (2-21)$$

where  $g_{max} = \frac{a_m}{g}$  and  $a_m$  is the peak acceleration.  $g_{max}$  is the terminology widely used in the packaging industry and is normally called 'peak-g' or  $G_m$ .

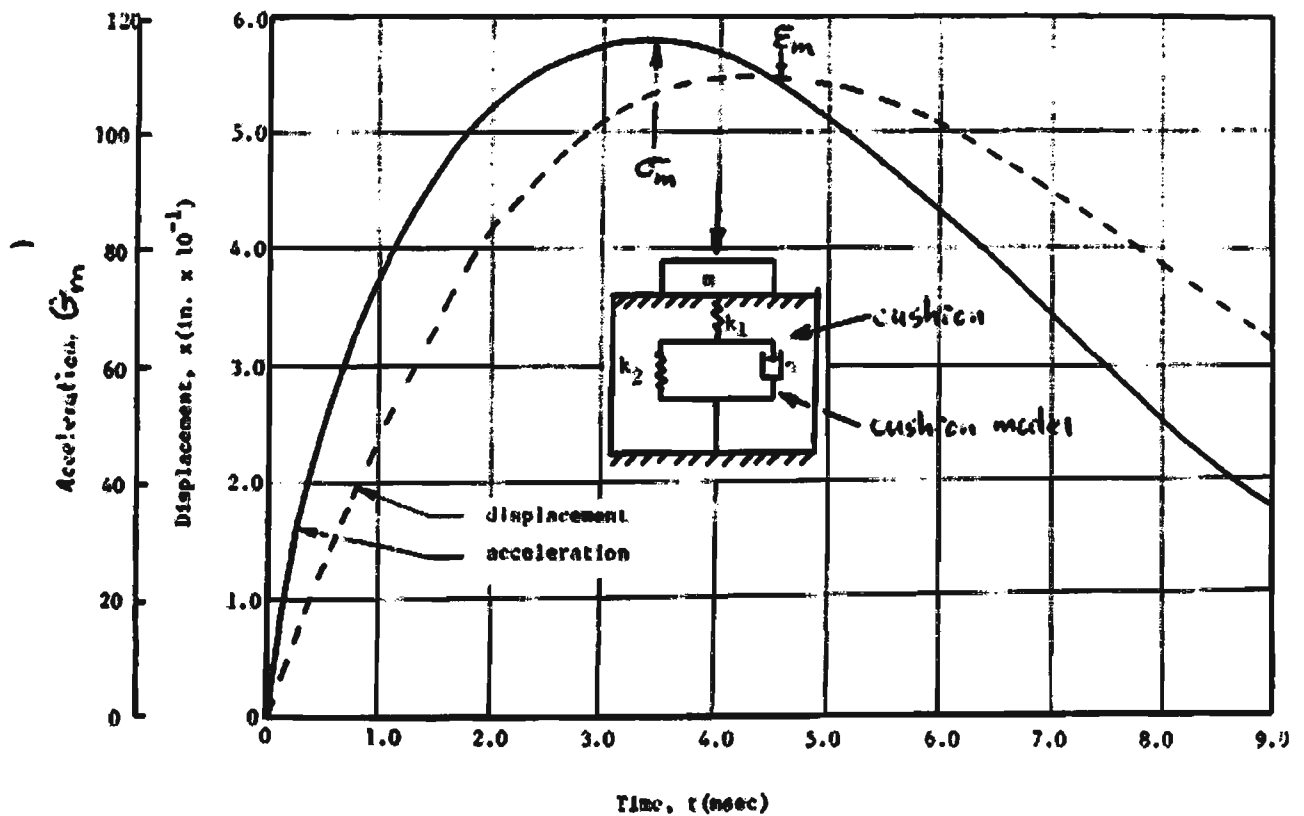


Figure 2.51 Histories of acceleration and displacement of impacting body against a 3-element model of viscoelastic cushion. From Cost and Dagen (1977).

By substituting Equation (2-20) into Equation (2-21), the expression becomes:

$$g_{\max} = \left( \frac{\sigma_m}{D} \right) \left( \frac{h_o}{T_c} + \varepsilon_m \right) - 1 = J \left( \frac{h_o}{T_c} + \varepsilon_m \right) - 1 \quad (2-22)$$

where  $J (= \sigma_m/D)$  is called the cushion factor by the early cushioning theoreticians and is dimensionless. It is the ratio of peak stress developed in the skin to the energy stored per unit volume of the skin, or  $\sigma_m/D$ . Since the drop height  $h_o$  will most likely be many times larger than the skin or cushion thickness,  $T_c$ , and the peak strain  $\varepsilon_m$  is less than 1.0,  $h_o/T_c \gg \varepsilon_m$ . Equation (2-22) may be further simplified to:

$$g_{\max} = J \left( \frac{h_o}{T_c} \right) - 1$$

or

$$J = \frac{g_{\max} + 1}{\left( \frac{h_o}{T_c} \right)} \quad (2-23)$$

From Equation (2-23), the last term can be so expressed without diminishing the overall accuracy since  $g_{\max}$  values on impact are normally hundreds of times higher than unity. Thus,  $g_{\max} \gg 1$  and Equation (2-23) may be rewritten as:

$$g_{\max} = J \left( \frac{h_o}{T_c} \right) \quad \text{or} \quad J = \frac{g_{\max}}{\left( \frac{h_o}{T_c} \right)} \quad (2-24)$$

Based on Equations (2-18), (2-19) and (2-24), the following relationship can be established:

$$J = f \left( \frac{mV^2}{2A_c T_c}, \frac{h_o}{T_c} \right) \quad \text{or} \quad J = f \left( \frac{\sigma_s h_o}{T_c}, \frac{h_o}{T_c} \right) \quad (2-25)$$

because at  $t = 0$ ,  $0.5mV^2 = mgh_o$ , and  $\sigma_s = mg/A_c$ .

Rearranging Equation (2-21) by the substitution of the definition of  $J$ , from (2-24), the new expression for  $g_{\max}$  can be written as:

$$g_{\max} = \frac{JD}{\sigma_s} \quad (2-26)$$

Equation (2-26) is commonly used for the design of cushion requirements in packaging technology. By experiment, a family of curves such as those shown in Figure 2.52 can be drawn for each cushion material thickness,  $T_c$ , at each drop height,  $h_o$ , plotting peak acceleration (deceleration) or, alternatively,  $g_{\max}$ , against static stress,  $\sigma_s$ . This family of curves can be fully characterized in Equation (2-23) by the term  $h_o/T_c$ . These curves are useful for the optimum design of the cushion requirements for the transportation and handling of fruits and vegetables against bruise damages,

Figure 2.53. The second term ( $h_o/T_c$ ) in Equation (2-25) shows strain-rate effects are present, meaning that a time lag may exist between the times of maximum displacement and force in the skin cushion. To be useful in practice, a family of curves with  $g_{max}$  versus static stress (in terms of effective area  $A_c$ ) for various cushion thickness,  $T_c$  needs to be established.

The cushioning equation of (2-26) is governed by  $J$ , which is a function of the two terms shown in brackets in Equation (2-25). This expression is comparable to one developed by Soper and Dove (1962), who used the Buckingham  $\pi$  theorem of dimensional analysis to arrive at functional equations for the behaviour of cushions, in the form:

$$J = f\left(\frac{mV^2}{2A_c T_c}, \frac{V}{T_c}\right) \tag{2-27}$$

where  $V$  is the velocity of load application at and beyond the instant when impact starts. Comparing both the second terms of Equations (2-25) and (2-27), with  $y$  being the vertical displacement of the skin cushion under the impact loading:

$$\frac{h_o}{T_c} = \left(\frac{1}{T_c}\right)\left(\frac{mV^2}{2mg}\right) = \frac{(mV)V}{2mgT_c} = \left(\frac{mV}{2mg}\right)\left(\frac{V}{T_c}\right) = f\left(\frac{V}{T_c}\right) = f\left(\frac{y/t}{T_c}\right) = f\left(\frac{y}{T_c t}\right) = f(\dot{\epsilon}) \tag{2-28}$$

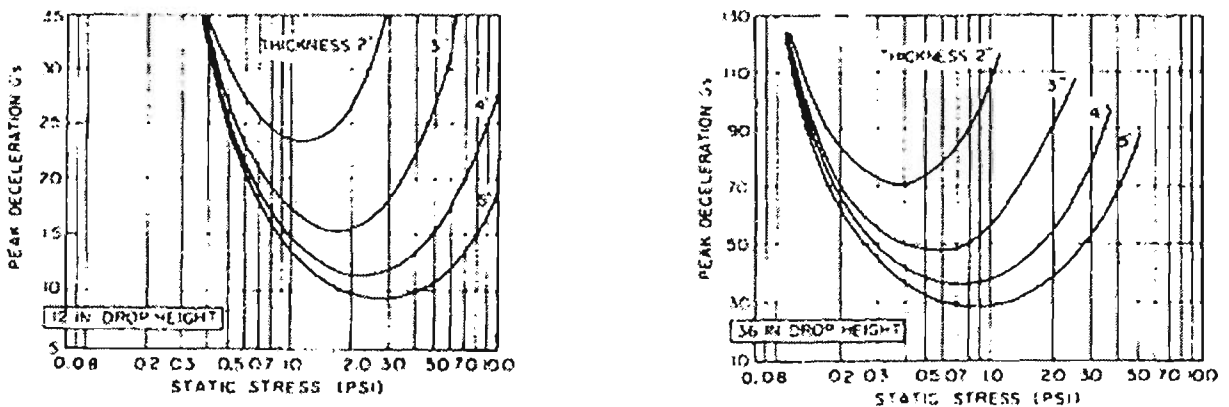


Figure 2.52 Design curves of peak-accelerations (in  $g_{max}$ ) versus static-stress ( $\sigma_s$ ) for a cushion of polyethylene foam. From Humbert and Hanlon (1962).

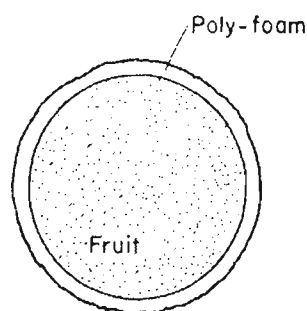


Figure 2.53 Protective foam cushion for fruits with thin skins.

The implications of Equation (2-28) are significant. By rearranging the little known expression first developed by Soper and Dove (1962) in terms of Equations (2-25) and (2-26), it is found that the second term of  $(h_o/T_c)$  in Equation (2-25) actually denotes the initial strain rate of deformation of the skin cushion in Equation (2-28), and that the momentum transfer,  $mV$ , from the free-falling impactor to the cushion is invariant. Equation (2-28) demonstrates the all-importance of strain-rate effects in the study of dynamic skin cushioning characteristics.

### 2.2.6 The Significance of Increasing the Duration of Impact for Damage Protection

Here we tried to correlate one of the major primary impact parameters, namely, the duration of impact, following the work related to Hertz contact analysis by Horsfield *et al.* (1972) and Studman (1995a). The latter assumes an elastic Hertz impact for modelling produce bruising and expresses the contact (or bruise) diameter as:

$$a = 0.2 \sqrt[3]{\left( \frac{kMh_o R^2}{E_o} \right)} \quad (2-29)$$

where  $a$  = contact (bruise) diameter (m),

$k$  = constant,

$M$  = mass of fallen object (kg),

$h_o$  = drop height (m),

$E_o$  = Young's modulus which depends on storage periods and water loss, and

$R$  = radius of curvature of the impact object (m), or radius of the fruit at the point of impact as defined in terms of  $x$  values in Equation (2-1) and Figure 2.9.

Equation (2-29) shows a representative bruise model that incorporates the major impact parameters and their individual contributions. Here the duration of impact,  $\tau$ , is of only secondary importance due to the unique  $\tau$  characteristics which seem virtually invariant for drop heights between 5 to 20 cm. However, the duration of impact becomes important if packaging protection plays a significant part in the analysis, as shown in Figure 2.54, Chen and Yazdani (1991). This experimental set-up did not simulate actual free-fall drops of fruits (Golden Delicious apples in this case) due to a light-weight Plexiglas fruit holder, which weighed 120 gm together with an accelerometer, strapped onto the fruit with a rubber band for each drop test. It shows, nevertheless, that  $\tau$  increases as the level of surface protection increases (that is, with increasing cushion thickness). As expected, the acceleration gradually decreases as  $\tau$  increases. The most notable change is the

uploading time during the impact due to the rheological property of the cushion, see Figure 2.54, which registers an increase from 1 ms without cushion to 3 ms with cushion thickness of 6.35 cm. The cushion used here is made of closed-cell neoprene sponge sheets.

The interrelation of the process can be illustrated in Figures 2.55 and 2.56, see Wyskida and McDaniel (1980), which explains the reason for the increase in  $\tau$  and gradual decrease in peak acceleration as the impact surface softens, see Figure 2.55. It is noted that no matter how the change would take place, the area under the acceleration-impact duration curve (that is, velocity change,  $\Delta V$ ) always remains unchanged. In other words, the area  $A_1$  is always equal to  $A_2$ , see Figure 2.56. If this is violated, then the impulse, or the momentum change during the impact, for the two cases would be different due to other complicated problems such as internal cracking of the materials.

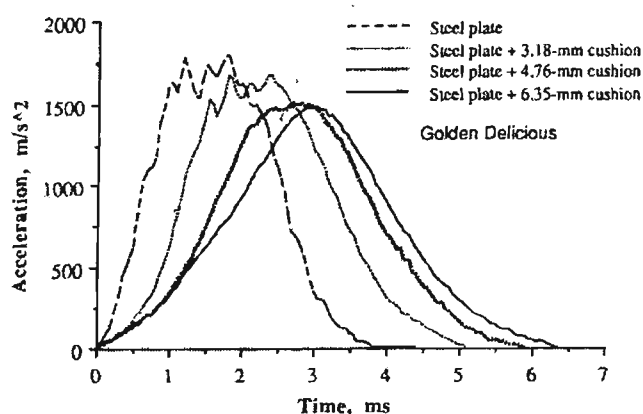


Figure 2.54 Relationship of acceleration and corresponding duration of impact,  $\tau$ , of Golden Delicious apples dropping from 30 cm on various surfaces. From Chen and Yazdani (1991).

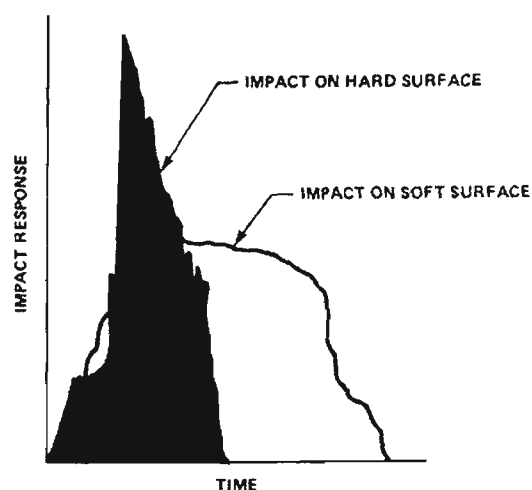


Figure 2.55 Shock pulse responses due to impact on hard and soft surfaces. From Wyskida and McDaniel (1980).

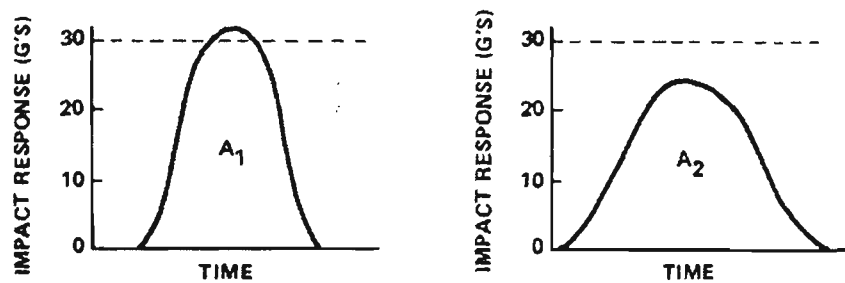


Figure 2.56 Shock pulse fragility level. From Wyskida and McDaniel (1980).  
(Here the unit “G’s” denotes  $g$ , the gravitational acceleration).

The pulses as shown in Figure 2.56 are of the typical haversine types that are the most commonly experienced pulses during the impact of produce. They are denoted as clean pulses without superimposed noise. For comparison, a standard (or ‘dirty’) shock pulse with noise is shown in Figure 2.57, Brooks (1967), which requires special consideration of maximum amplitudes and impact duration. These extra treatments for noisy data are sometimes essential for the elimination of possible data interpretation errors that have been estimated to be around  $\pm 5\%$  for  $\tau$  and  $\pm 10\%$  for  $\Delta V$ , according to Brooks (1967). Some available data-acquisition software packages are designed with built-in cut-off, for instance, a 10% cut-off of the velocity change as shown in Figure 2.57. The Kornhauser damage-sensitivity curve as shown in Figure 2.58, see Kornhauser (1954), has been the most significant representation in predicting sensitivity of equipment to damage during impact.

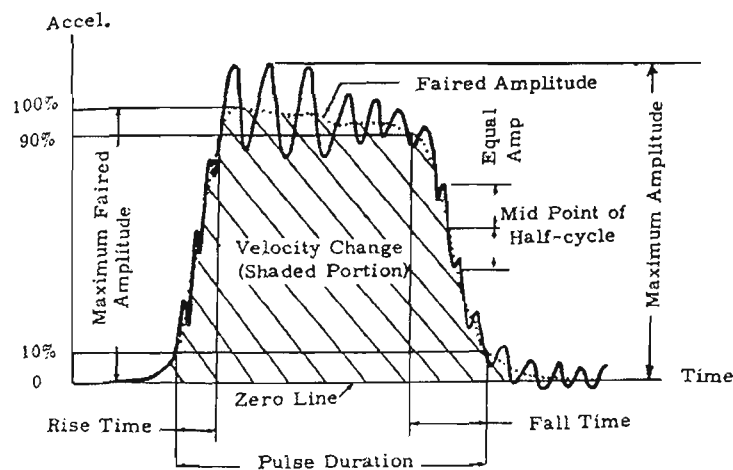


Figure 2.57 Standard interpretation of a shock pulse. From Brooks (1967).

It is clear that damage can be avoided even under a large shock pulse, or large  $\Delta V$ , as long as the pulse is contained below an acceleration level that is less than the damage threshold and coupled with a much extended impact duration. Maximum protection can be exerted onto the protected package if the duration of impact can be extended to the maximum amount possible. Since the

momentum change, and thus  $\Delta V$ , of an impacting object can be treated as a constant, the impact acceleration, called 'impact response' in Figures 2.55 and 2.56, can be kept at a minimum if the corresponding  $\tau$  can be maximized.

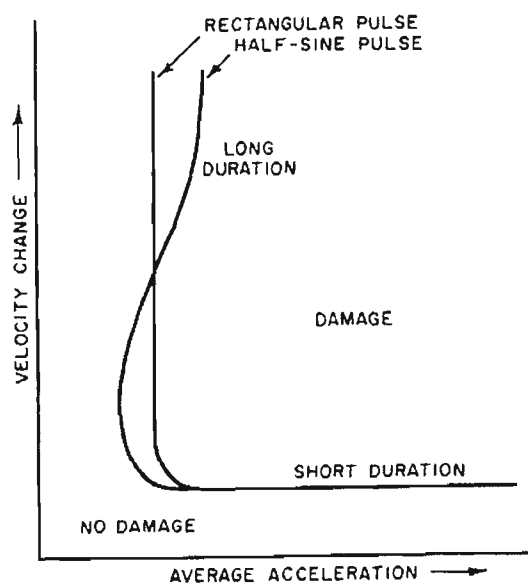


Figure 2.58 Kornhauser damage sensitivity curves of velocity change,  $\Delta V$ , versus average peak acceleration,  $g_{maxavg}$ . Solid lines are damage thresholds. From Kornhauser (1954).

### 2.2.7 Internal Energy Dissipation in Produce

Figure 2.51 shows typical displacement and acceleration histories of a rigid impacting body falling vertically onto a cushion modelled by a three-element viscoelastic Voigt solid. It illustrates a typical viscoelastic response representative of the initial stage of viscoelastic deformation in horticultural materials before yielding. Here the peak acceleration and maximum displacement do not occur at the same time. It is noted that the maximum strain lags behind the maximum force. Therefore, under Newton's second law, the force terms on the impacting body can be balanced only by the addition of a dissipative term to the system. This illustrates the fact that some of the kinetic energy dissipates into other forms of energy during an impact, and ultimately to heat. On the other hand, if a material is perfectly elastic, no heat dissipation is expected.

According to Sharma and Mohsenin (1970), horticultural materials are well represented by a 3-element Voigt structure before yielding. For a linear material with a Voigt structure,

$$E(t) = \left[ \frac{c_1}{d_1} \right] e^{-t/p_1} + c_0 \left[ 1 - e^{-t/p_1} \right] \quad (2-30)$$

where  $c_0$ ,  $c_1$ ,  $d_1$  and  $p_1$  are material constants, and  $E(t)$  the time-varying effective modulus. They are related to the Voigt model as follows:

$$c_0 = k_2, \quad c_1 = (k_1 k_2)/(k_1 + k_2), \quad d_1 = \eta/(k_1 + k_2), \quad \text{and} \quad p_1 = (k_1 \eta)/(k_1 + k_2) \quad (2-31)$$

Here  $k_1$  and  $k_2$  are spring constants, and  $\eta$  is viscosity. To account for any nonlinear effects of the horticultural materials as they are compressed during impact, the spring parameters of the produce material, primarily  $k_1$ , become strain dependent. This implies that the spring constants increase with increasing deformation. Here they are constants only at particular  $\varepsilon$  values. It is assumed that the change in  $k_2$  is small. The  $k_1$  parameter in Equation (2-31) can be rewritten in the form:

$$k_1 = k_3 + k_4 \varepsilon^{\alpha_1} + k_5 \varepsilon^{\alpha_2} \quad (2-32)$$

where  $k_3$ ,  $k_4$ ,  $k_5$ ,  $\alpha_1$  and  $\alpha_2$  are parameters to be determined by matching the mathematical expression to actual experimental data. Physically, the normal stress of the produce material is a function of normal strain, strain rate and time, as follows:

$$\sigma = f\left(\varepsilon, t, \frac{\partial \varepsilon}{\partial t}\right) \quad (2-33)$$

By substituting Equation (2-31) into Equation (2-30), it becomes:

$$E(t) = \left[ \frac{k_1 k_2}{\eta} \right] e^{-t/p_1} + k_2 \left[ 1 - e^{-t/p_1} \right] \quad (2-34)$$

Equation (2-34) shows that the spring parameter,  $k_1$ , of the Voigt element as shown in Figure 2.51 does become strongly strain dependent as the material is compressed upon impact. Also, since  $\sigma$  depends on the strain rate,  $d\varepsilon/dt$ , to a lesser degree, it can be seen, for instance, from Equation (2-17) that  $\sigma$  depends primarily on  $\varepsilon$ , even if this may not be easily realized based on mathematical expressions. For the application of Equation (2-34) to real situations, serious computational errors may possibly occur if invalid assumptions are made. The most commonly accepted assumptions for the deformation of viscoelastic materials include:

- (i) that the dynamic stress-strain relationship is dominated by the strains but not the strain rates, and
- (ii) that the strain rate throughout the pre-peak material deformation is invariant.

These assumptions do not take into account the time lag between the moments when peak stress,  $\sigma_m$ , as related to peak acceleration and peak strain,  $\varepsilon_m$ , as related to peak deformation occurs. Since  $\sigma$  is a

function of  $\varepsilon$  and  $t$ , it would be a rare coincidence if  $\sigma_m$  and  $\varepsilon_m$  occur at the same moment. Thus, an equation based on Newton's Second Law will be valid only with the addition of a dissipative term, due to the presence of internal energy dissipation in viscoelastic materials under loading.

The internal energy dissipation mechanisms are generally termed 'internal friction', according to Kosky (1963). For polycrystalline solids such as metals, heat loss is the most profound dissipation mechanism, Zener (1948). For semi-crystalline cellulose cell-wall structures, heat is also generated in imperfections such as micro-cracks and flaws, and also at the wall boundaries between cells. However, unlike metals, polymers with long-chain molecules such as the produce cell-wall structures suffer the most significant energy losses through viscous loss, as the losses are viscous in nature. This explains why the mechanical behaviour of these materials is on many occasions strain rate dependent, Kosky (1963). This loss mechanism can change the nature of a disturbance such as a wave pulse from impact in these materials in two fundamental ways:

- (1) Attenuation or dissipation of the disturbance – due to the viscoelastic nature of the materials, there is always a time lag between peak stress or force and peak strain or displacement, resulting in a phase difference commonly defined as  $\tan \delta$  as follows:

$$\tan \delta = E''(\omega) / E'(\omega) \quad (2-35)$$

where  $E'(\omega)$  is the storage modulus and  $E''(\omega)$  the loss modulus.

When a stress pulse propagates through viscoelastic materials, it will be severely attenuated if the wave period is close to the relaxation time,  $t^*$ , of the material, Kosky (1963), resulting in substantial energy losses.

- (2) Dispersion of the disturbance – a wave pulse that propagates in a viscoelastic material is normally dispersive. In other words, the pulse 'splits' into a whole spectrum of frequencies as it propagates, with wavelets of different wave-numbers each travelling with its own phase speed. As the single original hump now disperses into a whole oscillatory wave train, they superimpose on each other, forming groups, or wave packets, as shown in Figure 2.59, which propagate with a unique group velocity if the pulse originates with a reasonably narrow band, see Bedford and Drumheller (1994). However, a broad band of pulses is generated during an impact of fruit such as apples, Garrett (1970). The disturbance that travels with group velocity would be expected to change in shape continuously during its motion and be much more complex than that shown in Figure 2.59.

In a material that is dissipative as well as dispersive, such as horticultural materials, the relationship between group velocity and the sinusoidal phase velocity is not clear. This situation is

complicated and perhaps can only rely on experimental data. Here the tangent of the phase angle  $\delta$  is of particular interest. As mentioned earlier,  $\delta$  represents the angle by which the strain lags behind the stress. It correlates quite well with the 'internal friction' of a linear viscoelastic material, Findley *et al.* (1989); Haddad (1995).

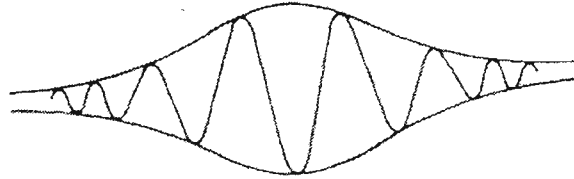


Figure 2.59 Sketch showing phase wave (sinusoidal) and group wave (envelope).

Under dynamic conditions, it is generally much more difficult to characterize viscoelastic and viscoplastic materials such as fruits, than elastic materials such as metals. This is primarily due to two factors, according to Fowler (1990):

- (1) Viscoelastic and viscoplastic materials under dynamic loading, even within their linear deformation range, dissipate a much larger fraction of the input (loading) energy into heat than do metals. For this reason, both the energy storage (elastic) and the energy dissipation (damping) characteristics require characterization and measurement. It is possible that the degree of energy dissipation can be expressed in terms of the coefficient of restitution,  $e$ , of materials under loading conditions.
- (2) The damping and elastic characteristics of viscoelastic and viscoplastic materials are functions of (i) excitation frequencies under dynamic loading and (ii) temperatures. These characteristics often vary significantly, especially for more dissipative materials. The effects due to frequency can be investigated using measurement techniques such as DMA. The effects due to temperature were eliminated in the present study for all tests, by carrying out tests at more or less the same ambient temperature (19°C to 22°C).

Traditionally, these materials have been characterized by mechanical models, using spring and viscous elements to represent, respectively, moduli which account for energies stored as potential energy by spring elements and dissipated energies such as heat by viscous elements.

One of the more convenient ways to evaluate energy losses in a system under impact, however, is to express the kinetic energy losses in terms of the coefficient of restitution,  $e$ , according to Mok and Duffy (1965).  $e$  is a measure of the final to initial velocity components of impacting

bodies in the direction normal to their contact surfaces. It is a function of the size of contact surface and friction, as well as the viscoelastic and viscoplastic properties of the impact bodies involved. The value of  $e$  will always be less than unity under all energy dissipating systems. The kinetic energy is usually dissipated in three principal ways:

- (i) Surface roughness should influence the nature of rebounds through frictional loss. For instance, the restitution can only achieve a value of 0.95 even for impacts between highly polished elastic steel balls and rigid surface, Lifshitz and Kosky (1964). It was found to be very sensitive to the conditions of the impacting surfaces.
- (ii) Kinetic energy can be lost at high strain rates of material deformation during collisions. This applies to anelastic materials which also accounts for part of the energy losses of the elastic steel balls mentioned above, in viscoelastic materials with dissipative effects, and in viscoplastic materials with strongly dissipative effects through internal frictions of a plastic flow field in the vicinity of the impacting surface. It is generally believed that the major loss of kinetic energy in elastic and anelastic systems is a consequence of these effects, Hunter (1957).
- (iii) A certain amount of kinetic energy can also dissipate into internal vibration motion in elastic or viscoelastic waves, as well as plastic/viscoplastic waves spreading out from damaged zones for severe loading. This third form of energy loss has been found to be small in elastic systems as compared to the second form (ii), Hunter (1957). In other words, if the impact velocity is small compared to the propagation velocity of elastic waves in the material, only a negligible proportion of the original kinetic energy is transferred during the collision. However, for the case of viscoelastic materials, the viscoelastic waves, particularly those with low frequencies, propagate at much lower velocities than elastic waves do. This slowing down of the propagating wave, in the form of acceleration waves, to be discussed in Chapter 3, becomes more profound when the waveform is dispersive. In the case of permanent damage in the material during collision, the plastic waves will spread out from the damaged zone propagating at even slower velocities than viscoelastic waves. The kinetic energy which is transferred and lost in these cases is no longer negligible, but becomes more significant and takes a more dominant role in materials with increasing plastic, or permanent, deformation. This will be discussed in more detail in Chapter 3.

For (ii) as listed above, energy losses will be more profound in viscoelastic and viscoplastic systems. This is because they will be lost in viscous and plastic effects, in the form of relaxation of the stress in the materials under transient loading, in the vicinity of the contact region of the impact surface. A direct mathematical relation has been established between the energy loss due to internal friction during impact and the relaxation spectrum,  $H(\tau)$ , of the material by Tillett (1954). She followed the approximate approach, developed earlier by Zener (1941), for the estimation of compressive stress in viscoelastic bodies under the assumption of the Hertzian theory of contact. The ratio of the energies,  $R_E$ , stored as shear to longitudinal compression energies, can be expressed, according to Dyson (1965) and Tillett (1954), as:

$$\frac{\text{ShearEnergy}}{\text{LongitudinalEnergy}} = \frac{2(1-\nu + \nu^2)}{(1-2\nu)(1+\nu)} = R_E \quad (2-36)$$

where  $\nu$  is the Poisson's ratio.

From their work, it follows that the shear energy can be expressed in terms of the total energy, assuming that the bulk of the total energy comprises shear and longitudinal energies only, and other forms such as heat dissipation are negligible. This can be expressed as:

$$R_{shear} = \frac{R_E}{R_E + 1} \quad (2-37)$$

where  $R_{shear}$  is the percentage of total energy which is in the form of shear energy.

According to Equations (2-36) and (2-37), if  $\nu$  equals 0.25, the ratio  $R_E$  is 2.6, implying that 72.2% of the energy is stored in the form of shear. If  $\nu$  equals 0.35, the ratio becomes 3.815, implying that 79.2% of the impact energy is stored in shear form. If  $\nu$  equals 0.49, the ratio becomes 50.34, implying that 98.1% of the impact energy is stored as shear. As  $\nu$  approaches 0.5, the impact energy, which is stored in the form of shear energy, approaches 100%. This implies that horticultural materials with high Poisson's ratio will be most likely having their energies stored in the form of shear energy. Equation (2-37) was plotted as Figure 2.60 as below.

There are many examples of soft biomaterials which do have Poisson's ratios equal to or greater than 0.5. For instance, cow's teat tissues can have a  $\nu$  value of up to 1.2 and locust membrane close to 1.0, see Vincent (1990). Figure 2.61 indicates two distinct levels of Poisson's ratio, at 0.33 and 0.5. In this Figure, the Maxwell body behaves as an elastic solid during the initial instant loading, and as a liquid at subsequent time intervals. The Kelvin-Voigt body and the standard linear solid behave as solids over

long intervals during which  $\nu = 0.33$ . At short intervals, both the Kelvin-Voigt and the standard solid behaves as viscoelastic solids, but the standard solid appears more elastic than the Kelvin-Voigt solid. Poisson's ratio can be useful to provide excellent indications regarding the mechanical properties of horticultural materials. Unlike most metals, which can have  $\nu$  ranging between 0.25 to 0.34, produce tissues rarely appear to be very stiff ( $\nu = 0.25$ ).

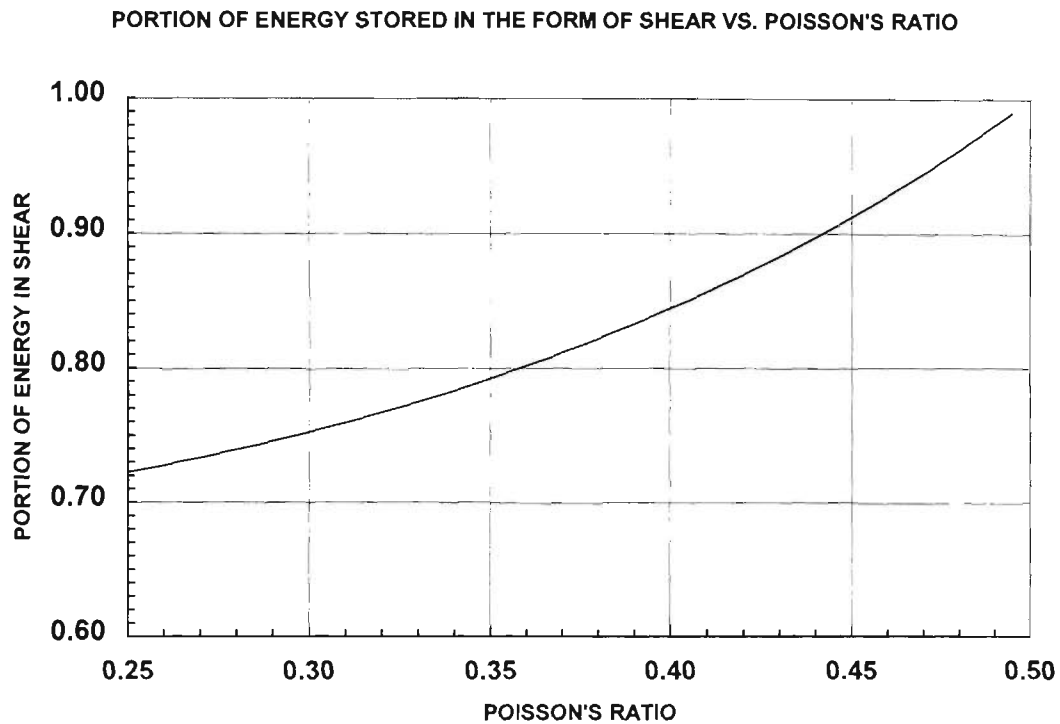


Figure 2.60 The relationship of impact energy as stored as shear energy versus Poisson's ratio.

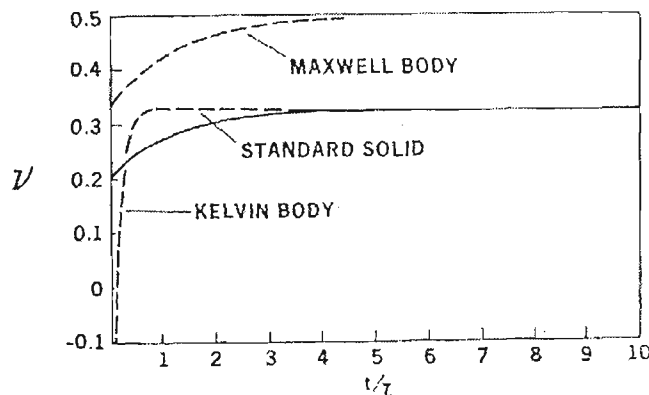


Figure 2.61 Relationship of Poisson's ratio versus the ratio of lapsed time to relaxation time, showing the lateral response of three simple mechanical models.

### 2.2.8 Characteristics of Shock Pulses

A shock pulse depicts the physical phenomenon of mechanical energy transfer from one body to another during a very short time. It provides a record and insights into the different impact conditions encountered. For instance, the impact of a rigid sphere onto a hard surface produces a shock pulse of large force amplitude but very short time duration of impact,  $\tau$ , but similar impacts on soft surfaces produce low-amplitude shock pulses but of longer duration.

In experimental IFA tests for typical apple drops,  $\tau$  is about  $4.18 \pm 0.15$  ms, Ip, Leonart and Marcondes (1995), for a 20-cm drop on rigid surface. Studman (1995b) who carried out dynamic impact experiments on apples obtained comparable  $\tau$  values using a high-speed video camera. For a low drop height of, say, 10 cm,  $\tau$  is very much the same in magnitude as in the 20-cm drop. Figure 2.62 shows the results of a typical shock pulse of a whole apple dropped onto a dynamic load cell as shown in Figure 2.2, with near symmetric haversine pulse feature. The gentler slope during the unloading cycle of a shock pulse is an indication of damping that can be caused by plastic deformation and/or damage to the structure. In the cases of drop tests of market-fresh apples onto rigid surfaces, bruising usually starts to occur at a drop height of about 5 cm.

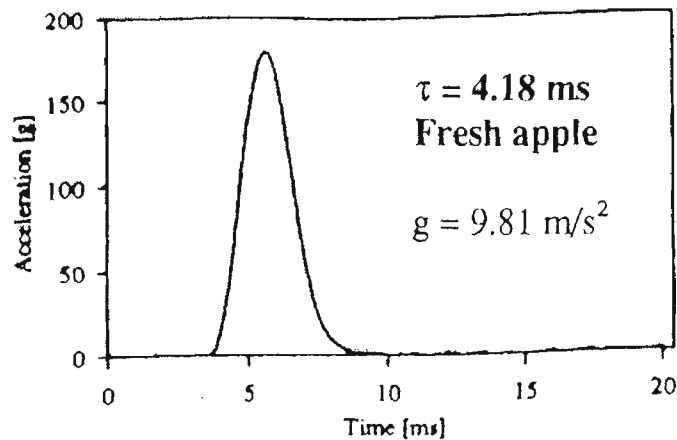


Figure 2.62 Typical haversine shock pulse of a whole market-fresh Golden Delicious apple dropping onto a dynamic load cell from 20 cm. (Run ST 24-20A) From Ip, Leonart and Marcondes (1995).

The variation of  $\tau$  seems insignificant as the drop height increases from 5 cm to 20 cm. Theoretical work in the past indicates that the duration of impact is only loosely proportional to the impact energy. It depends on the mechanical properties of the impactor as well as the contact surfaces, particularly if the impacted surface is not rigid and not smooth. Whereas this thesis focuses on the dynamic characteristics of produce within their skin boundaries, it will be of interest in future work to study the dynamic behaviour due to the transient interaction between the skin boundaries and the impact surfaces. It is possible that the contact surfaces can become ‘rough’, depicting the

dominant effect due to dynamic friction in those cases under low impact energies (or low drop heights). As such, it is possible that the transient interactions between the impact boundaries can substantially alter the coefficient of restitution.

For smooth surfaces, the duration of impact between a viscoelastic spherical impactor on a rigid surface including any instance of plastic deformation is expressed as a modified form due to Hunter (1960a):

$$\tau = \tau_0 (1 - 0.037\eta'\tau_0) \quad (2-38)$$

where  $\tau_0$  is the elastic impact duration and

$\eta'$  is the inverse relaxation time of the viscoelastic impactor.

$$\tau_0 = 2.94 \left( \frac{15M(1-\nu)}{32R^{0.5}G_i} \right)^{0.4} (2gh_0)^{-0.1} \quad (2-39)$$

where  $M$  is the mass of the impactor,

$\nu$  is the Poisson's ratio of the impactor,

$R$  is the radius of curvature of the impactor, and

$G_i$  is the instantaneous complex shear modulus of the impactor.

From Equation (2-39), it is clear that very small changes in  $\tau_0$  will be expected, even if the drop height,  $h_0$ , is doubled. In other words,  $\tau$  is only loosely proportional to the impact energy. According to Love (1954) Equations (2-38) and (2-39) were originally derived by Hertz, who established the theory of Hertzian contact which has been widely used in engineering applications. Its acceptance in the agricultural engineering community is mixed. Some researchers working on impact analysis of agricultural materials indicated that the Hertz law of contact is an appropriate model for spherical produce which are crisp – see, for instance, Lichtensteiger (1982). Others believed that the use of the Hertz contact theory for the estimation of contact stress during fruit impact, including the use of modified versions of the theory for viscoelastic materials, see Yang (1966), seems to be inappropriate. This is because some of the basic assumptions of Hertz are not fulfilled in the case of fruit impact, according to Manor (1978). Still others have experimentally confirmed that, under viscoelastic impacts, the pressure on the impact surface may or may not be distributed in the pattern assumed by Hertz, thus the Hertz assumption was not confirmed, see Luan (1990).

Early studies in the 1950's on shock pulse attenuation in viscoelastic materials, notably by Davies (1956) and Kosky (1956), show that the wave dispersion process occurs in a wave pulse with a large range of frequencies in the form of a wave packet. They believed this is the result of damping out of the high frequency components. A frequency spectrum or power spectral density of the shock

pulse as shown in Figure 2.62 is illustrated in Figure 2.63. It is obvious that the high frequency components, particularly those higher than 1,000 Hz, contribute much less energy than those below 1,000 Hz, indicating high wave dispersion activities. This is not to be confused with wave dissipation, which also contributes to wave attenuation and occurs in the main energy-carrying sector. As has been pointed out in Section 2.2.7, wave dissipation is associated with the wave loss as a result of the phase difference commonly defined by the storage and loss modulus of the material. Figure 2.63 illustrates that, for produce such as Golden Delicious apples, the bulk of energy dissipation in a wave pulse is predominantly below a frequency of 1,000 Hz under a drop height of 20 cm. Substantial energy loss due to wave dissipation was not observed here. This only occurs when the wave period is close to the relaxation time of the material.

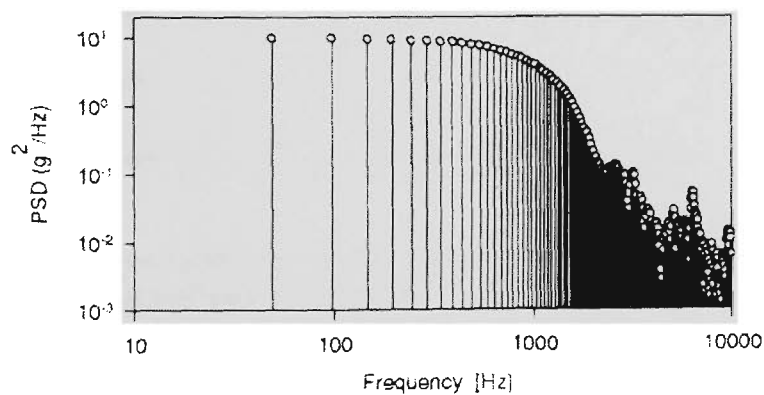


Figure 2.63 Frequency spectrum of pulse disturbance during an impact of Golden Delicious whole apple on a dynamic load cell showing broad band spectrum up to around power spectral density (PSD) of  $10^0 \text{ g}^2/\text{Hz}$  or energy dissipation up to 1,000 Hz. Apple weight is 154.19 gm. Drop height is 20 cm. (IFA Test Run ST 24-20A)

In general, a broad band of pulses is generated during an impact of fruits such as apples, Garrett (1970). The disturbance, which travels with group velocity, would be expected to change in shape continuously during its motion. A maximum drop height of 20 cm was so chosen to represent an upper limit expected within the range of human handling. In order to simplify the analysis of shock pulses that do not produce bruising, a drop height of 5 cm or less has to be chosen. Here, a pulse generated from a 5-cm IFA drop test is illustrated in Figure 2.64. If the drop height is held constant, the area under impact curves of different impact conditions should be equal, depicting that the change of velocities,  $\Delta V$ , and the impact energy that the produce receives should be unchanged under different impact conditions.

Now if we take the derivatives of all the shock pulse data points from Figure 2.64, and plot  $\partial g/\partial t$  versus impact duration as shown in Figure 2.65, a sharp rise of the derivative can be noticed

during the initial moments of contact. This curve was processed with a filtering frequency of 2,000 Hz. Physically, this shows the presence of a particular waveform during the initial stage of impact called the acceleration wave. The term 'acceleration wave' is an appropriate description of the energy-carrying wave pulse for common applications in plastics and a large variety of soft materials, and particularly this study, which concerns agricultural produce.

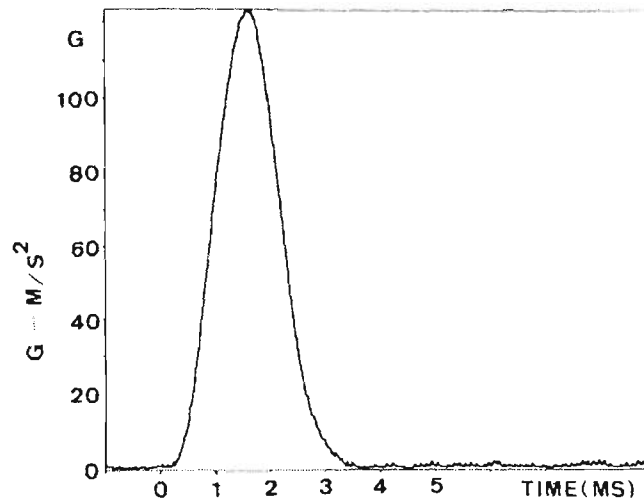


Figure 2.64 Shock pulse from a 5-cm free-fall drop of a whole-fruit market-fresh Golden Delicious apple showing typical haversine pulse shape. (IFA Test Run ST-20-5A) The unit adopted by packaging industries is G ( $9.81 \text{ m/sec}^2$  or 'g' of the S.I. units). Peak value reads 125 g, or  $1,225 \text{ metre/sec}^2$ . Apple weight is 128.12 gm.

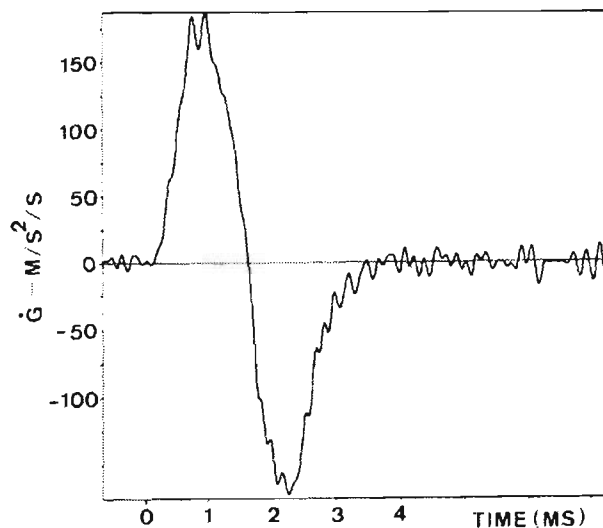


Figure 2.65 Plot of the derivative of a shock pulse against the duration of impact from a 5-cm free-fall drop of a whole-fruit Golden Delicious apple. The unit for  $\dot{G}$  is  $9.81 \text{ metre/sec}^2/\text{sec}$ . (IFA Test Run ST-20-5A)

An acceleration wave can be deemed as a propagating wave that suffers jump discontinuities in its acceleration. In other words, the time derivative of the acceleration at the wave front approaches

infinity. Under the assumption that the mass and the cross-sectional area of the medium through which the wave front passes through are invariant, the acceleration wave front can be re-defined as a stress front of near infinite gradient, or  $\partial\sigma/\partial t \rightarrow \infty$ , where  $\sigma$  is the stress at any moment during the impact. This can be illustrated in Figure 2.65 at about 0.4 ms. The implication is that during the early stage of impact in produce, wave fronts do exist and arguably cannot be flatly ignored in an analysis.

### 2.2.9 Wave Effects in Dynamic Deformation of Horticultural Materials

The most striking feature of waves is their capability of carrying energy over long distances, as well as vital information about energy dispersion and dissipation. We note that the one-dimensional (1-D) stress state of a wave pulse, propagating in linear viscoelastic medium, can be represented by a relationship between stress and strain, according to Christensen (1982), as:

$$\sigma(t) = \varepsilon(0)G(t) + \int_0^t G(t-\tau')\varepsilon(\tau')d\tau \quad (2-40)$$

where  $\sigma(t)$  is the shear stress at time  $t$ , the lapsed time of an event;  $\tau'$ , a particular time of interest,  $\varepsilon(t)$  is the shear strain in the material at time  $t$ , and  $G(t)$  is the shear modulus, or the stiffness of the produce material, whose value depends upon the material of interest.  $G(t)$  is the simplest form of  $G^*(\omega)$ , the complex shear modulus.

Here,  $G(t)$ , relates the stress-strain relationship of a linear viscoelastic material in the form:

$$\sigma = G(t) \varepsilon \quad (2-41)$$

By setting up the equation of motion for a volume of viscoelastic body with acting body forces per unit volume,  $f_i$ , it follows that:

$$\frac{\partial\sigma}{\partial x} + f_i = \rho \frac{\partial^2 u}{\partial t^2} \quad (2-42)$$

where  $\partial^2 u / \partial t^2$  is the acceleration term,  $u$  is the displacement normal to  $x$ ,  $\rho$  is the density, and  $x$  is the direction of wave propagation.

The strain and strain rate can be expressed in the  $x$ -direction as:

$$\varepsilon = \frac{\partial u}{\partial x} \quad \text{and} \quad \dot{\varepsilon} = \frac{\partial^2 u}{\partial x^2} \quad (2-43)$$

Under quasi-static conditions, the inertia term is negligible. It follows that:

$$\partial\sigma = -f_i \partial x \quad (2-44)$$

Equations (2-41) and (2-44) are identical.

Under dynamic conditions such as impact, the dynamic effects cannot be neglected. The inertial term  $\rho (\partial^2 u / \partial t^2)$  is non-zero, since the inertia of the viscoelastic materials will influence the stress field as they 'flow' through the deforming region. In this case, the solutions for stresses and displacements obtained could be interpreted as pulses (or waves) which propagate through the solid with characteristic speeds, see Kolsky (1963). Kolsky used Fourier representation of a stress pulse to analyze wave propagation in terms of the complex modulus description in a linear viscoelastic solid. However, an approach such as the Fourier transform treatment of 1-D stress wave propagation can handle only the simplest problems, see, for instance, Bland (1957), and can only be used when a linear (steady state) response is possible, see Lee (1960). First introduced by Gross (1953), the transformation techniques can either be of the Fourier or Laplace type. Using the Laplace transformation, Berry (1958a) showed that the stress-strain expression by Kosky (1963) and later by Bodner and Kosky (1958) is indeed not flawless. Later in this section we will also point out that the wave equation can be quasi-linear, a situation where transformations cannot be used. Viscoelastic wave fronts are predominantly nonlinear in nature. However, waves coupled with any dissipation process such as heat will be quasi-linear.

According to Ting (1975), if a wave front travels at its characteristic speed (sometimes called the energy-carrying group velocity,  $c_g$ ), the transport or momentum equation of the acceleration wave front (naturally, of order,  $N=2$ ) has to be nonlinear. For higher-order wave fronts ( $N>2$ ), the transport equation and thus the wave front characteristics behave linearly. In other words, only the nonlinearity of the acceleration wave front velocity affects the wave front characteristics. For higher-order waves, nonlinear wave speeds do not affect the linear wave front characteristics. In most cases, and in acceleration waves in particular, there is always a competition between two factors: the nonlinearity, which tends to deepen the wave fronts into shock waves, and any dissipation (such as heat), which tends to smooth wave front discontinuities. Waves can propagate in longitudinal, shear, or other waveforms. They can exist as shock waves with the wave discontinuity in their first derivatives of the displacement, or can exist as acceleration waves with the wave discontinuity in their second derivatives of the displacement. Also, they can be classified into elastic, viscoelastic or plastic wave types. In particular, the latter wave type exhibits significant transformation that will be discussed in Chapter 3. The unique properties of waves under various forms or types may somehow be reflected by their wave front properties.

While numerical modelling work of wave propagation will not be included in this thesis, it may be necessary to define the coordination system used for the description of the deformation. If we refer back to Equation (2-42), and assume no more body force,  $f_i$ , acting on the produce during the rebounding cycle, Equation (2-42) can be rewritten as:

$$\frac{\partial \sigma}{\partial x} = \frac{\rho \partial^2 u}{\partial t^2} \quad (2-45)$$

If Equation (2-45) is described under Eulerian coordinates, then the strain in Equation (2-43<sub>1</sub>) is described in the deformed state, and the instantaneous coordinates of a material particle at  $(x, y)$  are taken as the independent variables. This implies that the stress,  $\sigma$ , in Equation (2-45) denotes the true (Cauchy) stress, and the material density,  $\rho$ , is in the strained state. In actual dynamic measurements, it is always difficult to measure the instantaneous stress and material density, particularly in transient analysis of deformation such as the present study. Therefore, it is logical for the coordinates to resort to the Lagrangian formulation. It follows that the stress,  $\sigma$ , and material density,  $\rho (= \rho_o)$ , denote the engineering (Piola-Kirchhoff) stress and the density in the unstrained (or initial) state, respectively. Understandably these values, when compared to their Eulerian counterparts, are fairly easy to be measured. Now, in the sense of Lagrangian, the strain in Equation (2-43<sub>1</sub>) is described in the initially undeformed or undistorted state, and the initial coordinate of the material particle at  $(x_o, y_o)$  is considered as independent variables. Then, Equation (2-45) can be rewritten as:

$$\frac{\partial \sigma}{\partial x} = \frac{\rho_o \partial^2 u}{\partial t^2} \quad (2-46)$$

Since  $\sigma$  is always a function of  $\epsilon$ , see Equations (2-5) and (2-7) for both linear and non-linear cases, respectively, an expression can be established using Equation (2-43<sub>2</sub>) as:

$$\frac{\partial \sigma}{\partial x} = \frac{d\sigma}{d\epsilon} \left( \frac{\partial \epsilon}{\partial x} \right) = \frac{d\sigma}{d\epsilon} \left( \frac{\partial^2 u}{\partial x^2} \right) \quad (2-47)$$

Now if Equations (2-46) and (2-47) are combined, it becomes:

$$\frac{\partial^2 u}{\partial t^2} = \frac{1}{\rho_o} \left( \frac{d\sigma}{d\epsilon} \right) \left( \frac{\partial^2 u}{\partial x^2} \right) = c^2 \left( \frac{\partial^2 u}{\partial x^2} \right) \quad (2-48)$$

where the wave front velocity,  $c$ , can be expressed as:

$$c = \sqrt{\left( \frac{1}{\rho_o} \right) \left( \frac{d\sigma}{d\epsilon} \right)} \quad (2-49)$$

Equation (2-48) is a wave equation that is also a hyperbolic partial differential equation (PDE). This means that a viscoelastic material under disturbance will be expected to experience wave motion. A linear wave differs from a quasi-linear wave in that the phase shifting causes the gradual distortion and loss of linearity of the wave as it propagates. This dispersion of frequencies from the initial fundamental to ranges of harmonics has significant impact on the shape of the wave front and the energy transport, which depends on the energy-carrying wave packets. A unique wave-packet pattern is normally expected under quasi-linear waves, but with ever-changing patterns under nonlinear waves. The degree of wave distortion and the establishment of wave-packet pattern are

directly dependent on the wave amplitudes. In the case of undamaged (no cracking, fracturing, etc.) plastics such as Perspex, Figure 2.66, the attenuation of the wave amplitude is usually substantial during the propagation, accompanied by a gradual smoothing of the wave front.

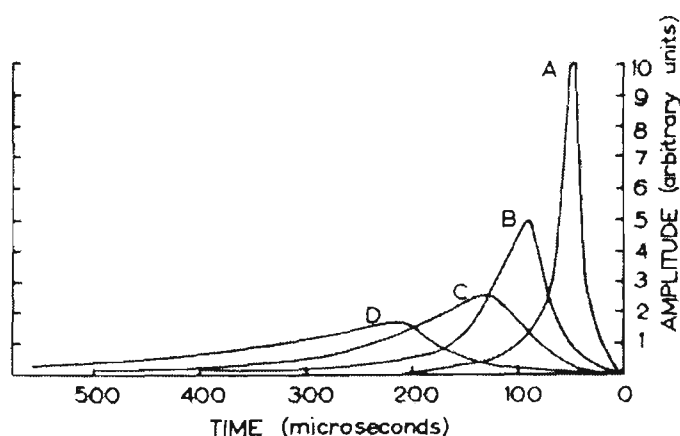


Figure 2.66 Strong attenuation of the wave amplitude as the wave propagates along a Perspex rod at  $15^{\circ}\text{C}$ , with gradual smoothing of the wave front as recorded at stations A: 120 cm (from source); B: 360 cm; C: 600 cm; and D: 840 cm. From Kosky (1956).

From Figure 2.66, questions may arise as to the decay characteristics between shock waves and acceleration waves. Coleman and Gurtin (1965) found, for the case of linear viscoelastic materials, that the decay of acceleration waves is of the form:

$$\frac{a(t)}{a(0)} = e^{-\left[\frac{1}{2}\left(\frac{G^*(0)}{G^*(0)}\right)'\right]t} \quad (2-50)$$

where  $a(t)$  and  $a(0)$  are the wave amplitude of arbitrary units at time  $t$  and  $0$ , respectively,

$G^*(0)$  is the complex shear modulus at time  $t = 0$ , and

$G^{*'}(0)$  is the derivative of the complex shear modulus at time  $t = 0$ .

Results from a seminal article by Chu (1962) show exactly the same wave decay expression in the form of Equation (2-50) for similar materials under shock waves during the initial stage of deformation (as compared to the acceleration wave above): Regarding the two major waves, an acceleration wave has been defined as a propagating wave that suffers jump discontinuities in its acceleration. In other words, the time derivative of the acceleration at the wave front approaches infinity. Under the assumption that the mass and the cross-sectional area of the medium through which the wave front passes are invariant, the acceleration wave front can be re-defined as a stress front of infinite gradient,  $\partial\sigma/\partial t$ , where  $\sigma$  is the stress at any moment during the impact. This has been illustrated in Figure 2.65.

Let us recall from Figure 2.65 that the interplay between a shock wave and an acceleration wave depends on the continuous changes of their propagating wave front. If the wave front deepens, it will develop into a shock wave with the velocity derivative approaching infinity, but the acceleration across the wave front is continuous. For acceleration waves, only the derivative of the acceleration approaches infinity. We also note that, in compressive Newtonian fluid, the wave front properties are indeed quite analogous to those for solids, as explained by Lighthill (1956) earlier. He pointed out the functioning of each individual term under the Navier-Stokes equation with regard to wave front formation. The convective term tends to deepen a compressive pulse, while the viscous term tends to decrease the depth. However, we are reminded by Coleman *et al.* (1966) that acceleration waves will never exist in Navier-Stokes fluids. Thus questions may arise as to whether a propagating wave front in disturbed fluids will behave similar to a shock or acceleration wave front in 'liquid-like' solids. Here a 'liquid-like' solid is in the sense of any viscoelastic materials under a perfectly-plastic 'flow' state. We will come back to this question again in Chapter 3.

Now let us look into the decay characteristics of shock and acceleration waves. Figure 2.67 shows the attenuation characteristics of a shock front under various damping conditions as simulated by a two-element viscoelastic Voigt solid model by varying the internal material parameters of the model. If the model is purely elastic, a distinctive step front is expected.

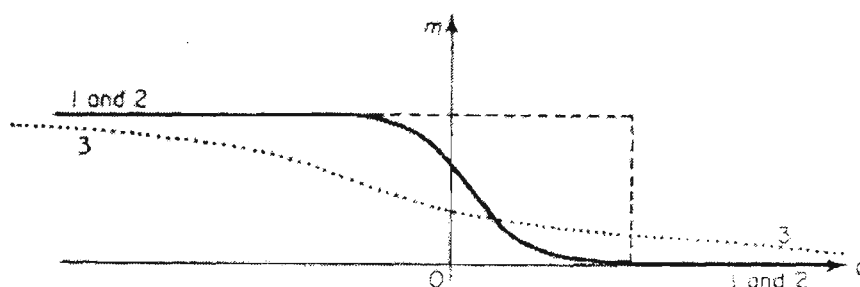


Figure 2.67 Normal components of the displacement gradient,  $m$  (or strain), in the direction of the Lagrangian co-ordinate,  $a$ , showing the wave front profiles under various damping conditions: (1) no damping “-----”; (2) low damping: solid line; (3) high damping “.....” for a 2-element Voigt viscoelastic solid. From Bland (1965).

As the contribution due to viscous damping increases with increasing liquid-like characteristics under a higher damping coefficient,  $\eta$  (sometimes called damping coefficient), the shock front tends to lose its characteristic structure and gradually degenerates into a smooth profile with decreasing amplitude towards the front as the wave propagates. This situation is shown in Figure 2.67. In other words, the wave characteristics disappear if the material parameters tend to be liquid-like such as in very soft produce, denoting the possibility of substantial wave attenuation. More importantly, the dynamics of the materials can no longer be expressed in terms of hyperbolic PDEs.

This fundamental transformation of energy transport from wave to other forms is significant in the dynamic characterization of liquid-like solids, which include many horticultural materials. The reason is that bruises are caused by large displacements as a result of wave generation. By eliminating the destructive wave pulses, materials can be spared from bruising. Figure 2.67 also illustrates a classic example of the interplay between shock and acceleration waves.

This smoothing action of a wave profile is primarily due to the difference in propagating velocities of the wave components, with those of higher frequencies propagating faster. This is shown in Figure 2.68 for the case of, again, a two-element Voigt viscoelastic material. The parameters under this model are Young’s modulus, elastic propagating speed ( $c_o$ ), phase velocity ( $c$ ), group velocity ( $c_g$ ), attenuation coefficient ( $\gamma$ ), relaxation time ( $t^*$ ), damping coefficient ( $\eta$ ) and frequency ( $\omega/2\pi$ ) of the sinusoidal waves. The relationship of velocity ratios was presented by Davies (1956) as:

$$\frac{c_g}{c_o} = \frac{2c}{c_o} \frac{1 + t^{*2} \omega^2}{3 + t^{*2} \omega^2 - \sqrt{(1 + t^{*2} \omega^2)^2}}; \frac{c}{c_o} = \sqrt{(2t^* \omega)}; t^* c_o \gamma = \sqrt{\left(\frac{1}{2} t^* \omega\right)} \quad (2-51)$$

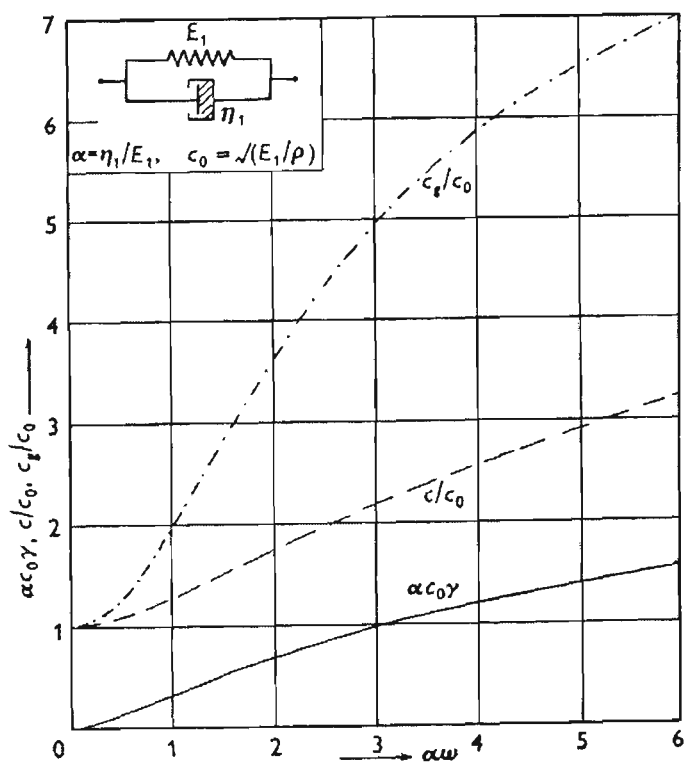


Figure 2.68 The variation of phase velocity ( $c$ ), group velocity ( $c_g$ ), and attenuation coefficient ( $\gamma$ ) with frequency ( $\omega/2\pi$ ) for sinusoidal waves in a 2-element Voigt solid. The relaxation time,  $t^*$ , is represented by  $\alpha$  in this figure. From Davies (1956).

We note that the wave packets with high frequencies in Figure 2.68 tend to increase towards infinity. In reality this will never be the case, because the attenuation coefficient,  $\gamma$ , will increase as  $\omega$

increases, implying that wave pulses with high frequencies will be quickly damped out. As pointed out by Johnson (1975), the attenuation of waves, particularly in heat-conducting elastic solids, is strong, with decay down to 1/1000-th of the initial amplitude in a copper bar specimen within the first 0.0048  $\mu$ sec of wave propagation. Since the wave speeds of various forms are crucial in determining the outcome of a wave profile, we will next look into the factors that affect these wave speeds in materials. Examples are abounding in the literature that seems ambiguous with regard to an appropriate definition of wave speeds propagating in materials.

For the speeds of shock and acceleration waves in nonlinear viscoelastic materials with memory, a formal definition has been provided by Coleman, Gurtin and Herrera (1965). The velocity of a shock wave,  $U_S$ , in this material can be expressed as:

$$U_S = \sqrt{\frac{E_S}{\rho_o}} \tag{2-52}$$

where  $\rho_o$  is the initially undeformed material density, and

$E_S$  is the instantaneous secant modulus of the material as shown in Figure 2.69.

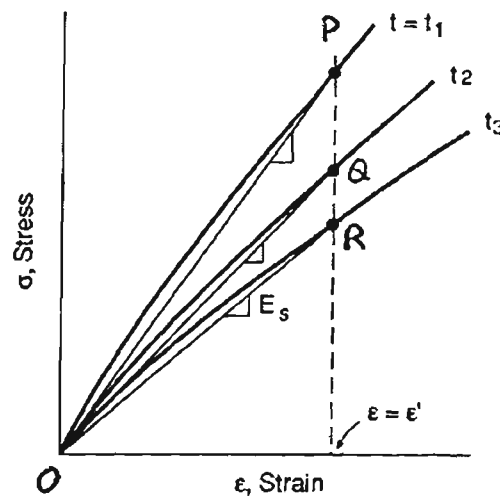


Figure 2.69 Secant modulus ( $E_S$ ) as represented by straight lines OP, OQ and OR. From Dowling (1993).

Some treat shock speeds as constants. While this is valid for linear elastic materials ( $E_S = E_o$ , the Young's modulus),  $E_S$  certainly varies slightly in the case of nonlinear elastic materials, and may vary substantially in others such as viscoelastic materials. But, our attention should not be too excessively focused at shock wave profiles and corresponding propagating speeds. As pointed out by Johnson (1975), much research effort has been inappropriately spent on shock waves in materials which, in reality, only account for the wave propagation characteristics during the very short initial

stage, perhaps only 1/1000-th or less of the total event or time history of deformation. Instead, our prime objective should be focused on the later stages that form the bulk of events. This requires careful studies of the acceleration waves, their energy transport characteristics during propagation, as well as the transformation of energies from waves to others such as heat diffusion.

The overall problem will become more complex if cracking damage or shear banding instabilities start to occur. However, instabilities and damage will not substantially alter the initial shock speeds according to their definition that is based on secant modulus. On the other hand, the wave profiles and propagating speeds of acceleration waves for nonlinear viscoelastic materials will be heavily affected by any crack damage and shear banding instabilities, as the definition of their propagating speeds,  $U_A$ , is based on their instantaneous tangent modulus,  $E_t$ , see Figure 2.70.

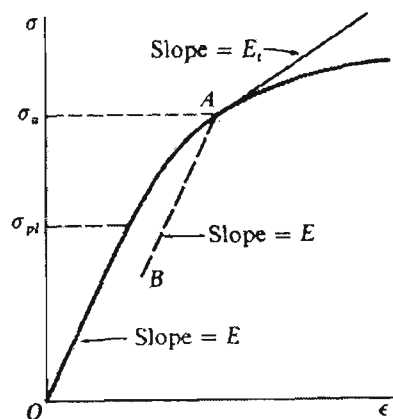


Figure 2.70 Instantaneous tangent modulus,  $E_t$ , as denoted by the tangent at point A as shown on the stress-strain curve. The unloading slope AB denotes the effective modulus,  $E$ , which in this particular case is equivalent to Young's modulus,  $E_o$ , meaning that no damage is involved during the deformation. From Gere and Timoshenko (1984).

The formal definition of the acceleration wave velocity,  $U_A$  has been provided by Coleman, Gurtin and Herrera (1965) in the form of:

$$U_A = \sqrt{\frac{E_t}{\rho_o}} \quad (2-53)$$

Referring to Figures 2.69 and 2.70, note that  $E_s$  and  $E_t$  are equivalent for a perfectly elastic material, with both equivalents to the Young's modulus,  $E_o$ . One may wonder, for a special case under strain slippage (for instance, during shear banding) what will happen to the acceleration wave speed,  $U_A$ . Based on its definition, anytime when  $E_t$  reaches zero,  $U_A = 0$ . In other words, the acceleration wave front may slow down to a standstill (if the wave front exists). This is the case when

the  $E_t$  on a typical work-hardening stress-strain curve approaches zero. Also, if there is negligible heat dissipation during the material deformation, or the material is a non-conductor of heat, then  $E_t$  in Equation (2-53) can be realized as an isentropic tangent modulus, denoting that the plastic deformation in this special case is isentropic, see Chen (1971). Otherwise, the plastic deformation is non-isentropic.

This slowing-down phenomenon of wave propagation is associated with the metamorphosis of waves that transform to other energy forms (notably to heat, resulting in the disappearance of the wave all together) and/or the occurrence of instabilities. From Equation (2-53), it is clear that the square root of the  $(E_t/\rho_o)$  term has to be positive, or the wave speed will become imaginary. If it happens to be negative, then the only explanation is the disappearance of the wave or the existence of instabilities or damage within the material. More specifically, Hill (1962), in one of the earliest theoretical studies on acceleration waves, pointed out that  $E_t$  under instabilities such as Luders bands must be negative (not just zero).

The phenomenon of wave decay, which can be illustrated by results from numerical techniques such as finite element analysis, is significant in the dynamic deformation of horticultural materials due to the nature of their internal energy dissipation characteristics in soft materials. In essence, this wave decay phenomenon involves a fundamental change in the mode of energy transport, most likely from wave propagation to heat diffusion, as well as to other forms of a minor nature. The gradually more dominating role of heat diffusion during the deformation, as a direct consequence of increasing internal friction and energy dissipation under high loading, tends to smooth out wave fronts propagating through the materials, see Figure 2.67. In particular, it is likely that the strain rates of deformation,  $\dot{\epsilon}$ , also play a significant role in the smoothing-out process of the wave profiles as first suggested by Malvern (1951) and illustrated in Figure 2.71. If this is true, then it seems that strain rates may also play a major role in wave decay and heat diffusion as well. Malvern used the following constitutive expression for his numerical analysis:

$$E_o \frac{\partial \epsilon}{\partial t} = \frac{\partial \sigma}{\partial t} + \frac{(\sigma - \sigma_{sy})}{t^*} \quad (2-54)$$

where  $E_o$  is Young's modulus,

$t^*$  is the relaxation time, and

$\sigma_{sy}$  the static yield stress of the material corresponding to strain rate,  $\dot{\epsilon}$ , of zero ( $\dot{\epsilon} = 0$ ) (that is, a perfectly-plastic or liquid-like solid – see Figure 2.27).

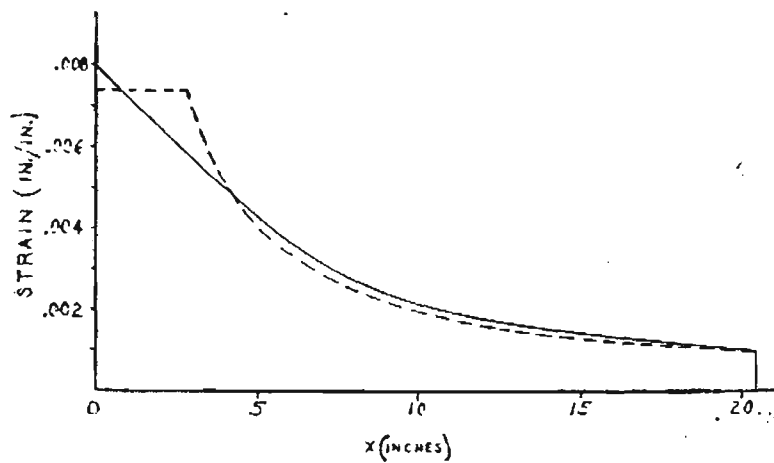


Figure 2.71 Numerical results of strain versus propagating distance of waves showing wave profiles (a) with (solid-line) and (b) without (broken-line) the influence of strain rate. From Malvern (1951).

This quasi-linear expression has been of far-reaching significance for the studies of plastic wave deformation. According to Cristescu (1960), the expression was first proposed by Sokolovskii (1948) and was developed independently by Malvern. Its significance was realized by Cristescu (1955) who further developed the expression as shown in Equation (2-54). The equation represents the coupling phenomenon between viscoelastic/work-hardening plastic and plastic/viscoplastic waves. With only the first wave groups on the right-hand side of Equation (2-54), the Equation is hyperbolic, while the second group appears in a fundamental change of form to the Equation. They are fully parabolic, and, arguably, cannot be called waves. Rather, they are better referred to as disturbances, which are thermal in nature. Occasionally we come across scientific articles that mention thermal shocks. These are in fact intensive thermal disturbances in the sense of shock waves in materials.

Since a heat diffusion process is expressed with a parabolic-type of PDE, a process that involves the transformation of wave to heat surely requires the coupling of the hyperbolic and parabolic types. The simplest equation combining both the nonlinear propagation effects and diffusive effects is the Burgers' equation, which in many occasions possesses solutions as special cases for both the hyperbolic and parabolic types, see Whitham (1974). Formal expressions for this coupled system, sometimes called dynamic thermoelastic system, has been provided in terms of PDEs by Kupradze *et al.* (1979) as:

$$\mu\Delta u + (\lambda + \mu)\text{grad}(\text{div}_- u) - \gamma'(\text{grad}_- \theta) + f_i = \rho \frac{\partial^2 u}{\partial t^2} \tag{2-55}$$

$$\Delta \theta - \frac{1}{\kappa} \frac{\partial \theta}{\partial t} - \eta * \frac{\partial}{\partial t} (\text{div}_- u) + \frac{1}{\kappa} Q = 0$$

where  $\mu$  and  $\lambda$  are instantaneous Lamé parameters, assuming isotropic materials,

$\gamma' = (2\mu + 3\lambda)\alpha$ , where  $\alpha$  is the coefficient of linear heat coefficient,

$\theta$  is temperature,  $\kappa$  is the thermal diffusion coefficient,  $Q$  is heat content,

$\eta^*$  is the specific entropy ( $= (\gamma' T_0)/K'$ ) where  $T_0$  is the absolute temperature (273 Kelvin),

$K' = (\kappa \delta')$ , and  $\delta'$  is the Kronecker delta.

The constants  $\gamma'$ ,  $\eta^*$ , and  $\kappa$  are normally determined experimentally.

Equation (2-55<sub>1</sub>) belongs to the degenerating hyperbolic type of wave propagation, whereas Equation (2-55<sub>2</sub>) of heat transfer belongs to the parabolic type. The difficulties associated with the dynamic thermoelastic processes are partly due to the fact that the system of equations (2-55) does not belong to any of the basic classes of equations of the mathematical physics. As pointed out by Kupradze *et al.* (1979), Equation (2-55) may lead to solution with no wave propagation or no eigenfrequencies at all. The disturbance then becomes purely thermal in nature. The authors also pointed out that the most difficult part in solving the systems of Equation (2-55) deals with the identification and determination of the initial and boundary conditions during the coupling processes. In their work, they mentioned only a handful of articles in this aspect, which are of substance, including an important paper by Dafermos (1968), who proved that the solution of Equation (2-55) with homogeneous initial-boundary conditions tend to be zeroing almost everywhere as time,  $t$ , approaches infinity. This will be illustrated with results from Chu (1962) and our experimental results in Chapter 3.

Lee was the first to introduce the dilemma of unknown initial and boundary conditions involved in the elastic/viscoelastic and plastic boundaries, see Lee (1953). This condition of unknown boundaries appears in the unloading (or work-hardening) stress-strain curves where the travelling discontinuities are dominated by acceleration waves. The difficulty stems from the fact that the boundary conditions that are instantaneous in nature actually change, or shift, as the material changes from an elastic state to a plastic state, according to Clifton and Ting (1968). We will come back to this issue of work-hardening shifting in Chapter 3. Because of this shift, in order to perform numerical analysis and modelling of the dynamic material characteristics due to wave effects, we have few options but to resort to constitutive equations, with very specific initial and boundary conditions. Up to this date, no definite method for the determination of boundary conditions is finalized. It seems constitutive equations such as the quasi-linear Equation (2-54) offers the best solutions.

Equation (2-55) but without the temperature,  $\theta$ , term, to our knowledge, was derived by G.G. Stokes for acoustic wave propagation. Most striking is that if we take the divergence or the curl of the equation, two wave speeds,  $C_p$  or  $C_s$ , can be obtained.  $C_p$  is usually called the longitudinal, dilatational, primary, or  $P$  wave speed, while  $C_s$  is the transverse, shear, secondary, or  $S$  wave velocity. They can be expressed as:

$$C_p = \sqrt{\frac{(\lambda + 2\mu)}{\rho}} = \sqrt{\frac{(\kappa' + \frac{4}{3}\mu)}{\rho}}; \text{ and } C_s = \sqrt{\frac{\mu}{\rho}} \quad (2-56)$$

where  $\lambda$  and  $\mu$  are the Lamé parameters;  $\mu$  (a Lamé parameter) can be regarded as the instantaneous complex shear modulus in isotropic viscoelastic materials.

Here the Lamé parameter  $\lambda$  is also instantaneous. In strict sense, both  $\lambda$  and  $\mu$  of nonlinear viscoelastic materials cannot remain constant under transient loading.  $\rho$  is the instantaneous material density corresponding to  $\lambda$  and  $\mu$ , and  $\kappa'$  is the instantaneous bulk modulus.

For a complete formulation of dynamic motion of viscoelastic materials, the entire history of displacements is required, in order to allow for memory effects. Since one of the best approaches to characterize these material properties is by constitutive equations, research workers have developed numerous equations for different materials under various loading and testing conditions, see, for instance, Chen and Saleeb (1982). This instantaneous nature of dynamic material properties is reflected by the Lamé parameters in Equation (2-56).

Naturally, our attention will then be drawn to the close resemblance of the expression for the propagation speeds between the acceleration waves in Equation (2-53), and the longitudinal and shear waves in Equation (2-56). This resemblance depicts that the instantaneous material properties, as represented by the instantaneous  $\lambda$  and  $\mu$ , hold the key to the shaping of, and are directly related to, the dynamic stress-strain curves. We believe Thomas (1957) was the first to point out this fact. In other words, dynamic stress-strain curves under different loading conditions can arguably be regarded as the best source of information for the instantaneous material properties, as well as the best reliable basis for the construction of constitutive equations.

A more elaborated development by Hodge (1980) for a 2-element Voigt viscoelastic material, as shown in Figure 2.68, gives similar arguments to Thomas. Referring to Figure 2.68, Hodge used the constitutive equation for the Voigt solid that can be expressed as:

$$\sigma = E \varepsilon + \eta \dot{\varepsilon} \quad (2-57)$$

where  $E$  is the effective modulus, and  $\eta$  the viscosity coefficient.

By substituting Equation (2-57) into Equation (2-46), the longitudinal and transverse wave speeds as shown in Equation (2-56) can be obtained. By substituting Equation (2-57) into Equation (2-55<sub>1</sub>), the equation of motion is no longer hyperbolic, but parabolic. We have pointed out earlier in this section that, when the velocity,  $c_g$ , of the higher-frequency components of a wave front seems to approach infinity, see Figure 2.68. In fact, it will never be the case. This is due to the higher degree of wave attenuation associated with the high-frequency wave components, which are damped out, resulting in heat dissipation. Now let us focus on this thermoelastic (wave and heat) coupling process itself.

The studies of wave propagation in elastomeric materials such as rubber began by Nolle (1947). Sips (1951), as well as Lee and Kanter (1953), carried out the pioneering work on wave propagation in isotropic linear viscoelastic materials. Their contributions, though significant, have been limited to special types of viscoelastic materials. Sips obtained, incorrectly, a single invariant propagating speed that is equivalent only to the shock wave speed,  $U_s$ , in Equation (2-52) throughout the propagation, but not the acceleration speed,  $U_A$ , of Equation (2-53), when the stress at the wave front should be expected to exceed the elastic limit. In other words, the wave front is expected to be plastic in nature. This is due to the difficulty he encountered during an attempt of the Laplace transform inversion that required simplification of his expression on the relaxation function. Lee and Kanter only focused on the Maxwell fluid model, but clearly illustrated, for the first time, the significance of material damping. Other significant works before Chu (1962) include Berry (1958a and 1958b) and the definite review article by Hunter (1960b). They obtained propagating speeds equivalent to  $P$ -wave (Equation 2-56<sub>1</sub>) and  $c = \sqrt{[E/\rho]}$  at  $t = \infty$ , which are of the generalized type but without involving the effect of thermoelastic process.

Chu (1962) established a generalized expression for wave propagation that shows thermoelasticity and thermoplasticity in viscoelastic materials. He studied the dynamic response of two extreme types of isotropic linear viscoelastic materials: (a) 'solid-like' in the sense of working-hardening, and (b) 'liquid-like' in the sense of perfectly-plastic response during deformation. Dillon also initiated his theoretical and experimental studies on thermo-coupling. His work resulted in a series of papers, see Dillon (1962, 1963, 1967, 1968) and Dillon and Tauchert (1966), showing a distinct serrated (staircase-like) stress-strain characteristic curves of thermo-coupling associated with the so-called Portevin-Le Chatelier effect, see Bell and Stein (1962), Dillon (1966) and Sharpe (1966). Incidentally, the Dillon (1963) article is one of the earliest works on coupled thermoplasticity. In essence, Dillon tried to match his and others' experimental data with the coupled systems of Equation (2-55). Dillon's focus was on the constitutive representation of material behaviour, rather

than the characteristics of wave propagation. He concluded that the stress-strain curve for materials under work-hardening plastic deformation could result in discontinuities and material instabilities, which he called mechanically unstable serrated curves, while in the heat dissipation part the  $\sigma$ - $\epsilon$  curve is smooth, see Dillon (1966). Let us see how the Chu (1962) model works. We will see how the coupling actually works in Chapter 3, based on our experimental data and the results of Chu (1962). We believe these results can be directly applied to the dynamic deformation of soft horticultural materials and can provide insights into the thermoelastic process.

In his model, as shown in Figure 2.72, Chu applied along the  $x_1$ -direction a constant shear stress,  $\sigma_o$ , on the surface of  $x_2 = 0$  of an isotropic linear viscoelastic material slab, of thickness,  $h$ , which can be represented by the constitutive Equation (2-40). This results in a transverse wave propagating normal to  $\sigma_o$  along the  $x_2$  direction. By substituting the constitutive expression into Equation (2-45) and setting up the initial and boundary conditions, the solution of the problem was then constructed by means of the Laplace transform of the velocity  $\partial u/\partial t$  and the stress component  $\sigma_{12}$ . A good source of discussion on the Laplace transform technique to shock wave front motions can be found in Chadwick and Powdrill (1960). This results in an initial shock wave velocity as given by Equation (2-52).

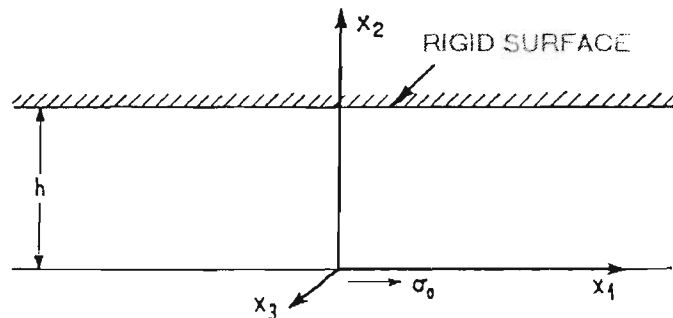


Figure 2.72 Sketch of the coordinate system of the isotropic linear viscoelastic slab under a shear stress of  $\sigma_o$  ( $\sigma_{12} = \sigma_o$  for time  $t = 0$ ). From Chu (1962).

Then, by expanding the shear modulus,  $G(t)$  in Equation (2-40) with a Taylor's series about time,  $t = 0$ , the wave decay Equation (2-51) can be obtained. Thus, the decay of the viscoelastic wave in terms of time can be monitored.

As expected, the elastic wave front degenerates rapidly into an elastic precursor wave in a way very similar to that as shown in Figure 2.66. Degenerated elastic wave profile is illustrated in Figure 2.73 with low stress amplitudes. As this precursor disturbance is the result without involving

any plastic deformation, the wave is always expected to propagate with the elastic or shock wave speed as shown in Equation (2-52), before any viscoelastic relaxation effects set in.

Following the degenerated precursor wave, the stress amplitude begins to rise sharply, denoting the presence of another wave front (plastic wave front) that propagates at the acceleration wave speed,  $U_A$ . This wave front contains the relaxation effects of viscoelasticity, as well as effects due to work-hardening plastic deformation. This latter property is evidenced from the gradual 'spreading-out' of the wave front profile as shown in Figure 2.67. A surprising aspect of this second wave front is that, in normal circumstances, the amplitude of this wave, or the maximum applied stress,  $\sigma_0$ , does not decay. The 'spreading-out' phenomenon of the wave front is governed by a diffusion-type process in terms of half-life,  $t_{1/2}$ . In other words, after a certain time  $t = t_{1/2}$ , the spreading length becomes  $\Delta x_2$ , see Figure 2.73. The stress amplitude,  $\sigma_{1/2}$ , of the corresponding centre of  $\Delta x_2$  retains only half of the strength, or  $\sigma_0/2$ , thus the 'half-time' is called.

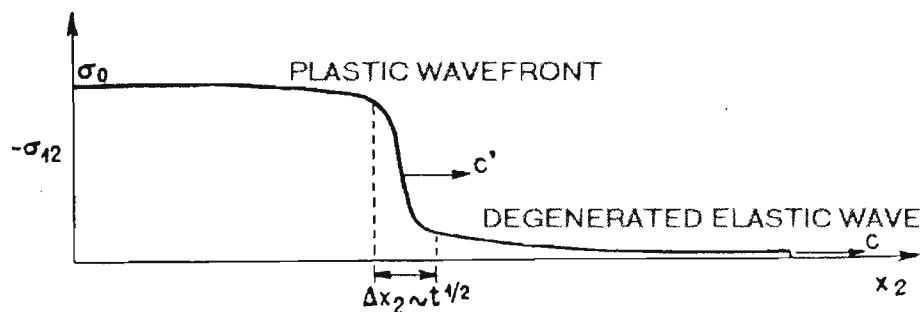


Figure 2.73 Numerical result for a work-hardening viscoelastic material slab showing decaying elastic precursor wave front followed by a plastic wave front. Here  $c =$  elastic wave speed ( $U_S$ );  $c' =$  plastic/viscoplastic speed ( $U_A$ ). From Chu (1962).

## 2.3 SUMMARY

This chapter presents the methodology for the dynamic characterization of produce materials based on an analysis of relevant theoretical principles of dynamic behaviour of these materials. This chapter also contains description of the experimental approach taken for validating the deductions made in the theoretical study.

The theoretical study begins with an overview on postharvest produce materials. In particular, their dynamic characteristics in terms of solid-like (arrheodictic) and liquid-like (rheodictic) behaviour were explained in terms of established material science processes such as elastic, viscoelastic, plastic and viscoplastic deformation. The dynamic characterization is based on the engineering stress-strain relationships of a variety of produce materials that includes both the softest and crispest specimens.

Another major aspect of the theoretical study includes efforts to distinguish the dynamics material behaviours due to instabilities from those caused by material deformation. In particular, the significance of these instabilities that result in different failure modes was emphasized. Both pre-critical and post-critical instabilities based on established theories of damage mechanics were studied.

Referring to recent experimental results of studies on pre-critical instabilities in materials such as composites, the degree of pre-critical damage on test materials used in the present study was monitored in terms of the effective modulus of the materials. Similarly, the degree of post-critical damage on test materials was monitored in terms of the softening modulus of the materials.

Both the dynamic deformation characteristics and the damage characteristics were established, using a laser-based displacement test apparatus. The output of the laser displacement measuring apparatus generated a wide spectrum of dynamic stress-strain curves for different materials. Special attention was placed on the dynamic strain rates applied to the test specimens. Based on an analysis of a theoretical equation, which points to the direct relationship between material strain rates, test specimen drop height and the cushion thickness.

In this study, the advantage of protection afforded by packaging materials, such as foam and corrugated fibreboard, was not explored. The major focus was placed on the direct relationship between strain rates and corresponding drop heights. These relationships were established by using Impact Force Analysis (IFA). These were achieved by using IFA to establish a series of relationships

between bruise volumes and drop heights. Then, using a Shock Tester, the relationship between bruise volumes and actual drop heights of whole-fruits at various duration of impact was finally established. The significance of the duration of impact was also analysed.

Based on previous established theories, it is accepted that stress-strain curves may provide valuable information of wave pulse characteristics during the loading cycle. A detailed theoretical analysis on wave propagation through the produce materials was included. The analysis showed that different forms of energy dissipation are possible in different produce materials.

Solid-like materials tend to retain most of the energy of disturbance in the form of plastic wave fronts; with very little energy dissipation. On the other hand, liquid-like materials dissipate energy associated with the wave pulse to other form of energy such as heat.

Based on the theoretical wave analysis, it seems there is a significant interplay between longitudinal waves and shear waves, giving rise to a conjecture that the nature of energies (such as longitudinal and shear energies) in the materials under dynamic load may play an important part in their dynamic characteristics.

As there is a direct relationship between the partition of energy (such as shear energy) and the Poisson's ratio, a series of Dynamic Mechanical Analysis tests were deemed necessary to establish values of Poisson's ratio under dynamic loading. These values may explain some distinct features associated with shear and longitudinal waves, such as cracking and heat dissipation in materials.

# CHAPTER 3

## RESULTS AND DISCUSSION

### 3.1 INTRODUCTION

This chapter presents the experimental results, which comprise those from the four kinds of tests in this study, each with their own objective of testing. They are: (1) dynamic mechanical analysis (DMA) tests, (2) laser displacement tests, (3) impact force analysis (IFA) tests, and (4) shock tests. Results of validation tests for the last three test methods are included. Although no validation tests were conducted on the DMA tester, the equipment was calibrated according to the instructions from the manufacturer prior to carrying out the test runs.

This chapter also includes a discussion of the processes that account for the bruise damage of the test specimens of horticultural materials, based on the experimental results of this study and theoretical interpretation of the results. This is included in Section 3.2 for the IFA tests, Section 3.3 for the shock tests, Section 3.4 for the laser-based tests, and Section 3.5 for the DMA tests. A detail discussion of the characteristics of the dynamic deformation in horticultural materials is presented in Section 3.6. A separate discussion on the dynamic instabilities due to damage in horticultural materials is presented in Section 3.7. This chapter concludes with a summary in Section 3.8.

## 3.2 IMPACT FORCE ANALYSIS

### 3.2.1 Duration of Impact

Experimental IFA results presented in Figure 3.1 show expected trends of invariance in  $\tau$  tested at different drop heights. The invariance also applies to whole apples with various degrees of maturity, from market-fresh up to a storage period of 3 weeks. In Figure 3.1, for drop heights of more than 5 cm,  $\tau$  stays at an almost constant value of 4.3 ms throughout. However, when drop heights are less than 5 cm, the effect due to frictional contacts seems to become more significant, and  $\tau$  starts to increase. On the other hand, for frozen apples with more or less rigid boundary conditions, the dynamic responses show little noticeable change in  $\tau$ , at about 4.0 ms, for drop heights of 5 cm to 20 cm. This indicates that dynamic friction effects may be insignificant during fruit bruising with gradual and rapid increase in contact areas between the skin boundary and rigid surface. However, dynamic friction effects seemingly play a significant role when the kinetic energies (or drop heights) become smaller.

#### DURATION OF IMPACT VS. DROP HEIGHT

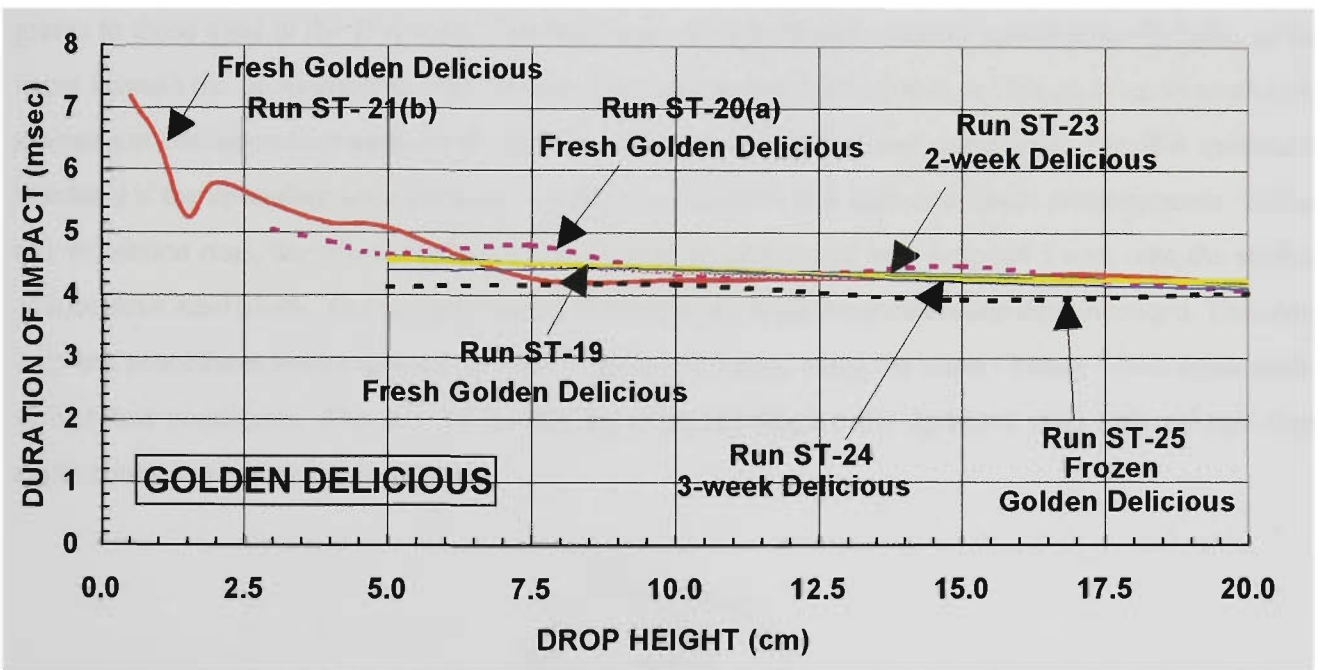


Figure 3.1 Records of impact duration of whole apple versus drop height. The critical drop height ( $h_{oc}$ ) denoting the damage threshold (Figure 3.5) is at about 5.0 cm.

Similar results were obtained by Fluck and Ahmed (1973) based on impact tests on American Bears lemons. In their tests,  $\tau$  is stable at about 12 ms for drop heights between 10 cm to 37.5 cm, but  $\tau$  increases substantially up to 20 ms as the drop height is reduced to 2 cm. This indicates that a factor

probably due to dynamic frictional effects between contact surfaces causes the increase in  $\tau$  as the drop height decreases.

The existence of the incremental curve towards higher  $\tau$ , as shown in Figure 3.1, for drop heights less than a critical drop height,  $h_{oc}$ , proves worth pursuing in future studies which is concerned with the dynamic surface conditions of produce. The critical drop height, which is the drop height that corresponds to the starting point of significant increase in  $\tau$ , seems to be related to the damage threshold of the produce.

### 3.2.2 Validation of the IFA Method

The IFA method was validated by comparing the dynamic responses of the apple texture; notably the uploading period of  $\tau$  based on the IFA method and direct measurements. Direct measurements were achieved using a whole apple with a buried accelerometer mounted as shown in Figure 3.2, the same accelerometer used in the IFA tests. In this study, the accelerometer was tightly fitted into a hole bored into market-fresh Granny Smith apples of comparable weights of about 140 grams to those used in the IFA tests. The hole was carefully bored until the cushioning thickness of the apple beneath the accelerometer was 10 mm. The thickness of 10 mm was so chosen in order to observe attenuation characteristics associated with the wave propagation in real conditions. The IFA method is validated if the uploading time duration is unchanged in both IFA tests and direct measurements. Before any validation runs, the whole apple with the buried accelerometer was dropped 5 mm onto the surface of a massive steel block. The run was repeated three times, with the acceleration data averaged. The same drop test procedures were repeated for drop heights of 10 mm, using the same Granny Smith apple under similar test conditions. The aim of these tests is to investigate the dynamic responses of real drop applications in no-bruising conditions.

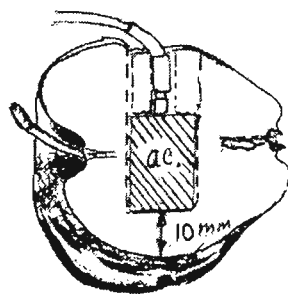


Figure 3.2 Drop test arrangement for Granny Smith apple with an accelerometer buried near the centre of the apple and 10 mm from apple surface.

The acceleration time histories for the cases with low drop heights of 5 mm (Run BUR-05) and 10 mm (Run BUR-10) were plotted in Figures 3.3, showing a marked increase in the duration of impact on the unloading path. During these runs and all other IFA tests, the duration of impact and acceleration histories were captured by Test Partner Version 1.25 software produced by Lansmont Corporation. For the two low-level drops as shown in Figure 3.3, there was no indication of bruising. So, lower secondary acceleration peaks and associated plateaus were not caused by damping. Instead, the best explanation seems to be that these secondary peaks are shear wave pulses. They are tensile in nature and normally travel at a lower speed than the main longitudinal wave fronts that are compressive in nature. The wave propagation phenomenon is perhaps not easy to realize physically, but can be recognized from the results of finite element modelling runs, see Chen (1985).

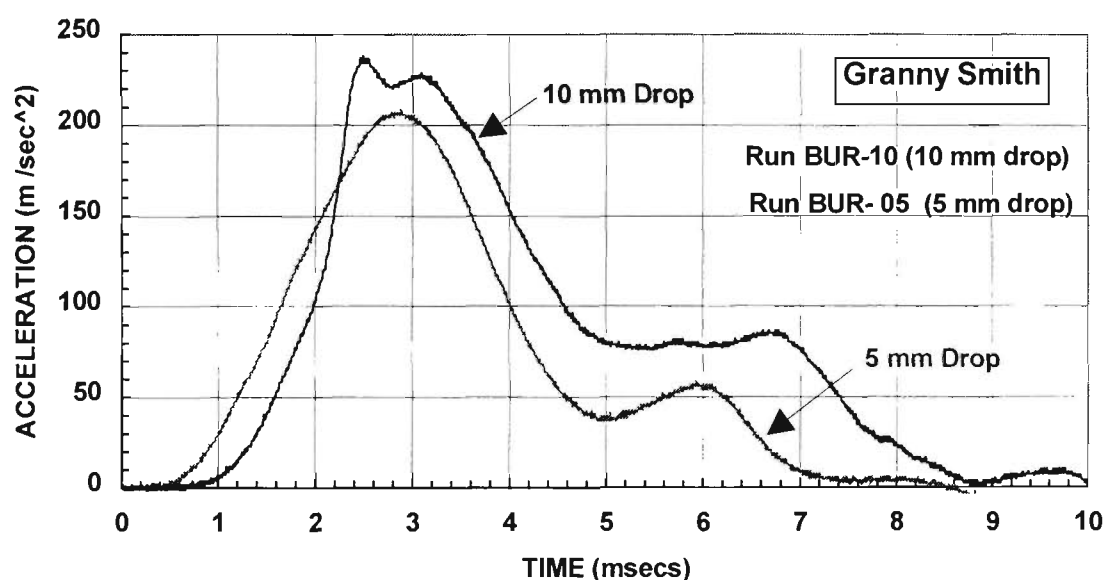


Figure 3.3 Acceleration time histories of whole apple at a spot inside the fruit 10 mm above the surface of impact, under drop heights of 5 mm (Run BUR-05) and 10 mm (Run BUR-10).

For Runs BUR-05 and BUR-10, the duration of impact is long enough for the accelerometer to capture these lateral wave fronts. For the validation test, only one run was allowed (Run BUR-50 with a drop height of 5 cm). The reason is that the drop height in this run might have exceeded the damage threshold, and any extra runs would have yielded no useful information. The run was successfully performed by carefully dropping the apple with the buried accelerometer onto the load-cell such that the thickness between the top surface of the load-cell and the bottom of the accelerometer was closest to 10 mm. This was achieved by applying marker paint at the desired spot of contact on the apple surface immediately before dropping, and placing a small piece of blank paper on top of the load-cell. An imprint on the blank paper indicated successful contact on the desired spot. It seems that the gentler slope

'CD' as shown in Figure 3.4 is due to shear waves. There is also a clear indication of low levels of damping or bruising activities, as the slope 'BC' is slightly gentler than the uploading slope.

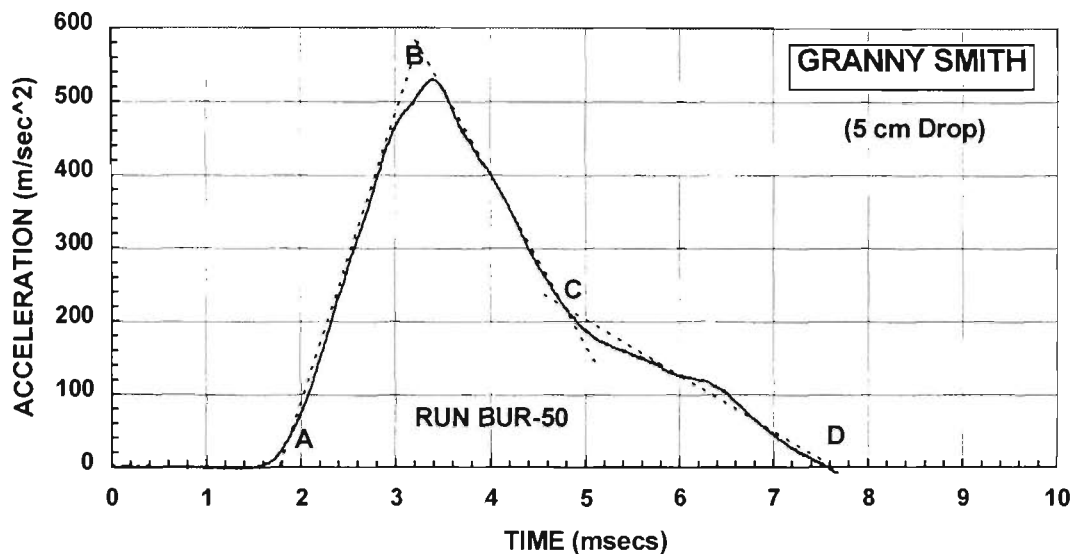


Figure 3.4 Acceleration time histories of Granny Smith apple at a spot inside the fruit 10 mm above the point of impact (the bottom level of the buried accelerometer). Drop height is 5 cm (Run BUR-50).

To validate the IFA method, careful comparison was made between Figures 3.3 and 3.4. This shows a good match of the duration of impact during the uploading period, of about 1.5 milliseconds, in both figures. As expected, there is always a discrepancy in the peak acceleration between those recorded in Figure 2.64 (at 1,225 m/sec<sup>2</sup>) and Figure 3.4 (at 530 m/sec<sup>2</sup>), as the wave intensity is attenuated after propagating 10 mm.

### 3.2.3 Coefficient of Restitution

The coefficient of restitution,  $e$ , is an important indicator of bruising in produce. The IFA results from three series of drop tests, involving various stages of fruit maturity, were used to study the effect due to different drop heights on the coefficients of restitution. The values of  $e$  were calculated using the impact velocity and velocity change for each corresponding drop height. Here, the velocity change is the area underneath an acceleration time history curve. The impact parameters are listed in Tables 3-1, 3-2, 3-3 and 3-4. Run ST-21B was a series of drop tests comprising two parts, both using market-fresh Golden Delicious apples. The first part included all tests with drop heights of 20 cm, 17.5 cm, 15 cm, 12.5 cm, 10 cm and 7.5 cm using the Kyowa 2kN dynamic load cell. The duration of impact, peak acceleration and velocity change were averaged with 4 apple drops at each drop height. The second part included all tests with drop heights of 5 cm, 4 cm, 3 cm, 2 cm,

1.5 cm, 1 cm and 0.5 cm, using a Sangamo 100N dynamic load cell, as shown located at the right side of the Kyowa load cell in Figure 2.2. As in the first part, four drops at each drop height, with the duration of impact, peak acceleration and velocity change averaged, were conducted. The complete data set of Run ST-21-B is listed in Appendix A. Examples of calculations for peak accelerations and velocity changes, as well as  $e$ , are listed in Appendix B. Runs ST-23 and ST-24 used aged Golden Delicious apples for two and three weeks, respectively.

Table 3-1 Comparison of the Impact Parameters of Market-fresh Golden Delicious Apple at different Drop Heights (Run ST-21B) – Whole Apple Drop

Drop Height (cm)	Peak Acceleration (m /sec <sup>2</sup> )	Duration of Impact (milliseconds)	Velocity Change (m /sec)
20.0	1193.9	4.25	2.96
17.5	1099.7	4.35	2.81
15.0	1124.2	4.18	2.73
12.5	1005.5	4.28	2.52
10.0	886.8	4.25	2.28
7.5	792.2	4.28	2.01
5.0	556.2	4.65	1.69
4.0	491.5	5.15	1.51
3.0	372.8	5.45	1.26
2.0	301.2	5.78	1.04
1.5	282.5	5.25	0.90
1.0	177.1	6.45	0.68
0.5	105.0	7.20	0.46

Table 3-2 Comparison of the Coefficient of Restitution of Market-Fresh Golden Delicious Apple at different Drop Heights (Run ST-21B) – Whole Apple Drop

Drop Height (cm)	Impact Velocity (m/sec)	Rebound Velocity (m/sec)	Coefficient of Restitution (e)
20.0	1.981	0.98	0.50
17.5	1.853	0.96	0.52
15.0	1.716	1.01	0.59
12.5	1.566	0.95	0.61
10.0	1.401	0.80	0.63
7.5	1.213	1.11	0.66
5.0	0.990	0.70	0.71
4.0	0.886	0.62	0.70
3.0	0.767	0.49	0.64
2.0	0.626	0.41	0.66
1.5	0.542	0.36	0.66
1.0	0.443	0.24	0.54
0.5	0.313	0.15	0.47

Table 3-3 Comparison of the Coefficient of Restitution of Golden Delicious after 2-week Storage, at 4°C and 100% RH, at different Drop Heights (Run ST-23) – Whole Apple Drop

Drop Height (cm)	Impact Velocity (m/sec)	Rebound Velocity (m/sec)	Coefficient of Restitution (e)
20.0	1.981	1.09	0.55
15.0	1.716	0.924	0.54
10.0	1.401	0.81	0.58
5.0	0.990	0.62	0.63

Table 3-4 Comparison of the Coefficient of Restitution of Golden Delicious after 3-week Storage, at 4°C and 100% RH, at different Drop Heights (Run ST-24) – Whole Apple Drop

Drop Height (cm)	Impact Velocity (m/sec)	Rebound Velocity (m/sec)	Coefficient of Restitution (e)
20.0	1.981	1.119	0.57
15.0	1.716	0.962	0.56
10.0	1.401	0.783	0.56
5.0	0.990	0.628	0.63

Impact parameters as listed in Tables 3-3 (2-week storage) and 3-4 (3-week storage) were compared with those in Table 3-2 (market-fresh) and plotted in Figure 3.5. From the Figure, it appears that for drop heights greater than a critical drop height,  $h_{oc}$ , of about 5 cm, energy loss remains unchanged, as shown by the relatively parallel curves in Figure 3.5 for various stages of storage. The trend clearly indicates that the coefficient of restitution appears to decrease as the fruit matures. This appears to be in line with some other conclusions based on  $e$  results using Golden Delicious, see Diener *et al.* (1979). They also obtained almost-parallel  $e$  curves from 2 batches of Golden Delicious apples that had a 3-month time lag in storage time.

Aged produce has a tendency to soften, thus reducing the occurrence of cracking. On the other hand, market-fresh produce such as apples is crisper than aged apples, and is more susceptible to cracking. From Figure 3.5, the values of  $e$  for the crisp market-fresh apples dip below those which were aged if the impact energy levels, or drop heights, exceed 16.5 cm, and energy sinks leading to crack formation may occur.

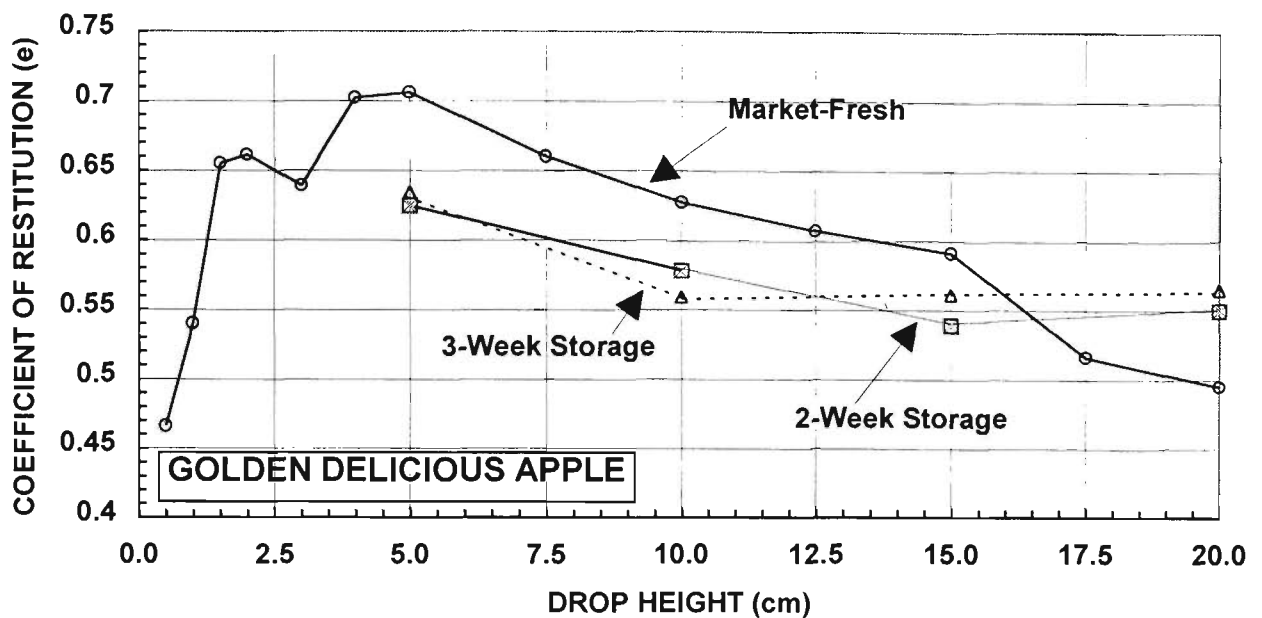


Figure 3.5 Comparison of the coefficients of restitution for Golden Delicious whole-apple drops with various periods of storage for different drop heights. The critical drop height ( $h_{oc}$ ) indicating the damage threshold is clearly shown at about 5 cm for the case of market-fresh apples.

Recently, much research effort has been focused on the damage threshold in horticultural materials, see, for instance, Schulte *et al.* (1992), Hyde and Mathew (1992), and Schulte *et al.* (1994). The approach of damage threshold is actually an ongoing attempt to relate relevant impact parameters for a full description of bruising. The approach also attempts to encompass the bruising of produce due to plastic/viscoplastic deformation as well as cracking damage. However, the selection of relevant impact parameters and the judgement of the contribution to bruising of individual parameters can be sometimes misleading. For example, a damage threshold for fresh Golden Delicious apples based on a maximum acceleration during an impact has been long recognized to be about 30 g. See for instance, Sober *et al.* (1990); Schueller and Wall (1991). This value corresponds to a drop height of about 2 cm in Figure 3.6, for an apple of about 150 grams by weight. In the present study, a damage threshold of 30.7 g for Golden Delicious was obtained based on many drop tests. However, the damage threshold for fresh Golden Delicious usually varies from 30 to 60 g, depending on whether the onset of any cracking activities begin. Cracking is considered a dynamic instability but not a material property, thus when it starts is unpredictable. For a more reliable value of damage threshold it is better expressed in terms of a range, and preferably not a constant value of drop height or peak acceleration. For a typical 150gm apple, a peak impact acceleration of 60 g normally corresponds to a drop height of about 5 cm. In this study it was lower than 4.5 cm, as shown in Figure 3.6. But it can also be as high as 7 cm, as shown in Figure 3.7. In Figure 3.6, the rebound velocities

( $V_2$ ) were calculated based on the recorded test data of impact velocity ( $V_1$ ) and velocity change ( $\Delta V$ ). The rebound velocity curve shows that instability such as cracking appears when the drop height reaches 3 cm, and the rebound momentum peaks when the drop height reaches 15 cm, global dynamic instabilities seem to initiate. We will return to cracking instabilities in Section 3.7.

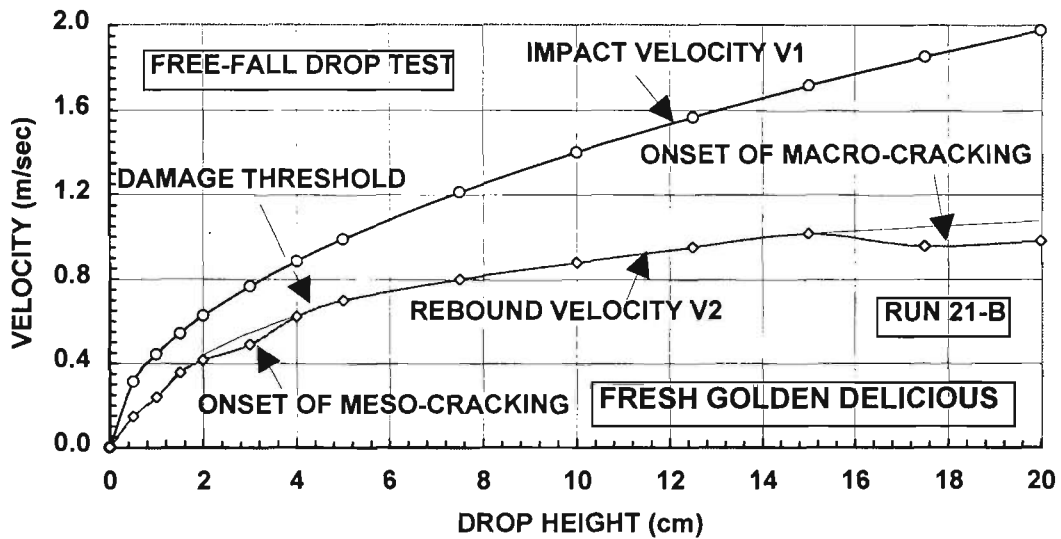


Figure 3.6 Plot of impact ( $V_1$ ) and rebound ( $V_2$ ) velocity data versus drop height from drop tests with market-fresh apples. (Run ST-21B)

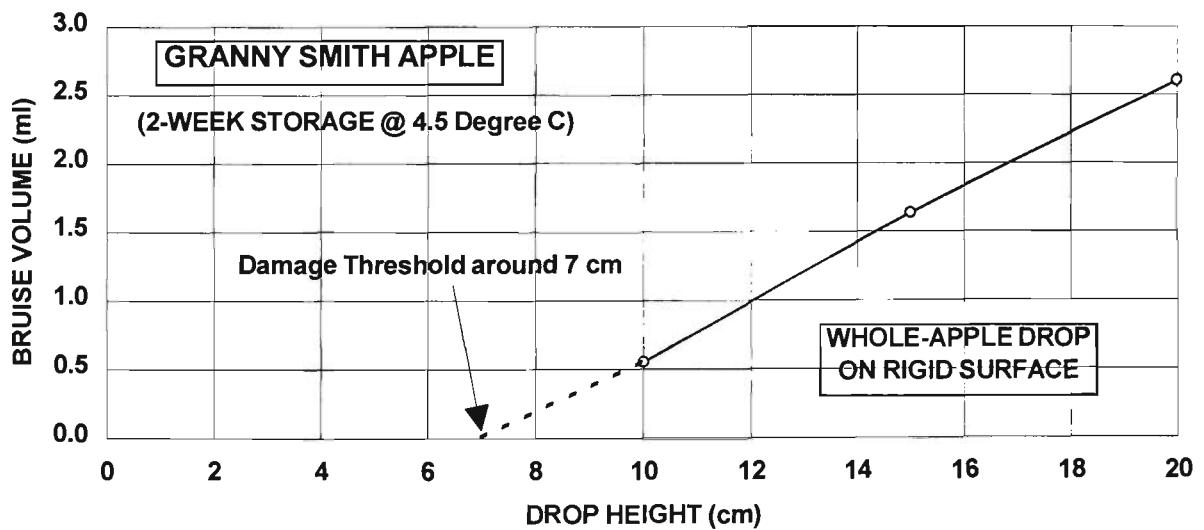


Figure 3.7 Bruise volume versus drop height for apples obtained from drop test. (Run ST-30-R)

The existence of cracking instability can be detected in other IFA tests by plotting the impact and rebound velocity data against drop heights similar to Figure 3.6. The velocity change ( $\Delta V$ ) data, obtained from the Test Partner PC-based software, show abrupt changes in the area under the

acceleration-time history curve whenever instability is encountered. On the other hand, the curve for impact velocity, which is drop-height dependent, should always be smooth. The values of  $\Delta V$  presented here represent the difference of the two velocity curves shown in Figure 3.6. When the drop height reaches a certain level (15 cm in the case of Run ST-21B in Figure 3.6), further increase in drop height does not increase the rebound velocity. This implies that the maximum possible level of elastic/viscoelastic deformation was reached. Any deformation beyond this level is irreversible. Any extra energy beyond this level has to be dissipated, either transforming into heat or creating propagating (or dynamic) energy sinks under global-scale activities such as fracturing.

### 3.3 SHOCK TESTS

#### 3.3.1 *Relationship between Bruise Volume and Drop Height*

Two series of whole-fruit shock tests were carried out to study the effects of the duration of impact on bruise volumes,  $BV$ , of Golden Delicious apples using a programmable shock tester, as shown in Figure 2.3. The tests were performed on market-fresh apples in Run ST-13 and aged apples in Run ST-16, after a two-week storage period in controlled conditions at 5.5<sup>o</sup>C and 100% RH. Test runs were carried out to establish a relationship between the coefficient of restitution of the shock tester and drop height. Due to the design of the shock tester, results from shock tests were corrected, because any set drop height of the shock tester does not reflect the true drop height of an object falling naturally. Correction to the data was performed using a technique based on a set of IFA test data with comparable drop heights. This is a crucial step before any relationship between bruise volumes and the corresponding duration of impact can be established.

The results of bruise volumes deduced in this study were calculated from measured parameters as shown in Equation (2-1) and Figure 2.9. Each data point obtained from shock tests is the average of four data points for bruise volume, with a statistical deviation (SD) of about  $\pm 2\%$ . For all IFA free-fall drop tests, the bruise volume at each drop height is the average value of 5 data points with a SD about  $\pm 5\%$ . The observable SD of bruise volumes from shock tests and IFA tests show a high consistency of bruise volume data from both drop test modes. Figure 3.8 shows the results of peak accelerations for all tests with fresh apples under different drop heights and at different duration of impact. For IFA tests, it was noted that  $\tau$  remained close to constant at 4.18 ms for all drop heights,

with a SD of about  $\pm 5\%$ . Therefore, only one curve can be plotted based on IFA data, as shown in Figure 3.8. This suggests that  $\tau$  is not dependent on drop heights and peak accelerations, but rather on the material properties of the impacting bodies and surfaces. Other values obtained for  $\tau$  under different storage periods of 1 and 2 weeks remain virtually unchanged at around  $4.20 \pm 0.08$  ms, which suggests that  $\tau$  is also virtually insensitive to the length of storage period.

It was noticed that, for all drop tests or shock tests, the shock signals resemble haversine pulses, characterized primarily by the peak acceleration and the duration of impact. The closer the resemblance of the curve types from drop tests or shock tests, the closer will be the match of the two haversine pulses. Therefore it follows that the loading history at an  $\tau$  of 4 ms for shock tests can simulate the loading history for drop tests at comparable drop heights. The relationship between bruise volumes of fresh apples and drop heights is shown in Figure 3.9 under different duration of impacts obtained from shock tests. Here the relationship was not automatically assumed to be linear, as suggested by Holt and Schoorl (1977) for apples. The reason is that a linear relationship depicts a direct proportionality between the bruise volume and absorbed impact energies. Such an assumption may not adequately cover the full range of produce.

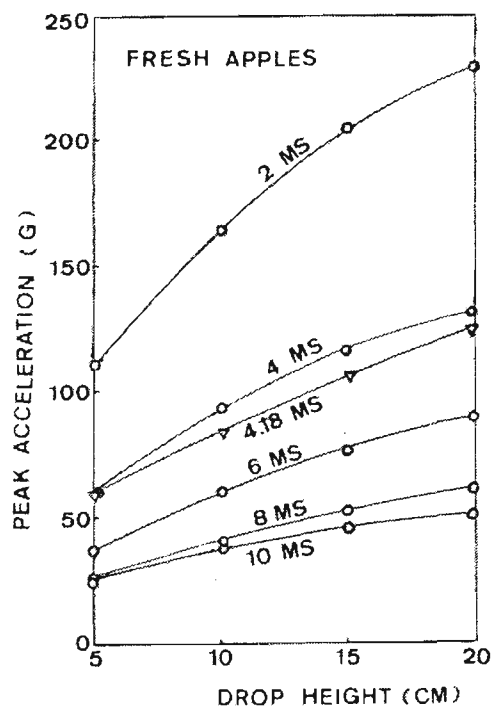


Figure 3.8 The relationship between peak acceleration and drop height for shock tests (o) and drop tests (v) for market-fresh Golden Delicious. Here  $G = g$ , gravitational acceleration. "MS" denotes milliseconds of duration of impact. Drop heights are shown in centimetres (CM). (Run ST-13).

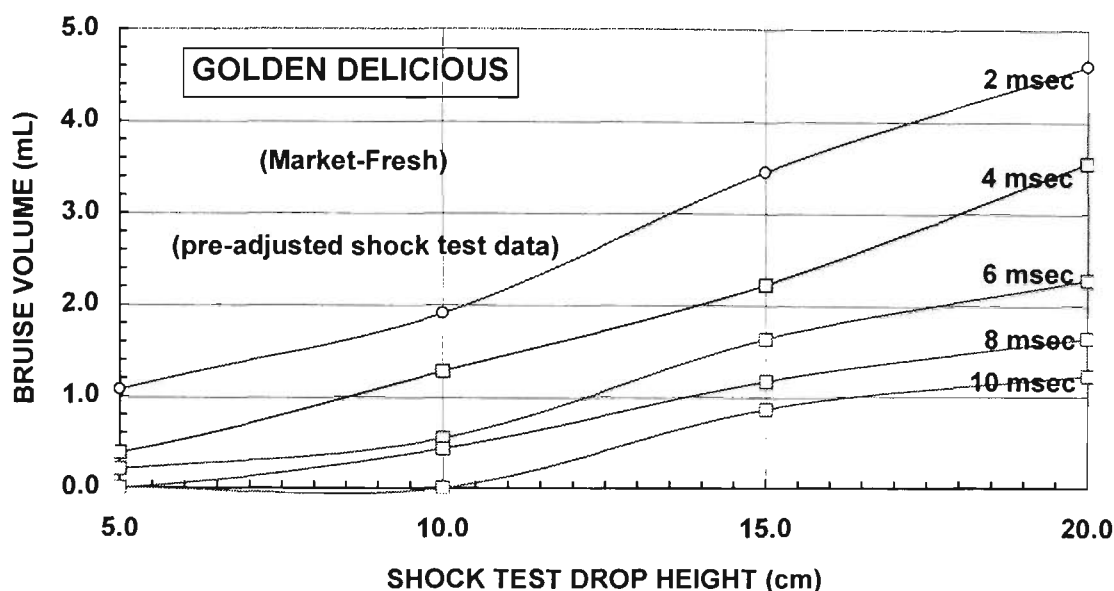


Figure 3.9 Bruise volumes of fresh Golden Delicious apples under various drop heights and duration of impact obtained from shock tests. “mL” denotes millilitre(s). (Run ST-13)

From the viewpoint of packaging protection, it is significant that the duration of impact can be extended substantially by changing the impact surface properties. This is possible by adding appropriate packaging materials such as cushions and corrugated fibreboard between the impactor and the surface. As shown in Figure 3.9, at a drop height of 20 cm, the bruise volume of an apple decreases almost threefold (3.55 mL/1.23 mL) if  $\tau$  was extended from 4 ms to 10 ms. Similar trends for bruise reduction may be expected for apples stored for two weeks, as shown in Figure 3.10.

Figures 3.11 and 3.12 show the direct relationships between bruise volumes and shock or drop tests under various drop heights, with storage periods of zero (market-fresh) to two weeks. The curves obtained from drop tests and shock tests differ significantly with comparable drop heights. This may be due to the difference in the coefficient of restitution,  $e$ , between the two types of tests during the impact rebound. For drop tests, the  $e$  value for market-fresh apples normally decreases linearly from 0.7 at a drop height of 5 cm to about 0.5 at 20 cm, as a result of viscoplastic deformation. For the shock tester, however, the  $e$  values remain unchanged at about 0.3 under different drop heights, with no rubber rings and cloth above the damper – see Figure 2.11. The results point out the inadequacy of using shock tester data without corrections. Here, shock data obtained from a shock tester cannot fully represent real life situations. Although shock testers have been widely accepted by the packaging industry to perform package fragility tests, their ability to reproduce actual impact conditions is questionable, according to Li *et al.*(1993).

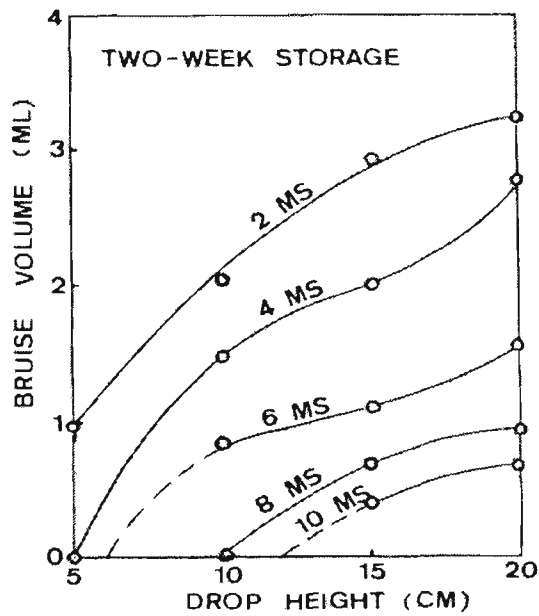


Figure 3.10 Bruise volumes of Golden Delicious apples after 2-week storage at controlled conditions under various drop heights and duration of impact obtained from shock tests. "mL" denotes millilitre(s). Drop heights are shown in centimetres (CM). "MS" denotes milliseconds of duration of impact. (Run ST-16)

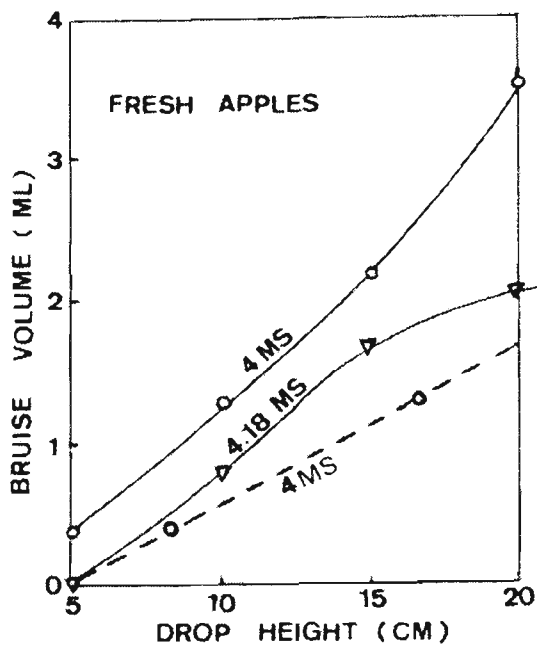


Figure 3.11 Bruise volumes of fresh Golden Delicious apples under different drop heights at duration of impact of 4 ms from shock tests (o) and drop tests (∇). "mL" denotes millilitre(s). Drop heights are shown in centimetres (CM). "MS" denotes milliseconds of duration of impact. (Run ST-13) (Dotted line represents 'corrected' equivalent free-fall drop heights for shock test data)

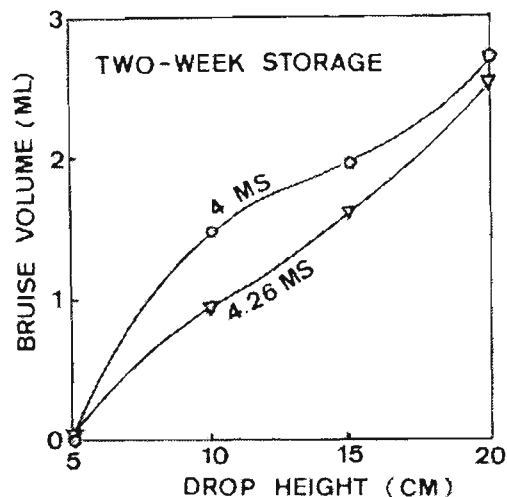


Figure 3.12 Bruise volumes of Golden Delicious after 2-week storage under different drop heights at duration of impact of 4 ms from shock tests (o) and drop tests (∇). “mL” denotes millilitre(s). Drop heights are shown in centimetres (CM). “MS” denotes milliseconds of duration of impact. (Run ST-16)

### 3.3.2 Validation of the Shock Test Method

A shock pulse is shown in Figure 3.13 captured by an accelerometer located at the centre of the shock table under a drop height of 5 cm with a Golden Delicious apple firmly fixed on top of the table centre. The actual duration of impact is about 6 ms, or 3.9 ms with the 10% cut-off, see Section 2.2.6. It took 3.3 ms, or 2.0 ms with 10% cut-off, to reach  $g_{max}$ . Let us compare this shock pulse with that shown in Figure 3.4 for the case of a whole-apple drop test with the same accelerometer buried inside the apple at 10 mm from the bottom skin. The drop height under free-fall was also 5 cm, similar to the shock test situation. It was noted that, although the values of the change in momentum,  $\Delta mV$ , of these two shock pulses were different, they were comparable in that:

- (1) the maximum pulse acceleration was  $568 \text{ m/sec}^2$  for the shock table case and  $538 \text{ m/sec}^2$  for drop test with the buried accelerometer, and
- (2) the unloading impact duration for drop test and shock test was 1.8 ms and 3.2 ms, respectively. In other words, the apple under a free-fall drop reached the maximum peak acceleration,  $g_{max}$  (or peak G) during an impact earlier than the shock table.

Therefore, the actual impact velocity experienced by the apple fixed on the shock table should be its true maximum velocity, which is contrary to a suggestion by Siyami *et al.* (1988). This is credible given the characteristically low coefficient of restitution of approximately 0.3 of the shock table, as shown later in this section in Figure 3.15.

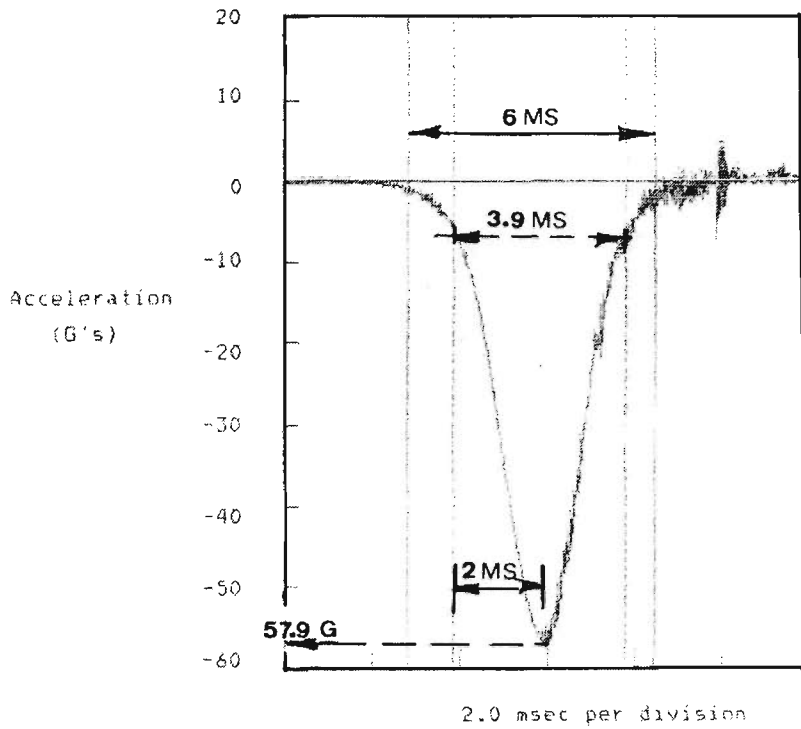


Figure 3.13 Shock pulse from shock test showing an impact duration of 6 milliseconds (3.9 milliseconds with 10% cut-off) and Peak G of 57.9 g (568 m/sec<sup>2</sup>). It took 3.3 milliseconds (or 2 milliseconds with cut-off) to reach Peak G. “MS” denotes milliseconds of duration of impact. (Run ST-13-5)

With this assurance, the next step would be to check whether the coefficient of restitution of the shock table could match that of real free-fall fruit drops. This was achieved by firstly simulating the actual whole-apple drop using the programmable function of the shock tester in terms of impact duration and drop heights, as shown in Figure 3.14, based on free-fall IFA Run ST-21B.

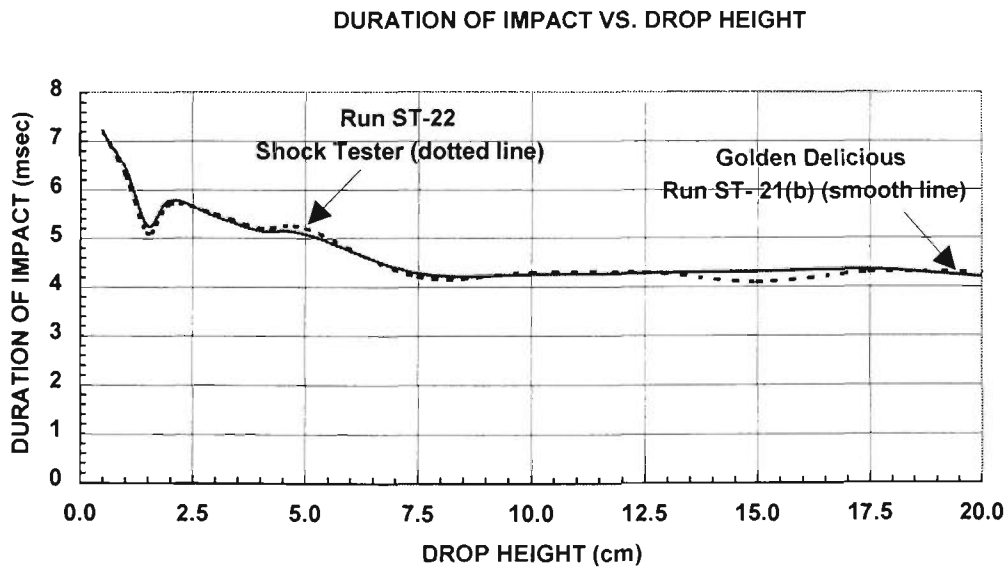


Figure 3.14 Simulation of whole apple drops by a programmable shock tester in terms of impact duration and drop heights for the estimation of restitution coefficients of the shock tester, based on free-fall IFA Run ST-21B.

Then, the impact parameters as generated from the simulation tests (Table 3-5) would be used for the estimation of the corresponding coefficients of restitution for the shock tester. The simulation is necessary as the shock table of a shock tester is normally designed to rebound instantaneously with impact duration of 2 ms, according to Li *et al.* (1993). The aim of this exercise was to confirm, using a spectrum of drop heights for the shock tester, that the shock tester could simulate a whole-apple drop in terms of its corresponding coefficients of restitution, when both cases are compared on the same values of  $\tau$ . The results are plotted in Figure 3.15.

Table 3-5 Comparison of the Coefficient of a Programmable Package Shock Tester Table at different Drop Heights on Piston Cylinder (Run ST-22).

Drop Height (cm)	Impact Velocity (m/sec)	Rebound Velocity (m/sec)	Coefficient of Restitution (e)
20.0	1.981	0.619	0.31
17.5	1.853	0.547	0.30
15.0	1.710	0.490	0.29
12.5	1.560	0.440	0.28
10.0	1.394	0.406	0.29
7.5	1.221	0.379	0.31
5.0	0.990	0.210	0.21
4.0	0.886	0.164	0.19
3.0	0.767	0.074	0.17
2.0	0.626	0.058	0.12

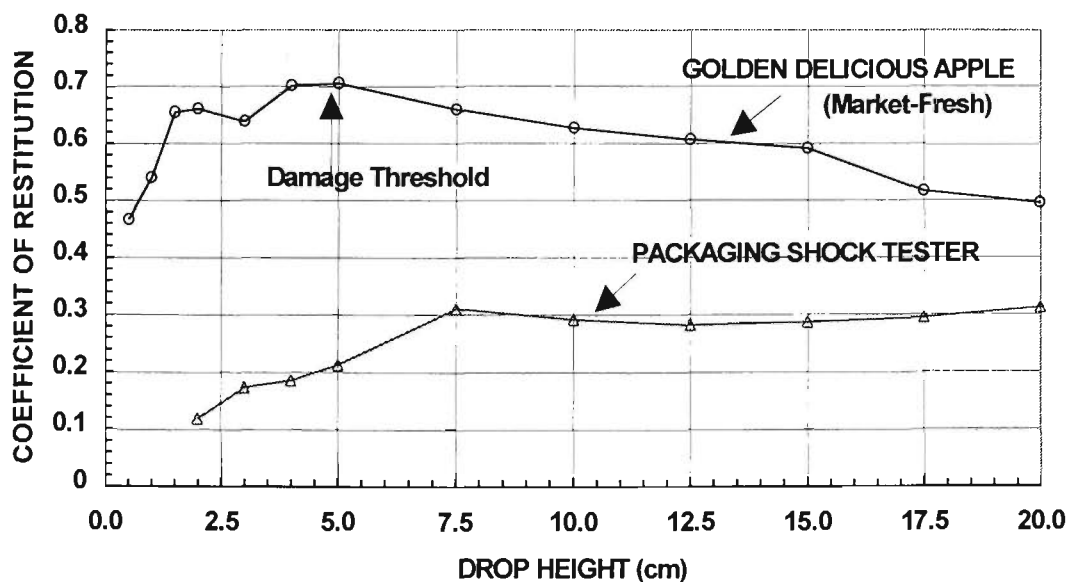


Figure 3.15 Relationship of the coefficient of restitution and drop heights for a shock tester and free-fall whole-apple IFA test (Run ST-21B).

Two observations stand out:

- (i) For Golden Delicious apple,  $e$  values peak at a damage threshold of about a drop height of 5 cm. This is normally acknowledged as the critical drop height,  $h_{oc}$ . Beyond the damage threshold, as expected,  $e$  values tend to decrease gradually due to damping and internal energy dissipation. On the other hand,  $e$  values also tended to decrease when the drop height was less than  $h_{oc}$ . This decrease in the latter is possibly due to the dynamic frictional effect between the produce boundary and the impacted surface. It is suggested that drop tests can be performed in the future to investigate these surface effects. These tests may illustrate the dynamic characteristics associated with frictional effects, particularly under very small drop heights, or under medium drop heights of 5 to 20 cm for point-to-point impact - see Pang *et al.* (1992).
- (ii) Regarding shock tests, it is generally believed that the actual impact velocity,  $V_I$ , of test objects such as a whole apple pre-fixed on top of the shock table may be higher than the theoretical impact velocity. It is so believed because the apple may possibly respond to an impact much slower than the shock table due to the rheological properties of the apple. Thus, it may be possible that the actual impact velocity experienced by the apple is the sum of the free-falling velocity plus the maximum rebound velocity of the shock table, as claimed by Siyami *et al.* (1988). If this is true, then the bruise volume due to the impact will be larger than expected. For the shock tester,  $e$  values remain constant for a wide range of drop heights at about 0.3, and edge gradually toward zero as the drop height decreases. This implies that the rebound velocity of the shock table will always be less than that of the apple, showing the shock tester to be incapable of generating extra damage to the apple. Thus shock tests can be performed on whole-fruits in situations related to determining duration of impact.

### 3.3.3 Shock Test Method

It is a straightforward process to transform the shock tester drop heights to their free-fall equivalent. For each whole-fruit drop test and corresponding shock test performed using the same batch of fruits, the changes of velocities ( $\Delta V$ ) during the moment of impact for both tests can be plotted against the test range of drop heights, as shown in Figure 3.16. Owing to the uniqueness of rebound characteristics of the shock tester with a constant  $e$ ,  $\Delta V$  of the fruit is always less than that under free-fall drops. Assuming the loss in momentum transfer during the impact duration is negligible, the 'corrected' or equivalent free-fall drop height under shock test at, for instance, 5.0 cm should be 9.0 cm, as illustrated in Figure 3.16. At this level both tests share the same value of  $\Delta V$  of 1.65 m/sec, and the same

momentum transfer. A similar estimation of equivalent drop heights can be made or other drop heights. Using this approach, drop heights of 10 cm and 15 cm may be transformed to 16.7 cm and 24.4 cm, respectively. The 'corrected' free-fall drop heights for the shock tests can then be plotted against their testing drop heights as shown in Figure 3.17.

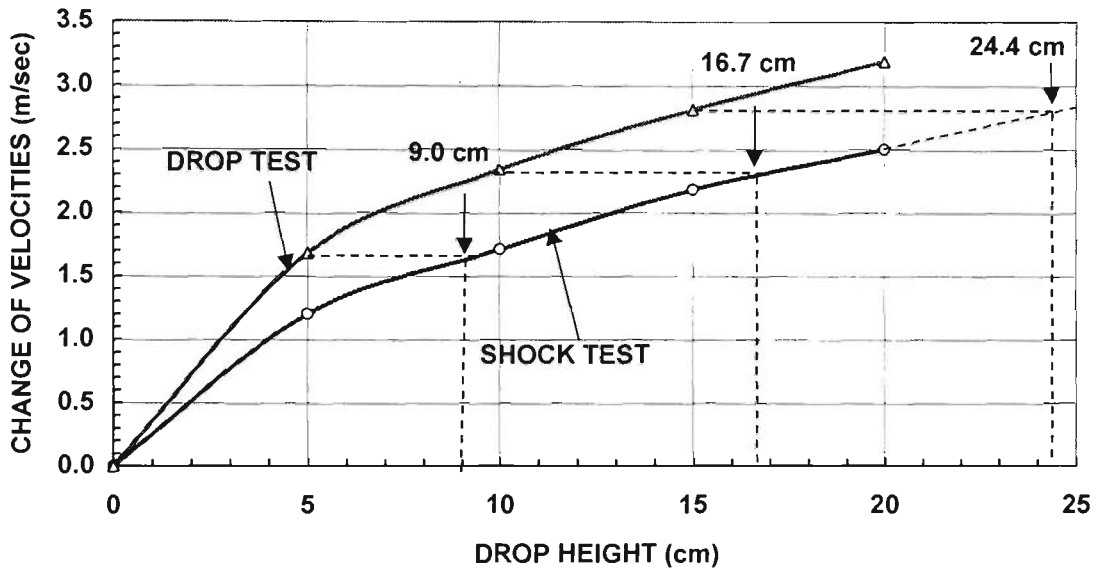


Figure 3.16 Data of changes of velocity ( $\Delta V$ ) versus drop heights from drop tests ( $\Delta$ ) and shock tests (o) with Golden Delicious apples. (Run ST-13)

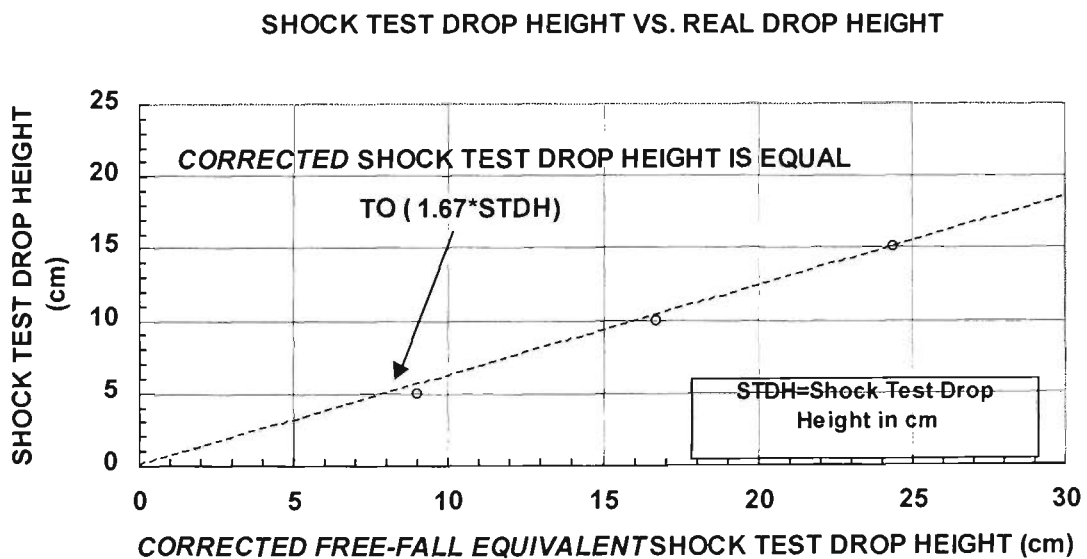


Figure 3.17 Original shock test drop heights versus corrected shock test drop heights for Golden Delicious drop tests. (Run ST-13)

In the case of market-fresh Golden Delicious apples, 'corrected' or equivalent drop heights are related to the original testing drop heights which were pre-set at the shock tester console, by a factor of 1.67 for this particular case of market-fresh apples, as shown in Figure 3.17. This factor will change for aged apples and has to be estimated case by case. The 'corrected' shock-test drop heights were applied to the data in Figure 3.11 and are re-plotted as a dotted line. The same procedure was applied to Figures 3.9 and 3.10. The drop-height 'corrected' Figure 3.9 is reproduced here as Figure 3.18, representing a true free-fall situation.

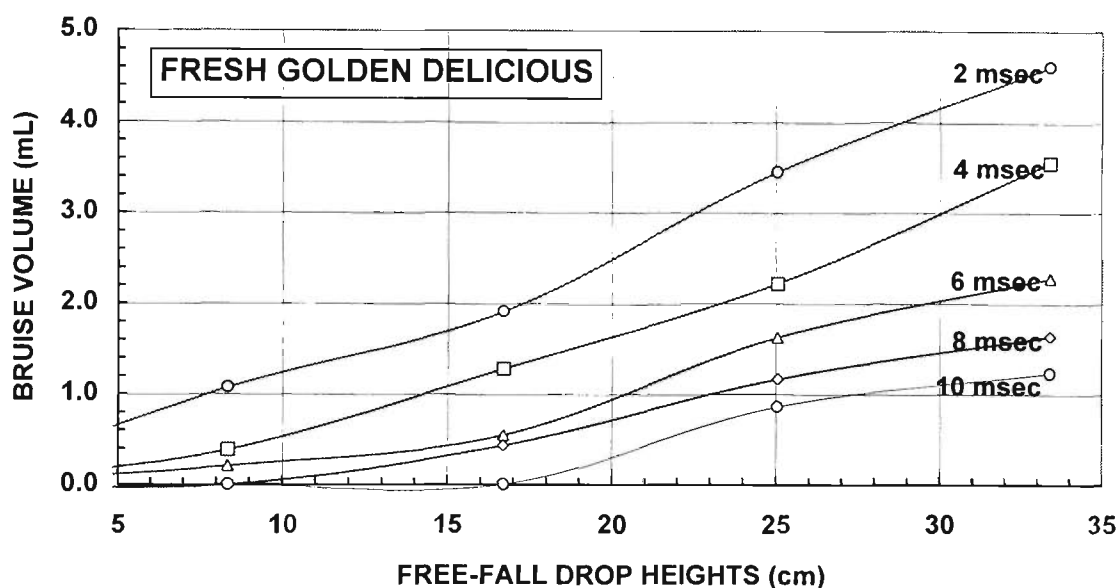


Figure 3.18 Bruise volumes of fresh Golden Delicious apples under various 'corrected' free-fall drop heights and duration of impact obtained from shock tests. (Run ST-13)

A comparison between the pre-adjusted and 'corrected' relationships of bruise volume and free-fall drop height reveals that the pre-adjusted figures are too conservative. For example, for a drop height of 20 cm, the pre-adjusted plot (Figure 3.9) shows a bruise volume of 4.6 millilitres under a  $\tau$  of 2 ms, whereas the 'corrected' plot (Figure 3.18) shows 2.5 millilitres under 2 ms. Design plots such as Figure 3.18 are useful for the design of protective packaging for shipment of horticultural produce, as they provide direct and accurate data based on test results. The tests are easy to perform, as whole-fruits are used for testing.

### 3.4 LASER DISPLACEMENT TESTS

The experimental design of the laser displacement tests was presented in Section 2.1.3.1. Produce for the tests were grouped in terms of their textural properties, that is, in terms of very soft, soft, moderately crisp and crisp produce. A succinct definition of crisp and soft horticultural materials is a challenging exercise. In this study, the definition was based on the textural characteristics according to Szczesniak (1963) and Szczesniak and Kleyn (1963). It was based on the mastication force required to break the food texture during the first chew. In this sense, produce like raw potatoes, carrots, apples and pears were considered crisp, but baked sweet potatoes and ripe tomatoes were soft.

#### 3.4.1 *Validation of the Laser Displacement Method*

As was described in Section 2.1.3.1, the laser displacement method makes use of produce materials for testing in the form of cylindrical specimens. All cylindrical specimens have only one size, with a diameter of 26 mm and a length of 10mm. Whether the acceleration time histories of loading based on this method agree with those from practical situation needs to be verified.

We recall the drop test of a whole apple with the same accelerometer buried securely in the centre of the apple, as shown in Figure 3.2, to simulate real drops. In that figure, the depth of the apple flesh between the bottom of the accelerometer and the apple skin boundary was positioned at 10 mm. This was chosen, along with other reasons given in Section 3.2.2, so that both the laser test specimens and real drop test specimens had an equivalent thickness of 10 mm of apple flesh beneath the accelerometer. The acceleration time history from a 5cm drop with the ‘buried’ accelerometer is shown in Figure 3.4. The experimental set-up for laser displacement testing is shown in Figure 3.19. The cylindrical specimen (kiwifruit in Figure 3.19) sits on top of an impact platform. The impact platform is a massive steel block of 12 kg with specific dimensions to fit the laser sensor. The laser beam strikes vertically upward and reflects from the platen bottom (marked by white arrow).

Figure 3.20 shows the acceleration time history of loading, or shock pulse, of a cylindrical Golden Delicious apple specimen selected from laser-based Run AX-05-a1 and depicts one of a series of 8 runs. As has been described in Section 2.1.3.1, each series of tests with crisp specimens comprises 5 to 10 drops.



Figure 3.19 Experimental set-up showing a variable strike-weight wire-guided platen (top) and a precision laser displacement sensor (bottom).

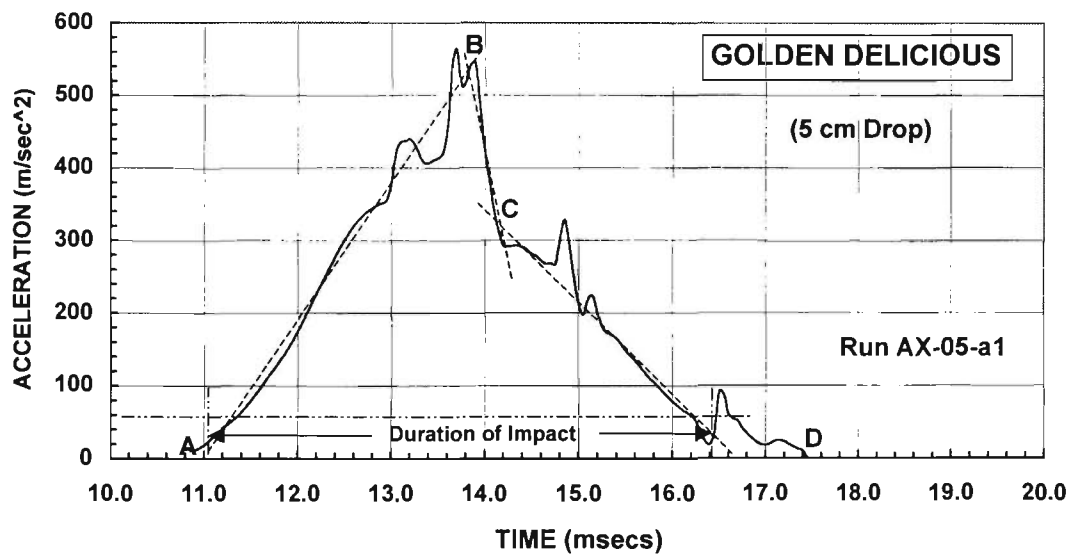


Figure 3.20 Acceleration time history of a cylindrical market-fresh Golden Delicious apple specimen. Strain rate is 87/sec. (Run AX-05-a1)

The drop height was chosen to be 5 cm. A strike weight of 135.75 gm was selected to model the actual weight of a real apple. For all laser displacement tests, the duration of impact denotes the time of the pulse with acceleration greater than zero, unless otherwise specified. It is common practice in the packaging industry to assume  $\tau$  to be the period of acceleration time history equivalent to an acceleration

of 90%, with 10% cut-off period, as shown in Figure 2.57. It was found that the acceleration time history curve as shown in Figure 3.20 is similar to that shown in Figure 3.4. They were comparable in the duration of impact, peak acceleration  $g_{max}$ , and unloading characteristics as shown by Curve *BCD* in both figures. Peak acceleration in both cases matched closely, reaching 550  $g$ . The duration of impact in both cases was comparable, at about 5.6 ms. The only major deviation of the two Figures was the time to reach  $g_{max}$ . By definition, the velocity change  $\Delta V$  associated with an acceleration time pulse is represented by the area under the pulse. By comparing Figure 3.20 with Figure 3.4, the area underneath the pulse curve *AB* in Figure 3.4 is smaller than that in Figure 3.20 to reach  $g_{max}$ . This indicates that, when the wave front from initial loading first reaches the accelerometer, the decrease of the accelerometer velocity as represented by smaller  $\Delta V$  in Run BUR-50 shown in Figure 3.4 is less pronounced than Run AX-05-a1 in Figure 3.20. This indicates that the much greater structural integrity of the whole-fruit can change its rate of deformation. However, any effects due to the structural integrity of the produce on  $\tau$  and  $g_{max}$  will be less significant.

The data in Figure 3.20 was converted to stress versus strain and is shown in Figure 3.21. Some pre-peak instability seems to have occurred, as shown by peaks when the stress exceeds 90 kPa with the corresponding strain of 25%. At such a high strain, it is likely that the troughs after the peaks were caused by cracking.

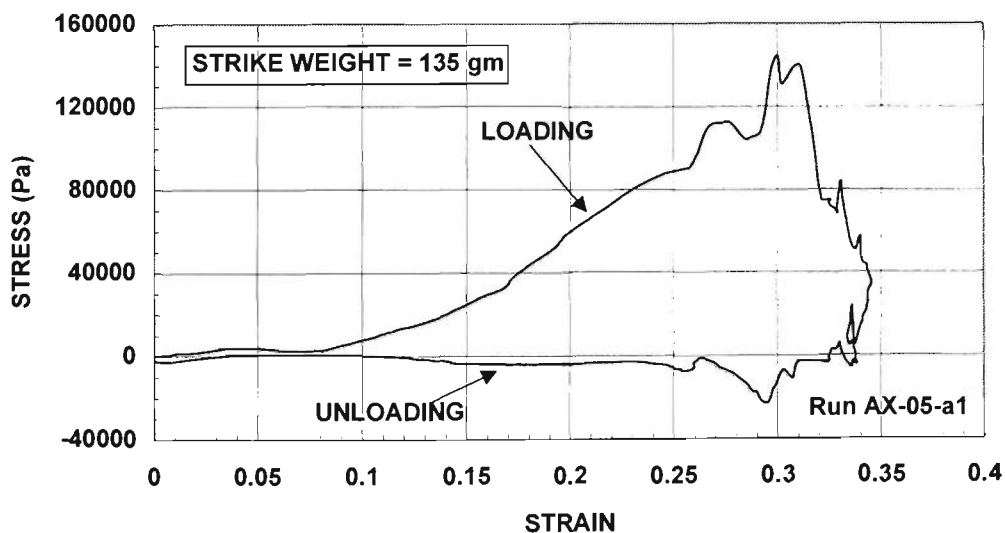


Figure 3.21 Dynamic stress-strain relationship of cylindrical market-fresh Golden Delicious apple specimen under a strain rate of 87/sec. and 5 cm drop using the laser-based method.

Any damage, if it exists, is not reflected in the curve. There was no permanent strain when the unloading path returned to zero strain, as shown in Figure 3.21. However, we recall Gordon (1978)

pointed out that cracks can exist in a material without leading to cleavage as long as they remain shorter than a critical size. Krajcinovic (1996) pointed out that these are called micro-cracks. From Figure 3.21, this strongly suggests the existence of a form of damage with no indication of permanent strain that may well be micro-crack instabilities in the pre-peak domain. Micro-cracks, and indeed any cracks, are able to absorb a significant amount of energy in order to generate free surfaces (but not necessarily free volumes). The absorbed energy by the micro-cracking process is unable to create permanent deformation, see Gordon (1978). However, if the isolated micro-cracks start to join up, there will no longer be micro-cracks present and permanent global-scale deformation in the specimen results. The transitional cracking process from micro- to macro-scale will propagate and it must be dynamic in nature.

### **3.4.2    *Soft Horticultural Materials***

This section (3.4.2) presents the results of dynamic characterization tests based on laser-based displacement measurements on soft horticultural materials. Up to this section, focus has been placed on the characteristics of produce materials in term of whole fruits, based on results of drop tests and shock tests to study some of the more important impact parameters and their relationships with bruising. From this section onward, the aim is to present the results of the dynamic characteristics and associated subtleties of specific phenomena in a more classical way, namely in terms of the dynamic stress-strain characteristics of the produce, based on transient responses from cylindrical produce specimens under high loading. The results are presented according to the rheological nature of the produce that varies from liquid-like to solid-like, as has been discussed in Section 2.2.3. Results vary from viscoplastic deformation in Section 3.4.2.1 to predominantly crisp deformation in Section 3.4.4. This approach was chosen to answer the question: what are the root causes of bruising in soft and crisp horticultural materials?

#### **3.4.2.1    Viscoplastic Deformation**

Produce with soft textures is more susceptible to plastic or viscoplastic deformation, with the softest tending to deform viscoplastically. Examples of primarily viscoplastic deformation include banana flesh. Figure 3.22 shows 10 mm thick banana specimens under three different conditions, all with an initial diameter of 26 mm taken from the same banana. As the kinetic impact energies increase when the drop heights increase, the banana specimens tend to deform viscoplastically. This is evident from Figure 3.22 that shows an increase in diameter under viscoplastic deformation but no observable fracturing or cracking. Whether the impacted banana flesh specimens actually underwent

viscoplastic deformation can be tested by comparing the dynamic stress-strain curves obtained from laser-based impact tests as depicted in Figures 3.23 (5 cm drop) and 3.24 (10 cm drop).

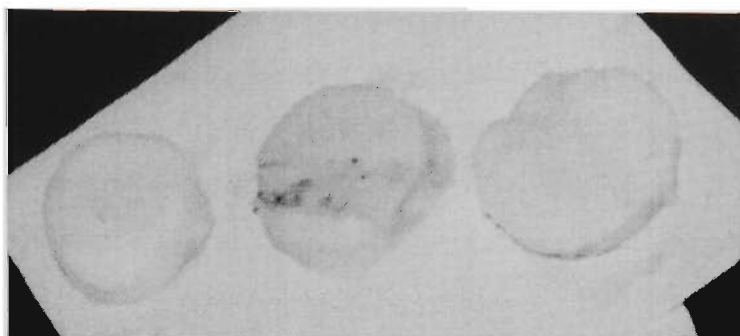


Figure 3.22 Predominantly viscoplastic deformation of banana specimens with a strike weight of 0.9 kg using the laser-based tester: (left) A specimen before impact test; (middle) same-sized specimen after 5 cm drop impact; (right) same-sized specimen after a 10 cm drop impact.

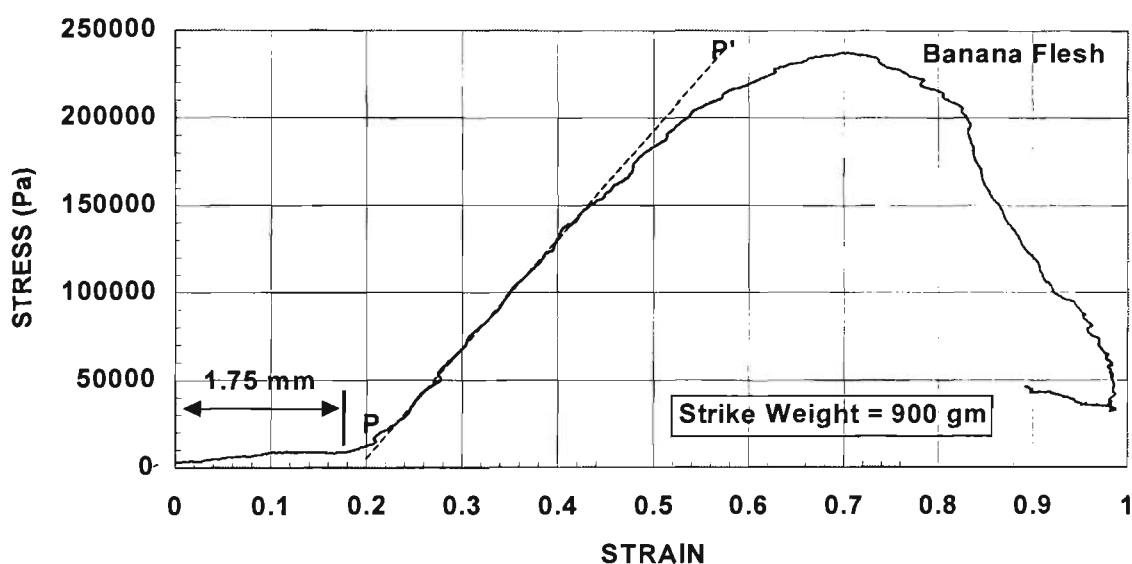


Figure 3.23 Dynamic stress-strain characteristics of banana flesh specimen using the laser-based tester under a strain rate of 100/sec. (Run BN-05-m1) (5 cm drop)

Both cases used the same strike weight of 0.9 kg. The strain rates of deformation in the two cases were different: at 100/sec. and 107/sec. for the specimens with 5-cm drop and 10-cm drop, respectively. As shown in these Figures, the straight moduli P-P' and R-R' originate from a similar spot on the 'toe'. Each modulus clearly developed different paths. Both curves have ultimate stresses occurring at comparable strain level of about 65%, but with substantial difference at the ultimate stress levels. This shows that different strain rates of deformation would produce completely different dynamic curves in the case of banana flesh, clearly denoting viscoplastic deformation. This is illustrated in Figure 3.25 by replotting Figures 3.23 and 3.24. As shown in Figure 3.25, there are no distinct yield points on both curves, which is also one of the more distinctive characteristics of

viscoplastic deformation. Here, the viscoplastic deformation of banana flesh was very rate-sensitive, with higher stress producing higher strain rate.

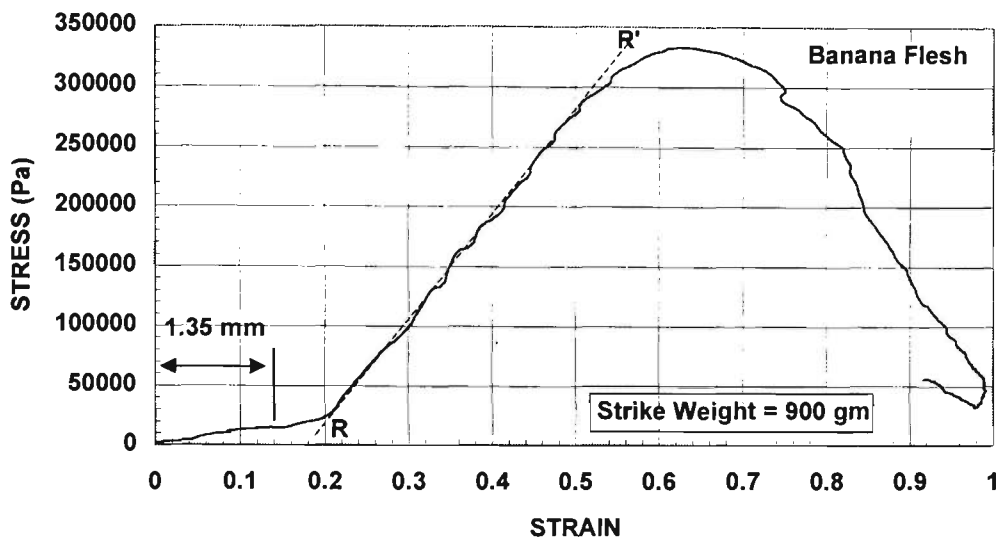


Figure 3.24 Dynamic stress-strain characteristics of banana flesh specimen using the laser-based tester under a strain rate of 107/sec. (Run BN-10-m1) (10 cm drop)

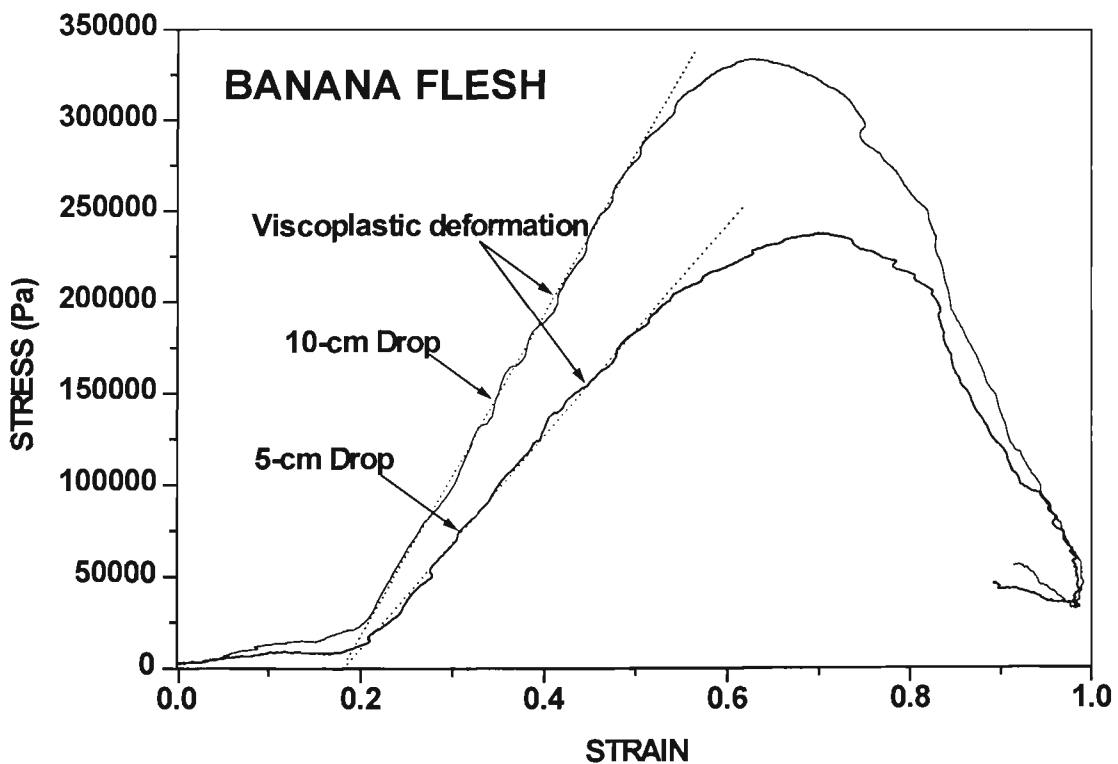


Figure 3.25 Dynamic stress-strain responses of banana flesh under strain rates of 98/sec. (5 cm drop) and 110/sec. (10 cm drop) under a strike weight of 0.9 kg. Curves show strong rate-dependent dynamic viscoplastic deformation processes under different paths of deformation.

The initial 'toe' sections of both stress-strain curves show the maximum extent of the sigmoidal curves at comparable strain levels of about 20% (or 2 mm) in Figure 3.23 and also about 20% (or 2 mm) in Figure 3.24. This suggests that the initial deformation underwent the same process of initial unwinding of cell-wall micro-fibrils, in the sense of Gordon and Jeronimidis.

#### 3.4.2.2 Skin Protection for Soft Produce

The protective ability of produce skins can be illustrated by the dynamic stress-strain characteristics of banana skin and flesh, with direct displacement data captured by the laser displacement sensor. The size of each banana skin specimen tested, as shown in Figure 3.26, is 40 (length) x 10 (width) x 3.6 (thickness) mm, carefully cut from the same banana specimen. Each specimen was tested within five minutes after it was cut to size. An optimized size of the skin specimens was chosen to achieve the best spread of loading during the impact by the rectangular strike hammer with similar length and width dimensions. Under an impact with a drop height of 5 cm, the banana skin failed at 1.05 MPa, with 1.75 mm of displacement of the skin thickness, as shown in Figure 3.27. The banana flesh remained undamaged within the 'toe' region with only minimal rise in stress, as can be seen in Figure 3.23.

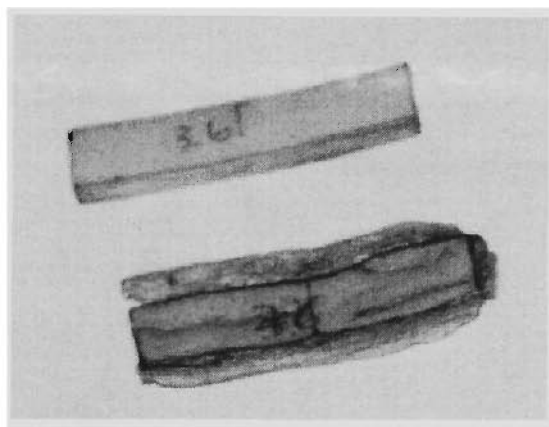


Figure 3.26 Specimen of banana skin before and after impact with a 0.9 kg hammer under 10 cm drop height. (Run BS-10-m1) Specimen size: 40 (length) x 10 (width) x 3.6 (thickness).

With a drop height of 10 cm for the 0.9 kg hammer, the banana skin failed at 1.30 MPa with 1.35 mm of displacement to the skin thickness, as shown in Figure 3.28. At a level of displacement of 1.35 mm, the banana flesh remained undamaged within the 'toe' region with only minimal rise in stress, as shown in Figure 3.24. It is significant to note that banana skins deform at much higher strain rates than the flesh under the same testing conditions, with the strain rates of the skins deforming at 250/second and 340/second, respectively, for the corresponding strain rates of banana flesh at 100/second and 107/second. In both cases, the skin took up most of the loading under an impact.

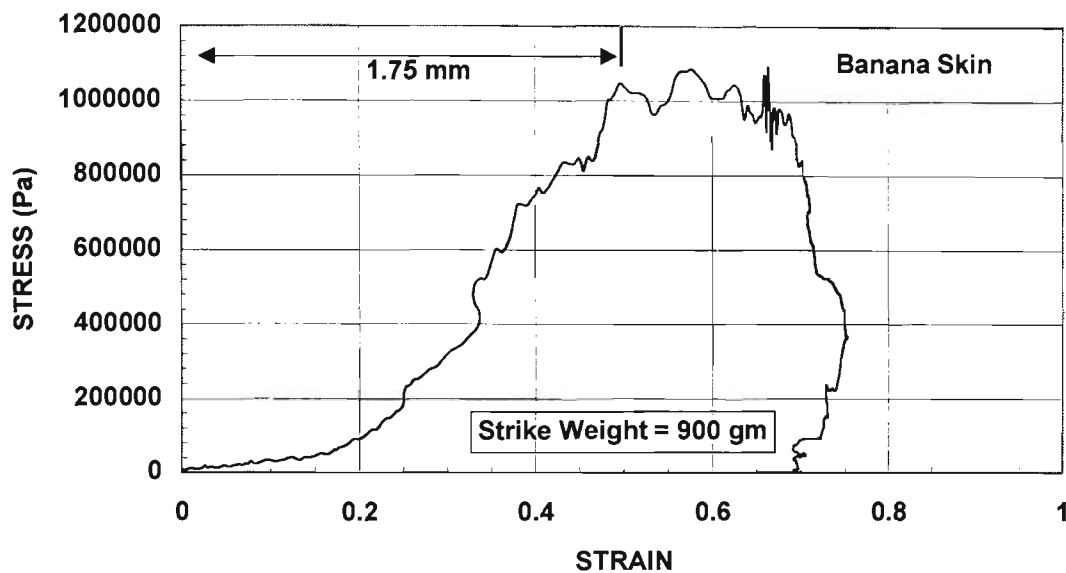


Figure 3.27 Dynamic stress-strain characteristics of banana skin. (Run BS-05-m1) (BS-05-m1 is for internal use that denotes *banana-skin 5 cm drop testing trial No.1* with *medium-type* striker of 0.9 kg). Elastic modulus is 3.25 MPa under a strain rate of 250/sec.

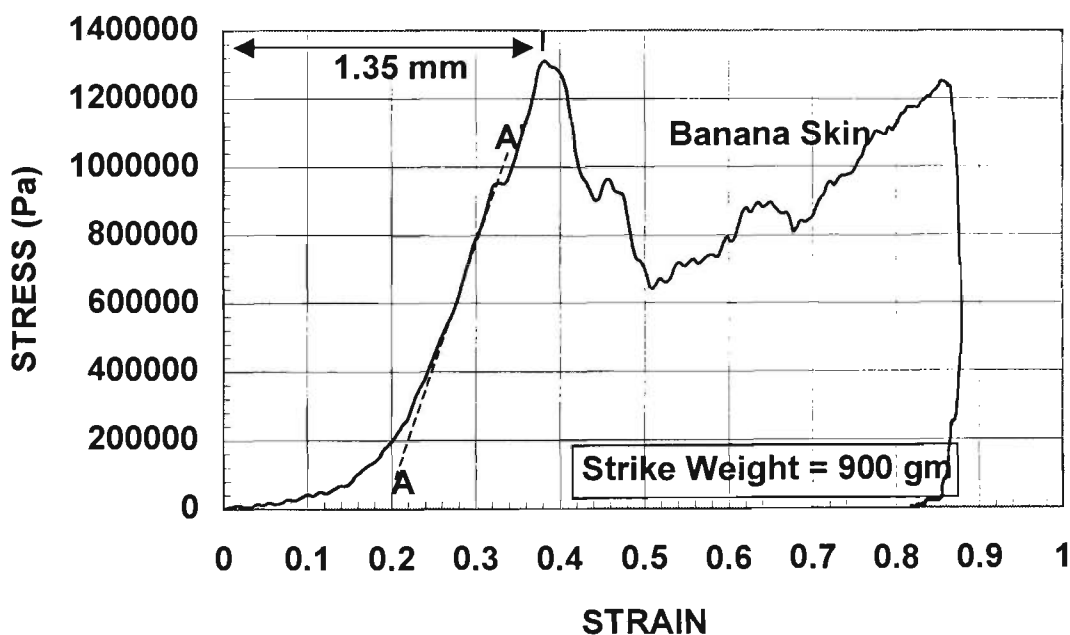


Figure 3.28 Dynamic stress-strain characteristics of banana skin under a 10 cm drop of a 0.9 kg hammer. (Run BS-10-m1) Young's modulus, A-A' is 7.27 MPa under a strain rate of 340/second.

All skin and flesh specimen results shown in Figures 3.22 to 3.28 were from the same banana specimen. The initial thickness of each of the banana skin specimen was 3.60 mm. At the bio-yield point, the skin was compressed 1.75 mm, as shown in Figure 3.27, at a strain of 50%. The strong

protective function of the banana skin was clearly evident by comparing the skin data with the corresponding banana flesh as shown in Figure 3.23. Here, at the same level of compression of 1.75 mm, there has been no increase in the dynamic stress in the banana flesh, shown at 12 kPa only, so that the flesh was protected against bruising by the sacrificial nature of the skin.

A similar result was found in the cases with a drop height of 10 cm of the 0.9-kg hammer. The banana flesh was deformed within the 'toe' part of the dynamic stress-strain curve when the banana skin failed first at 1.35 mm of deformation in both cases, as shown in Figures 3.24 and 3.28. Figure 3.28 shows that the banana skin fibrils were stretched to the limit, as illustrated by its Young's modulus of 7.27 MPa, denoted by A-A'. The linear moduli of typical fibrous skins like banana shows that they are highly rate-dependent. These fibre chains (bottom photo in Figure 3.26) are orthotropic in nature and run longitudinally along the banana fruit. Produce with thick skins such as bananas is highly rate sensitive as has been shown experimentally. They protect produce flesh by sacrificial failures. The cushioning capability of skins will be complete only if both the initial drop height,  $h_o$ , and cushion thickness,  $T_c$ , are taken into account in the form of a ratio of ( $h_o/T_c$ ). This ratio is actually a function of the strain rate,  $\dot{\epsilon}$ , during the deformation of the cushion, as shown by Equation (2-28). In particular, fibrous skins deform as Hookean springs and are susceptible to failure instabilities probably in the form of cracking.

#### 3.4.2.3 Plastic Deformation

The process of plastic deformation is one of the more complex material processes in many engineering materials such as steel and aluminium. Under plastic deformation, these materials are able to maintain their structural strength without failure when undergoing large deformation, usually demonstrated by a large plateau. In nature, some of the structurally weakest produce textures have similar attributes by undergoing plastic or even perfectly-plastic deformation under high loading. Two examples of the latter are shown here, selected from two series of tests on kiwifruit and persimmon. Figure 3.29 shows the dynamic stress-strain characteristics of a kiwifruit specimen under plastic deformation with low strain rates.

Here the dynamic curve approaches the elastic-perfectly plastic mode. Under perfectly-plastic deformation, strain rates have no effect on the dynamic curve, as shown in Figure 3.29. A similar mode of elastic/perfectly plastic deformation was also noted in persimmon that has a very soft texture, as shown in Figure 3.30. A comparison of Figures 3.29 and 3.30 shows that, at a strain rate of about 100/second, the kiwifruit specimen underwent perfectly-plastic deformation, indicating the absence of any damage processes, as shown by the horizontal curve in Figure 3.29. On the other hand, the

persimmon specimen registered perfectly-plastic deformation as well as strain softening, indicating gradual damage. Within the post-peak strain-softening domain, the process is expected to be the same, as characterized by an almost constant strain softening modulus,  $-h$ , see Figure 3.30. Here the minus sign denotes the negative slope of the stress-strain curve in the softening region. This type of deformation has been represented by Equation (2-16).

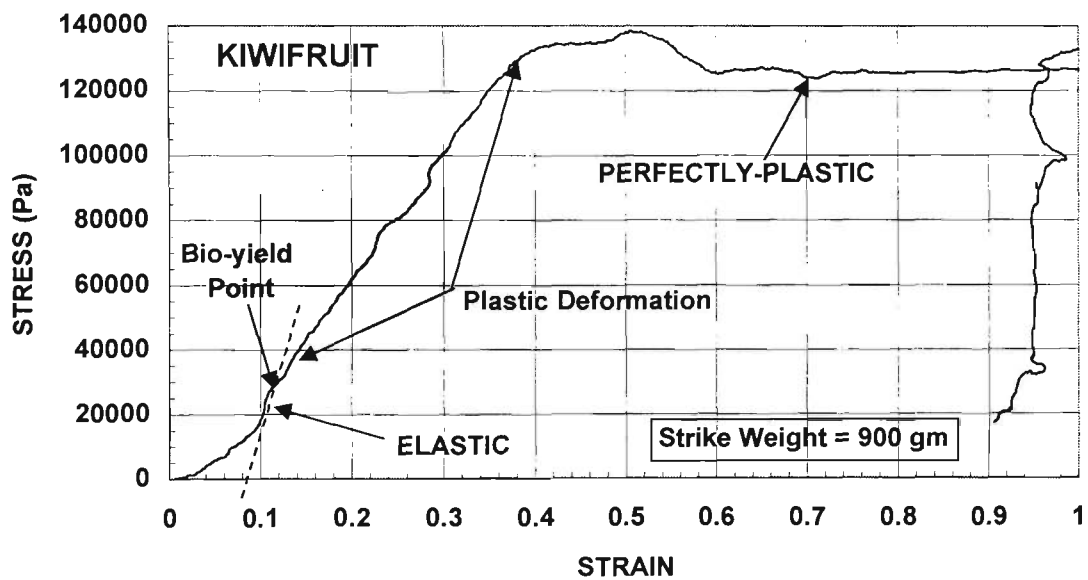


Figure 3.29 Dynamic stress-strain curve of kiwifruit using the laser-based tester under a 5 cm drop with a strain rate of 94/sec. (Run KW-05-m2)

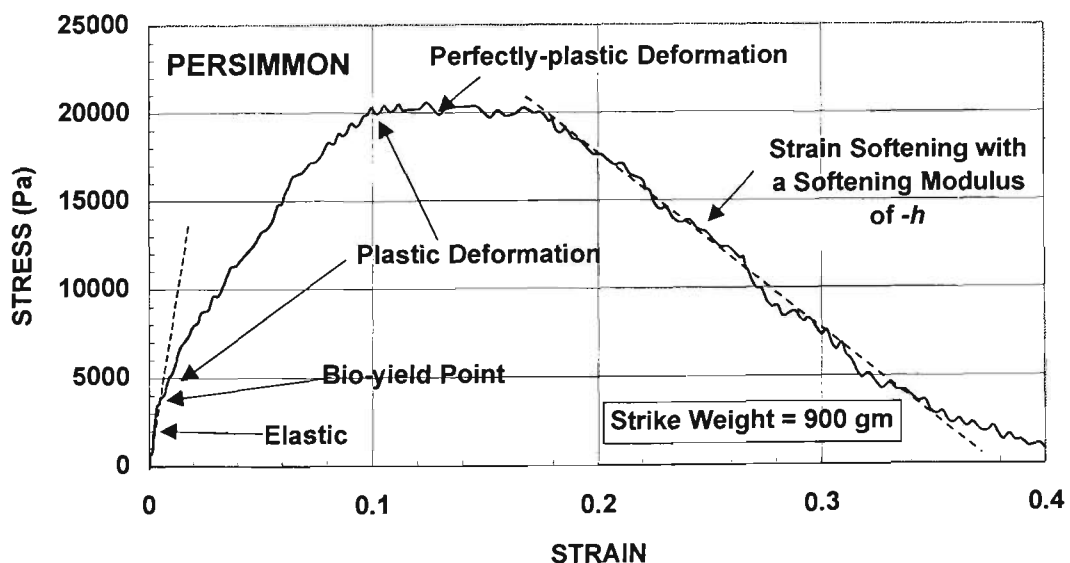


Figure 3.30 Dynamic stress-strain curve of persimmon deformation using the laser-based tester, showing elastic/plastic and perfectly-plastic modes under a 10 cm drop with a strain rate of 103/sec. (Run PR-10-m1)

#### 3.4.2.4 Plastic/Viscoplastic Deformation coupled with Heat Diffusion

This section presents two examples of the produce with arguably some of the weakest structures available. These include ripe persimmon and bilocular tomato. For this produce, the strongest part of their textures is perhaps their skin. Under high loading, the ability of these produce textures to mitigate the loading and minimize bruising becomes significant.

When a material completely loses its structural integrity and strength, such as the case of persimmon specimen that reaches a strain level of about 42% in Figure 3.30. The nature of the loss of strength is due to shear banding, a form of material instability purely due to plastic deformation, leading to the formation of fractures. This is shown in Figure 3.30 with the occurrence of perfectly-plastic deformation followed immediately by instability (strain softening). The bulk of the texture should remain intact. However, when the persimmon texture is further deformed, as shown in Figure 3.31, it resists and mitigates the increasing loading by heat diffusion, as indicated by a characteristic straight line, commonly referred to by materials science workers as the Rayleigh line. The Rayleigh line serves as a distinctive indicator of the occurrence of heat diffusion within a material that is under high loading. When the strain level reaches 95%, a sharp rise in stress indicates the presence of viscous flow as all the persimmon textures become sap.

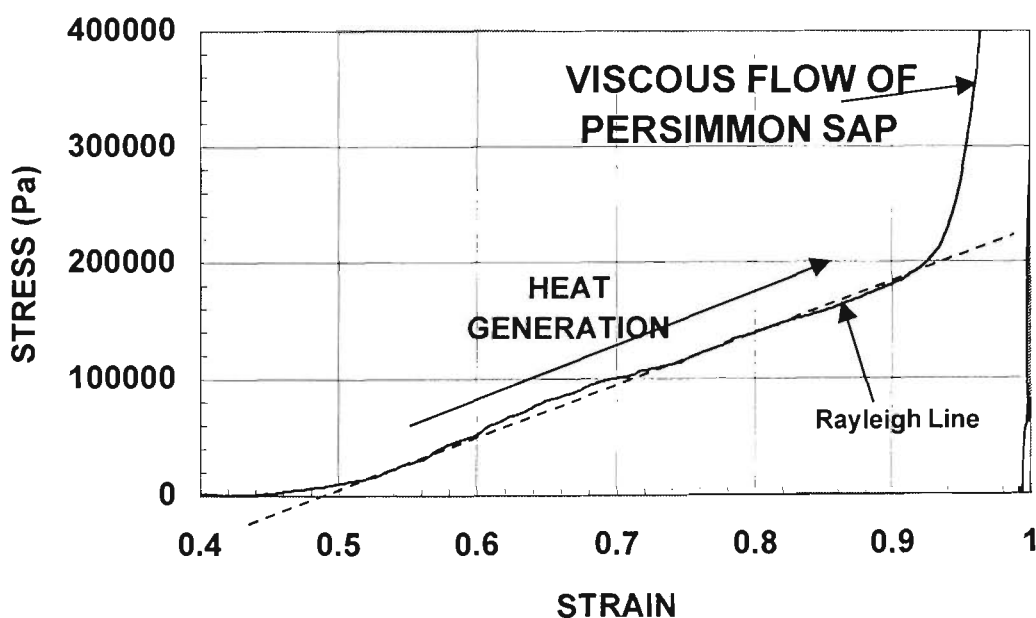


Figure 3.31 Dynamic stress-strain curve of persimmon deformation using the laser-based tester, showing elastic/plastic and perfectly-plastic modes under a 10 cm drop with a strain rate of 103/sec. (Run PR-10-m1)

Figures 3.32 and 3.33 show typical viscoplastic deformation modes for tomatoes. The viscoplastic deformation mode was best illustrated in Figure 2.29 where the viscous stress,  $\sigma_v$ , and the viscoplastic strain,  $\epsilon_{vp}$ , was sensitive to strain rates. As a result, any unique strain rate,  $\dot{\epsilon}$ , under the viscoplastic mode will result in a characteristic dynamic stress-strain curve unlike any other curves. The deformation paths would be completely different, although they are expected to reach their ultimate stress level at a unique critical strain,  $\epsilon_c$ , due to instabilities. This situation is illustrated in Figures 3.32 and 3.33 for the case of ripe cylindrical tomato specimens, under similar test conditions but with strain rates of 85/second and 115/second, respectively.

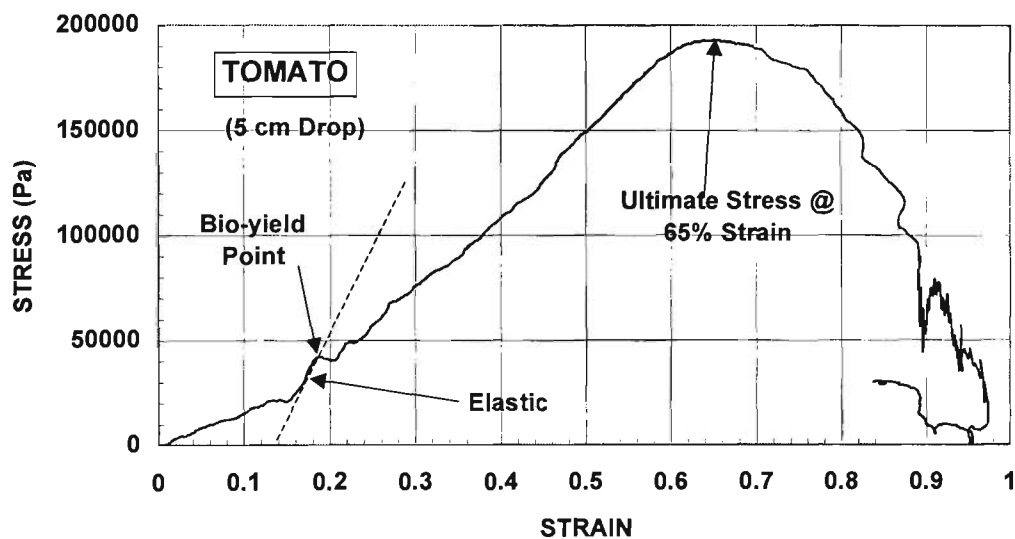


Figure 3.32 Dynamic stress-strain curve of ripe tomato flesh showing the rate-sensitive viscoplastic deformation characteristics. (Run PO-05-m1) (5-cm drop) Strain rate is 85 /sec.

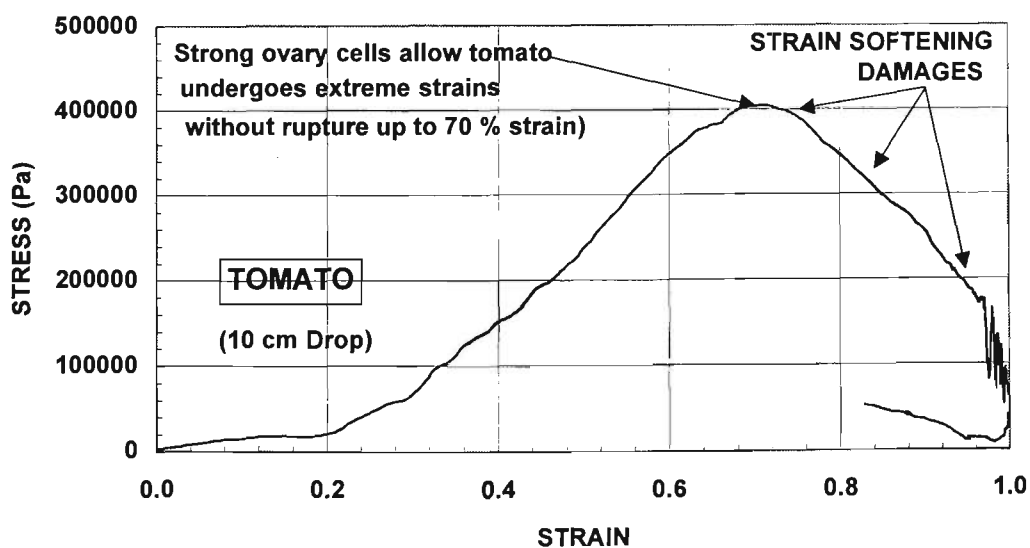


Figure 3.33 Dynamic stress-strain curve of ripe tomato flesh showing the rate-sensitive viscoplastic deformation characteristics. (Run PO-10-m1) (10-cm drop) Strain rate is 115 /sec.

In the case of viscoplastic deformation of banana flesh, the rate-sensitivity is even more profound, as shown in Figures 3.23 at 100/sec. and 3.24 at 107/sec., resulting in ultimate stress levels of 230 kPa and 330 kPa, respectively. Their critical strain,  $\epsilon_c$ , is about 65% in both cases. The dynamic responses of tomato specimens are shown in Figure 3.34 by reploting Figures 3.32 (for 5-cm drop) and 3.33 (for 10-cm drop) and by incorporating the results of the 15-cm drop test. The deformation is dominated by a rate-sensitive viscoplastic process between strain rates of 85/sec. (5-cm drop) and 115/sec. (10-cm drop). Curves show strong viscoplastic deformation processes under different paths, as well as plastic deformation when a critical strain rate of 115/second is reached, see the 10-cm and 15-cm curves. The appearance of the linear Rayleigh line indicates the existence of a heat diffusion process. A Rayleigh line, which appears as a straight line, is a unique feature of the dynamic characteristics of material structures when it completely fails and enters a stage of viscous flow.

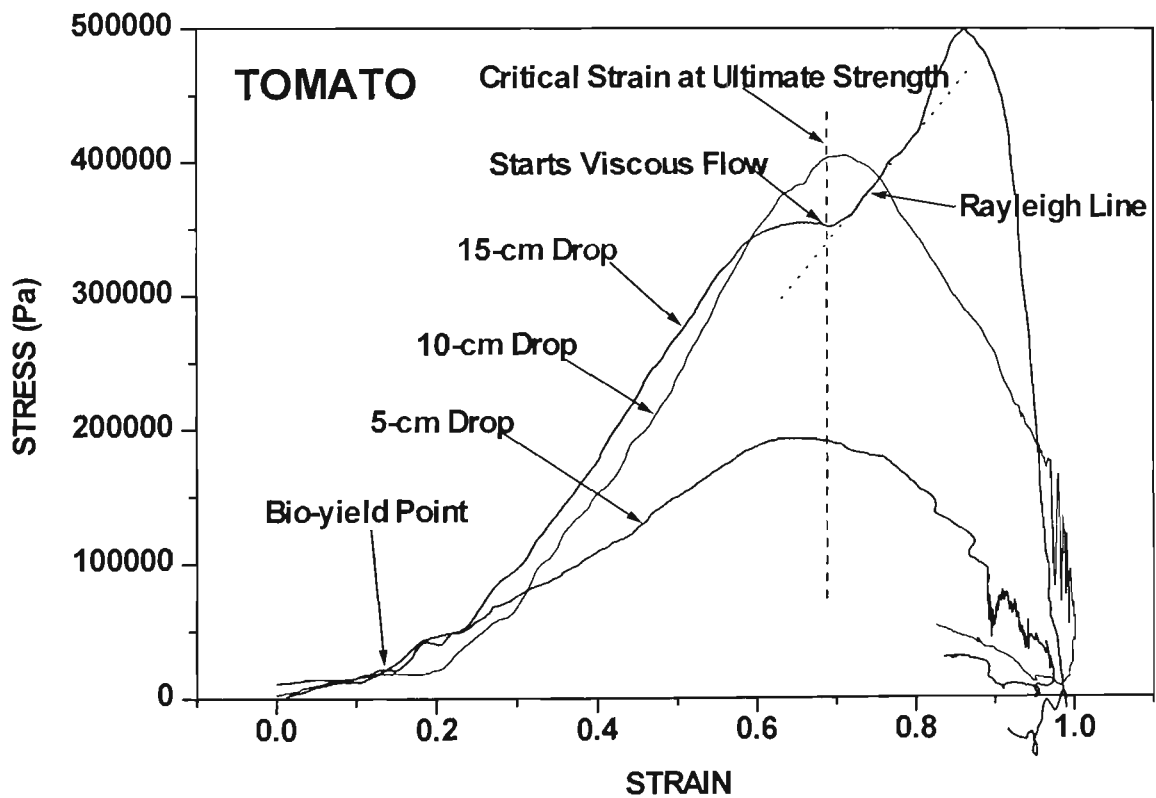


Figure 3.34 Dynamic stress-strain responses of tomato under strain rates of 85/sec. (5-cm drop), 115/sec. (10-cm drop) and 115/sec. (15-cm drop) under a strike weight of 0.9 kg.

Above the 10-cm drop height threshold, the strain rate seems to be insensitive to any increase in drop heights or impact energy, as shown in Figure 3.34. At a drop height of 15 cm, the strain rate remains at 115/second. It is noted that there seems to be a critical failure strain,  $\epsilon_{cr}$ , for

tomato at about 70% strain, above which the texture either softens (5-cm and 10-cm drop) or initiates a heat diffusion process. The diffusion is followed immediately by viscous flow when it completely breaks down (15-cm drop), as evident by the existence of the linear Rayleigh line. The critical strain rate was 115/sec. for tomato.

Plastic/viscoplastic deformation was shown as the primary mode of dynamic characterization for the softer produce such as banana flesh, tomato, kiwifruit and persimmon. Based on Figure 2.29, it was noted that the sensitiveness of the materials to strain rates determined the dynamic characteristics of the materials. The deformation of soft produce can take place under a wide range of  $\dot{\epsilon}$ , beginning with the strain-rate independent plastic deformation mode ( $\dot{\epsilon} = 0$ ), progressing to the rate-dependent viscoplastic mode. At the other extreme,  $\dot{\epsilon}$  approaches infinity, indicating viscous flow.

#### 3.4.2.5 Consistency of Dynamic Deformation Characteristics in Soft Produce

There seems to have been a misconception about the material properties and behaviour of horticultural materials in that their behaviours are truly unpredictable. This suggestion does not seem to apply to soft produce. The acceleration time-histories of soft horticultural materials showed high consistency among different test runs under comparable testing conditions.

For soft produce which deforms under the classical plastic/viscoplastic deformation, their characteristic loading curves are surprisingly consistent, as shown in Figures 3.35 to 3.38 for kiwifruit under plastic deformation and tomato under viscoplastic deformation. The high consistency of their displacement time-histories is illustrated in Figures 3.39 and 3.40 for the case of tomato. In these two figures, the displacement history curves only deviate slightly when the displacement time of the specimens is 7.0 ms and 8.4 ms (at peak acceleration). In general, the acceleration time-histories of soft produce specimens were highly consistent under similar testing conditions, and extremely consistent in their displacement histories.

When instabilities become more profound, the degree of consistency deteriorates, as shown in Figures 3.41 and 3.42 for the case of market-fresh Granny Smith apple specimens. Apples do not belong to the soft produce category, due to their crisp textures they are susceptible to cracking instabilities, which can substantially alter their dynamic characteristics, see Figures 3.41 and 3.42. Their corresponding strain time-history plots are shown in Figures 3.43 and 3.44. Estimations of strain rates can be done using these strain history plots.

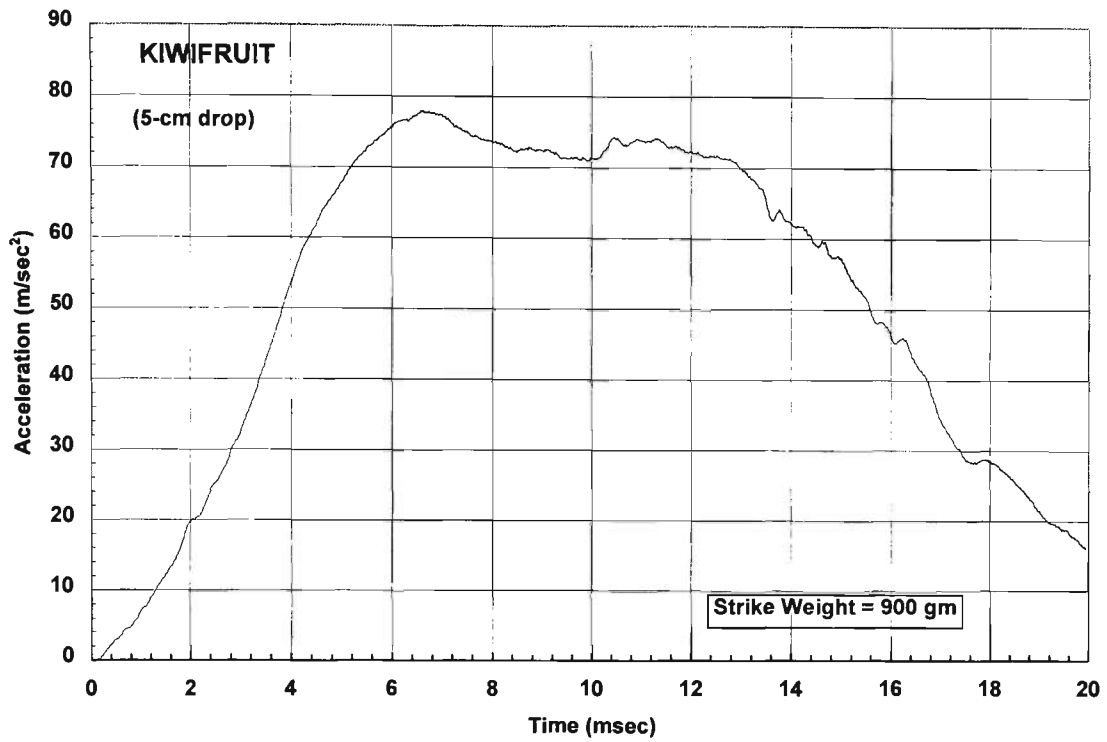


Figure 3.35 Acceleration time history of kiwifruit under impact (Run KW-05-m1).

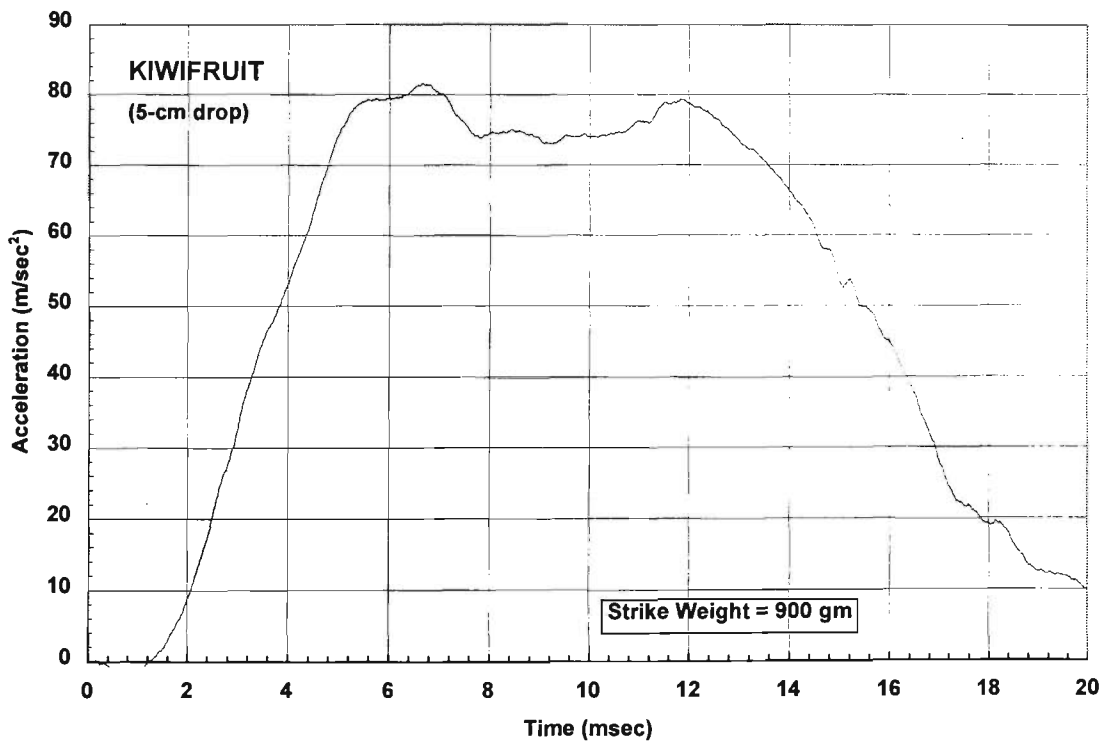


Figure 3.36 Acceleration time history of kiwifruit under impact (Run KW-05-m2) showing similar dynamic characteristics to Run KW-05-m1 under the same test conditions.

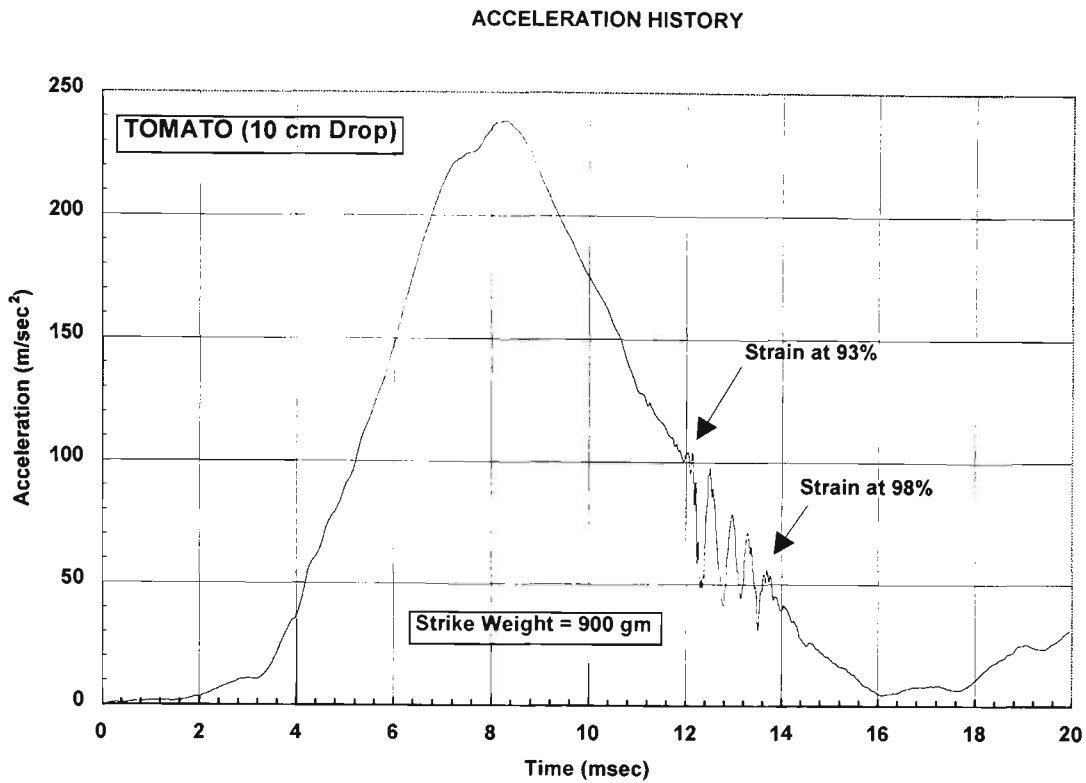


Figure 3.37 Acceleration time-history of tomato under impact (Run PO-10-m1). Result shows unique instabilities between strain of 93% to 98%.

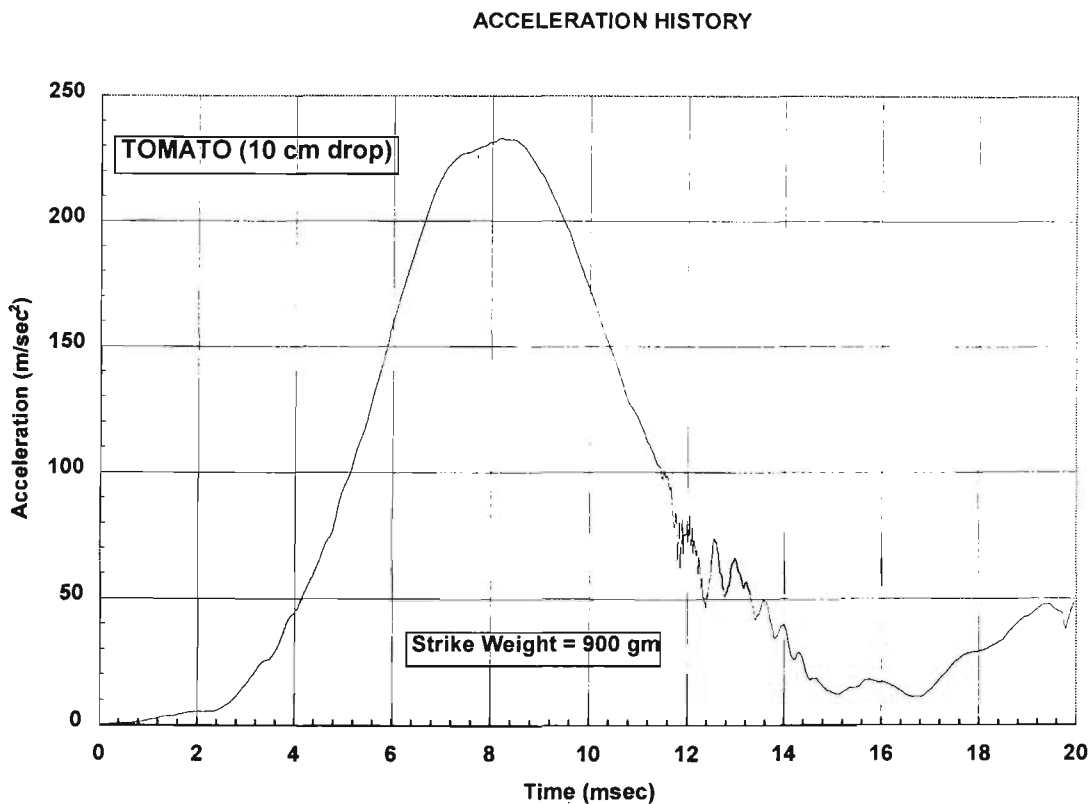


Figure 3.38 Acceleration time-history of tomato under impact (Run PO-10-m2) showing very similar dynamic characteristics to Run PO-10-m1 under the same test conditions.

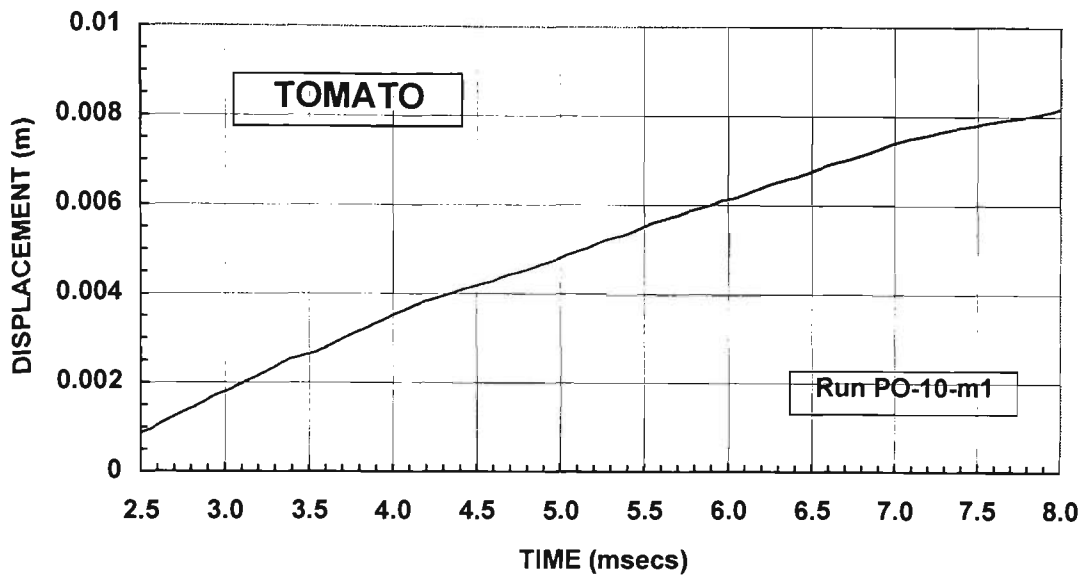


Figure 3.39 Displacement time-history of tomato under impact (Run PO-10-m1). Data were captured by laser displacement sensor. The displacement data represent the real-time travel distance of the strike weight.

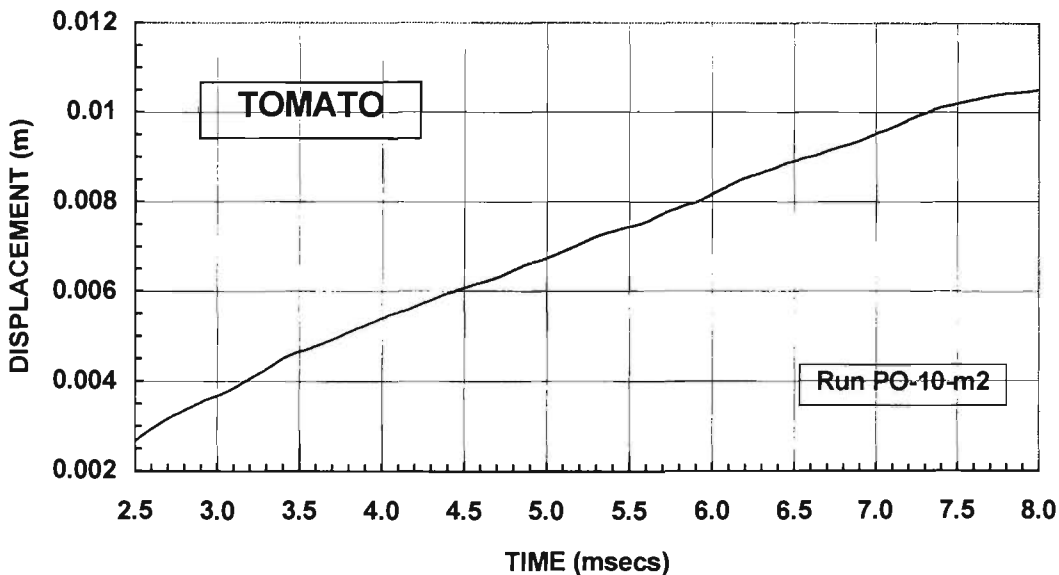


Figure 3.40 Displacement time-history of tomato under impact (Run PO-10-m2) showing very similar displacement characteristics to Run PO-10-m1 under the same test conditions. The difference of travel distance of the strike weight of about 2 mm at comparable time history in Figure 3.39 is due to the slight difference in the triggering time of the laser sensor between the two runs. This difference does not affect the accuracy of the actual displacement histories of the specimens.

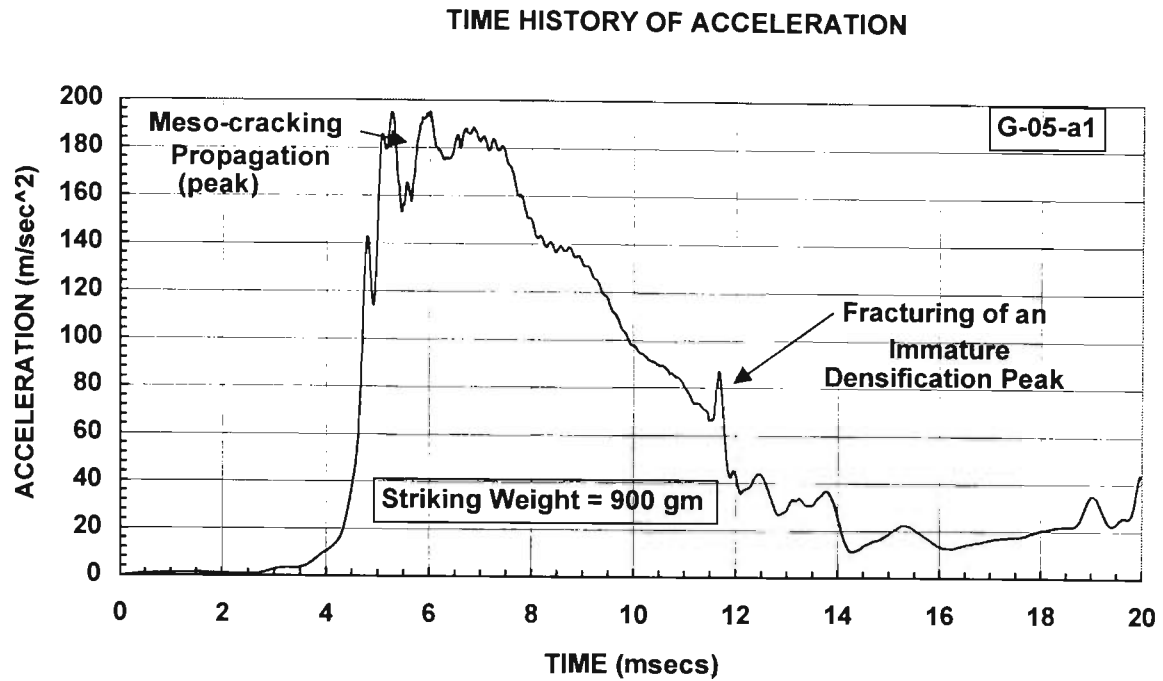


Figure 3.41 Acceleration time history of market-fresh Granny Smith apple specimen using laser-based tester under a strain rate of 93/ second. (Run G-05-a1) (5 cm drops).

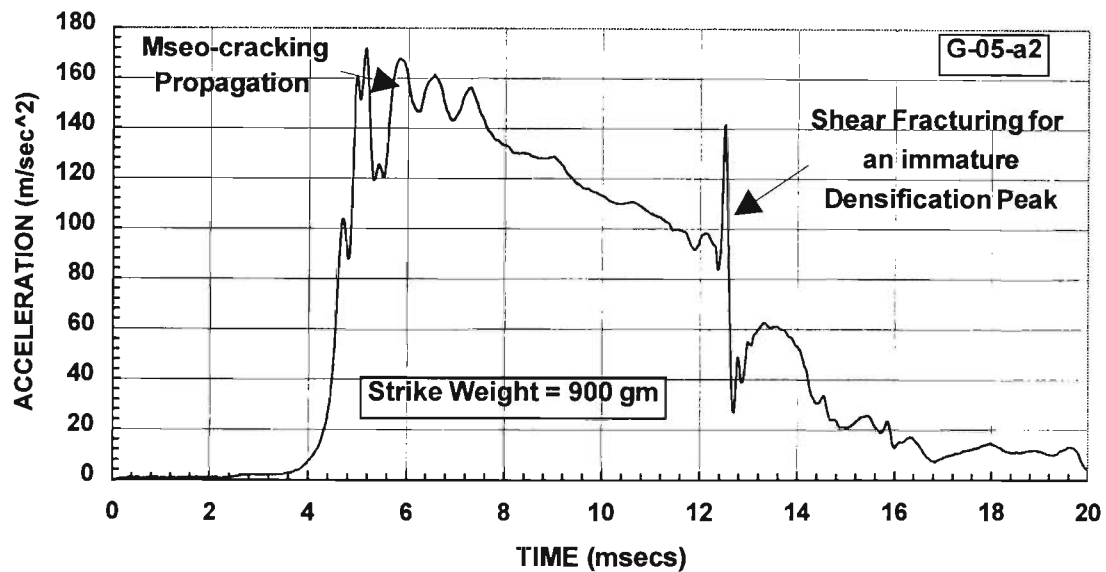


Figure 3.42 Acceleration time history of market-fresh Granny Smith apple specimen under a strain rate of 108/ sec. (Run G-05-a2) (5 cm drop).

Figure 3.42 shows similar pre-peak and peak dynamic responses and instability characteristics to Run G-05-a1 under similar test conditions. Their post-peak dynamic softening characteristics are due to propagating macro-scale cracks and can change unpredictably.

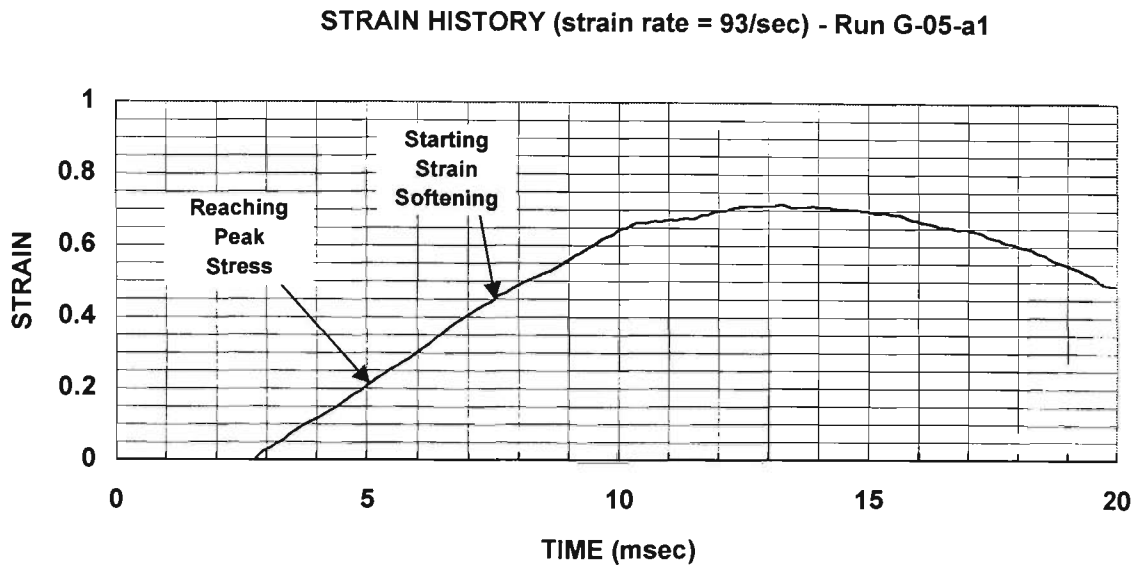


Figure 3.43 Strain time-history of market-fresh Granny Smith apple specimen using laser-based tester under a strain rate of 93/ second. (Run G-05-a1) (5 cm drop).

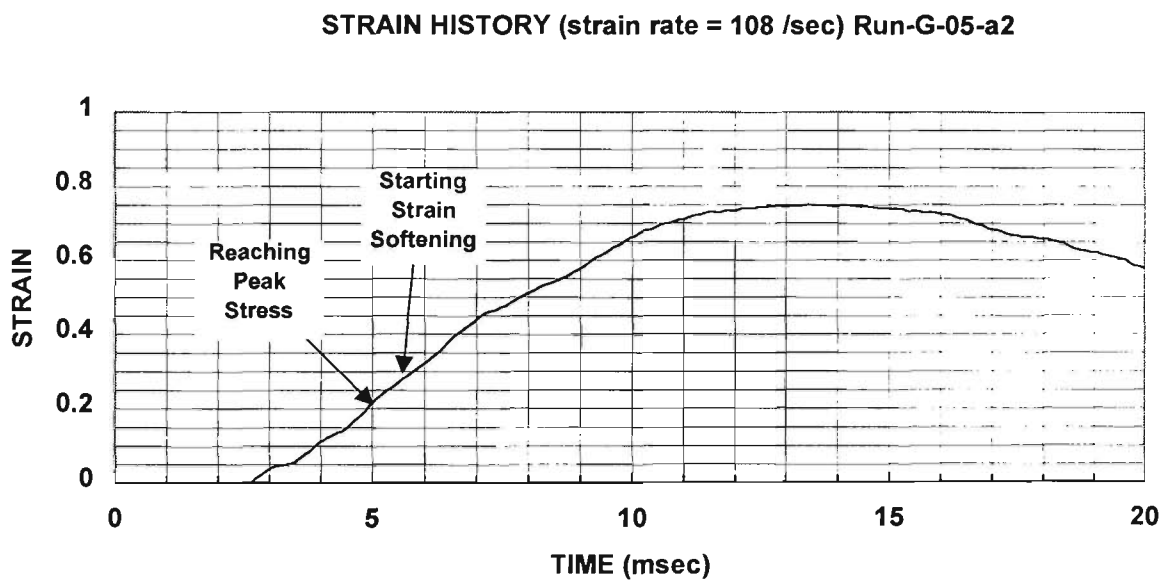


Figure 3.44 Strain time-history of market-fresh Granny Smith apple specimen under a strain rate of 108/ sec. (Run G-05-a2) (5 cm drop).

It is clear that, although both runs had few pre-peak cracking activities, see Figures 3.41 and 3.42, their marked difference in pre-peak strain rates of 93/sec. and 108/sec. for Runs G-05-a1 and G-05-a2, respectively, have a profound effect on their peak and post-peak characteristics. The results suggest that higher strain rates limit the meso-scale peak activities, Figures 3.43 and 3.44.

### 3.4.3 Moderately-Crisp Horticultural Materials

From last section, it was noted that the dynamic characteristics of soft produce were governed by classic plastic/viscoplastic theories. As such, their behaviours are predictable and virtually free of instabilities. The only exception seems to be shear banding which occurs only as an extreme form of plastic deformation. At the other extreme, crisp produce is normally associated with the occurrence of instabilities either in the pre-peak or post-peak domain, due to the crisp nature of their textures. Produce that exhibits both attributes may be categorized as moderately-crisp materials. They may show strongly rate-dependent behaviours, denoting viscoplastic characteristics. Examples include pawpaw. They may exhibit instabilities under various scales, ranging from micro-scale pre-peak cracks to global-scale fractures that may occur in the pre-peak or the post-peak domain. Experiments were conducted on papaya and eggplant. It is remarkable that some fruits and vegetables are virtually free of dependence on strain rates, a distinctive indicator of plastic work-hardening, see Figure 3.45 for the results of tests of papaya and Figure 3.46 for the case of eggplant. They exhibit uploading curves that closely resemble each other. The dynamic deformation of produce in this category was predominantly plastic in nature, with the occurrence of instabilities most likely attributed to shear banding, an extreme form of plastic deformation, but also attributed to pre-peak fibrillar slippage.

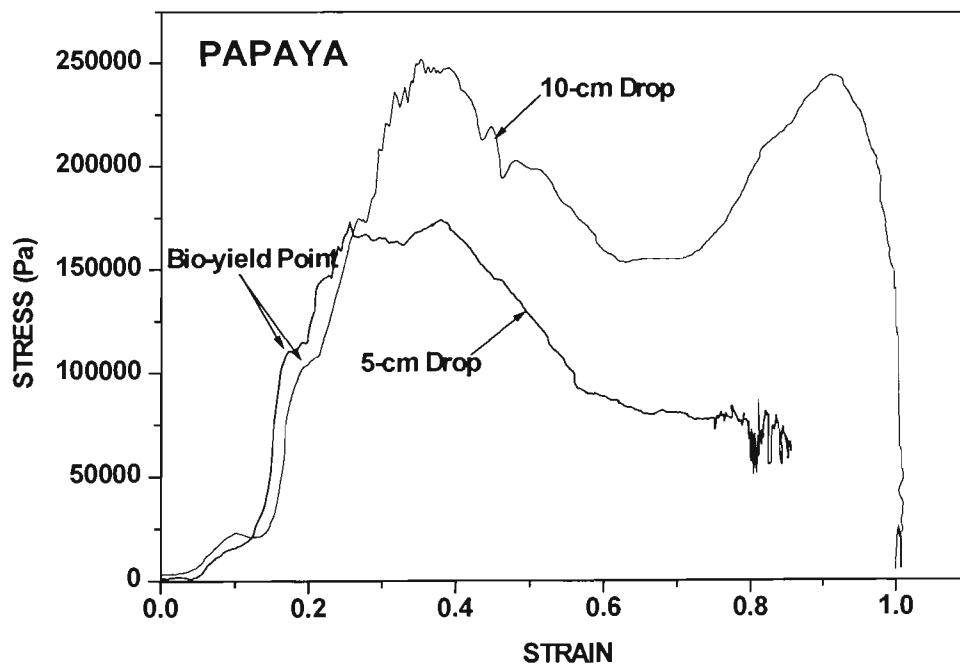


Figure 3.45 Dynamic stress-strain responses of papaya under strain rates of 88/sec. (5-cm drop) and 127/sec. (10-cm drop) and a strike weight of 0.9 kg. Curves show close resemblance of rate-independent plastic deformation as well as instability characteristics.

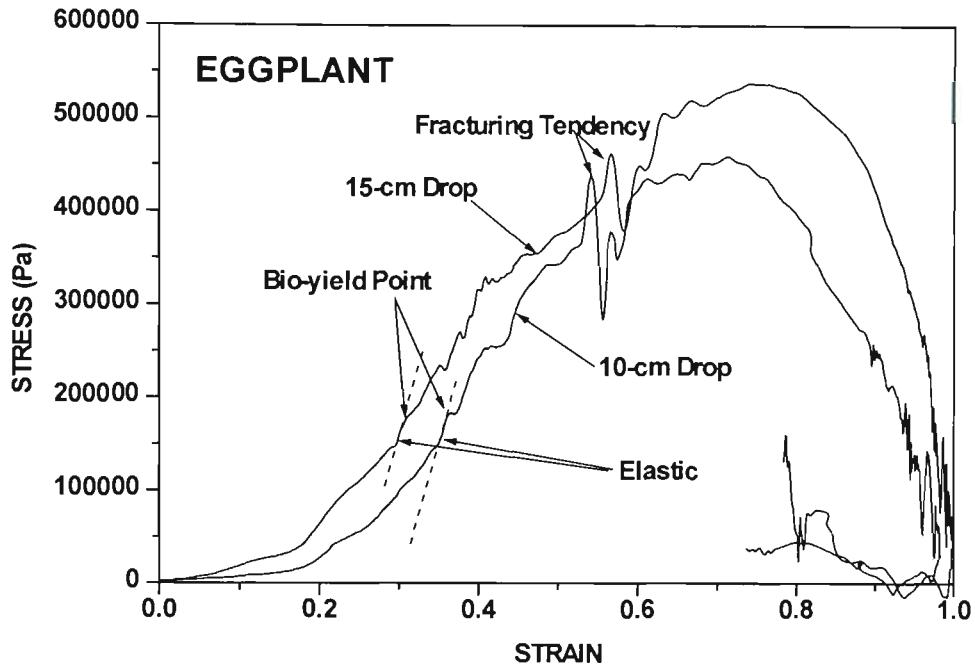


Figure 3.46 Dynamic stress-strain responses of eggplant under strain rates of 142/sec. (10-cm drop) (Run EG-10-m1) and 147/sec. (15-cm drop) (Run EG-15-m1) under a strike weight of 0.9 kg. Curves show close resemblance of rate-independent plastic deformation as well as instability characteristics.

Under plastic work-hardening, dynamic stress-strain curves of produce like papaya and eggplant do not only include their plastic deformation characteristics, but also their dynamic instabilities as well. For papaya, the resemblance in instability characteristics can be seen in Figure 3.45. With pre-peak cracking activities, it first appears at the bio-yield points, and results in instant degradations of their effective moduli. Referring to the 5-cm drop curve in Figure 3.45, redrawn as Figure 3.47, the degradation of the effective modulus can be seen to have occurred in several stages, with each degradation occurring immediately after each event of slippage. Papaya normally deforms plastically under loading. Under high loading, they fail either under perfectly-plastic deformation, as shown in Figure 3.47, or by cracking instabilities, as shown in the 10-cm drop curve in Figure 3.45.

The resemblance in dynamic instability activities can also be seen in Figure 3.46 in the fracturing tendencies for the case of eggplant, under the same testing conditions except different drop heights. From Figure 3.46, it can be seen that, at different drop heights of 10 cm and 15 cm, pre-peak instabilities in the form of cracking tendency occur at the same and unique stress of about 450 kPa and strain of about 55%. The criteria and characteristics of material instabilities in produce and their relationship with the overall deformation will be discussed in detail in Section 3.7.

STRESS VS. STRAIN (Papaya) (5 cm drop)

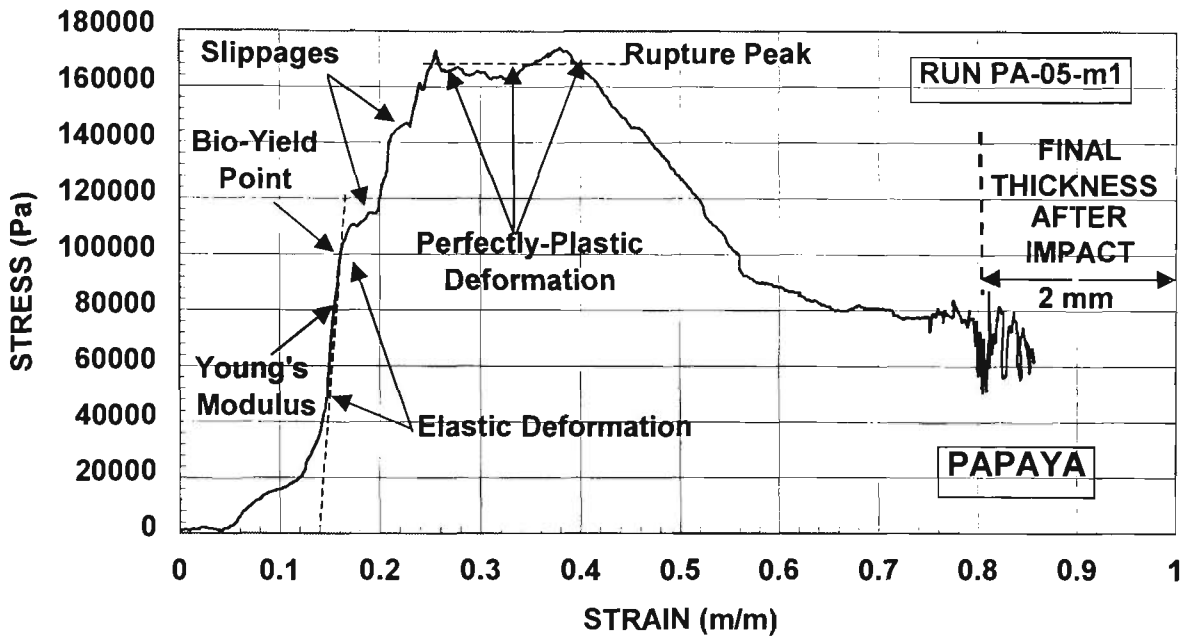


Figure 3.47 Dynamic stress-strain characteristics of the deformation of market-fresh cylindrical papaya specimen under a strain rate of 88 /second showing distinct pre-peak material instabilities during plastic deformation (Run PA-05-m1) Strike weight is 0.9 kg.

Other produce such as pawpaw exhibits some unique characteristics, with both attributes of plastic/viscoplastic deformation and instabilities as shown in Figure 3.48.

STRESS VS. STRAIN (Pawpaw) (Various Drop Heights) (Strike Weight = 0.9 kg)

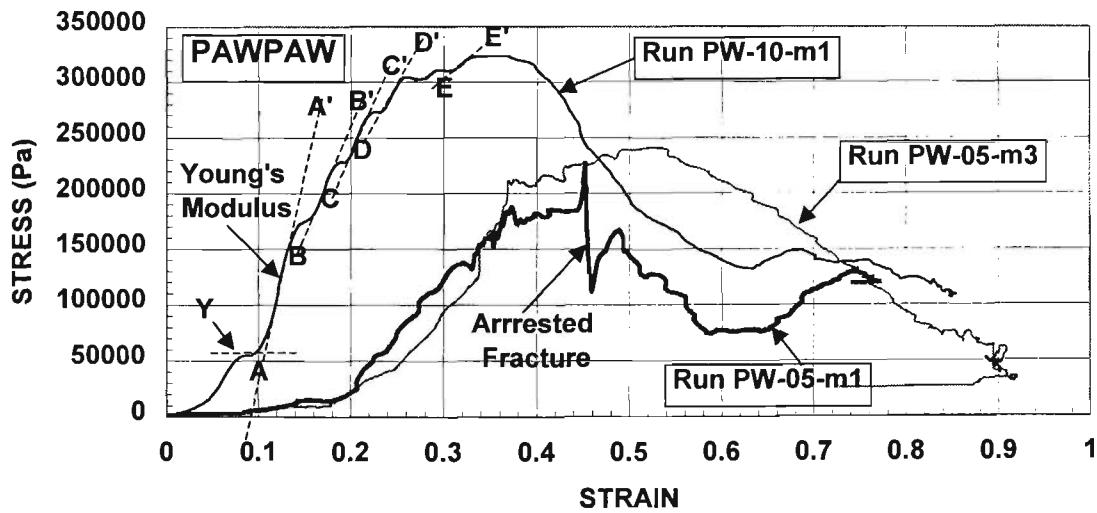


Figure 3.48 Dynamic stress-strain response of pawpaw under drop heights of 5-cm (Runs PW-05-m1 and PW-05-m3) and 10-cm (Run PW-10-m1), showing viscoplastic deformation, pre-peak cracking and fracturing characteristics.

The occurrence of material instabilities in some produce, particularly those with crisper textures under high loading, seems to be related to the relatively stronger cell-wall structures, due to the layered fibrillar orientation of the cell-wall fibres, Waldron (1996). It also seems to be attributed to cell-wall structures that are less homogeneous, due to the sharp contrast of material strength between the fibrils and their surrounding material matrix. This crisp textural behaviour applies to pawpaw, with distinct features of gradual degradation of its effective modulus as illustrated by the changing slopes of A'A, denoting the Young's modulus, to E'E in Figure 3.48 for Run PW-10-m1 with 10-cm drop.  $\dot{\epsilon}$  is 113/sec for Run PW-10-m1. On the other hand, strong evidence of rate-dependent viscoplastic deformation can be seen from the different loading paths taken by the 5-cm and 10-cm drops. For the 5-cm drops, substantial pre-peak cracking activities, as can be seen from the unloading curve for Run PW-05-m1 at a strain rate of  $\dot{\epsilon} = 73/\text{sec}$ , may lead to macro-scale fracturing and can be seen in Figure 3.48, but the fracture was arrested. Also, the curve for Run PW-05-m3 shows how the dynamic response without macro-scale cracking under a 5-cm drop may appear.

We consider another example of dynamic response with potato cylindrical specimens, as shown in Figure 3.49, based on a series of tests with drop heights of 10 cm and 20 cm. The figure exhibits the occurrence of pre-peak cracking, as evident from the 10-cm drop test. On the other hand, the appearance of plastic shear banding appears in the 20-cm drop test.

From the 10-cm drop curve, pre-peak cracks are seen to have initiated, altering the material modulus from CC' (Young's) to DD' (effective), under a strain rate of 125/second. A distinctive S-shape curve denoting abnormal stretching ability during the initial stage of strain can be observed. Under a higher strain rate of 165/sec., the potato texture was stretched to its elastic limit, that is, the Young's modulus, as shown by the 20-cm response curve that is parallel to CC'. Evidence of shear banding activities is shown by the Young's modulus between 400 kPa and 640 kPa. The 20-cm drop curve provides evidence of elastic deformation with shear banding activities of instability up to material failure. The 10-cm drop curve shows plastic deformation with strong evidence of pre-peak cracking.

Evidently, the dynamic response curves as shown by the 10-cm and 20-cm drop curves for potato indicate two major processes that are responsible for the loading of each of these two potato specimens: instabilities due to damage as well as plastic/viscoplastic deformation. The only comparable dynamic response is the failure stress, of which both occurring at around 650 kPa. The possible appearance of both of these processes characterizes the moderately-crisp produce textures.

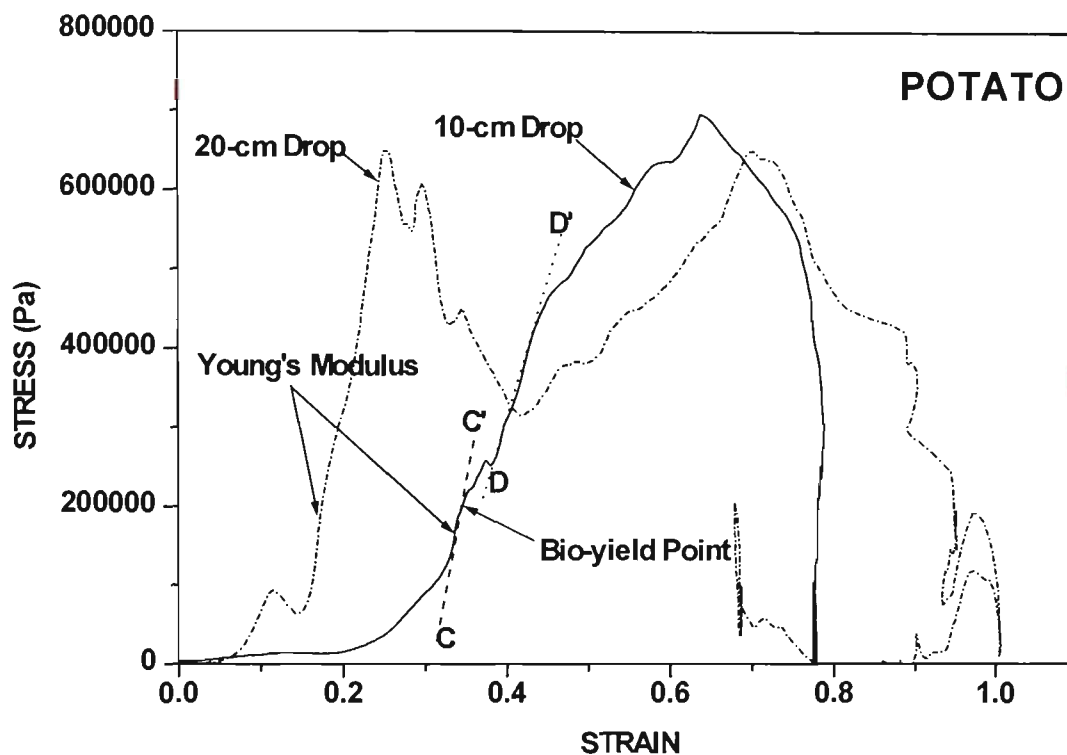


Figure 3.49 Dynamic stress-strain responses of potato under strain rates of 125/sec. (10-cm drop) and 165/sec. (20-cm drop) with a strike weight of 0.9 kg. (Run PT-20-m1)

#### 3.4.4 Crisp Horticultural Materials

A number of about 70 series of drop tests were performed using cylindrical specimens of market-fresh and aged crisp produce that includes Golden Delicious apple, Granny Smith apple and nashi, under different drop heights.

The aim of these series of tests, with each series comprises an averaged of five tests, is:

- (i) to investigate the strain-rate dependence of crisp produce,
- (ii) to investigate the pre-peak cracking process and peak transition,
- (iii) to investigate dynamic responses due to aging, and
- (iv) to investigate the effect of protection due to the presence of naturally attached skin.

Selected examples from these series of tests are presented here to illustrate these factors.

## 3.4.4.1 Strain-Rate Dependency

In most cases, produce materials can be characterized as strain-rate independent if the materials undergo either elastic deformation or plastic deformation with work hardening. The possibility of pre-peak cracking can co-exist, but this would not alter the rate independence of the materials. The distinctive characteristics of rate independence in horticultural materials is the similarity of uploading stress-strain response curves showing comparable dynamic properties, as shown in Figure 3.50.

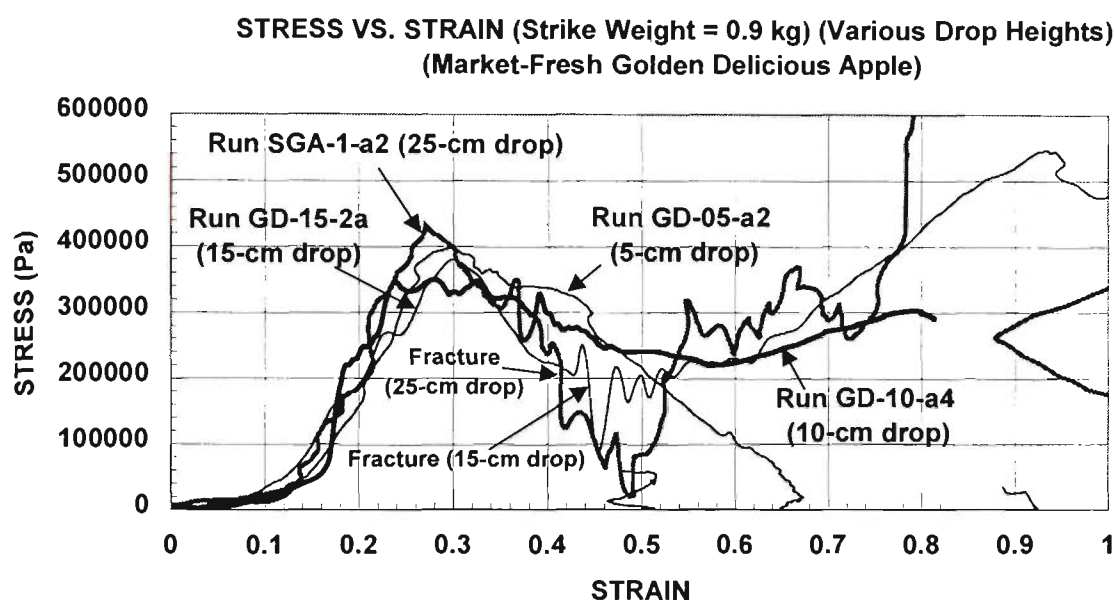


Figure 3.50 Dynamic stress-strain responses of market-fresh Golden Delicious apple under various drop heights under a strike weight of 0.9 kg.

The curves include results from Run GD-05-a2, with 5-cm drop and a strain rate,  $\dot{\epsilon}$  of 94/sec., Run GD-10-a4, with 10-cm drop and  $\dot{\epsilon}$  of 133/sec., Run GD-15-2a, with 15-cm drop and  $\dot{\epsilon}$  of 150/sec., and Run SGA-1a-2, with 25-cm drop and  $\dot{\epsilon}$  of 156/sec. Strong evidence of pre-peak instabilities can be seen by the presence of the rough uploading curves. Upon reaching peak strength of about 350 kPa to 400 kPa, the Golden Delicious specimens failed either with a transitional peak plateau for lower drop heights (with lower strain rates) or with abrupt change in strength, such as the 25-cm drop case. The post-peak activities show marked difference between cases with high and low drop heights. Those cases with low drop heights, such as 5-cm and 10-cm, show a well-developed process of post-peak strain softening, whereas those with higher drop heights, such as 15-cm and 25-cm, tend to fracture.

## 3.4.4.2 Pre-Peak Cracking and Peak Transition

As has been pointed out in Section 2.2.4.2, strain softening is the direct result of pre-peak cracking, leading to ‘prolonged’ transitional failure. The transition begins with the formation of pre-peak micro-cracks, progressing to meso-scale crack joining and strain softening and finally to macro-fractures. These instabilities are due to damage in the materials and are thus unpredictable. For instance, pre-peak cracks may or may not occur when the cylindrical horticultural specimens such as market-fresh Golden Delicious apple are under high loading, as shown in Figure 3.51. From the figure, Run GD-10-a4 with a 10-cm drop height shows pre-peak instability, whereas Run GD-10-a5, also with a 10-cm drop height, shows no pre-peak instability.

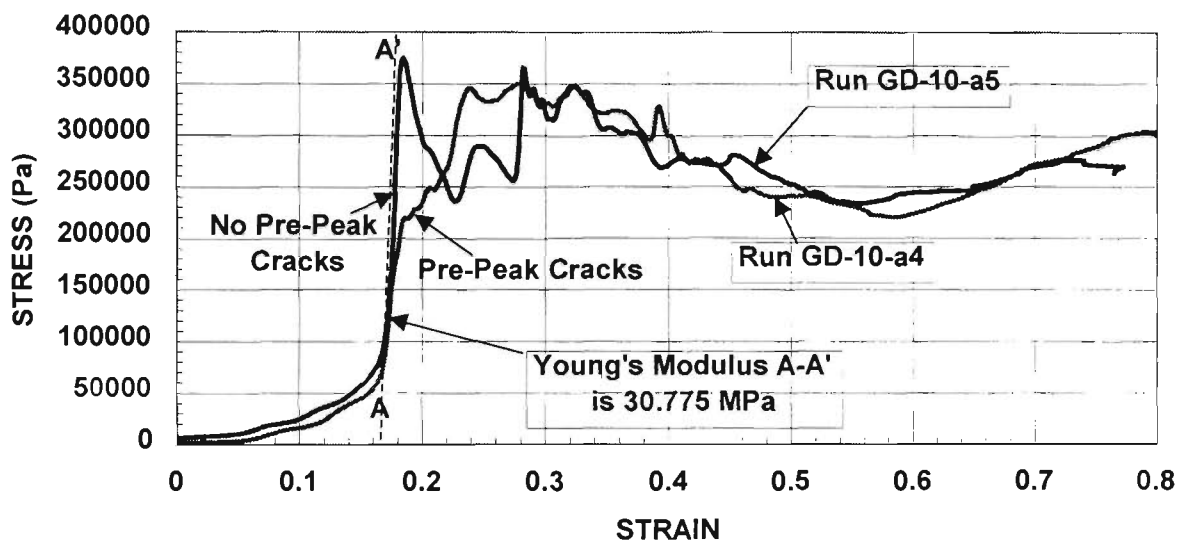


Figure 3.51 Dynamic stress-strain relationships of cylindrical Golden Delicious apple specimens from same batch, with both under the same strain rate of 133/second and a strike weight of 0.9 kg.

Plastic deformation instabilities like shear banding are those illustrated in Figures 3.45 and 3.46 with ‘predictable’ characteristics. Any other instability that originated from damage such as fibrillar slippage and matrix cracking of the produce cell walls, as pointed out in Section 2.2.4.2, cannot be predicted with currently available technology. Nevertheless, regardless of whether or not the materials suffer any pre-peak damage, there is always a strong indication of similar post-peak softening processes, as shown by the comparable softening characteristics in Figure 3.51. It seems that once the damage process passes the peak transitional stage, or the ultimate strength of materials, the cracking characteristics tend to undergo a similar progressive damaging process during the meso-cracking stage.

An interesting loading phenomenon commonly encountered during laser-based testing are the serrated, or staircase-like, instabilities. One of the examples presented in Figure 3.52 is from Run SGN-1a-1 with a drop height of 25 cm, obtained from a series of tests with nashi specimens. The most distinctive feature of the serrated instabilities is the horizontal slippage on the dynamic curve, depicting bursts of plastic flows (or jumps) at A, B, C and D in an otherwise rate-independent work-hardening deformation. The Rayleigh line denotes that the nashi texture, under such a high strain rate, lost its textural integrity and began viscous flow. This is a mixed process of heat diffusion and plastic jumps.

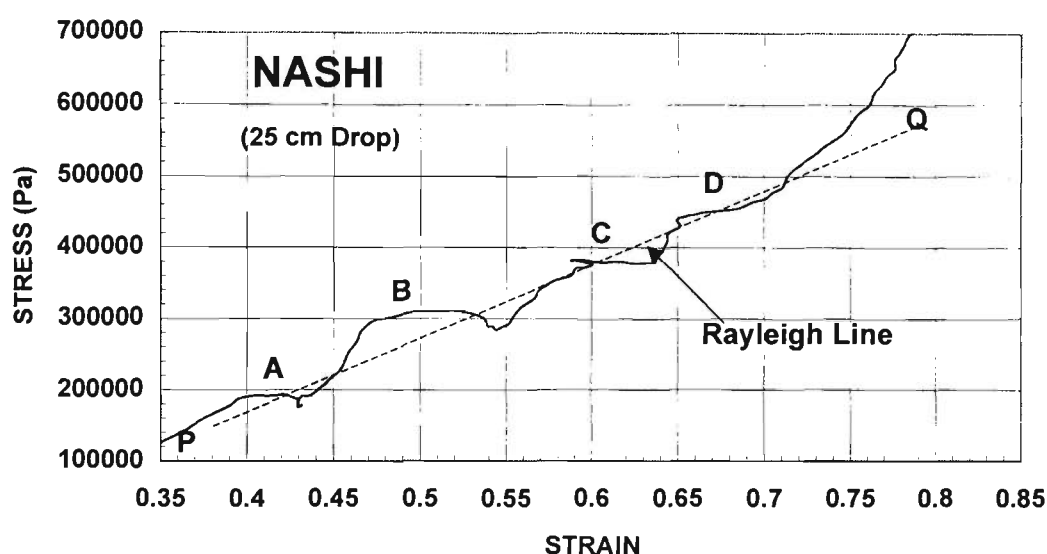


Figure 3.52 Dynamic stress-strain relationships of cylindrical nashi specimen under an extremely high strain rate of 550/second and a strike weight of 0.9 kg. (Run SGN-1a-1)

#### 3.4.4.3 Dynamic Response of Aged and Market-fresh Crisp Produce

Dynamic response to drop tests with market-fresh and aged Golden Delicious apple specimens is shown in Figure 3.53. Response curves with fresh specimens have been shown before in Figure 3.50, including Run GD-05-a2 with drop heights of 5-cm and  $\dot{\epsilon}$  of 94/sec., and Run GD-10-a4 with 10-cm and  $\dot{\epsilon}$  of 133/sec. Those with aged specimens include Run OD-05-a2 with drop heights of 5-cm and  $\dot{\epsilon}$  110/sec. and Run OD-10-a1 with 10-cm and  $\dot{\epsilon}$  111/sec., tested after a 7.5-month storage period at 4°C and 100%RH.

It is clear from Figure 3.53 that the aged specimens show a consistent but markedly decreased level in ultimate strength, of about 200kPa, when compared to that of the market-fresh apples which reach to about 350 to 400 kPa. We will come back to this comparison again in Chapter 5 to investigate whether the damage process remains the same for apples when they are aged for

several months. In Figure 3.53, a sign of softening in the structure of the aged apple tested at drop heights of 10 cm becomes evident in the ability of the specimen to reach 17% strain before failure compared to 25% strain for comparable fresh specimens. If the strain rates in both cases are compared, as in Figure 3.54, there is a strong indication that a critical strain rate for fresh Golden Delicious specimens exists. For a particular drop height, if the critical strain rate is exceeded, the material fails. In this study, all the six strain rates were selected from the test results presented in Figures 3.50 and 3.53.

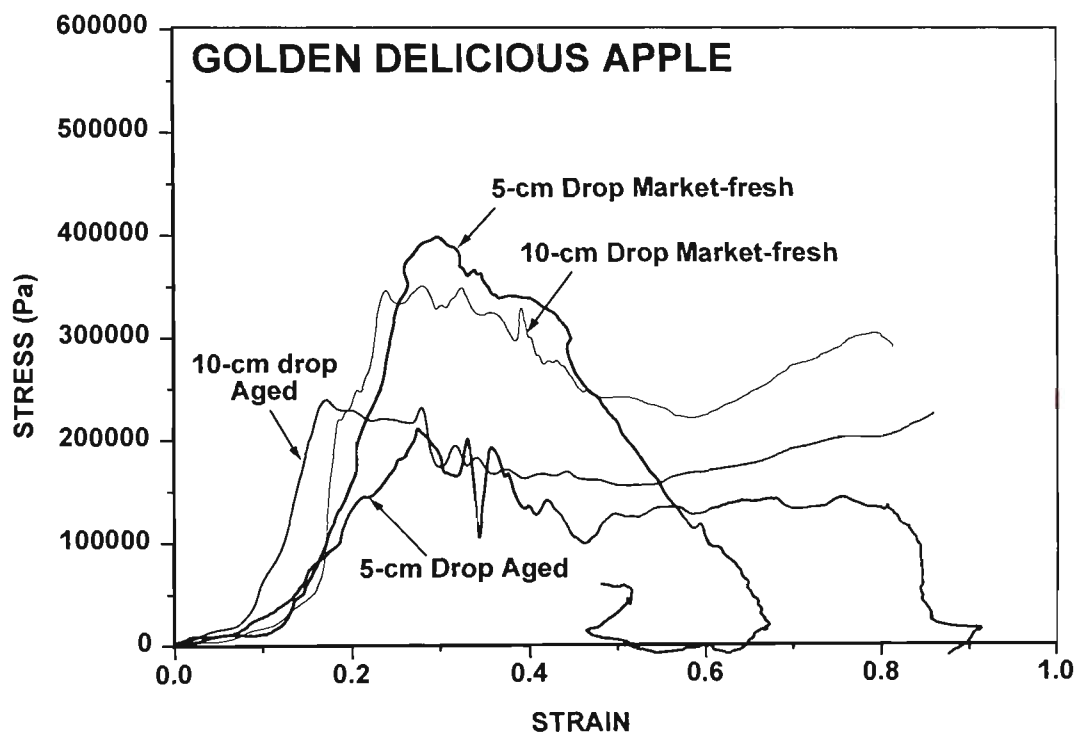


Figure 3.53 Dynamic stress-strain responses of Golden Delicious apple under drop heights of 5-cm and 10-cm drop tests, with both market-fresh and aged specimens.

The strain rate curve shown for the aged specimens was obtained for two drop heights only, due to a lack of aged specimens, as each drop height level would require five cylindrical specimens. A high percentage of the aged apples suffered serious water loss after 7.5 months of aging and could not be used for testing, see Figure 3.55. There is uncertainty as to the accuracy of the estimated section of the strain rate curve for the aged specimen in Figure 3.54. However, there is a high possibility that the estimated strain rate would go up as drop height increases, if this is compared to a similar plot with the Granny Smith apples shown in Figure 3.56.

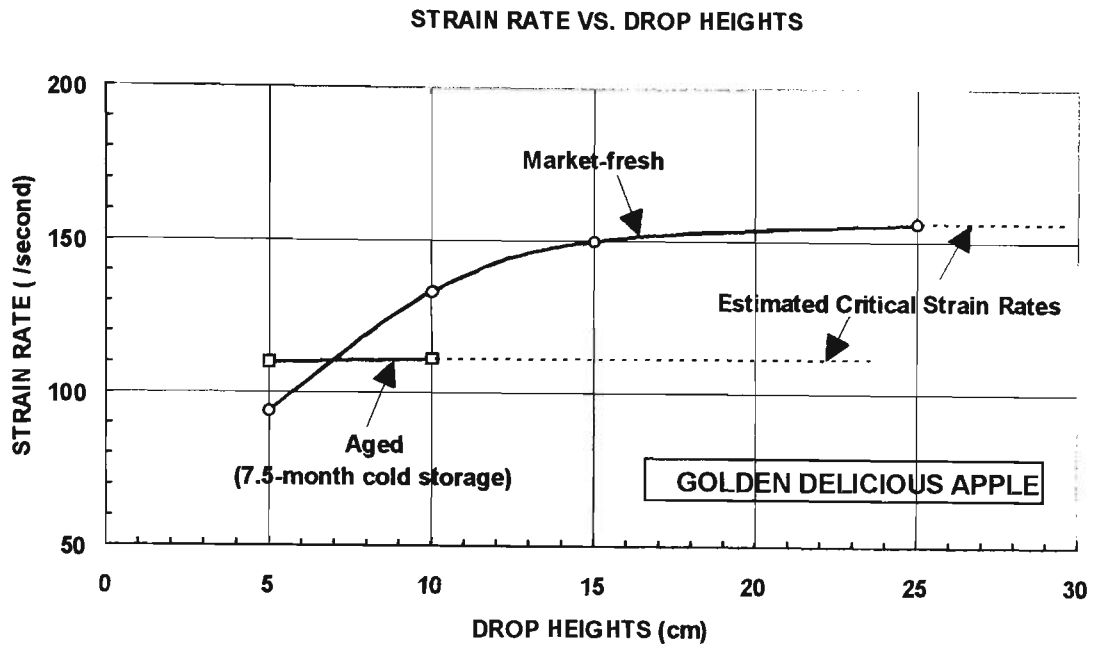


Figure 3.54 Estimated critical strain rates for market-fresh and aged Golden Delicious apple specimens showing possible existence of a critical strain rate.



Figure 3.55 Aged Golden Delicious apple that suffered severe water loss after 7.5 months storage (left) and market-fresh apple (right).

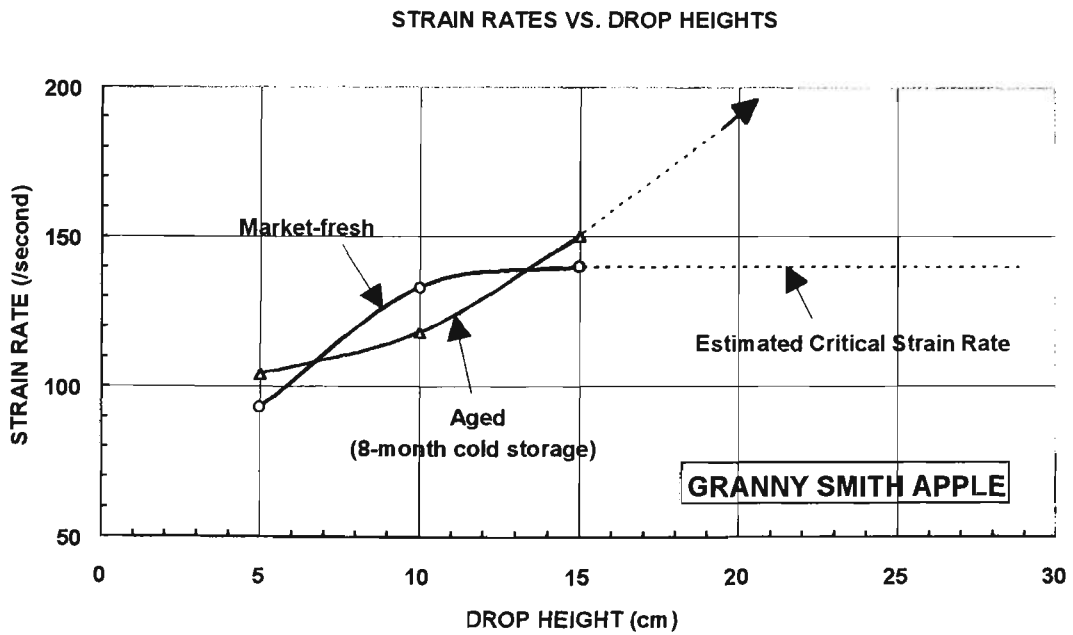


Figure 3.56 Strain rates of market-fresh and 8-month aged Granny Smith apple specimens.

Figure 3.56 shows the possible existence of a critical strain rate for Granny Smith apple specimens, as well as a clear indication of an increasing trend in strain rates for aged specimens as the drop heights increase, along with viscous flow tendencies under high strain rates. The results are from a series of laser-based drop tests with fresh and aged Granny Smith apple specimens, performed similarly to those with fresh and aged Golden Delicious apple specimens shown in Figure 3.54. The storage conditions for both the Granny Smith and Golden Delicious apples were the same.

The dynamic responses of fresh and aged nashi under various drop heights are presented in Figures 3.57 and 3.58, respectively. The aged specimens were prepared from nashi after a 6-month cold storage period at 5°C and 100% RH. The strain rates for the fresh sample tests are 90/sec. with 5 cm drop height (Run N-05-X-2a), 109/sec. with 10 cm drop height (Run N-10-X-1a) and 550/sec. with 25 cm drop height (SGN-1a-1). The strain rates for the aged sample tests are 83/sec. with 5 cm drop height (Run ON-05-b1) and 107/sec. with 10 cm drop height (Run N-10-X-1a). Failure stress is registered at about 200 kPa for fresh samples but only 140 kPa for the aged ones. There is little difference in the loading section of the dynamic curves in the aged nashi specimens, denoting strong rate-independent characteristics. In the case of fresh nashi specimens, the deviation between the 5 cm and 10 cm loading curves were caused by cracking instabilities under plastic deformation rather than rate-dependent deformation. This is evident as shown by the perfectly-plastic deformation for both the 5 cm and 10 cm cases as shown in Figure 3.57, as well as in Figure 3.59.

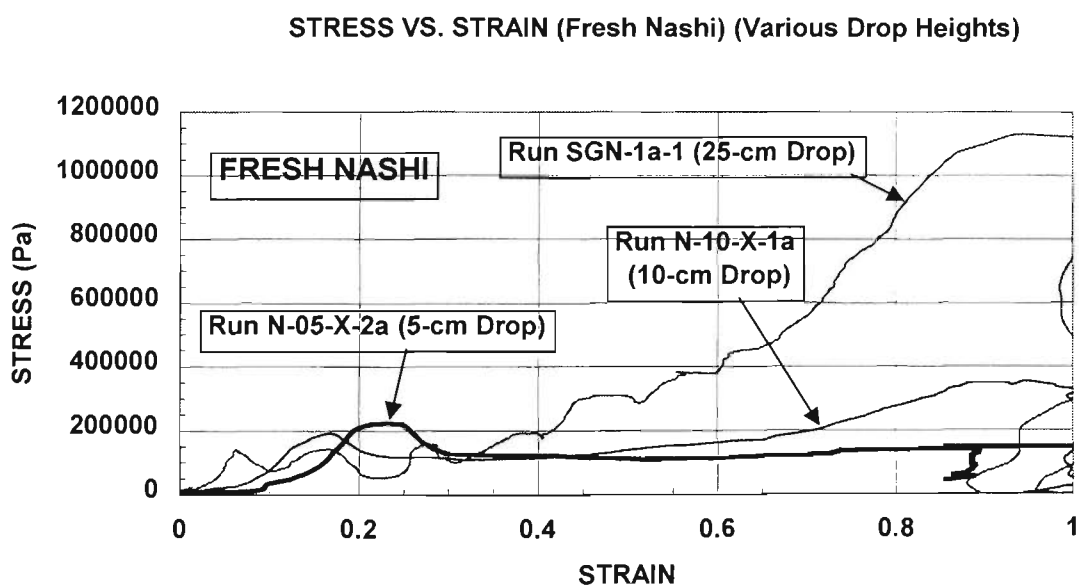


Figure 3.57 Dynamic stress-strain curves of market-fresh nashi specimens under drop heights of 5-cm, 10-cm and 25-cm, with a strike weight of 0.9 kg. The dynamic curve for Run SGN-1a-1 has been plotted as Figure 3.52.

Curves in Figure 3.58 also show strong perfectly-plastic tendency. Figure 3.59 shows that nashi specimens, like apple, tend to fail with cracking under drop heights of 5 cm or 10 cm, as evident from the cracks shown in the two upper right-hand corner specimens. However, unlike apple specimens, which tend to undergo softening beyond the failure stress, nashi tends to deform with liquid-like perfectly-plastic characteristics, as shown by the horizontal dynamic curves in Figure 3.57. The more interesting characteristics appear to be the presence of staircase-like features in the dynamic curve under an extremely high strain rate of 550/sec., as shown in Figure 3.52 (replotted in Figure 3.57).

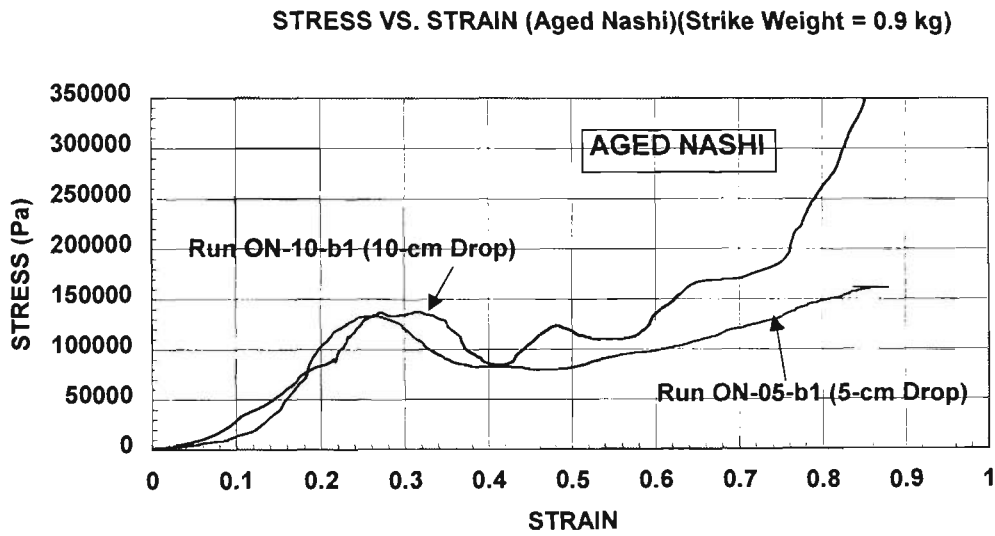


Figure 3.58 Dynamic stress-strain curves of aged nashi specimens under drop heights of 5-cm and 10-cm, with a strike weight of 0.9 kg.

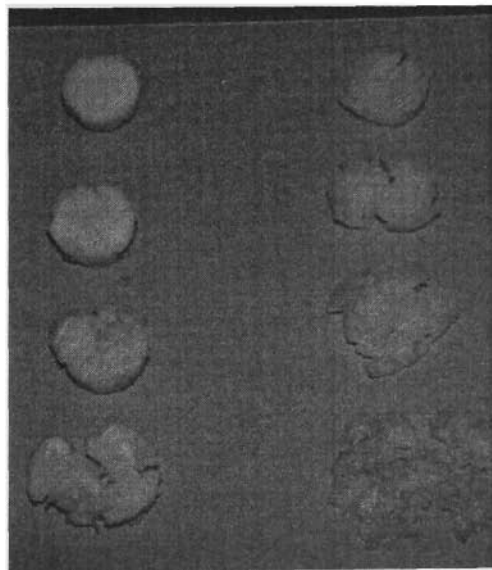


Figure 3.59 Market-fresh Golden Delicious apple (left) and nashi (right) specimens after impact by a 0.9 kg strike weight under drop heights (from top to bottom) of 5 cm, 10 cm, 15 cm and 20 cm.

Here, four observations stand out:

- (i) Under higher strain rates or drop heights of 15 cm and 20 cm, unlike apple, nashi tends to completely lose its structural integrity and become liquid-like, see Figure 3.59.
- (ii) Under high strain rates of deformation, the Rayleigh line appears, see Figures 3.52 (replotted in Figure 3.57). However, the Rayleigh line in this case is disrupted by the presence of the serrated features, showing a combination process of (or competition between) heat diffusion and plastic slippage instabilities (jumps).
- (iii) The liquid-like perfectly-plastic state of deformation is the ‘prerequisite’ condition for the occurrence of the Rayleigh line in produce materials, as shown in Figure 3.52.
- (iv) Pre-peak micro-cracking for both fresh and aged nashi tends to be less intense compared to apples, as shown in Figures 5.52 (replotted in Figure 3.57) and 5.58. These figures also indicate strong post-peak tendency to perfectly-plastic deformation. This suggests that debonding could be the dominant activity between cells, as a direct result of the loss of cohesion in the pectin gel of the middle lamella, Jarvis (1984). The debonding activities can be seen in Figure 3.60. In the case of aged apples, the pectin gel is replaced by more esterified forms (or fenestrated) with weaker cohesion, Jarvis (1984). Unlike pears, the middle lamella of apples, though transformed (or deteriorated), still exists structurally when aged. This can be seen in Figure 3.61.

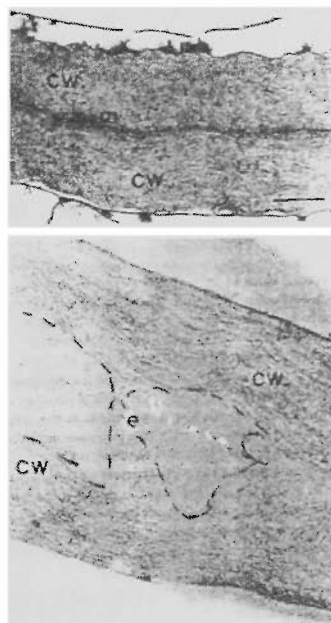


Figure 3.60 Structure of cell walls of adjacent cells in pears, showing (top) cell walls of fresh and crisp pear with tightly-packed micro-fibrils in the cell walls (cw) and a distinctive middle lamella (m); (bottom) cell walls in aged pear showing loss of integrity, disoriented fibrils, the complete disappearance of the middle lamella and the formation of voids (e). (X 20,000)

From Ben-Arie *et al.* (1979).



Figure 3.61 Scanning electron micrographs showing cell wall structures of Golden Delicious apple: (top) Aged apple with deteriorating middle lamella which appears fenestrated. Cell walls (with dark-color micro-fibril bands) are at the top and bottom left of the middle lamella. Light-color region at the very top is cell-sap; (bottom) Fresh apple with middle lamella with no fenestration. Micro-fibril orientation (lighter color bands from top centre to right centre) is normal and runs parallel to the cell wall axis. (X 30,000) From Glenn and Poovaiah (1990).

#### 3.4.4.4 Natural Protection by Produce Skin

The protective effect of skins in minimizing bruise damage is illustrated in Figures 3.62 and 3.63. They show dynamic responses of market-fresh Golden Delicious apple specimens with or without skin naturally attached to one side of the specimen. For the cylindrical specimens with skins, which were attached to the bottom surfaces of the specimens, careful selections were made to core out specimens with the flattest skin surface possible. The cylindrical Golden Delicious specimen without skin attached to the impact surface reach failure stress of about 400 kPa as shown in Figure 3.62, under a deformation strain rate of 94/sec. The protective function of apple skin against bruise damage can be seen in Figure 3.63, with similar testing conditions. Here the peak stress of the market-fresh Golden Delicious apple specimen is limited to around 270 kPa, due to the presence of skin. It is clear that, apart from local instabilities, the dynamic response curve as shown in Figure 3.63 does not exceed the expected failure stress of about 350 to 400 kPa for Golden Delicious apple. The specimen remained intact after the impact test without bruising.

In the experiments on market-fresh nashi specimens, Figures 3.64 (5 cm drop) and 3.65 (10 cm drop) demonstrate the protective function of nashi skins. For the nashi specimens without skins the failure stress was always between 200 kPa and 240 kPa. The dynamic stress of nashi with skins was less than 140 kPa. For both apples and nashi, the presence of the skins serves to redistribute the dynamic loading in such a way that the peak load is dissipated.

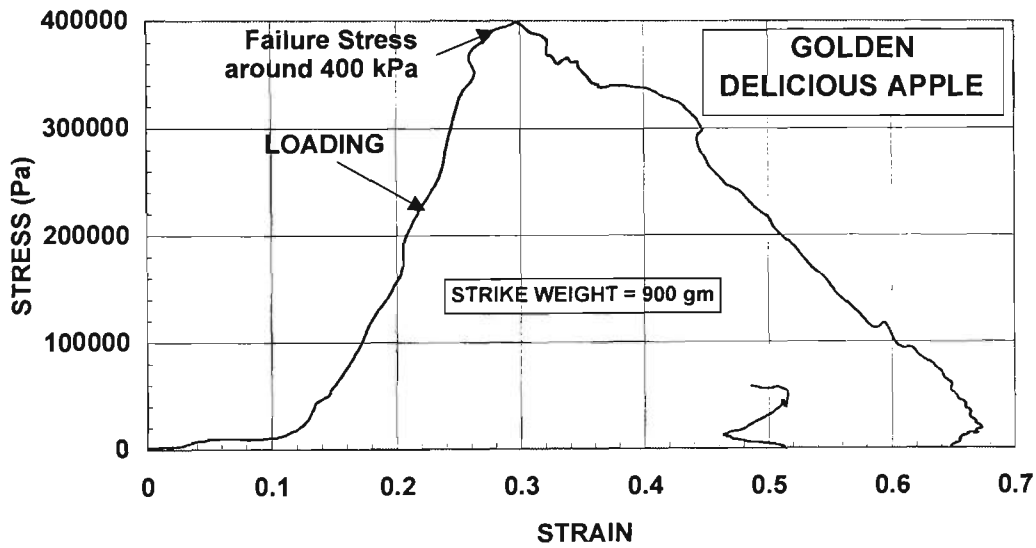


Figure 3.62 Dynamic laser-based stress-strain characteristics of market-fresh Golden Delicious apple specimen under a strain rate of 94/sec at 5 cm drop. (Run GD-05-a2) Specimen is without skin.

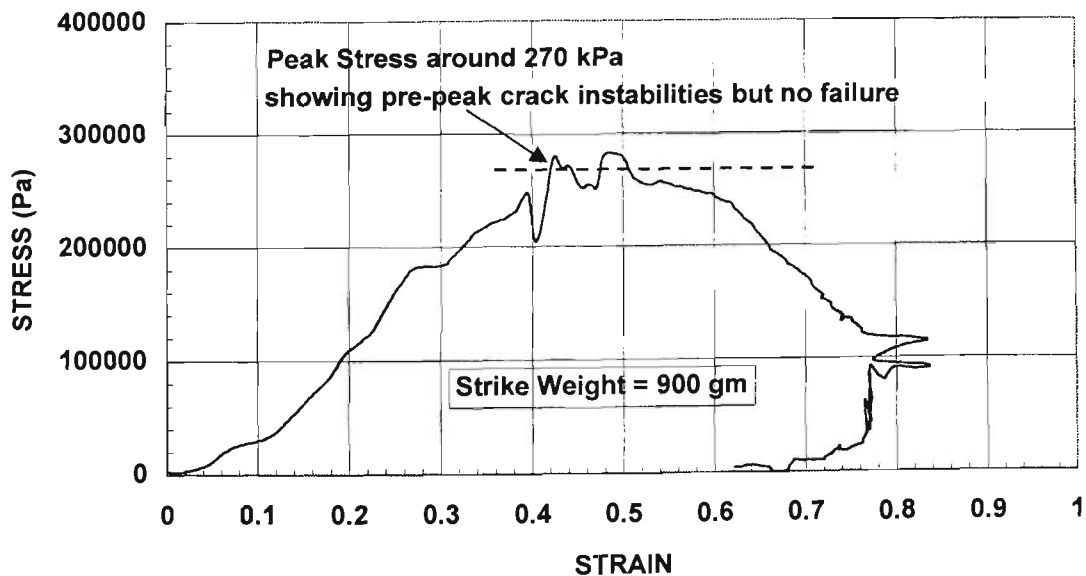


Figure 3.63 Dynamic laser-based stress-strain characteristics of market-fresh Golden Delicious apple specimen with skin naturally attached to impact surface under a strain rate of 97/sec. at 5 cm drop. (Run GS-05-a1)

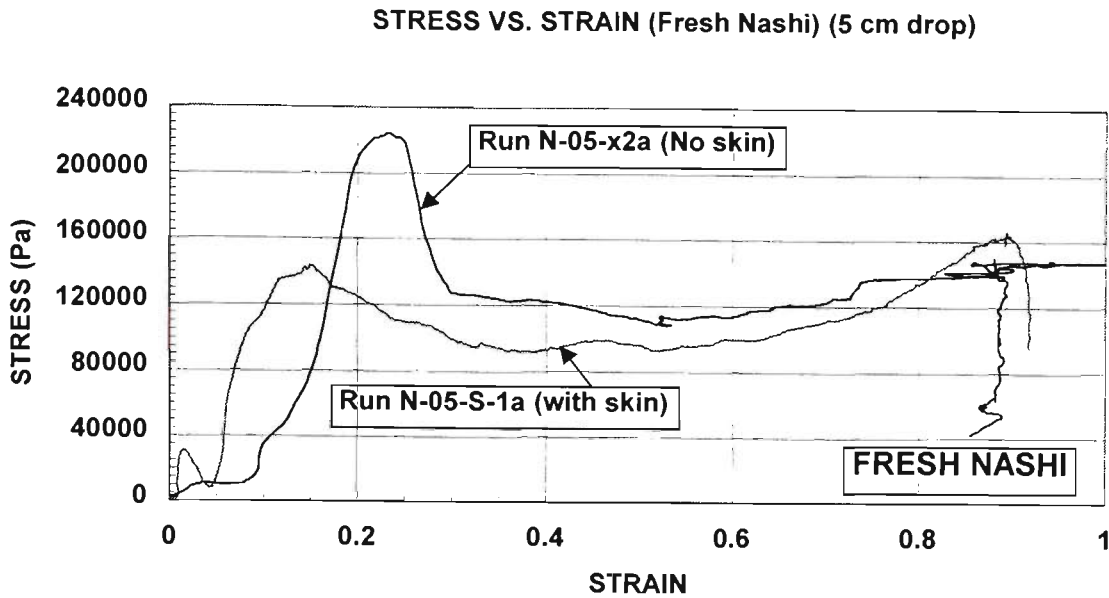


Figure 3.64 Dynamic laser-based stress-strain curves of market-fresh nashi under a 5 cm drop with 0.9 kg strike weight with or without skin naturally attached to one side of the specimen.

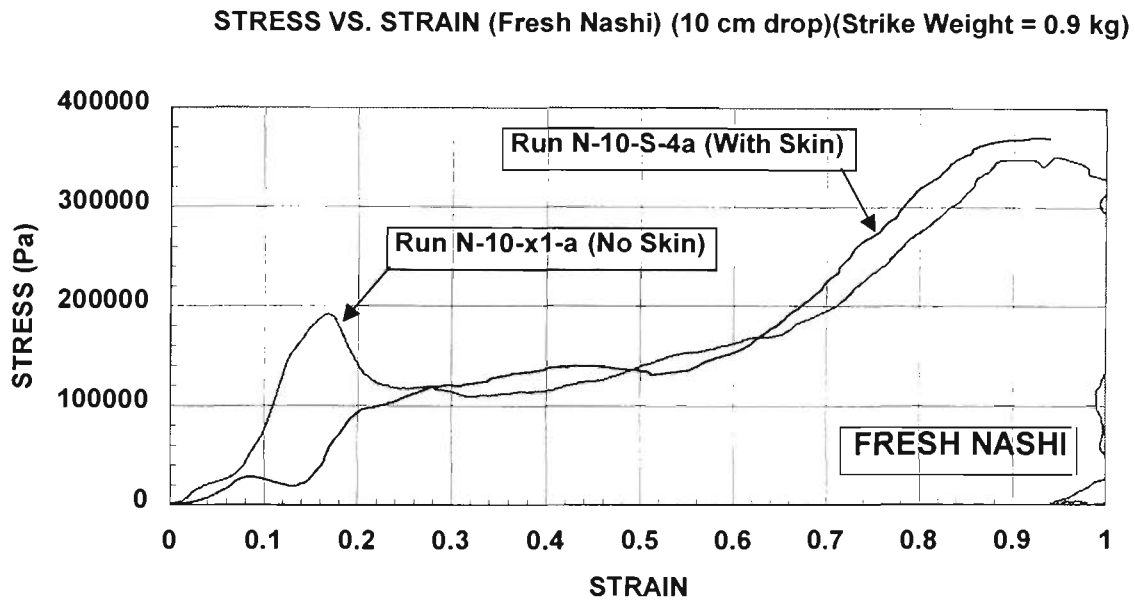


Figure 3.65 Dynamic laser-based stress-strain curves of market-fresh nashi specimens under a 10 cm drop with 0.9 kg strike weight with or without skin naturally attached to one side of the specimen.

### 3.5 DYNAMIC MECHANICAL ANALYSIS

There are two main objectives of performing the dynamic mechanical analysis (DMA) in this study. The first objective is an attempt to determine the rheological state of selected produce specimens. Some of the most representative material states are solid-like, liquid-like and viscoelastic. The second objective is to determine the dynamic Poisson's ratio of produce specimens using DMA-measured material parameters such as the storage and loss Young's modulus as well as the storage and loss shear modulus. In the present study, results based on market-fresh Golden Delicious apple specimens are presented here.

#### 3.5.1 Rheological State

A DMA test (Run F02-AP-12-4) under frequency analysis mode was performed with Golden Delicious apple specimens. The resulting complex modulus plot is shown in Figure 3.66.

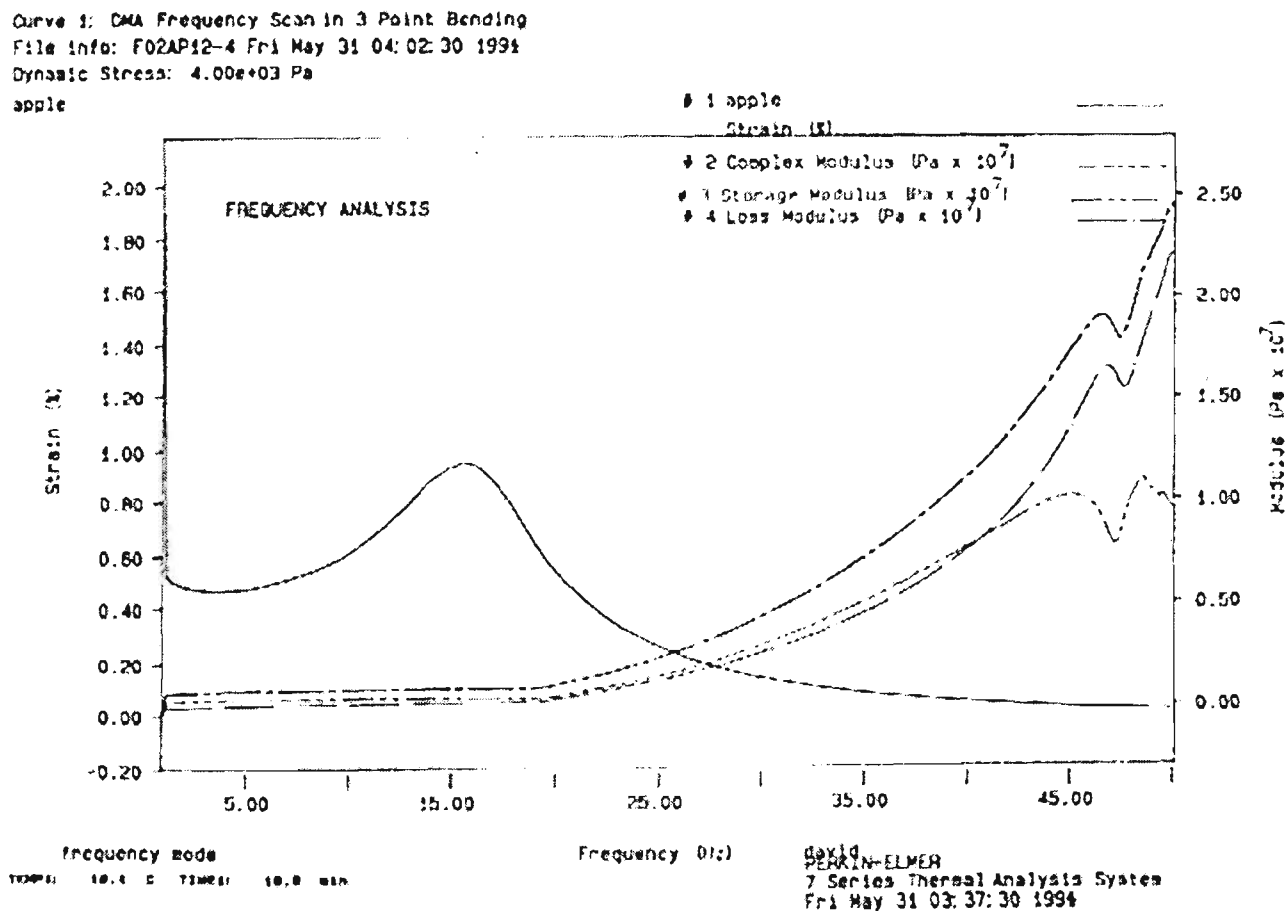


Figure 3.66 Dynamic response from DMA Run F02-AP-12-4 of complex modulus,  $E^*(\omega)$ , storage modulus,  $E'(\omega)$ , and loss modulus,  $E''(\omega)$  under frequency range of 1 to 50 Hz for Golden Delicious apple specimens. Dynamic stress is 4 kPa with specimen thickness of 4.138 mm.

In Figure 3.66, the parameters for the vertical axis are % strain (left) and modulus in Pa x 10<sup>7</sup> (right), and for the horizontal axis the operating frequency in Hz. The values that are of interest to this study are the storage Young's modulus,  $E'(\omega)$ , and loss Young's modulus,  $E''(\omega)$ , registered as the two bottom dotted lines in Figure 3.66. Results are presented in Table 3-6, including calculated values of the  $\tan \delta$  using Equation 2-35.

Table 3-6 DMA data under a frequency range of 2 to 50 Hz with Golden Delicious apple specimen under a dynamic stress of 4 kPa and test temp of 18.4°C with specimen thickness of 4.138 mm. (Run F02-AP-12-4)

Frequency (Hz)	$E'(\omega)$ -storage Young's modulus (MPa)	$E''(\omega)$ - loss Young's modulus (MPa)	$\tan \delta$ (Equation 2-35)
2	0.8187	0.1955	0.238793
4	0.8787	0.2419	0.275293
6	0.973	0.2966	0.30483
8	0.9162	0.3311	0.361384
10	0.9344	0.3599	0.385167
12	0.9437	0.3832	0.406061
14	0.9507	0.4038	0.42474
16	0.978	0.4222	0.431697
18	0.9725	0.4439	0.456452
20	1.063	0.5739	0.539887
22	1.405	0.9018	0.641851
24	1.798	1.28	0.711902
26	2.264	1.712	0.756184
28	2.828	2.22	0.785007
30	3.51	2.802	0.798291
32	4.248	3.467	0.816149
34	5.09	4.233	0.831631
36	6.033	5.166	0.85629
38	7.036	6.272	0.891416
40	8.142	7.697	0.945345
42	9.332	9.454	1.013073
44	10.39	11.98	1.153032
46	10.42	15.59	1.496161
48	10.56	16.18	1.532197
50	10.07	22.37	2.22145

For many common polymers such as polyethylene, polystyrene and polymethylmethacrylate,  $\tan \delta$  varies little with frequency, according to Kosky (1960), except if the polymers reach their glass transition temperature. With reference to these characteristics, Lethersich (1950) developed a technique for the description of the rheological state of polymeric materials, based on a log-log plot of the  $\tan \delta$  and operating frequency, as shown in Figure 3.67.

Based on actual values of  $\tan \delta$  and frequency in Table 3-6, the rheological state of the Golden Delicious apple specimen is presented as a log-log plot in Figure 3.68.

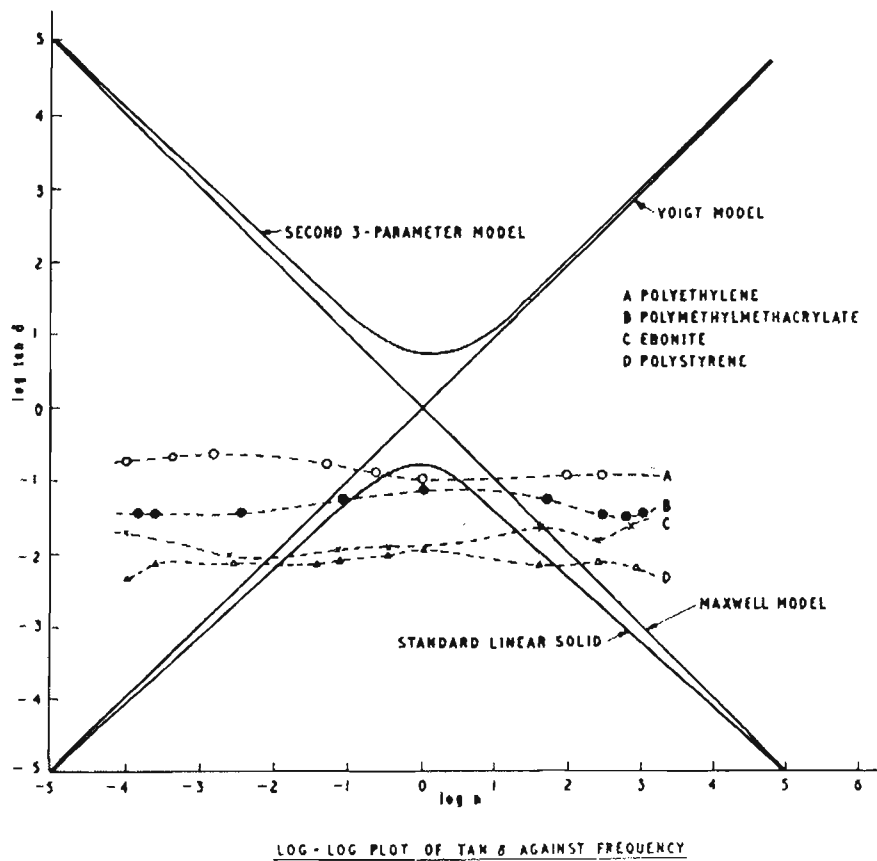


Figure 3.67 Comparison between response of model solids and values of  $\log(\tan \delta)$  and  $\log(\omega)$ .

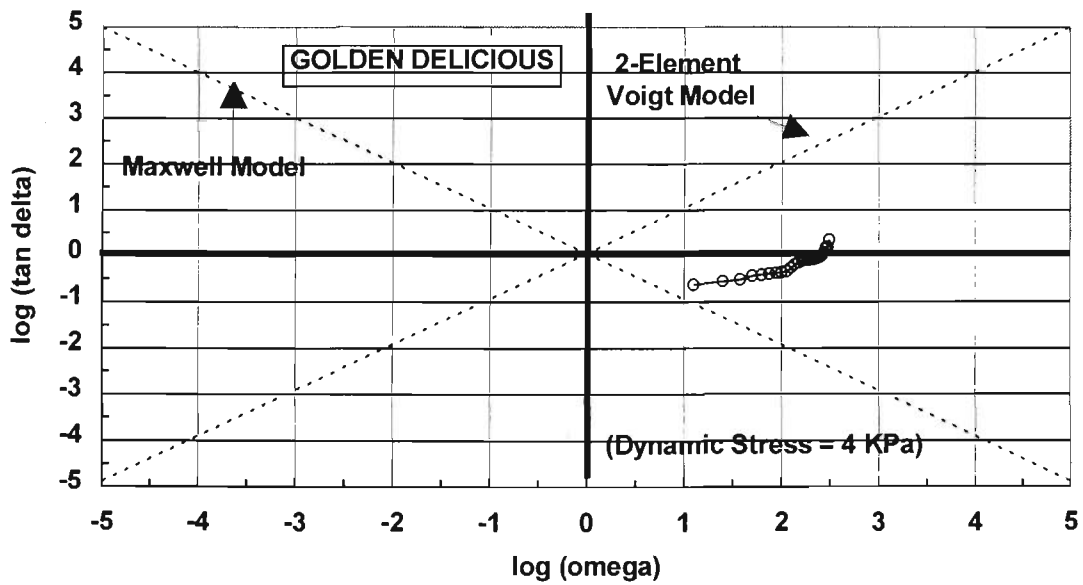


Figure 3.68 Comparison between response of model solids and actual values of  $\log(\tan \delta)$  and  $\log(\omega)$  for Golden Delicious apple specimen (DMA Run F02-AP-12-4).

In terms of  $\log(\tan \delta)$  and  $\log(\omega)$  values, the Golden Delicious apple flesh responds in similar way to polymeric materials such as polyethylene within the frequency range of 1 to 50 Hz (Figures 3.67 and 3.68). According to Figure 3.68, the rheological properties of the Golden Delicious apple specimens behave between a Voigt solid and Maxwell liquid, but more resemble Maxwell fluid as the operating frequency decreases towards zero.

### 3.5.2 Dynamic Poisson's Ratio

Accurate values of Poisson's ratio of horticultural materials are necessary in modelling studies such as the finite element analysis of the dynamic behaviours of produce materials under transient conditions. It has been pointed out, however, that accurate techniques for the 2-dimensional straining of horticultural materials have yet to be established, see Vincent (1992). Accurate measurements of Poisson's ratios of horticultural materials are difficult.

An indirect technique was used in this study to estimate Poisson's ratios of selected produce specimens based on accurate DMA data of storage Young's modulus,  $E'(\omega)$ , loss Young's modulus,  $E''(\omega)$ , storage shear modulus,  $G'(\omega)$  and loss shear modulus,  $G''(\omega)$ .

Poisson's ratio may be estimated by using the following equation developed by Rigbi (1967):

$$\nu = \nu' + i\nu'' = \left[ \left( \frac{E'G' + E''G''}{2(G'^2 + G''^2)} \right) - 1 \right] + i \left[ \frac{E''G' - E'G''}{2(G'^2 + G''^2)} \right] \quad (3-1)$$

where  $\nu'$  and  $\nu''$  are the real and imaginary parts of the Poisson's ratio,

$E'$  and  $E''$  are the storage and loss Young's modulus, and

$G'$  and  $G''$  are the storage shear modulus and loss shear modulus, respectively.

Poisson's ratio calculated from Equation (3-1) would show a time lag in its lateral response compared to its longitudinal response. Following Equation (3-1), Poisson's ratios can be established from DMA data. They are presented in Table 3-7 for DMA Run F02-AP-12-4 with Golden Delicious apple specimen under a dynamic stress of 4 kPa.

Table 3-7 Elastic parameters of Golden Delicious apple specimen for the estimation of dynamic Poisson's ratio in a frequency range of 2 to 50 Hz. (Run F02-AP-12-4)

Frequency (Hz)	$E'(\omega)$ (MPa)	$E''(\omega)$ (MPa)	$G'(\omega)$ (MPa)	$G''(\omega)$ (MPa)	Poisson's Ratio
2	0.8187	0.1955	0.2806	0.06516	0.461042
4	0.8787	0.2419	0.3038	0.08064	0.449913
6	0.9730	0.2966	0.3150	0.09887	0.540604
8	0.9162	0.3311	0.3247	0.11040	0.420902
10	0.9344	0.3599	0.3338	0.12000	0.412308
12	0.9437	0.3832	0.3395	0.12770	0.405182
14	0.9507	0.4038	0.3443	0.13460	0.398514
16	0.9780	0.4222	0.3551	0.14070	0.396061
18	0.9725	0.4439	0.3563	0.14800	0.387537
20	1.0630	0.5739	0.4028	0.19130	0.359598
22	1.4050	0.9018	0.5564	0.30060	0.331443
24	1.7980	1.2800	0.7358	0.42680	0.315643
26	2.2640	1.7120	0.9459	0.57050	0.308519
28	2.8280	2.2200	1.1980	0.74010	0.304187
30	3.5100	2.8020	1.4970	0.93410	0.302314
32	4.2480	3.4670	1.8280	1.15600	0.300039
34	5.0900	4.2330	2.2070	1.14110	0.415490
36	6.0330	5.1660	2.6470	1.72200	0.296703
38	7.0360	6.2720	3.1420	2.09100	0.294259
40	8.1420	7.6970	3.7350	2.56600	0.292570
42	9.3320	9.4540	4.4280	3.15100	0.293276
44	10.390	11.980	5.2850	3.99200	0.301971
46	10.420	15.590	6.2510	5.19700	0.344290
48	10.560	16.180	6.4410	5.39400	0.349394
50	10.070	22.370	8.1790	7.45800	0.440517

Poisson's ratio was found by Garrett (1970), using sonic methods, to be around 0.30 to 0.32 throughout the spectrum of pulse velocity passing through market-fresh and aged Rome Beauty apple specimens during an impact.

In this study with varying applied frequencies of 1 to 50 Hz, the Poisson's ratio has been shown to vary from 0.30 to 0.45 for market-fresh Golden Delicious apple specimens, based on the modulus data in Table 3-7, and shown in Figure 3.69. A careful check on the precision height data revealed that the knife-edge wedge, see Figure 2.15, started to cut into the apple specimen towards the very final stage of the 20-minute frequency sweep. This occurred at a frequency of 48 Hz and presumably affected the accuracy of the result beyond 48 Hz. On the other hand, the Poisson's ratio in the low frequency range is accurate down to about 10 Hz. The accuracy erodes below 10 Hz, see Figure 3.69.

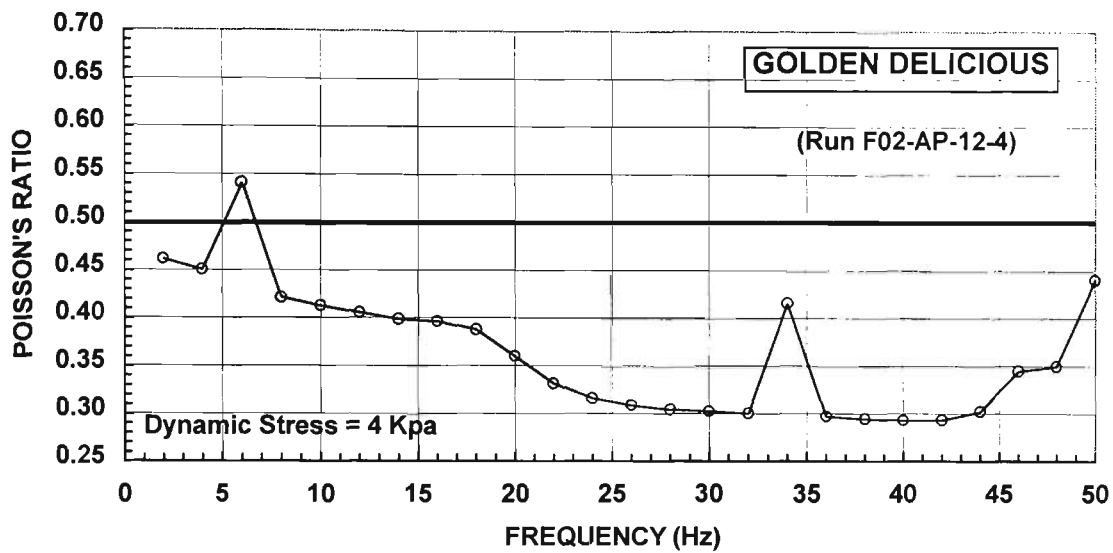


Figure 3.69 Relationship of dynamic Poisson's ratio versus frequency range at a dynamic stress of 4 kPa (DMA Run F02-AP-12-4).

Using Equation (2-37), the percentage of total energy in the form of shear energy during the DMA test run is shown in Figure 3.70. The figure shows that the bulk of the potential energy appears as shear energy under the 3-point bending test mode, and is consistently at a level of about 70 to 80% throughout the sweep of the frequency range of Run F02-AP-12-4. Figure 3.70 shows that results between 4 and 8 Hz are unreliable. So, it is safe to conclude that the range of applicable Poisson's ratio is between 0.30 and 0.405 in Figure 3.69, with the average appears close to 0.30.

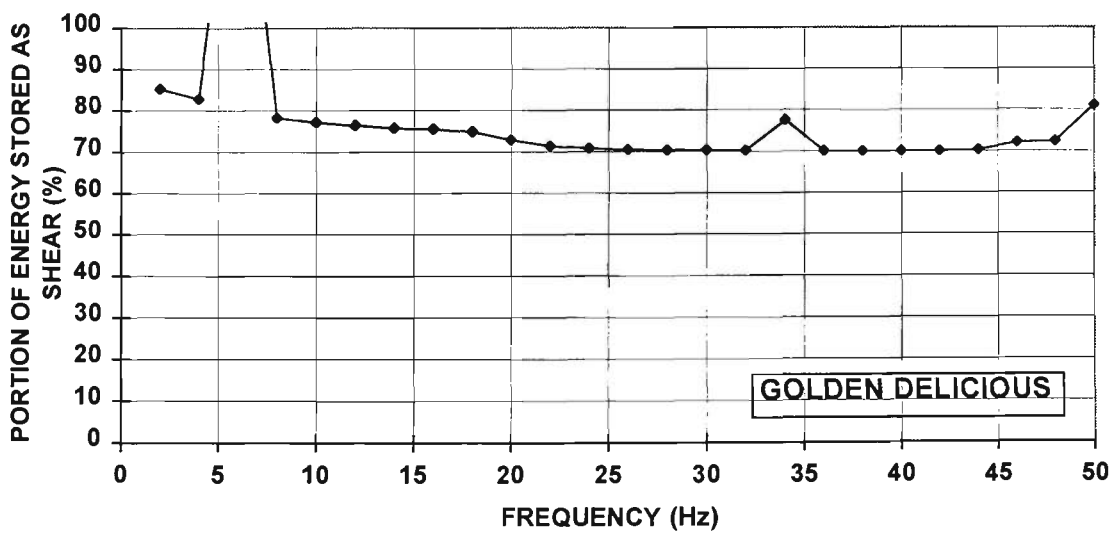


Figure 3.70 Relationship of portion of energy stored in the form of shear versus frequency range at a dynamic stress of 4 kPa (DMA Run F02-AP-12-4).

DMA tests under the frequency test mode were performed using two applied stress levels: 2 kPa and 4 kPa. Results presented so far are associated with an applied stress of 4 kPa (Run F02-AP-12-4).

The dynamic mechanical responses under a smaller applied stress of 2 kPa for Run F03-AP-12-4, performed at the same testing conditions, is shown in Figure 3.71. The corresponding elastic parameters within the frequency range of 2 to 50 Hz for this run are listed in Tables 3-8.

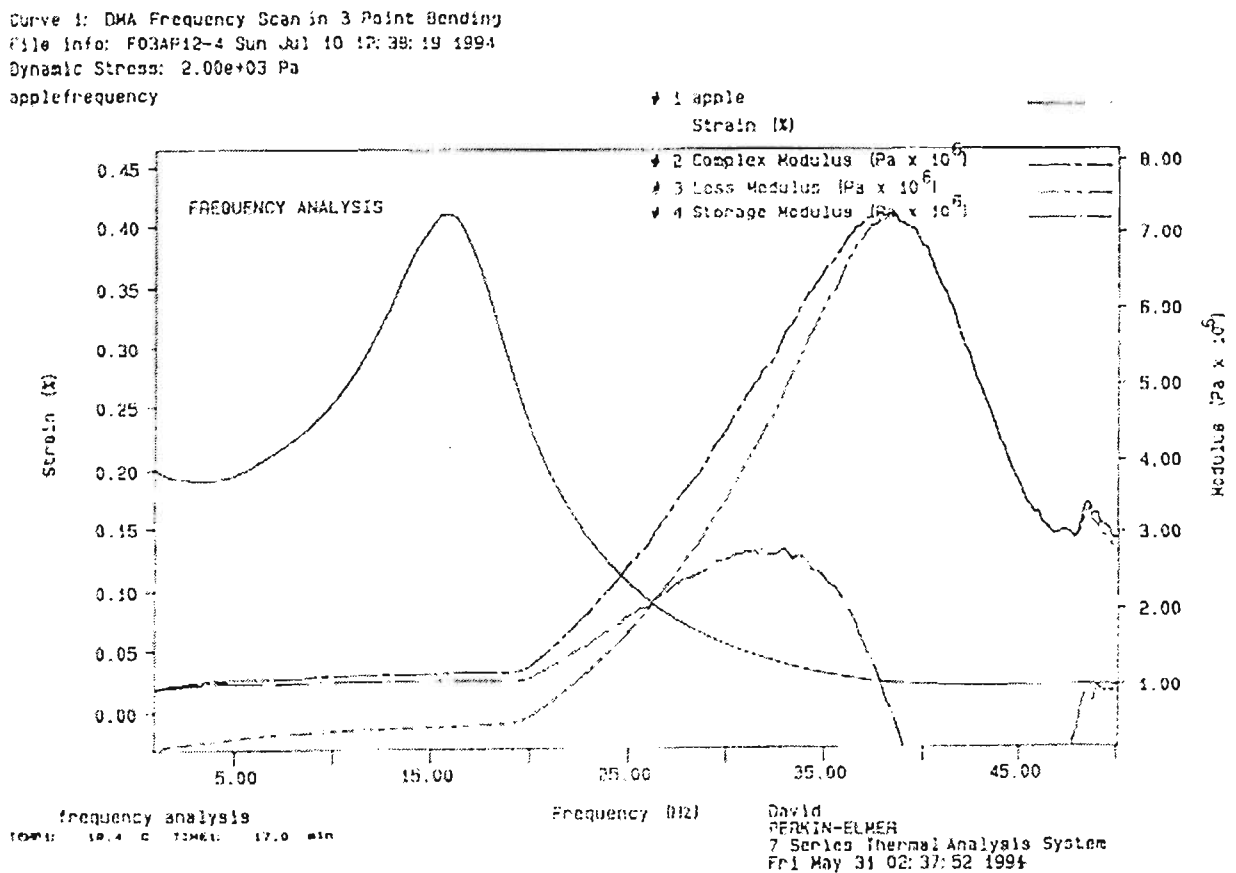


Figure 3.71 Dynamic response from DMA Run F03-AP-12-4 of complex modulus,  $E^*(\omega)$ , storage modulus,  $E'(\omega)$ , and loss modulus,  $E''(\omega)$  under frequency range of 1 to 50 Hz for Golden Delicious apple specimens. Dynamic stress is 2 kPa with specimen thickness of 3.883 mm.

A comparison between Figures 3.66 and 3.71 shows a shift of the modulus peak toward higher frequency range if the applied dynamic stress was increased from 2 kPa to 4 kPa. On the other hand, the peak value of the complex Young's modulus increases at least three times higher due to the increase in applied stress. Owing to the operating frequency limit of the DMA to 50 Hz, the modulus peak is revealed only partially, as shown in Figure 3.64 under the applied stress of 4 kPa. From Run F03-AP-12-4, the Poisson's ratio has been shown to be between 0.30 and 0.67, based on modulus data in Table 3-8, shown in Figure 3.72. A check on the precision height data revealed that the knife-edge wedge, see Figure 2.15, started to sink into the apple specimen during the final 12 minutes of the 20-minute

frequency sweep. This commenced at a frequency of 34 Hz and affected the accuracy of the result beyond 34 Hz.

Table 3-8 Elastic parameters of Golden Delicious apple for the estimation of dynamic Poisson's ratio in a frequency range of 2 to 50 Hz. (Run F03-AP-12-4)

Frequency (Hz)	$E'(\omega)$ (MPa)	$E''(\omega)$ (MPa)	$G'(\omega)$ (MPa)	$G''(\omega)$ (MPa)	Poisson Ratio
2	1.016	0.2388	0.3478	0.07961	0.46264
4	1.057	0.3004	0.3664	0.1001	0.446691
6	1.056	0.3634	0.3724	0.1211	0.42642
8	1.061	0.396	0.3774	0.132	0.41699
10	1.076	0.4242	0.3855	0.1414	0.409366
12	1.081	0.4473	0.39	0.1491	0.402252
14	1.082	0.4652	0.3927	0.1551	0.396309
16	1.094	0.4813	0.3983	0.1604	0.393523
18	1.088	0.508	0.4003	0.1693	0.383786
20	1.12	0.6019	0.4237	0.2006	0.361052
22	1.419	0.9932	0.5774	0.3311	0.318145
24	1.734	1.468	0.7575	0.4894	0.29716
26	2.041	1.999	0.9524	0.6663	0.29259
28	2.414	2.705	1.208	0.9015	0.29921
30	2.671	3.467	1.459	1.156	0.317256
32	2.747	4.431	1.738	1.477	0.361077
34	2.67	5.479	2.032	1.826	0.4206
36	2.099	6.534	2.288	2.178	0.522076
38	0.9404	7.165	2.409	2.388	0.671348
40	1	6.826	2.275	2.275	0.655348
42	1	5.632	1.877	1.877	0.627878
44	1	4.249	1.416	1.416	0.578283
46	1	3.308	1.103	1.103	0.52365
48	0.4099	2.943	0.9905	0.981	0.664317
50	1.018	2.763	0.9815	0.9209	0.490277

From Figure 3.72, the range of Poisson's ratio is from 0.30 to just above 0.45, with the bulk of values close to the average of 0.35. Using Equation (2-37), the percentage of total energy in the form of shear energy during this DMA test run is shown in Figure 3.73. The figure shows that the bulk of the potential energy appears as shear energy under the 3-point bending test mode, and is consistently at a level of about 70 to 80% throughout the sweep of the frequency range of Run F03-AP-12-4. Figure 3.71 shows that the results between 34 and 50 Hz are unreliable. The reliable range of Poisson's ratio is between 0.30 and 0.40 in Figure 3.72, with the average value close to about 0.35.

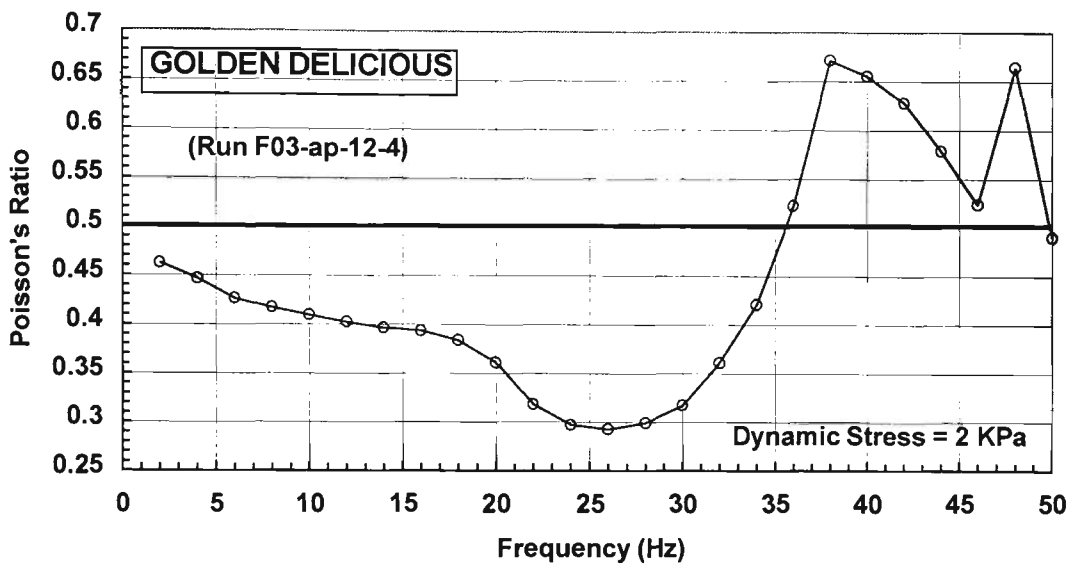


Figure 3.72 Relationship of dynamic Poisson's ratio versus frequency range at a dynamic applied stress of 2 kPa (DMA Run F03-AP-12-4).

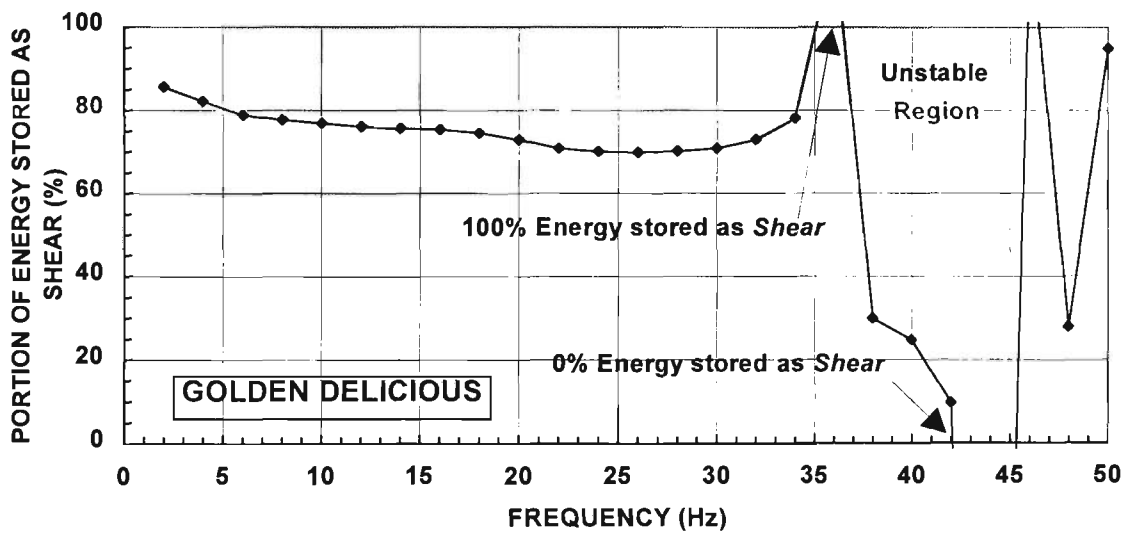


Figure 3.73 Relationship of portion of energy stored in the form of shear energy versus frequency range at a dynamic applied stress of 2 kPa (DMA Run F03-AP-12-4).

An interesting feature of the measurements is the level of shear energy that stands consistently at about 75% of total energy, regardless of the substantial change in the frequency of direct loading. This seems to enhance the possibility of shear wave presence as discussed in Section 3.2.2.

### 3.6 CHARACTERISTICS OF DYNAMIC DEFORMATION IN HORTICULTURAL MATERIALS

Both Sections 3.6 and 3.7 serve to analyze and identify the various dynamic features associated with the bruise damage processes in horticultural materials, with reference to the experimental results. In this section, a theoretical analysis on the dynamic deformation in horticultural materials based on the wave pulse propagation and associated processes are presented.

In general, horticultural research workers accept that wave effects in soft produce can be ignored if they are generated from impact on rigid surfaces with an impact velocity of less than one to two metres per second, depending on the types of produce. This section analyzes this aspect and illustrates why and how an elastic wave front generated as a result of dynamic loading can degenerate quickly in produce, and the destructive plastic wave front which follows can transform into other forms of energy transmission, notably heat diffusion. As heat diffusion activities within horticultural materials do not involve large material deformation, the plastic wave front diminishes significantly and may be ignored. However, during the early stages of impact, wave fronts do exist. Relevant background information to this section has been provided in Section 2.2.9.

#### 3.6.1 *Wave Propagation and Heat Diffusion in Soft Horticultural Materials*

We recall from Section 2.2.9 that the wave amplitude of an elastic precursor wave front can degenerate rapidly and exponentially according to Equation (2-46). Following the precursor wave, the sharp rise in stress amplitude, denoting the plastic wave front that is caused by work-hardening plastic deformation, propagates at the acceleration wave speed with negligible decay in amplitude. This latter property is only altered by the gradual 'spreading-out' of the wave front profile, a distinctive characteristics of energy dispersion mechanism.

The experimental results obtained for the dynamic stress-strain characteristics of kiwifruit (Figure 3.29), persimmon (Figure 3.30) and tomato (Figures 3.32) clearly illustrate the elastic precursor wave. This also exists in some moderately crisp produce such as papaya (Figure 3.45) and eggplant (Figure 3.46). However, no precursor wave can be identified in viscoplastic produce materials such as banana flesh (Figure 3.25). An analogous situation in the case of certain produce materials and packaging materials like bubble-wrap may be realized using the model as shown by Chu. Assuming the upper bound of plastic deformation of fruit cells (or, similarly, closed-cell bubble-



For plane waves, the wave diffusion process is illustrated in Figure 3.75. It shows that the elastic wave front propagates from a point source,  $0$ , at speed  $a$  towards undisturbed region. The wave front covers distance  $(at)$  and  $(-at)$  at time  $t$ . The plastic wave front only reaches  $x_0$  at time  $t$  due to its lower speed of  $x_0/t$ , which is only a fraction of  $(at)$ . Suppose it were able to propagate at speed  $a$ , it would have covered a distance of  $(at)$ , as shown by the slope of the cone with slope length of  $(at)$ . A further reduction in speed results in decreasing tangent modulus,  $E_t$  (see Figure 2.70), leading to a spreading-out of the circle as well as the cone roof. When  $E_t$  equals zero, the circle will spread out to the maximum limit with a radius of  $(at)$ . Then, by plotting out the locus of all the cone roofs, it can be seen that the cone roof spreads out asymptotically, and can be expressed in terms of error-functions, which clearly indicate the diffusion characteristics.

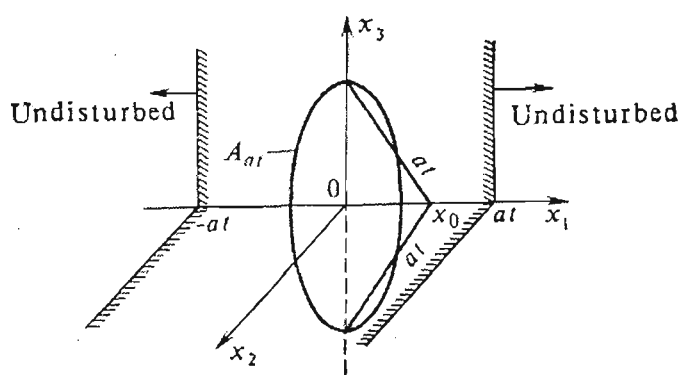


Figure 3.75 Sketch showing wave propagation with wave diffusion process. From Vladimirov (1984).

This purely diffusive process can be realized in the Chu model shown in Figure 3.76 with disturbance propagating through a 'liquid-like' (in the sense of perfectly-plastic) viscoelastic slab. Apart from the degenerating elastic precursor wave front which propagates at a speed of  $c$  according to Equation (2-52), no secondary front can be identified. Instead, the main disturbance propagates by (predominantly heat) diffusion, with the maximum amplitude ( $\sigma_0$ ) always occurring at the source point only. Thus, in dynamic deformation of produce such as kiwifruit that deforms under comparable elastic/perfectly-plastic conditions, we expect the maximum stress level of  $\sigma_0$  associated with the precursor wave to be damped out quickly and substantially. For the main (secondary) disturbance, the maximum stress,  $\sigma_0$ , occurs only at the point of impact.  $\sigma_0$  approaches zero as  $t \rightarrow \infty$ .

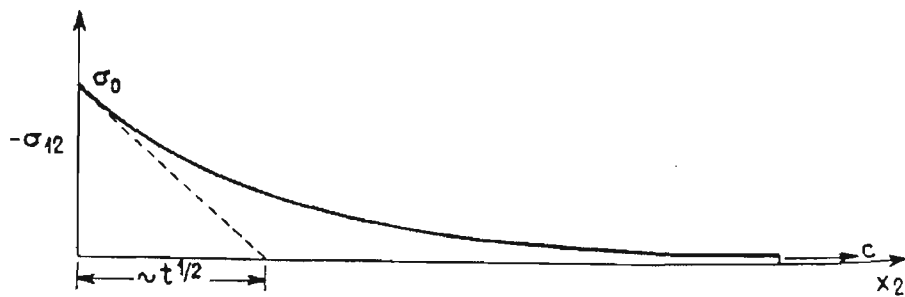


Figure 3.76 Numerical result for a perfectly-plastic 'liquid-like' viscoelastic material slab showing decaying elastic precursor wave followed by a purely diffusive disturbance, with the absence of any plastic wave forms. Here  $c =$  elastic wave speed ( $U_S$ ) and the half-time,  $t_{1/2}$ , for diffusion is substantially longer than that of a wave discontinuity. From Chu (1962).

Thus, during an impact, soft horticultural materials are 'immunized' from destructive propagating wave fronts, which are the main causes of wide-spreading bruising. This natural 'immunization' is the result of damping of the elastic precursor wave front and diffusion of the main disturbance. Produce materials with crisper textures will be discussed in Section 3.7.

One may query the unique shape of the shear wave front as illustrated in Figures 3.74 and 1.7 (apple). This is actually a combination of the spherical shear wave front and a longitudinal wave-induced shear wave, shown as hatched area in Figure 3.77. Complete mathematical derivations can be found in Bedford and Drumheller (1994, PP.151-165). This secondary disturbance can also be reflected in Equation (2-56<sub>1</sub>) in that the longitudinal wave speed is also a function of the Lamé parameter,  $\mu$ , which here denotes the instantaneous shear modulus. The wave front AB is commonly called head wave by the geophysics workers.

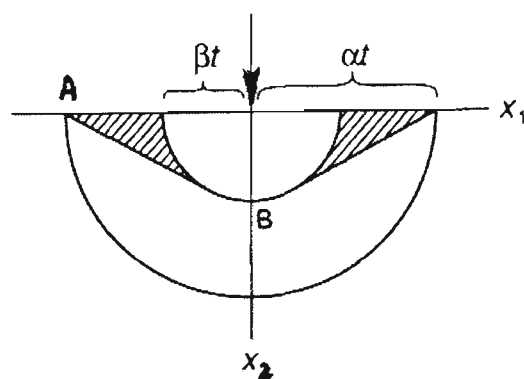


Figure 3.77 Schematic diagram showing the propagating spherical wave fronts under a sudden impact load (direction of arrow at  $x_2$ -direction) of (a) longitudinal waves at speed  $\alpha$  and (b) shear waves at speed  $\beta$ , as well as the longitudinal wave-induced shear waves (hatched area) which propagate with speed  $\alpha$  at A and speed  $\beta$  at the tangent on the spherical shear wave front surface near B.  $t =$  propagating time. From Bedford and Drumheller (1994).

The laser-based stress-strain characteristic curves, particularly within the work-hardening domain under plastic deformation, are informative. Based on Equations (2-52) and (2-53), the wave front propagates through the horticultural material and the inherent properties can be deduced. For instance, for the case of dynamic deformation of kiwifruit, it clearly indicates an elastic precursor wave front in the form of shock wave, but almost immediately substantially damped and degenerated (see Figure 2.73) as the wave front propagates.

This precursor wave can be better illustrated by the Lensky (or Riemann) wave plots, Lensky (1949), shown in Figure 3.78 as Line  $OB$ .

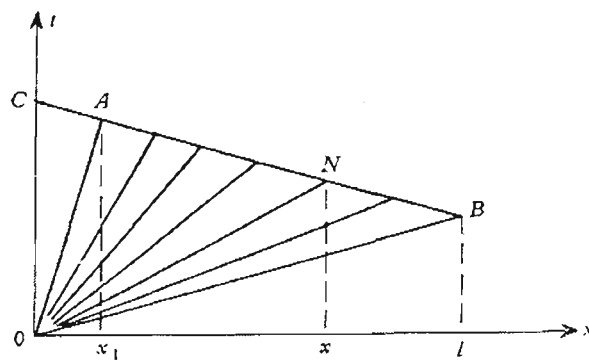


Figure 3.78 Lensky wave front displacement history plot, or better known as Riemann wave diagram, for an elastic precursor and a plastic front. From Lensky (1957).

Referring to kiwifruit deformation shown in Figure 3.29, the elastic portion of the characteristic curve shows the existence of an elastic precursor wave front followed immediately by an extensive plastic wave. In this Figure, when the tangent modulus,  $E_t$ , approaches zero, wave propagation stops. At this point, the main plastic wave front transforms into heat disturbance by the diffusion of the wave front. This change from elastic to perfectly-plastic state can be represented by area  $OAB$  in Figure 3.78, which contains either non-diffusive or diffusive plastic wave front. This is the domain for work-hardening of the materials. The plastic waves within  $OAB$  have been commonly referred to as Riemann waves. For the case of wave propagation in elastic materials, the area  $OAB$  does not exist. The lines  $OA$  and  $OB$  actually coincide. Within the domain  $OAC$ , the kiwifruit texture reaches the perfectly-plastic state, implying that there will be no more wave disturbance within this domain other than the (now negligible) elastic precursor. Instead, heat disturbance plays the dominant role, see Figures 3.76. This can be recognized by inspection of the unloading stress-strain curve of kiwifruit by re-plotting Figure 3.29 as Figure 3.79.

Using the acceleration wave speed expression given in Equation (2-53), wave speeds at various stages of dynamic deformation in kiwifruit can be calculated with measured values of tangent

moduli,  $E_t$ , from Figure 3.79, assuming unity density for kiwifruit textures. Their density is in general marginally denser than water. From this Figure,  $E_t$  values of 0.20 MPa, 1.00 MPa, 0.53 MPa, respectively, were obtained with corresponding wave speeds of 44.3, 99.0, and 72.3 m/sec. These wave speeds and their corresponding strain values were plotted as Figure 3.80. From this figure, the elastic precursor wave which peaks at a wave speed of 99 m/sec dominates the initial deformation stage of up to about 10% strain. This is followed by the main work-hardening plastic wave that propagates at a speed of 72.3 m/sec. When the strain reaches 36%, heat diffusion plays an increasingly significant role.

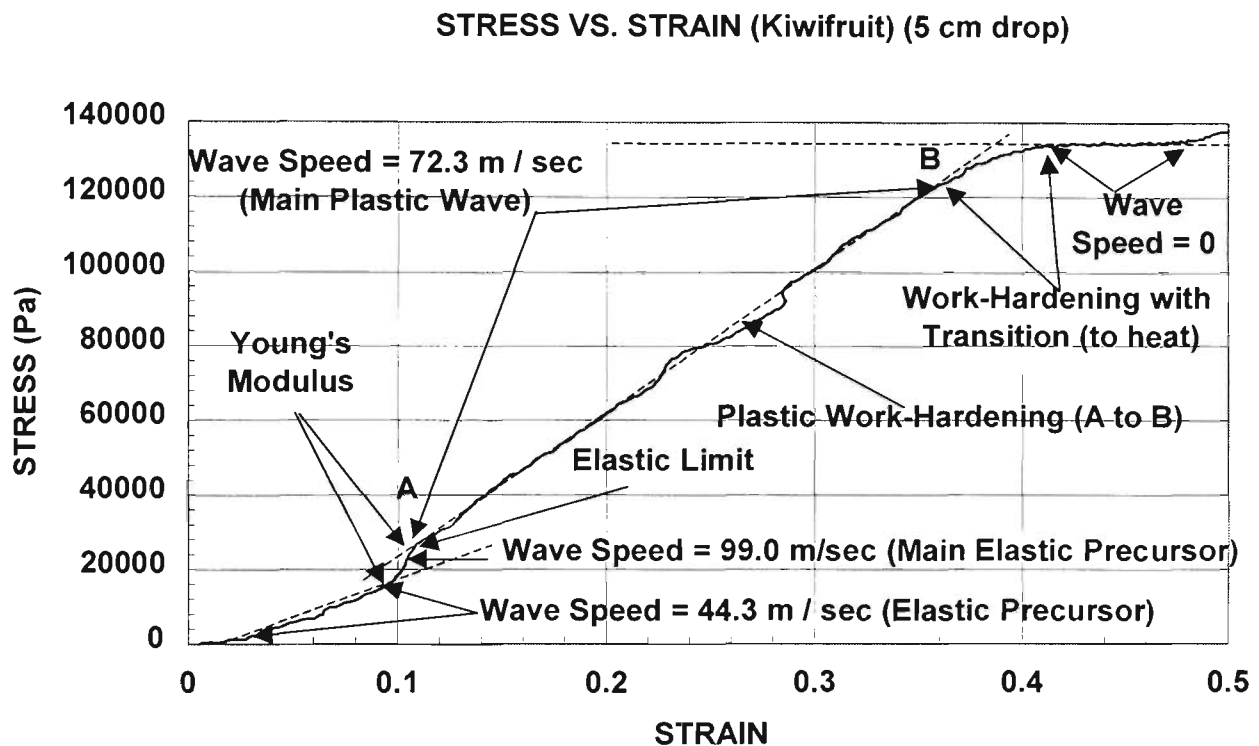


Figure 3.79 Replotting of Figure 3.29 showing the elastic and plastic uploading stress-strain curve for the estimations of wave speeds. (Run KW-05-m2) (5 cm drop).

Wave front speeds expressed in terms of stresses are shown in Figure 3.81. Thermoelasticity is a coupled process of plastic work-hardening and heat diffusion and results in wave diffusion and gradual disappearance of the wave front. In a pure plastic deformation process of work-hardening, without diffusion, the speed of the plastic wave front does not seem to suffer any significant change and is more or less constant at 72.3 m/sec.

In general, the plastic wave front velocity of materials under work-hardening are more sensitive to the severity of the applied loading, as illustrated in Figures 3.82 and 3.83. From the figures, it is clear that the higher the applied load is, the higher the plastic wave speed will be. For the

case of mild steel, Figure 3.82, only plastic deformation can be observed, but both plastic deformation and wave diffusion are present for the case of uranium, Figure 3.83.

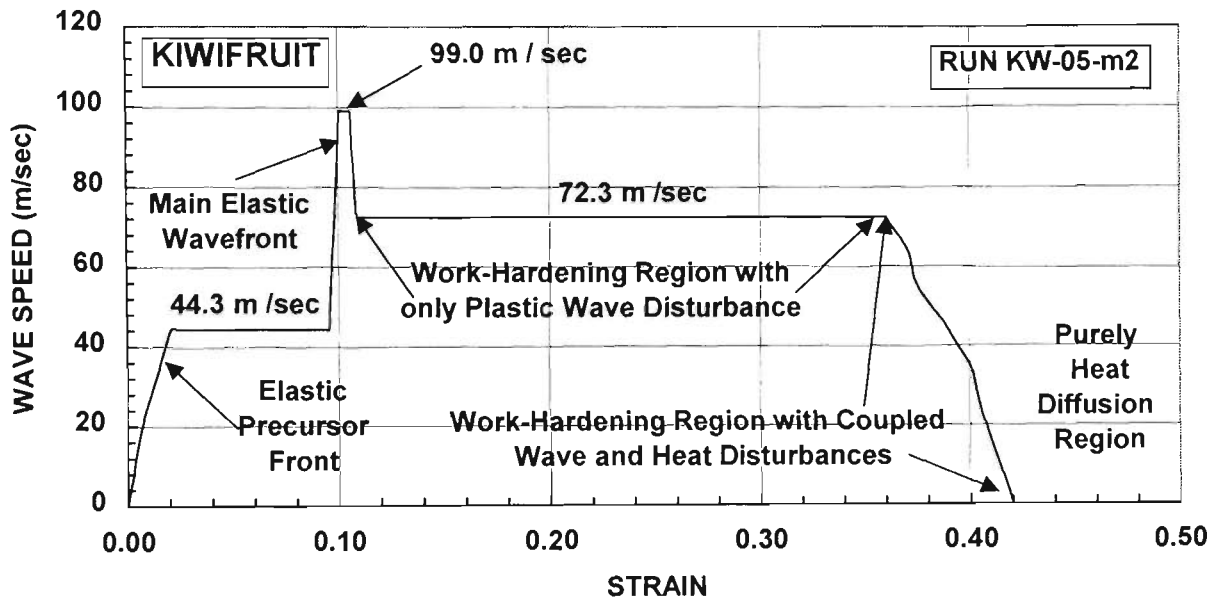


Figure 3.80 Wave speeds versus strain under different forms of disturbances: elastic deformation, plastic work-hardening, and plastic work-hardening plus heat diffusion.

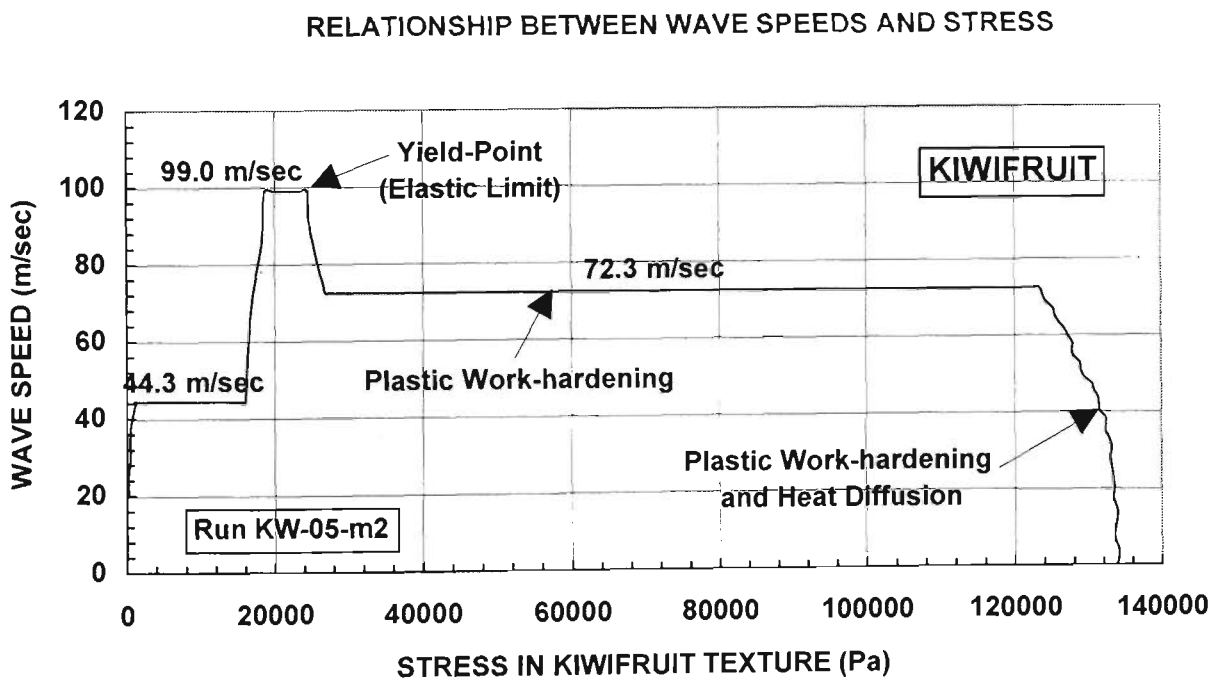


Figure 3.81 Wave speeds versus stress under different forms of disturbances: elastic deformation, plastic work-hardening, and plastic work-hardening plus heat diffusion.

Heat diffusion occurs when the materials are more 'liquid-like', in the sense of perfectly-plastic condition, but without work-hardening. Work-hardening processes precede the occurrence of any perfectly-plastic deformation (see, for instance, Figures 3.29 and 3.30). This denotes a change in phase within the materials. It may be easier for us to recognize this if we resort to pressure-volume (PV) diagrams of the material behaviours for explanations. We will briefly highlight some of the characteristics based on PV diagrams (or Hugoniot curves), when we complete our discussion on coupled and uncoupled processes.

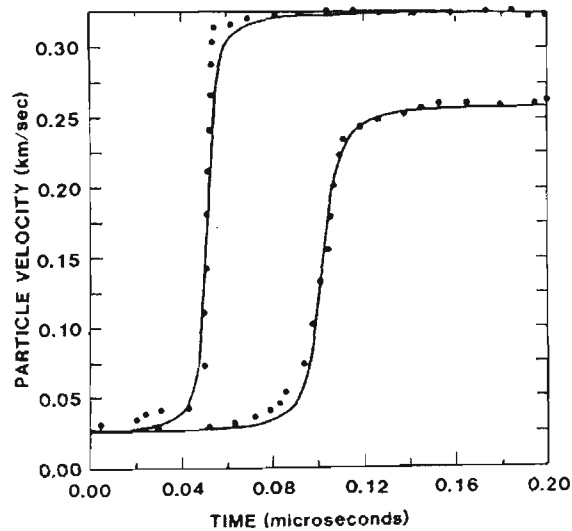


Figure 3.82 Experimental (dotted line) and numerical (solid line) for wave front profile history in mild steel under an applied stress of 13.1 GPa (upper curve) and 10.3 GPa (lower curve), showing fairly constant plastic wave speeds with no diffusion. From Swegle and Grady (1985).

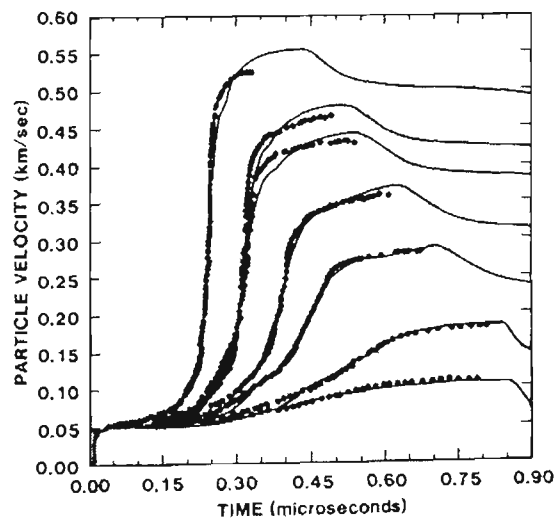


Figure 3.83 Experimental (dotted line) and numerical (solid line) for wave front profile history in uranium, showing diffusion and wave degradation, under applied loads of 16.7 GPa (uppermost curve), 14.4 GPa, 13.2 GPa, 11.2 GPa, 8.7 GPa, 5.7 GPa and 3.3 GPa. From Swegle and Grady (1985).

Basically all the pioneering works on thermoelasticity are based on the uncoupled concept. These include Sokolovskii (1948), Malvern (1951) and Chadwick (1960). The latter first introduced an isothermal coupling constant,  $\bar{\epsilon}$ , which was used to link up independent wave and thermal problems. Referring to Figure 3.84, what are the roles of the wave and heat disturbances within the plastic work-hardening domain of  $OAB$  (Figure 3.78), and, if they do depend on one another, how does this coupling process work?

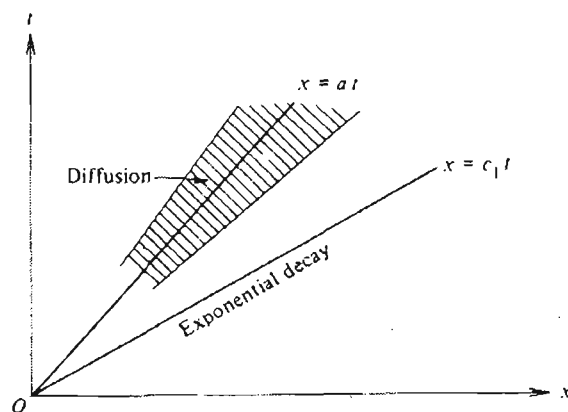


Figure 3.84 Schematic Riemann wave diagram showing (a) exponentially decaying elastic precursor (speed  $c_1$ ), and (b) gradually more diffusive plastic wave front (speed  $a$ ). From Lick (1983).

We can approach this question by focusing on the work-hardening process. Referring back to Figure 3.77, the plastic front is actually composed of many plastic wavelets, each propagating with its own speed, as denoted by the straight lines between  $OA$  and  $OB$  within the plastic work-hardening region. More significantly, this implies that all work-hardening stress-strain curves are, from a microscopic point of view, actually serrated (staircase-like)! This phenomenon can sometimes be observed during material testing with, for instance, soft aluminium and polymeric materials, Brinson and Gupta (1975), and has been referred to as mechanical instabilities during work-hardening, see Figure 3.85.

Under dynamic deformation, a stress-strain curve of rate-sensitive materials can shift upwards, forming a new curve at higher level, as shown in Figure 3.86. We recall that, during the work-hardening domain, there exists many plastic wavelets, each propagating with its own wave speed. This can be interpreted as the presence of many levels of plastic curves, each with its unique level of yield strength. We need to emphasize that the rate-sensitivity is in the sense of the material yield strength, as shown here in Figure 3.86 as  $\sigma$  for simplicity. It is more appropriate to be expressed as shown in Figure 3.87.

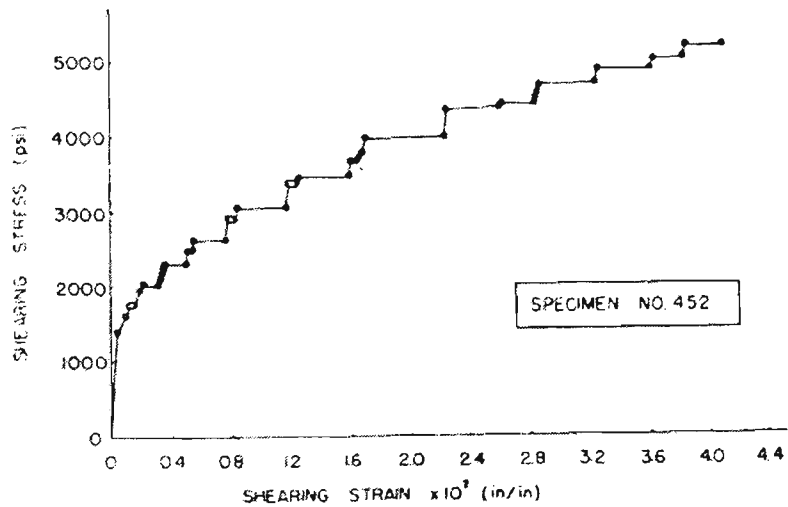


Figure 3.85 Shear stress-strain curve of soft aluminium specimen under very slow rate of quasi-static testing, showing serrated work-hardening characteristics. From Dillon (1966).

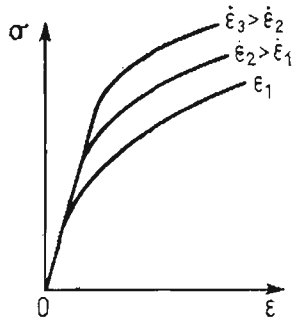


Figure 3.86 Stress-strain curves of a rate-sensitive isotropic material. From Ilyushin and Lensky (1967).

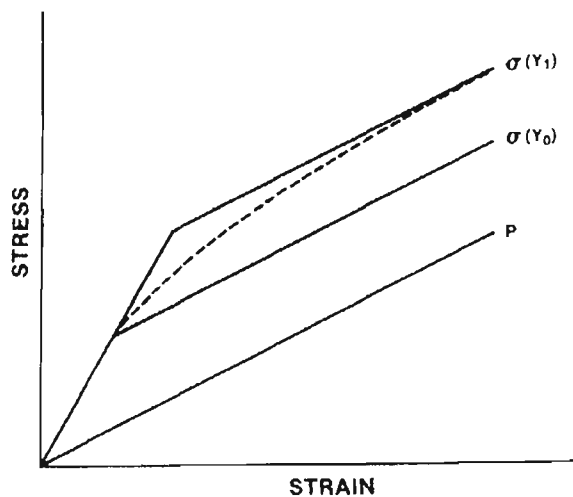


Figure 3.87 Stress-strain curves for rate-sensitive material at two levels of yield strength. The stress values only denote longitudinal components. The dotted line shows work-hardening effect of the shift of yield strength from  $\sigma(Y_0)$  to  $\sigma(Y_1)$ . From Swegle and Grady (1985).

For instance, a higher strain rate would cause a plastic curve, Figure 3.87, to shift from a yield strength of  $\sigma (Y_0)$  to  $\sigma (Y_1)$ . If the deformation rate is really slow, this shift may be discontinuous, resulting in staircase-like hardening curve similar to Figure 3.85. But under normal strain rates of deformation, the shift in the hardening curve is continuous, as shown as a dotted line in Figure 3.87. Here this Figure can be interpreted as a primitive Hugoniot curve, with the P curve denoting the hydrostat curve. If a plastic curve at a particular level is parallel to the hydrostat curve, the plastic curve denotes a perfectly-plastic situation. A higher or lower slope of plastic curves than the P curve implies a strain hardening or a softening process.

Recalling the introduction in Chapter 2 of the strain softening process, which is of importance in the study of material behaviour in horticultural materials. We may illustrate the softening process using a Hugoniot stress-strain curve as shown in Figure 3.88.

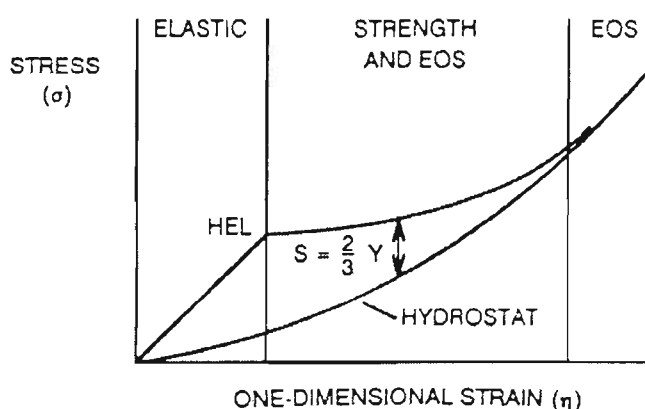


Figure 4.26 Hugoniot stress-strain curve under uniaxial compression of an isotropic material showing material responses as governed by elastic, plastic work-hardening, and equation of state (EOS). Hugoniot stress is the sum of hydrostatic pressure and deviatoric stress,  $S$ . The yield point, HEL, denotes Hugoniot elastic limit, above which  $S$  is equal to two-thirds of the yield strength ( $Y$ ) of the material. From Zukas *et al.* (1992).

In terms of wave characteristics, an elastic wave is responsible for compressing the material up to the Hugoniot elastic limit (HEL), see Figure 3.88, depicted by the yield-point in Figure 3.79. Thereafter, the second main plastic wave front would further compress the material to the final stress amplitude of  $\sigma_p$ . The loading path of the plastic wave does not follow the Hugoniot curve; instead, it follows a straight line called the Rayleigh line, see Figure 3.89. The main reason for the loading path of the plastic wave to follow a Rayleigh line is that, under normal conditions, the plastic wave shape does not change with time, as has been discussed before. During the passage of the steady plastic wave front, the stress is linearly related to the strain, as shown by the typical plastic wave plateau of constant speed, see Figures 2.73 and 3.81. At the uppermost stress domain of EOS, the material

becomes a fluid and its behaviours can be expressed only in terms of the equation of state (EOS). At this point, no material strength remains.

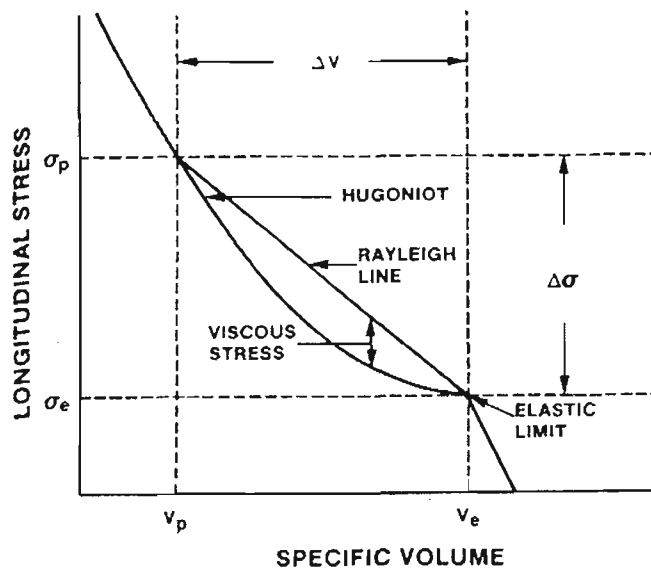


Figure 3.89 A redrawn Hugoniot curve in terms of stress and specific volume,  $v$ .

As the material approaches its ultimate strength, plastic slippage and instabilities may occur before the critical value is reached. This results in some micro-scale instantaneous losses of stress together with the corresponding slip of strain. Thus 'release waves' can be formed. An oversimplified unloading process is shown in Figure 3.90. The unloading process normally follows the Hugoniot curve, which by and large represents the equilibrium states of the material, as the material state changes relatively slowly comparing to the state under loading. It is noted that, due to the difference in the plastic wave speed which is higher (see Figure 3.90) in the unloading path (Hugoniot curve) than in the loading path (Rayleigh line), the 'release waves' will eventually catch up with the loading waves. If this happens, the supposedly unchanged plastic wave shape will be attenuated (see, for instance, Figure 3.80), resulting in the transformation of wave structures into heat disturbances. We believe that this is the fundamental cause of wave and heat diffusion in soft and moderately crisp horticultural and certain packaging materials. The generated heat can be accounted for within the hatched area in Figure 3.90 that is enclosed by the Rayleigh line and the Hugoniot curve.

Regarding the 'release waves', we need to point out that the plastic instabilities which cause the unloading, in the sense of release, may not be the true root cause. They may be just the consequences of the root cause. Although we do not have experimental data to substantiate our claim, it seems the root cause of these sudden micro-scale release or unloading is due to combined stresses, or, strictly speaking, the complex interplay between the transient longitudinal and shear stresses

during rapid loading, according to Ting (1973). This phenomenon most likely appears in the hatched area in Figure 3.77. Within this area the applied stresses are under the direct influence of both the dilatational and shear waves. Since the initiation of studies on combined stresses due to waves by Rakhmatulin (1958) and Cristescu (1959), Clifton has renewed the interest in these studies, see Clifton (1966). Clifton discovered that, under the combined stress waves, a plastic wave might travel at elastic wave speed. Within the hatched area in Figure 3.77, a shear wave, always slower than a dilatational wave, can propagate at the dilatational wave speed at point A (see Figure 3.77). Point A is the outermost front a shear wave can ever reach. Then it follows that shear waves in the hatched area, particularly near the tip A, must play a significant role in the material phase change, in the sense of exceeding the yield point and beyond, because plastic waves can only initiate at the yield point.

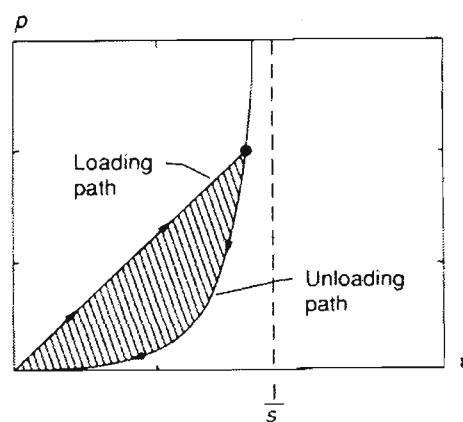


Figure 3.90 Schematic pressure (stress)-strain diagram showing Rayleigh line and Rankine-Hugoniot curve as the loading and unloading path, respectively, for plastic waves. From Bedford and Drumheller (1994).

Plastic waves heavily contributed to shear waves during any form of unloading. The reason is that when the tangent modulus,  $E_t$ , becomes negative, the wave velocity becomes imaginary, and the equation of motion will no longer be hyperbolic, but elliptic. This implies that the velocity direction vectors of the wave speeds now transform into an ellipse, with much decreased magnitude of the dilatational wave vector, and the corresponding (much increased) shear wave vector normal to the dilatational wave vector. We recall that the ratio of dilatational wave speed,  $C_p$ , to shear wave speed,  $C_s$ , can be expressed, according to Bedford and Drumheller (1994), as:

$$\frac{C_p}{C_s} = \frac{2(1-\nu)}{1-2\nu} \quad (3-2)$$

where  $\nu$  is the Poisson's ratio.

This implies that when the contribution due to the dilatational wave becomes negligible as compared to the shear wave, the value of the Poisson's ratio approaches one. This can be deemed as the extreme case when the dilatational wave completely disappears. From Equation (2-56),  $\lambda = 0$ ,  $C_p = \sqrt{2} C_s$ . Now, with the disappearance of the  $\lambda$  term, the dilatational wave speed becomes purely shear wave in nature, with the shear wave propagating at the dilatational wave speed. This situation occurs at Point A, see Figure 3.77.

Clifton (1966) discovered that, under combined stresses, unexpected (in the sense of instabilities) unloading may occur near the shifting boundary when the stress state at the boundary suddenly changes from a lower yield surface to a higher yield surface, see Figures 3.85, 3.86 and 3.87, implying that the material is rate-sensitive work-hardening. It is speculated that the rate-dependent characteristics of some horticultural materials under plastic work-hardening deformation can be related to the combined-stress states experienced by these materials.

Detailed studies of waves propagating under combined stresses can also be referred to Bleich and Nelson (1966), Clifton (1968), Clifton and Ting (1968), Ting (1969), Ting and Nan (1969), Ting (1970), Goel and Malvern (1971), and Ting (1972). One of the most significant aspects among these studies is that, under waves of combine stresses, the number of elastic precursor fronts and plastic wave fronts does not have to be restricted to one each. For instance, in the case of kiwifruit, two elastic wave fronts are present (see Figure 3.80), indicating a drastic change in the loading path within the (fully reversible) elastic limit has taken place. The first loading path is referred to by the biomechanics workers as the S-shape 'Sigmoid' curve and will be discussed in Section 3.7.6.

Examples of the heat diffusion phenomenon can be illustrated in Figure 3.91 with a persimmon specimen during its last stage of deformation that started at a strain of 40%. Prior to this, the specimen was under elastic-perfectly plastic deformation, before losing all material strength at 35% strain. Another example of the heat diffusion process in bubble-wrap packaging material specimens under impact is shown in Figure 3.92. It indicates that the initial stage of deformation on the plastic bubble membranes is elastic (up to  $Y$ ), and plastic afterwards, as shown by the constant wave speeds, as evidenced by the constant slopes in Figure 3.92, of both stages. Beginning at a strain of around 40%, a combined heat diffusion-plastic deformation process can be seen immediately before reaching the EOS region.

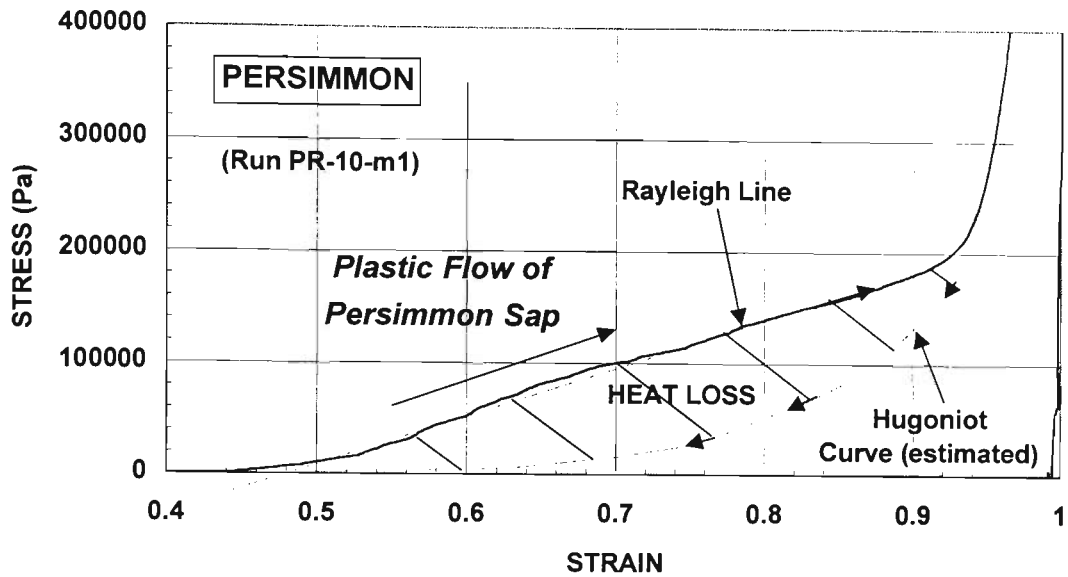


Figure 3.91 Heat diffusion process of persimmon under impact deformation under a strain rate of 103 /second. Laser-based Run PR-10-m1.

STRESS VS. STRAIN (0.9 Kg Strike Weight on Bubble Wrap) (10 cm drop)

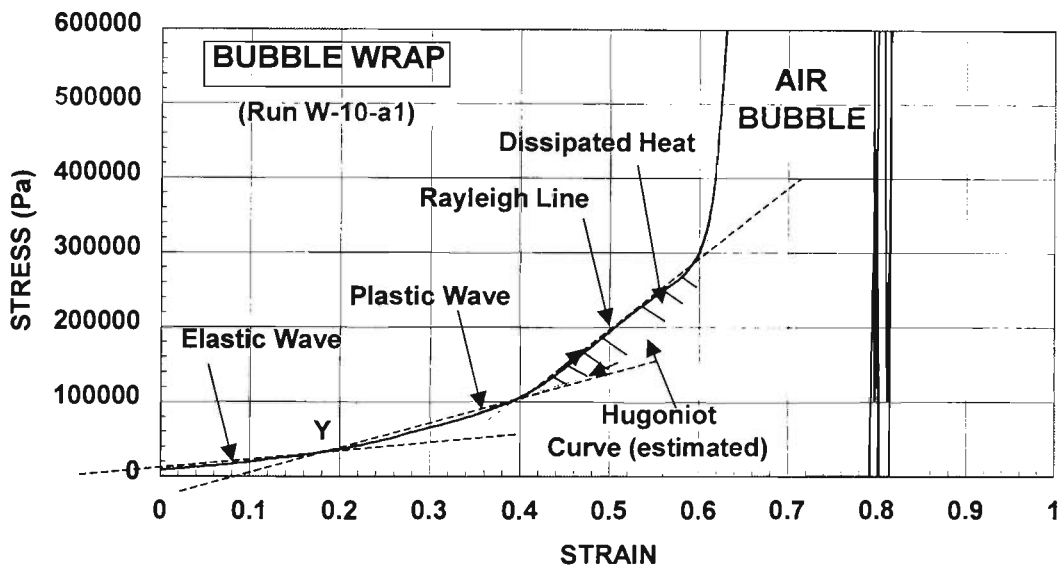


Figure 3.92 Heat diffusion process of a bubble-wrap packaging material under a high strain rate of 555/second. Laser-based Run W-10-a1. Specimen size is 25 x 50 mm. Drop height is 10 cm.

In Figure 3.91 the presence of the Rayleigh line is the clearest indication of the existence of a discontinuity within the material. The material flow of the persimmon sap is viscoplastical in nature (see the middle region in Figure 3.88). In other words, it deforms as viscous flow that can be quantified with a kinematic viscosity term similar to a Newtonian fluid. Within this second or middle region, the response of dynamic plasticity can vary from rate-independent perfectly-plastic to rate-

dependent viscoplastic, depending on the dynamic state of the medium. Within this domain, the viscosity of the medium is exactly analogous to that of a Newtonian fluid, according to Chu (1962). The material can be deemed as liquid-like.

This should not be confused with the rate-independent work-hardening plastic deformation we have discussed over the last few pages, because work-hardening denotes a expansion of the equipotential yield surface on the deviatoric plane as the material ‘hardens’. It also denotes solid-like material behaviours. Here the viscosity does not intervene in this domain as shown in the middle region of Figure 3.88, as well as the elastic domain as shown in the first region. The boundary conditions are here well defined at every stage or region of the material, see Mandel (1974).

The sharp rise in stress levels beginning at 60% strain in Figure 3.92 can be shown in Figure 3.93. The dynamic response of bubble wrap is one of the typical closed-cell packaging materials which is ideal-locking, Figure 3.93, see Hanagud (1966). Unless cells burst, the maximum strain cannot exceed 1 with locking density  $\rho_l$ . For non-ideal locking materials, Figure 3.94, such as sponge, they do not possess a distinct locking, see Hanagud (1966). No sharp jumps such as that shown in Figure 3.92 or 3.93 in stress levels are expected.

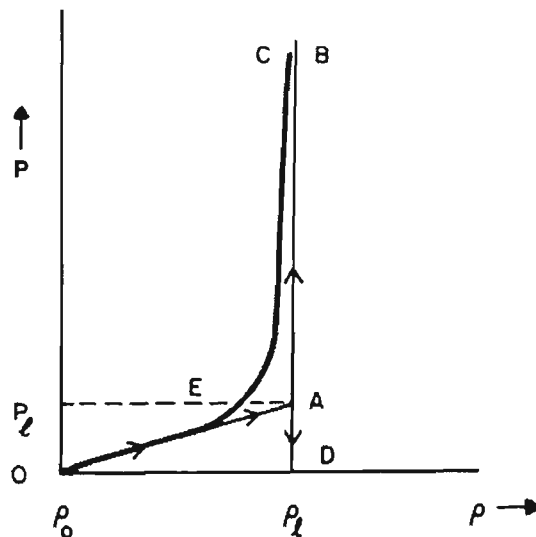


Figure 3.93 Schematic pressure-material density ( $P$ - $\rho$ ) curve typical of the closed-cell foam packaging materials such as bubble wrap and polystyrene foam. Subscripts “ $o$ ” and “ $l$ ” denote ‘original’ and ‘locked’, respectively. Curve is in the sense of stress-strain representation. Maximum possible strain reached is at density of  $\rho_l$ .

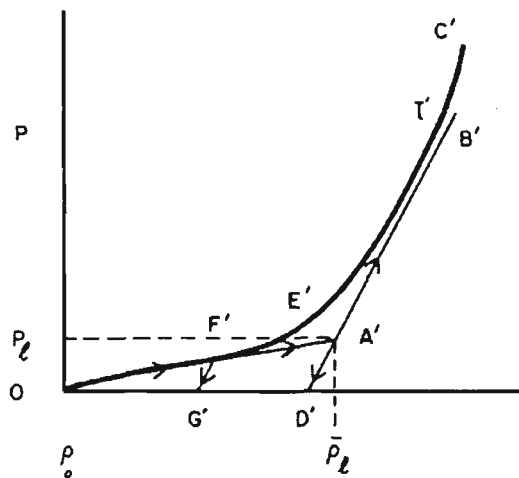


Figure 3.94 Schematic pressure-material density ( $P$  vs.  $\rho_0$ ) curve of non-ideal locking materials typical of the open-cell foams such as polyurethane foam or sponge. If fully reversible, the unloading path takes place along  $B'A'$  and  $A'O$ . If not fully reversible, the material will suffer plastic deformation. Material density can increase beyond the locking density  $\rho_l$ .

Heat diffusion processes, as shown by the presence of the Rayleigh line, occur as a means of energy dissipation predominantly in very soft produce. This includes tomato when its textures become perfectly-plastic, see Figure 3.95. Under perfect-plastic conditions, an upward trend of the dynamic curve in the form of a straight line (Rayleigh line) as for the case of tomato, Figure 3.95, provides evidence of heat diffusion. A perfectly-plastic condition denotes substantial deformation of produce textures that is insensitive to deformation rates, indicating the existence of viscous flow of the cell sap, see Figure 3.96.

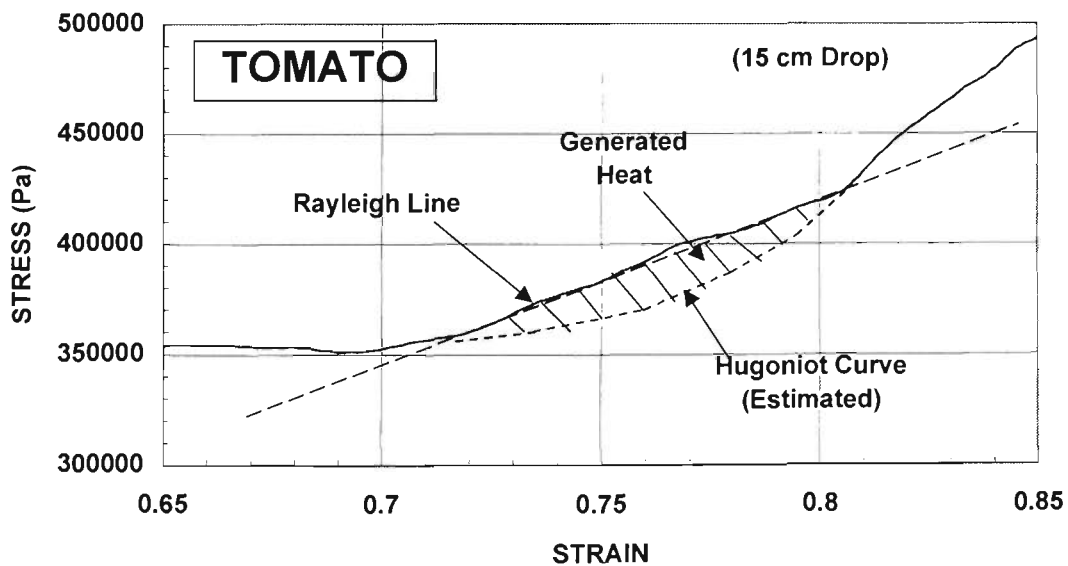


Figure 3.95 Heat diffusion process of tomato under impact deformation with a strain rate of 115 /second. Laser-based Run PO-15-m2.

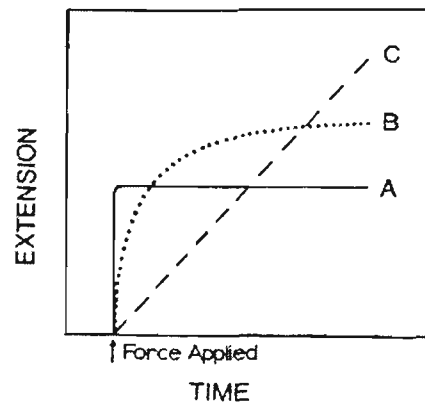


Figure 3.96 Schematic diagram showing the relationship between and time for instantaneous plant cell-wall extension under loading with (A) elastic, (B) viscoelastic, and (C) viscous flow of cell-sap. From Cleland (1971).

Based on Equations (2-55) with wave and heat representation, we have shown another expression in terms of the longitudinal and shear wave velocity. Their close resemblance to the acceleration wave speed implies that the dynamic properties of materials based on experimental data provide the best source of information for the development of constitutive equations for materials under dynamic regimes. For instance, the direct substitution of constitutive equations into the 1-D hyperbolic equation such as Equation (2-46) may reveal a loss in hyperbolicity and a gain in ellipticity, implying the presence of heat disturbance in the materials under loading. Based on the work of Chu (1962), we have shown the characteristics of propagating elastic, plastic and diffusion-type of disturbances in solid-like and liquid-like materials, and their direct relationships with longitudinal, shear, and wave-induced shear waves. Using experimental data from laser-based dynamic fruit testing, we have illustrated the various possible disturbance regimes ranging from elastic, plastic work-hardening, with or without heat diffusion, to pure heat diffusion. An illustration of heat dissipation has been made, using a thermodynamic approach, for the deformation of soft horticultural materials such as persimmon and certain cushioning materials such as bubble-wrap.

### 3.6.2 *The Onset to Plastic Instabilities in Soft and Moderately Crisp Horticultural Materials*

There is always competition between dynamic processes in horticultural materials under high loading: whether the materials undergo purely plastic deformation, resulting in perfectly-plastic ‘liquid-like’ deformation or, alternatively, would experience instabilities. Here let us focus on the possibility of the occurrence of instabilities. Material instabilities in produce textures can be categorized into two main types: (i) those arising as a result of plastic deformation such as shear banding, or (ii) as a result of damage due to fibrillar slippage and debonding of cell walls in produce. Shear banding tends to appear in soft and moderately crisp produce such as papaya, but cracking damage of fibrillar slippage and debonding tend to be the dominant instability type in crisper produce such as apple and pear. However, both shear banding and cracking may co-exist, particularly for those produce such as papaya the textures of which fall between soft and crisp. We will attempt to illustrate the dynamic features of instabilities using constitutive equations.

Most of the evaluations and modelling of the softening process use the softening plasticity models, that is, classical plasticity models with fracture mechanics theory. The two best viscoplastic models developed in recent years are the Perzyna and the recent Duvaut-Lions types. Both models are based on rate-independent assumptions but deform with viscoplastic strain rate,  $\dot{\epsilon}_{vp}$ . While it is not our intention to elaborate on the mathematical formulation and numerical procedures of the two models here, their major differences are addressed. Schwer (1994) pointed out that the Duvaut-Lions model is attractive in its ease of numerical implementation during the stress updating procedure of each loop of calculation, which is required for the conversion of the rate-independent elastoplastic to elastic-viscoplastic constitutive equations. A comparison of their mechanical models and stress-strain curves are shown in Figures 3.97 and 3.98.

The Perzyna and Duvaut-Lions model can be expressed by Equations (3-3) and (3-4), respectively, according to Sluys *et al.* (1992):

$$\sigma = \sigma_p + \sigma_{vp} = \bar{\sigma}_0 + h\epsilon_{vp} + \frac{\bar{\sigma}_0}{\gamma} \dot{\epsilon}_{vp} \quad (\text{Perzyna}) \quad (3-3)$$

where  $\bar{\sigma}_0$  is the yield strength as denoted by the friction element,

$h$  is the softening modulus,

$\gamma$  is the fluidity parameter,

$\sigma_p$  is plastic stress, and

$\sigma_{vp}$  is viscoplastic stress.

$$\sigma = \sigma_p + \sigma_{vp} = \bar{\sigma}_0 + h\varepsilon_p + \eta E \dot{\varepsilon}_{vp} \quad (\text{Duvaut-Lions}) \quad (3-4)$$

where  $\eta$  is the viscosity parameter (relaxation time), and  $E$  is the effective modulus,

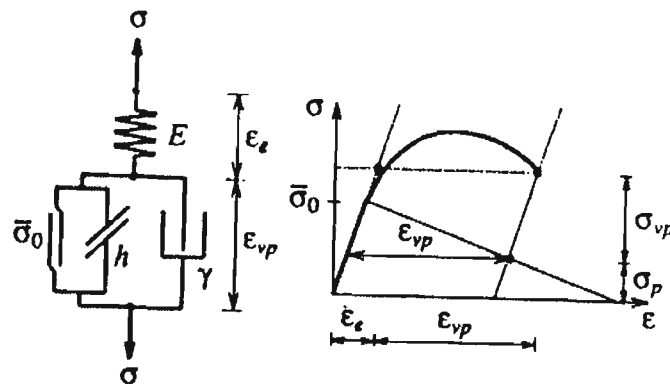


Figure 3.97 Representation of the Perzyna type of mechanical model and schematic stress-strain diagram. Subscripts 'e', 'p' and 'vp' denote 'elastic', 'plastic' and 'viscoplastic'. From Sluys *et al.* (1992).

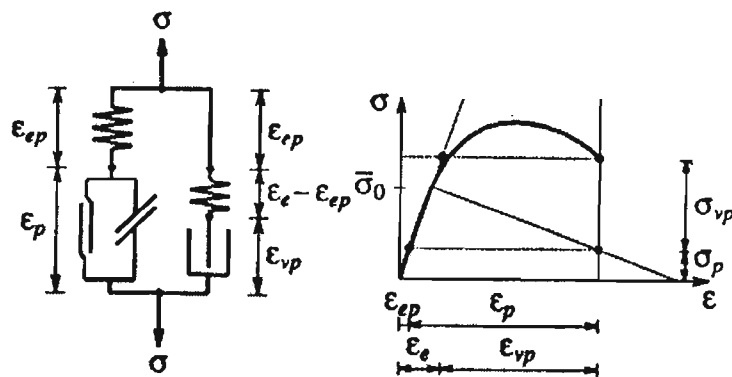


Figure 3.98 Representation of the Duvaut-Lions type of mechanical model, first proposed in 1972 by Duvaut and Lions, and schematic stress-strain diagram. From Sluys *et al.* (1992).

These two Equations are significant in the study of viscoplastic and softening behaviours of materials. In particular, a close comparison between the Perzyna model with the earlier Schwedoff model shown in Figure 3.99 for the dynamic response of kiwifruit looks very much the same, except that there is an extra softening element in the Perzyna model. However, like the Schwedoff model, all other mechanical models do not accurately represent the softening phenomenon, although in general they can well describe the uploading stress-strain behaviours of produce. In a stricter sense, perhaps we need to point out the misconception that softening behaviours are commonly assumed to initiate at the ultimate material strength. As shown in Figures 3.97 and 3.98, softening effects, as denoted by the

softening modulus,  $h$ , with a negative slope, should be taken into account immediately after a material exceeds its yield point ( $\bar{\sigma}_0$ ).

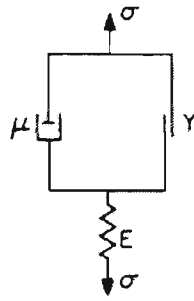


Figure 3.99 Schematic diagram of the Schvedoff model with its corresponding rate-independent elastic-perfectly plastic stress-strain characteristics. ‘Y’ denotes yield stress. From Reiner (1971).

For produce, the softening process is controlled by the  $h$  term (negative slope in a stress-strain curve) for linear softening as well as the viscous term, shown as the last term in both Equations (3-3) and (3-4). A linear softening will therefore not be expected to occur in very soft produce. In this sense, Equation (3-4) can be rewritten as:

$$\sigma = \sigma_p + \sigma_{vp} = \bar{\sigma}_0 + h\varepsilon_p + \bar{c}\dot{\varepsilon}_{vp} \quad (3-5)$$

where  $\bar{c}$  ( $= \eta E$  or  $\eta G$  depending whether the material is under dilatational or shear deformation) can be called the gradient influence material parameter.

Here the true meaning behind gradient influence (or, in a stricter sense, gradient deformation) requires some explanation. Aifantis (1984) first conjectured the existence of a well-posed solution for localized deformations under a softening process with a new approach. He successfully demonstrated this approach by introducing higher-order deformation gradients of the strain. Schreyer and Chen (1986) pointed out that a non-local constitutive equation with the stress as a function of strain and strain gradient works very well in the description of a softening process. Later, the term under the name of ‘gradient plasticity’ was finally coined by Muhlhaus and Aifantis (1991). The essence of the gradient plasticity theory is that the yield function,  $F$ , of a material under softening not only depends upon the stress  $\sigma$  and the inelastic strain  $\varepsilon_{in}$ , but also clearly depends on the second-order strain gradient,  $\partial^2 \varepsilon_p / \partial x^2$ . In other words, for a gradient-dependent strain softening, according to de Borst and Muhlhaus (1992):

$$\sigma = f\left(\varepsilon_p, \frac{\partial^2 \varepsilon_p}{\partial x^2}\right) \quad (3-6)$$

Also, here in the sense of Figure 2.29:

$$\varepsilon = \varepsilon_e + \varepsilon_p = \frac{\sigma}{E} + \varepsilon_p \quad (3-7)$$

Since  $h = \frac{\partial \sigma}{\partial \varepsilon_p}$ , it can be rewritten as:

$$\dot{\sigma} = h \dot{\varepsilon}_p \quad (3-8)$$

By substituting Equations (3-7), (3-8) and (2-43<sub>1</sub>) into Equation (2-45), the wave equation depicting the straightly linear softening condition, or with no gradient-dependency, can be expressed, according to Sluys *et al.* (1995), as:

$$\rho \frac{\partial^2 u}{\partial t^2} = \left( \frac{hE}{h+E} \right) \frac{\partial^2 u}{\partial x^2} \quad (3-9)$$

For the gradient-dependent case, by differentiating the Devaut-Lions Equation (3-5), the wave equation can be expressed, according to Sluys *et al.* (1995), as:

$$\rho \frac{\partial^2 u}{\partial t^2} = \left( \frac{hE}{h+E} \right) \frac{\partial^2 u}{\partial x^2} + \frac{\bar{c}}{h+E} \left( \rho \frac{\partial^4 u}{\partial x^2 \partial t^2} - E \frac{\partial^4 u}{\partial x^4} \right) \quad (3-10)$$

Though only expressed as a one-dimensional case, the implication of Equation (3-10) is significant. Equation (3-10) appears to be the best constitutive equation to date to have the potential of representing the softening process of virtually all horticultural materials. This is particularly so for those textures with dynamic stress-strain characterized by smooth peaks and relatively smooth post-peak softening curves as shown in Figures 3.97 and 3.98, see, for instance, Figures 3.23 and 3.24 for the case of dynamic deformation in banana flesh. In addition, the fact that viscoplastic deformation and its induced shear-banding instabilities and possibly micro-cracking can be fully represented here by a single wave equation allows workers to discern the interplay between the post-yield deformation and the initiation of instabilities, as well as the occurrence of diffusion.

Then, we assume that the harmonic wave which propagates through the material as the result of an impact be expressed as:

$$u(x, t) = A e^{i(kx - \omega t)} \quad (3-11)$$

By substituting Equation (3-11) into the linear softening wave equation (3-9), the wave frequency,  $\omega$ , can be expressed as:

$$\omega = ick \sqrt{\frac{-h}{E+h}} \quad (3-12)$$

where  $c$  is the elastic wave speed equivalent to the elastic precursor as shown in Figure 2.73, and  $k$  is the wave number.

The implication of Equation (3-12) is significant for produce with crisp textures, as well as for most of the closed-cell type of packaging materials like bubble-wrap. Equation (3-12) denotes that the wave frequency and speed becomes imaginary, meaning that the wave becomes a stationary wave at a singularity but unable to move. Here the wave front is ‘trapped’. The concentration of this large amount of wave energy at a single plane will immediately result in shear banding and possibly fracture the material at this plane. Here the thickness of the shear-band approaches zero. Most significantly, a process such as this is non-dispersive. This can be easily demonstrated by differentiating Equation (3-12) twice. A system can be considered to be dispersive if  $\partial^2 \omega / \partial k^2 \neq 0$ , according to Whitham (1974).

On the other hand, for the case of gradient-plasticity, by substituting Equations (3-11) into (3-10), the following expression for the positive root of the wave frequency,  $\omega$ , can be obtained:

$$\omega = ck \sqrt{\frac{h + \bar{c}k^2}{E + h + \bar{c}k^2}} \quad \text{or} \quad c' = c \sqrt{\frac{h + \bar{c}k^2}{E + h + \bar{c}k^2}} \quad (3-13)$$

where  $c'$  is the plastic/viscoplastic wave front speed, see Figure 2.73.

Here we note that  $c'$  is positive (or propagating) if:

$$\sqrt{\frac{h + \bar{c}k^2}{E + h + \bar{c}k^2}} > 0 \quad \text{or} \quad k \geq \sqrt{-\frac{\bar{c}}{h}} \quad (3-14)$$

In Equation (3-14<sub>2</sub>), since  $h$  is negative by nature, the value inside the square root is positive. In other words, there exists a critical wave number,  $k_c$ . If  $k > k_c$ , the plastic/viscoplastic wave front propagates, or  $c > 0$  (see Figure 3.100-right). If  $k < k_c$ , the wave front comes to a standstill. However, unlike the case with crisp produce, here in Equation (3-13<sub>1</sub>),  $\partial^2 \omega / \partial k^2 \neq 0$ , indicating that the system must be dispersive when the wave front comes to a stop, Whitham (1974). This clearly indicates why shear banding, and any subsequent fracturing, does not occur in soft produce under dynamic loading. Any tendency of shear band formation will be immediately dispersed, with the concentration of wave front energy now distributed through a more finite thickness instead of being trapped at a singularity plane with zero thickness, when the wave front stops propagating (see Figure 3.100-right).

Actually, this wave dispersion condition has been shown in Figure 3.90 with the ‘release wave’ on the unloading path. As the initial unloading release waves travel faster (as shown by a higher slope on the Hugoniot curve) than the later waves (lower slope), the ‘release waves’ diverge as time goes on. From Figure 3.100-right, we note that for the gradient-softening case, as  $k$  and  $\omega$  increases (that is, those of high frequency components), the wave speed of their wavelets approaches

the elastic wave front speed. But, as has been discussed in Section 2.2.8, these high-frequency components will be damped out quickly, see Figure 2.68.

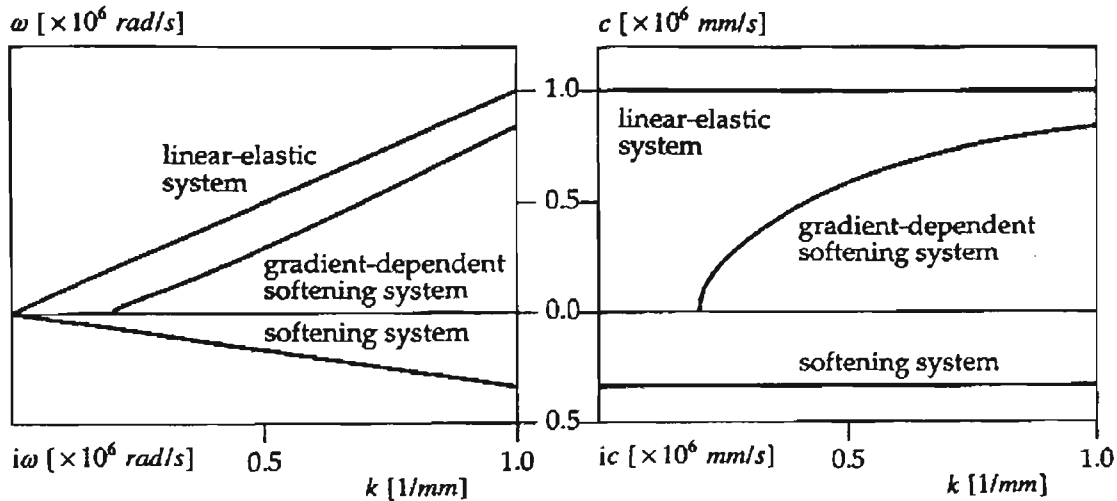


Figure 3.100 Schematic diagram showing relations of (left) wave frequency  $\omega$  vs. wave number,  $k$ , and (right) plastic wave front speed,  $c'$  vs. wave number,  $k$ , for linear-elastic, gradient-softening and straight linear-softening cases. From de Borst *et al.* (1995).

Referring to Equation (3-12), shear bands, sometimes called shear localizations or thermoplastic shear instabilities, are plastic deformation instabilities, first pointed out by Zener and Hollomon (1944). Their formation occurs primarily in polycrystalline solid metals under high strain rates, but also in a significant number of amorphous polymers, concrete, and other non-metals including horticultural produce. According to Equation (3-12), shear bands are highly concentrated plastic deformation in a narrow band form, and most likely act as an immediate precursor to catastrophic damage such as fractures. The reason for the formation of shear bands is the thermal softening of materials that overcome work hardening. Their occurrence in materials is governed by the critical shear strain rate,  $\dot{\gamma}_c$ , and the corresponding material parameter  $\{-C_v n / (\partial\tau/\partial T)\}$ . As shown by the straight line in Figure 3.101, it is clear that below a certain threshold, a shear band does not form. From this figure, a few other parameters (together they form the material parameter  $\{-C_v n / (\partial\tau/\partial T)\}$ ) which are related to the temperature field, play a dominant role in the formation of shear bands. The width,  $\delta$ , of a shear band has been elaborated in Equation (3-12). Here, as pointed out by Meyers (1994), a recently-obtained expression for shear band width,  $\delta$ , obtained by Bai *et al.* (1986), can be expressed as:

$$\delta = 2 \sqrt{\frac{\lambda T}{\tau \frac{\partial \gamma}{\partial t}}} \quad (3-15)$$

where  $\lambda$ ,  $T$ ,  $\tau$  and  $\partial\gamma/\partial t$  are the thermal conductivity, temperature, shear stress and shear strain rate, respectively.

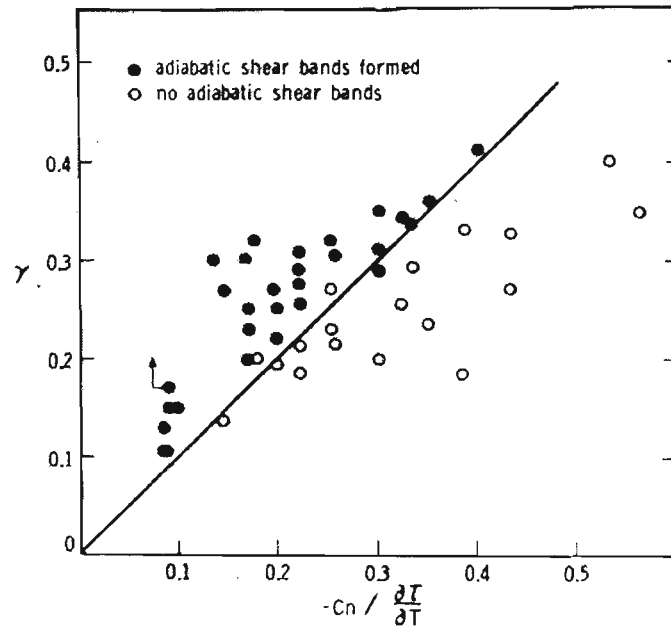


Figure 3.101 Relationship between measured true shear strain  $\gamma$  and the material parameter  $-C_v n/(\partial\tau/\partial T)$  where  $C_v$  is volumetric specific heat,  $n$  is strain hardening exponent,  $\tau$  is shear stress and  $T$  is temperature. (Here  $\tau$  is negative for compressive conditions) From Staker (1981).

Bai *et al.* (1986) arrived at an expression for the onset of instability that leads to shear banding. It assumes that the shear band formation is adiabatic, that is, the term  $\lambda$  in Equation (3-15) vanishes. Their result also relates the instantaneous effective shear modulus, the purely shear stress and strain,  $\tau$  and  $\gamma$ , respectively, within the shear band, and the material parameter  $-C_v n/(\partial\tau/\partial T)$  from Figure 3.101, as:

$$\frac{\partial\tau}{\partial\gamma} (> \text{ or } <) \tau \frac{\left(\frac{\alpha}{\rho}\right)}{\left(C_v/(\partial\tau/\partial T)\right)} \quad (3-16)$$

where  $\alpha$  is the coefficient of thermal expansion, and  $\rho$  is the material density.

Here the signs of “>” and “<” denote the instability or perturbation condition. The term at the right-hand side of Equation (3-16) is related to the slope of the line in Figure 3.101 and is pivotal in the interpretation of the onset of shear band formation. It is the introduction of this temperature perturbation that initiates a localization process. In other words, the perturbation triggers the formation of localized shear banding instabilities. This occurs when the “<” sign is applied to Equation (3-16).

Shear banding occurs predominantly in produce textures that are soft and moderately crisp, but our results do not indicate that they occur in crisp produce such as apple and pear in the pre-critical domain. The experimental stress-strain relationships obtained for papaya and potato are shown in Figures 3.102 and 3.103, respectively. The results provide evidence of shear band formation. Like fibrillar slippage, shear band instabilities also occur in the pre-peak domain of deformation in soft and moderately crisp produce. One feature of shear banding which is distinctively different to instabilities due to damage relates to the material modulus before and after the occurrence of instabilities. Within the pre-peak and peak domain, fibrillar slippage and horizontal plastic jumps in the form of staircase result in the degradation of the effective modulus. This does not apply to shear banding, as can be seen in Figures 3.102 and 3.103. There is evidently negligible change in the effective modulus of the material before and after the occurrence of shear banding.

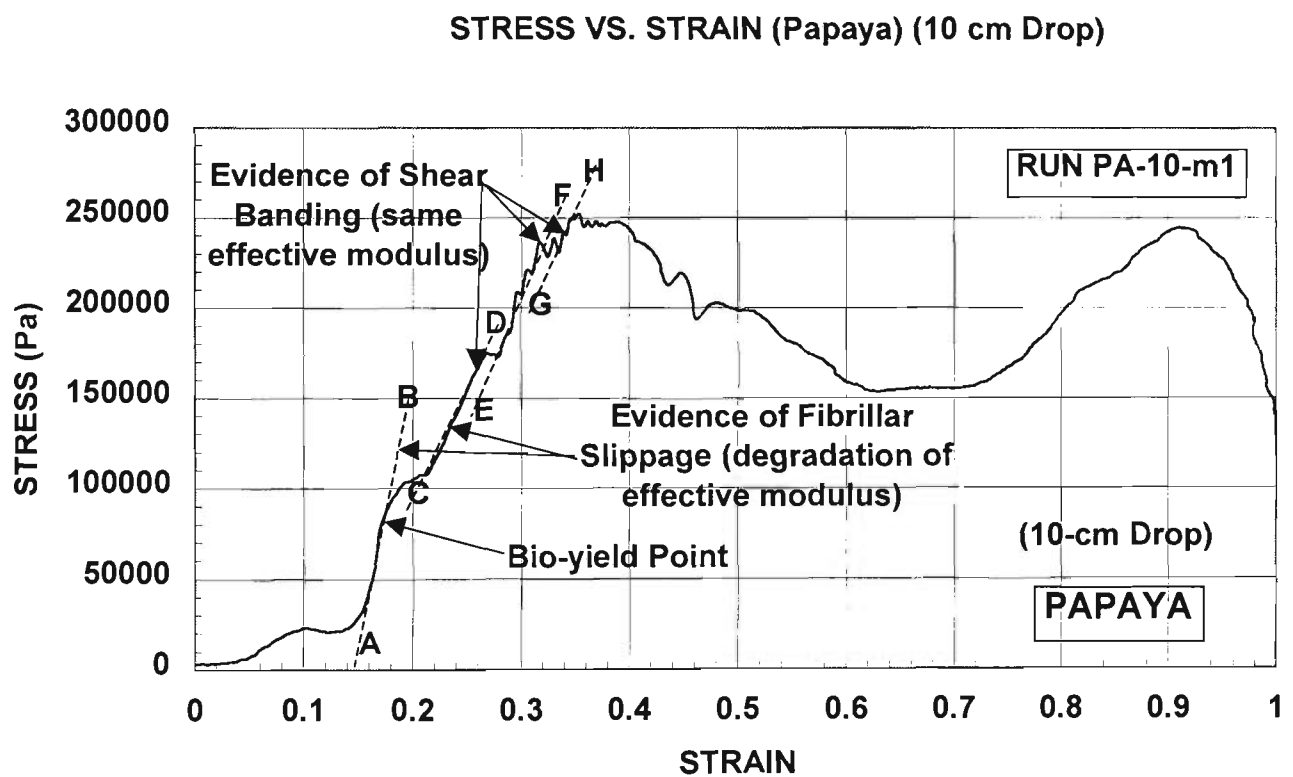


Figure 3.102 Stress-strain relationship of papaya highlighting the evidence of fibrillar slippage and shear banding activities beyond bio-yield point in laser-based test Run PA-10-m1. (Drop height is 10 cm; strain rate is 127/sec.)

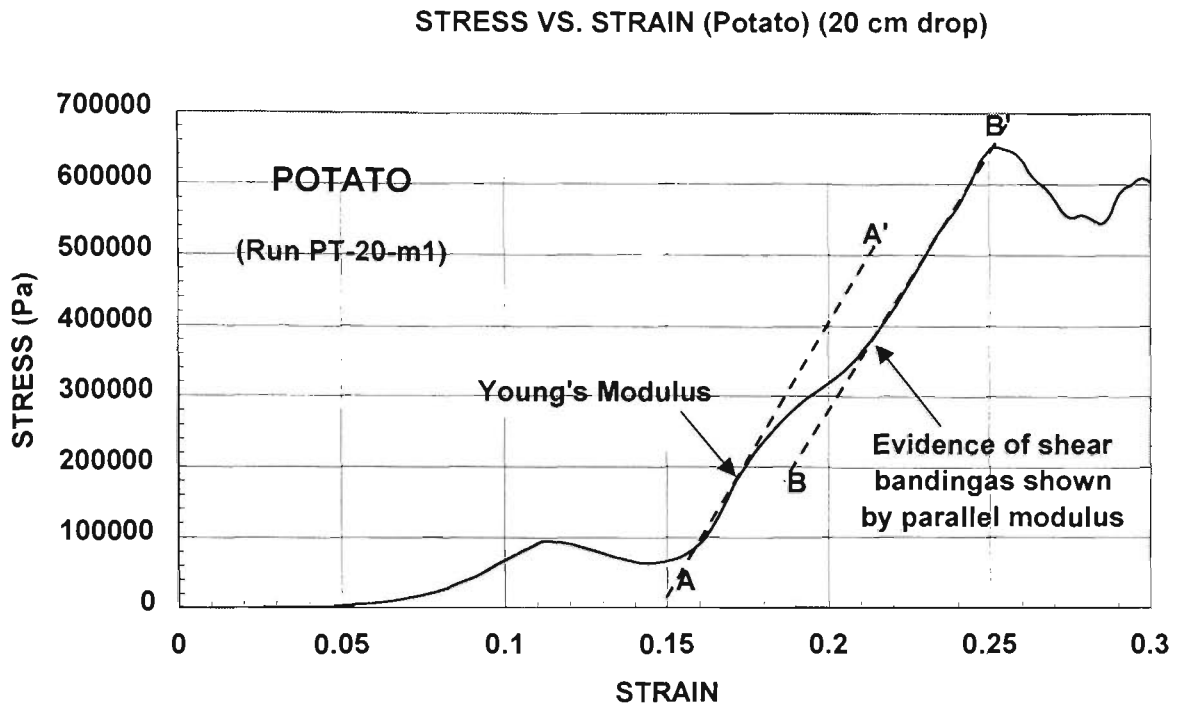


Figure 3.103 Stress-strain relationship of potato highlighting the evidence of shear banding activities in laser-based test Run PT-20-m1 with strain rate of 142/sec.

## 3.7 DYNAMIC INSTABILITIES DUE TO DAMAGE IN HORTICULTURAL MATERIALS

### 3.7.1 *Introduction: Crack Growth in Horticultural Materials*

According to a review on mathematical modelling in materials science prepared by the National Research Council of the U.S. National Academy of Sciences (1993), there are basically three hierarchical levels of materials characterization; namely, microscopic, mesoscopic and macroscopic levels. This chapter is concerned with the phenomenon of dynamic crack growth in horticultural materials under microscopic and macroscopic levels, and the mesoscopic transition between microscopic and macroscopic levels.

The microscopic level is concerned with the characterization of materials at their atomic or molecular scale such as the atomic lattice layers in a metallic crystal or fibres on cell walls of produce that are made up of molecular chains of polymers. The dynamics of individual particles or chains at microscopic level have been successfully described by fundamental theories such as Newton's Laws (many-body problems). However, the complete description of material behaviour at the microscopic level is often complicated, because the entire molecular-chain structures are involved. Most of the material characterization work was done in the past at the macroscopic (or continuum) level, and described by simplified mathematical models using the available computational tools, but still preserving the relevant physics and dynamic responses of the materials. However, many materials exhibit distinct characteristics too small to be treated at the macroscopic scale and need to be investigated at microscopic level. Examples can be drawn from the phenomenon of micro-crack instabilities in horticultural materials under dynamic loading.

If the micro-cracks begin to join up, the instabilities tend to propagate. In that case, the phenomenon is often too large for a microscopic scale of treatment. On the other hand, they cannot in many cases be effectively treated macroscopically, although they often possess material properties that are large enough to be treated under such scale. The most common examples are phenomena such as phase-transition in metallic materials and localized-to-global cracking of fibre-reinforced composites, concrete, horticultural produce and many strain-softening materials that undergo transition of material characteristics. The dynamic behaviours and distinct features of these materials under such conditions can only be satisfactorily treated under meso-scales that fall between the microscopic and macroscopic scales.

The phenomenon of crack growth in horticultural produce has not been given due attention in the past, and, with the exception of a few monographs such as Vincent (1991b), little published research is available. In this section, focus is on the various causes of the cracking process under dynamic loading conditions. Crack growth in engineering materials at room temperature has been the subject of much research work associated with linear-elastic fracture mechanics (LEFM). In general, LEFM can be well characterized by the fracture toughness ( $K_c$ ), stress intensity factor ( $K$ ), crack resistance and crack velocity in the materials undergoing fracture. For horticultural materials, however, the crack growth phenomenon is more complex and heavily influenced by the following dynamic processes:

- (i) Pre-peak micro-structural instabilities such as shear banding in materials, which are characterized by negligible reduction of the effective modulus throughout the loading process - see Section 3.6.2. Shear banding is a direct consequence of dynamic plastic deformation. It is not the consequence of any material damage. However, it often initiates material damage.
- (ii) Pre-peak dynamic material damage in horticultural materials, which often manifests itself in the form of a distinctive serrated stress-strain curve and results in fibrillar slippage. This phenomenon always results in pre-peak degradation of the effective modulus during the loading process. The immediate consequence of fibrillar slippage is localized micro-cracking, leading to propagation of meso-cracking if the micro-cracks start to join up.
- (iii) Various scales of crack propagation or, in the most severe case, fracture characteristics. These processes can be the direct consequences of (i) and (ii). However, if the dynamic response of the material is relatively brittle, they will be independent of (i) and (ii). In contrast to fracture, macro-scale cracking is usually a gradual process often associated with strain softening, although both are global (or non-local) phenomena.

We note that the material instabilities covered in (i) are caused primarily by plastic deformation, and eventually will most likely end up as cracking or even fracturing, as in some cases of crisp textures. The most prominent instability due to plastic deformation is shear banding. We also recall from Equation (3-12) that shear banding is directly caused by a stationary (or ‘trapped’) wave in a singularity plane with negligible thickness and wave dispersion. The ‘trapped’ heat softens the materials, forming a shear band, as has been elaborated in Section 3.6.2.

In this section, we will also focus our discussion of dynamic instability on fibrillar slippage that is plastic in nature, particularly on the often serrated, or staircase-like, material hardening characteristics under dynamic loading conditions, see (ii)..

For (iii), material damage is the primary cause of crack growth under the general category of cracking within the broad context of fracture mechanics, with negligible effect due to plastic deformation. Here cracking can vary from meso-cracking to macro-cracking. We will focus on the cracking characteristics of the relatively crisp produce textures, as they are prone to be dominated by the meso-scale and macro-scale cracking failure modes. We will also focus on the special features in viscous cracking of the softer produce textures.

### ***3.7.2 Dynamic Instabilities due to Fibrillar Slippage***

There is a marked difference between a brittle cracking process in materials such as concrete and fibrillar slippage in horticultural materials. For brittle materials such as concrete, they are best to be characterized by their degree of damage rather than slippage. Damage is primarily a cracking process, whereas slippage, and in horticultural materials, fibrillar slippage, is a complex mix of plastic slippage and cracking processes. Fibrillar slippage, which occurs in most produce with crisp texture, signifies a microscopic phenomenon with the micro-fibrils on the cell-walls of produce slipping passed one another when the cell-wall surface is under loading. Slippage activities begin with plastic deformation but evolves into micro-crack damage. Plastic deformation of material often allows the material to undergo much higher strain than that in brittle material. As a result, meso-scale damage starts to form in brittle bodies such as concrete at a much earlier stage than horticultural materials, because the individual micro-cracks in brittle materials are unstable and much easier to link with their neighbours to form propagating meso-cracks. On the other hand, the damage process in horticultural materials which involves a complex combination of plastic slippage and cracking is often referred to as ‘viscous cracking’ by materials scientists and can be viewed as more ‘stable’ than concrete. This is so because material failure can be delayed by the presence of plastic deformation, and is revealed in dynamic response curves as horizontal jumps. In this study, examples of fibrillar slippage were found in pawpaw fruit, as shown in Figure 3.104.

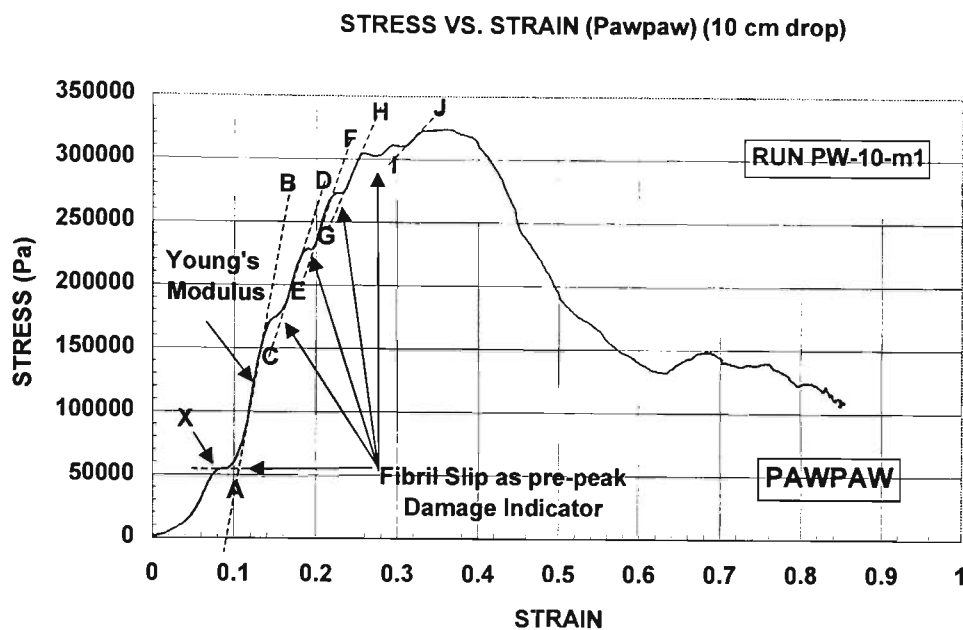


Figure 3.104 Dynamic stress-strain relationship of pawpaw from laser-based test showing well-developed pre-peak degradation of the effective modulus due to fibrillar slippage. Strike weight is 0.9 kg at 10-cm drop height. (Run PW-10-m1)

As Figure 3.104 shows, fibrillar slippage is distinctively different from shear banding. In shear banding, no pre-peak degradation of the effective modulus is expected. Rather, Young's modulus is maintained on the unloading curves after each slippage due to shear banding. On the other hand, Figure 3.104 shows that pre-peak degradation of the effective modulus is a distinct feature of fibrillar slippage, as shown by the gradual decrease of the effective modulus from AB (Young's modulus) to IJ. The unloading curve, characterized by horizontal slippage (or jumps) that represent plastic deformation in nature, exhibits a distinctive staircase-like feature. We will next turn our full attention to fibrillar slippage.

Biomaterials, including horticultural produce, are sensitive to the scale of their sizes as far as the analysis of their strength and toughness is concerned. In general, the strength of the individual components of biological materials is affected by the scale of their component sizes that range from micro-scale, such as the long molecular chains of micro-fibrils, to macro-scale, such as fruit tissues and cell walls. At the micro-scale in terms of molecules or molecular chains of fibrils, the toughness parameter is controlled by interfacial adhesion with low shear modulus between the interfaces, that is, wall-to-wall contacts among the fibrils. This implies that each fibril acts independently of the other. However, if an individual fibril fracture occurs, the load is immediately redistributed evenly among the remaining fibres. This is one of the characteristics of micro-fibrils that constitute the cell walls in a highly complicated structural form. In other words, biological materials are highly notch-sensitive.

By piercing a hole in a produce specimen, we can significantly reduce its strength and raise the level of risk of micro-crack initiation. Because the fibrils are bonded together with heavy shear connexion, the fracture of one fibril will influence its neighbouring fibrils, releasing and transmitting energy from the micro-crack to other fibrils in a 'domino' fashion. As a result, instabilities like fibrillar slippage, which is the dominating form of instability within the cell walls of crisp textures, will commence, and the ultimate strength of the specimen will be lowered. The most common culprits for hole piercing of plant cell walls are fungi on plant surfaces. Under a dynamic loading process, how much the ultimate strength is reduced depends heavily on the instantaneous kinetics of the propagating instabilities, as a result of different loading conditions. The study of fracture mechanics is concerned with how the failure stress (ultimate strength) of materials will be affected by factors such as the size of cracks, notches, flaws and defects. For biomaterials, additional parameters are also involved, such as loading conditions, micro-cracking kinetics, micro-/macro-cracking interactions, material anisotropy (for fruit textures and timbers, for instance), and the list goes on.

The relationships between the applied strain and the amount of dissipated energy in the composite material matrix during dynamic deformation are complex, and much more so for biomaterials and horticultural produce that are composed of fibres with sophisticated structures. One of the examples of complex fibre-dominated materials can be found in animal tendons, which are primarily made of fibre-bundles, Figure 3.105.

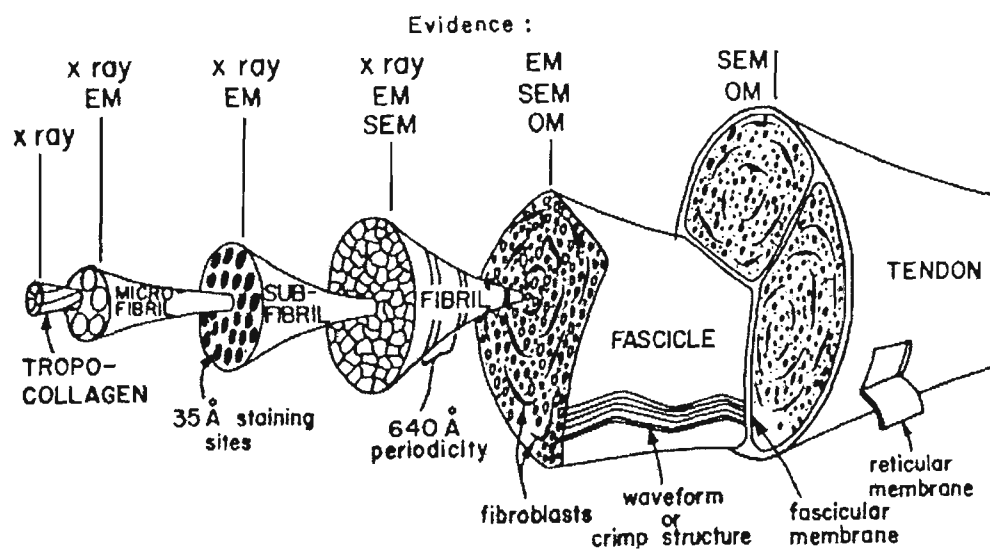


Figure 3.105 Structure of an animal tendon as evidence from X-ray, electron microscopy, scanning electron microscopy and optical microscopy. From Kastelic *et al.* (1978).

During the initial deformation stage, their fibrous materials tend to elongate with a relatively flat 'toe' part, see region from O to A in Figure 3.106. This feature is commonly found in produce under dynamic loading. When this low-stress stretching process occurs, the molecular structures of the polymeric cell walls start to rearrange and straighten. This results in an OA 'toe' and undergoing extension from A to C. The stress-strain curve goes from O to A, then to C. It contributes to the plastic deformation, while beyond C the slipping of the molecular polymeric structures contributes to damage. Pre-peak slippage can also occur between A and C. The S-shape OABC feature is called Sigmoid curve by Gordon (1978). The chain stretching from O to A is related to cell volume fraction and turgor in cells, as well as activities of loosening of the cellulose micro-fibrils, Atkins and Mai (1985). Beyond A, fibrillar slippage is expected to commence, see Figure 3.107.

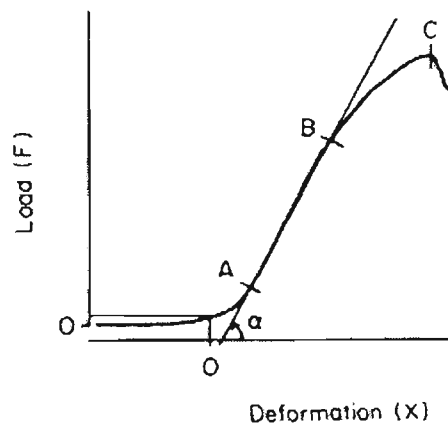


Figure 3.106 Load-deformation curve for a rabbit limb tendon brought to failure with a constant rate of elongation. A-B is almost linear. At point C the maximum load is reached. From Fung (1993).

As shown in Figure 3.107, the polymer-chain straightening and subsequent extension towards the ultimate limit of the chain contributes to the plastic deformation of the chain, while molecular slipping results in damage. In the case of produce, the ground tissue (or parenchymatous tissues) is composed of largely undifferentiated sap-filled cells protected by cell walls. The main constituents of the cell walls are primarily cellulose, the unbranched long-chain polymer of  $\beta$ -glucose. They organize into unbranched threads called micro-fibrils with diameter around 300 Angstroms of indefinite length. These micro-fibrils are the building blocks of a thread-like structure called fibrils in a way much like the animal fibrils as shown in Figure 3.105. But, unlike the animal fibrils, which in turn group themselves forming tendons, micro-fibrils of produce form the structural skeleton of the produce cell walls and largely determine their physical properties. Mature produce cell walls are commonly divided into a number of discrete layers, Duckworth (1966), and the micro-fibrils are more regularly arranged, lying almost parallel to each other within the wall-layer, as can be seen in Figure 3.108. Conflicting reports such as that of Esau (1965) regarding the parenchyma cell wall as a primary one with no secondary deposition of additional layers seem out-dated. A sketch of

the fibrillar slippage mechanism is shown in Figure 3.109 that can represent this process within the cell-wall structures of produce.

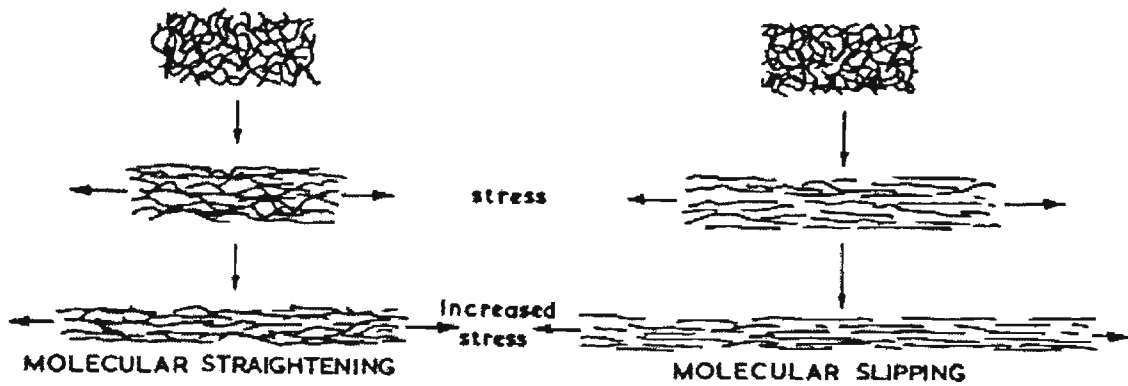


Figure 3.107 The effect of stress on the molecular structure in a linear polymer under initial straightening (left) and slipping (right). From Higgins (1994).

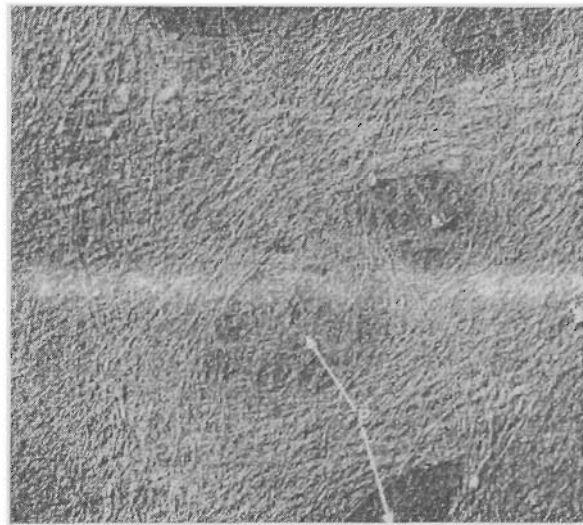


Figure 3.108 An electronic micrograph of the surface of a parenchyma cell-wall from Jerusalem artichoke showing the micro-fibrillar structure, and pit fields (p) which are thin areas of cell-walls coinciding in walls of adjacent cells to permit communication between the protoplasts of different cells. (X 7,710) From Duckworth (1966).

According to Fry (1989), it is more precise to define the slippage as the breakage of the cross-link non-covalent bonds between cellulose micro-fibrils. The slippage can also be due to the breakage of the stronger covalent bonds between the more rigid cellulose micro-fibrils and the more flexible ‘glue’ matrix (called glycoprotein extensin) where micro-fibrils are embedded, according to Swords and Staehelin (1989), without breaking the primary structures of the interwoven cellulose micro-fibrils. Detailed discussion on the microscopic observations of these interwoven structures has been presented by Roland & Vian (1979), Peterlin (1983), and McCann & Roberts (1991).

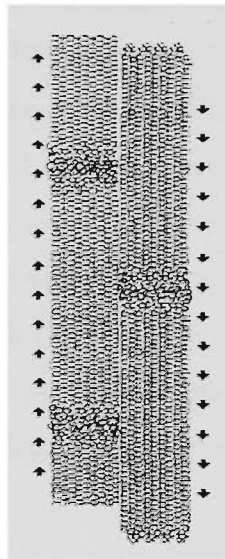


Figure 3.109 Fibrillar slip process in long-chain polymers and fruit cell walls. Note the opposite directions of movement as indicated by arrows. From Stachurski (1987).

Results obtained from the laser-based dynamic response of Golden Delicious apple are shown in Figure 3.110, after the cell-wall micro-fibrils are straightened out in region OA, They undergo deformation where Young's modulus is characterized by AB. Fibrillar slippage instabilities can be seen in region BC, as evident in the reduced effective modulus CD that follows immediately after the damage. A distinctive plateau DE can be observed.

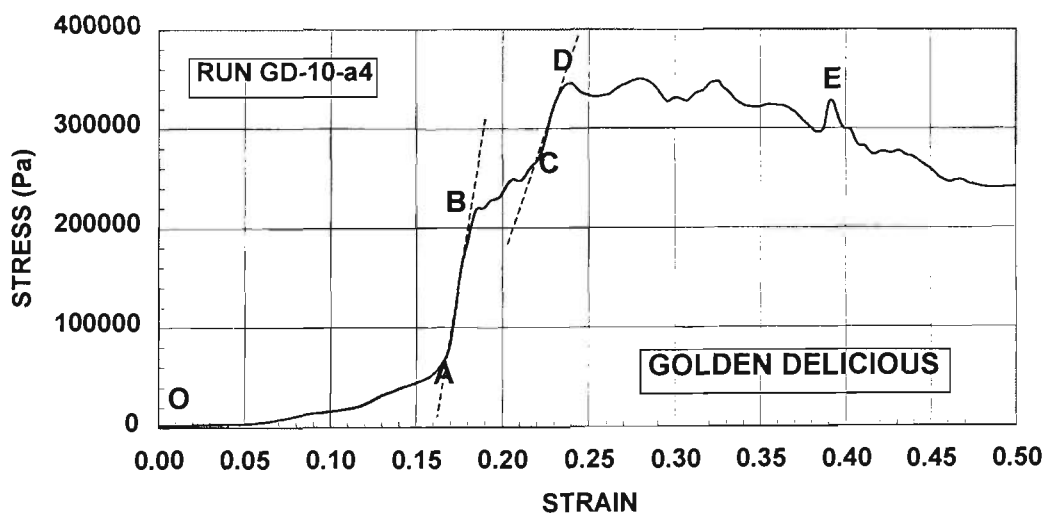


Figure 3.110 Dynamic stress-strain relationship of market-fresh Golden Delicious apple tissue under a laser-based test at 10 cm drop with strain rate of 133/sec. and strike weight of 0.9 kg. (Run GD-10a-4)

Summing up fibrillar slippage, we note that, for most cases, the fibrillar slippage mechanism can be characterized by two features: (i) a horizontal plastic strain slippage on the stress-strain curve

and (ii) a distinctive pre-peak degradation of the effective modulus of the material. Many examples of fibril slips similar to Figures 3.104 and 3.110 can be found in our study in produce with crisp textures under dynamic loading. It is a form of pre-peak instability that is distinctive from shear banding instability. Successive serrated features, such as abrupt stress jumps and horizontal slippage of plastic strain, are predominantly found in produce with relatively crisp textures. This damage process is unpredictable. Pre-peak plastic instability such as shear banding may be ‘predictable’, with consistent dynamic responses under different loading conditions. Examples can be found in moderately-crisp produce such as papaya (Figure 3.45) and eggplant (Figure 3.46). As has been pointed out in Section 3.4.3, both shear banding and fibrillar slippage can concurrently occur in the pre-peak domain of moderately crisp produce.

### 3.7.3 *Micro-Crack to Meso-Crack Transition in Horticultural Materials*

Let us focus on the slippage instabilities by re-plotting the region BC in Figure 3.110 on an enlarged scale in Figure 3.111. The growth of micro-cracks is in quite an orderly fashion, following the staircase-like BCDEFGH path. It is orderly in the sense that disorderly fibrillar slippage, which is realized here as micro-crack formation in a way similar to composite fibre debonding, is, from time to time, arrested by regions of superior cohesive energy (or work of fracture). The micro-fibrils slip in orderly fashion passing each other at particular stress levels, BC, DE, FG, according to the shear modulus of the cement bonding which holds the fibrils together.

The micro-crack growth in these damage-tolerant solid materials may also be seen as a purely random process that develops in many small but finite increments. Micro-crack growth increments such as those shown in Figure 3.112 are attributed to the increasing applied dynamic stress, according to Krajcinovic (1996). From Figure 3.111, the micro-cracking due to fibrillar slippage can be seen growing from an initial slip at a strain of 18.5% at Point B to a strain of 21.2% at Point G. This corresponds to an applied stress of 0.22 MPa at the bio-yield point B, and to 0.248 MPa at Point G. Here, Point B can be interpreted as the material point with a crack size,  $\alpha_0$  (from defects which originally exist). When the micro-crack grows to a critical size,  $\alpha_c$ , macro-fracturing will initiate. These kinds of solid, which are initially stable with micro-crack growth but subsequently becoming unstable (macro-cracking), have been named micro-heterogeneous solids, while the more unstable and brittle solids, which suffer instantaneous fracturing when their yield points are exceeded, are termed micro-homogeneous solids, see Krajcinovic (1996).

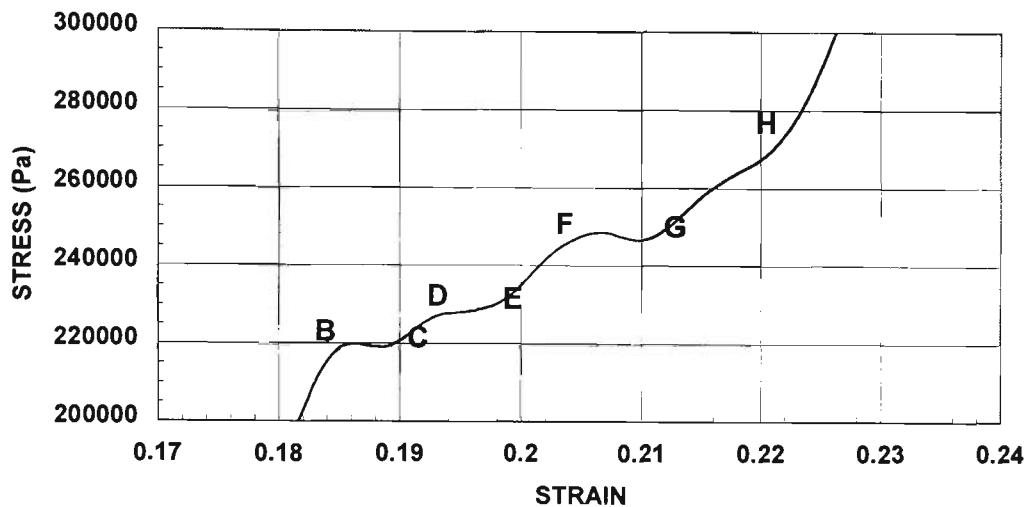


Figure 3.111 Dynamic stress-strain relationship of market-fresh Golden Delicious apple tissue showing bio-yield point and subsequent instabilities due to fibrillar slippage (Run GD-10a-4)

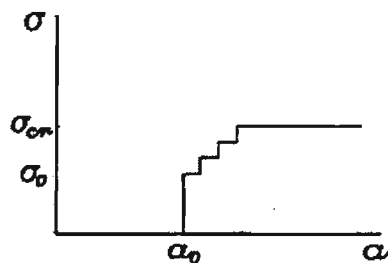


Figure 3.112 Schematic stress-strain diagram of an initially stable micro-heterogeneous solid. ( $\sigma_0$  = bio-yield point;  $\sigma_{cr}$  = fracture (critical) stress; and  $\alpha_0$  = initial crack size). From Krajcinovic (1996).

Micro-crack growth can be stable initially. The cracks extend individually but do not join together. Once they start joining, the mechanism becomes unstable, and the joint micro-cracks start propagating forming meso-cracks. At the meso-scale level, the analytical models should be focused on statistical ensembles of micro-cracks and their crack densities, rather than the global scale. This so-called 'meso-scale' damage state denotes full homogeneity within the representative volume element (RVE), see Jeronimidis (1991). In other words, the material properties are locally and statistically uniform in the RVE.

The statistical approach is a relatively recent development, and has become more significant in the past 10 years or so, as a result of growing discontent with the regular macro-scale analysis that is often erroneous. Here, macro-scale analysis denotes all continuum damage mechanics (CDM) models extensively used by engineers. For example, a cylindrical apple specimen with no initial defects subjected to high loading (called unnotched specimens) will find most of the impact energy

dissipated in creating and propagating new micro-cracks. Thus, a macro-scale model, or engineering model, based on the energy sinking only onto a single macro-crack, is unable to account for the actual work of fracture in creating the numerous micro-cracks and thus provides erroneous analysis. Here, it is not our aim to discredit the significance of the macro-scale models. Rather, we should point out their major limitations. To be applicable, a macro-scale model requires (i) a valid and realistic estimation of damage parameters, as well as (ii) a truly representative constitutive model that is normally fairly restrictive in terms of applications.

The macro-scale models, which are in fact most commonly used, are phenomenological in nature in the context of CDM, a term believed to have been coined by Rice (1975). In this seminal article, Rice endeavored to establish a direct link between macro-scale (global) and micro-scale (local) defects and damage processes in terms of the (more classical) thermodynamic approach such as entropy, temperature and/or the internal energy density associated with materials. Using this micro-/macro-mechanical approach (or this type of model), one can define the dynamic state of the materials in a more definite sense, in terms of the internal energy density of the materials, and monitor the kinetics of change or damage evolution in the materials. Our approach, as elaborated in Section 3.7.5, was based on Rice's.

The most recent attempts of developments have been more focused on the (global) statistical averaging or ensembles of (local) parameters over the RVE. The global reference comprises macro-scales, while the local reference comprises meso-scales. A summary of the scales for analysis is here listed in Table 3-9, Krajcinovic and Sumarac (1987):

Table 3-9 Volume scales of cracks and their relations to analytical models.

<b>Scale</b>	<b>Material</b>	<b>Defects</b>	<b>Models</b>
Micro-scale	Atoms, molecular chains	Dislocations	Material sciences
Meso-scale	Ensembles of cracks	Micro-cracks, pores, fibrillar slippage	Micro-mechanics
Macro-scale	Test specimen structure	Macro-cracks, shear band	Continuum mechanics

The relation between CDM and fracture mechanics is a matter of scale. It often seems contradictory if the wrong scale is used. For instance, a micro-crack, once initiated, is supposed to keep growing unchecked until failure occurs, if the applied external load is ever so slightly increasing. However, the fact is that a large population of micro-cracks can exist in most solids

without showing signs of failing. A micro-crack sees the surrounding medium as strongly inhomogeneous and reinforced by many energy barriers, see Figure 3.113. Once the meso-crack starts propagating it can be arrested only by energy barriers that are normally associated with a change of the micro-structural texture of the material. These crack-arresting barriers can be penetrated only at the expense of additionally supplied (external) energy. Jackson *et al.* (1988), as shown in Figure 3.114 has observed a crack growth path of this nature in biomaterials.

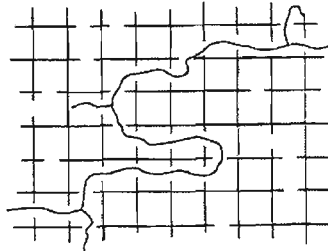


Figure 3.113 Schematic diagram of micro-crack growth in a network of energy barriers. Micro-cracks that are encircled by barriers will be arrested. From Krajcinovic (1996).



Figure 3.114 Crack growth path through nacre viewed in an orientation parallel to the nacre surface. From Jackson *et al.* (1988).

The ‘engineering’ definition of a macro-crack is the size of the crack that exceeds the distance separating the nearest adjacent cracks. At that point, the crack may be assumed to be a macro-crack and rupture is imminent. This has been generally recognized as the onset of global failure. The problem of scaling is in many ways a result of the choice of analytical models. The strong preference for global continuum models, including virtually all CDM models that deal with homogeneous continua and (preferably, incrementally and smoothly) varying parameters, is understandable for their relatively simple mathematical structures and computational ease. However, the range of applications based on such available continuum theories should always be limited to volumes of material which contain a statistically large ensemble of samples including matrix bodies, defects, micro-cracks, etc. to render the averaged values representative. There is always a risk factor involved when dealing with global parameters such as macro-cracks whether they are enclosed by at least a RVE.

Up to recent times, experimental data from the observations of macro-scale events are still the single most reliable and important source of information in the analysis of micro-crack growth and meso-crack propagation instabilities and their transformation to macro-fractures. The reason is that the studies of micro-crack kinetics primarily depend on global (meso-scale continuum) theories which are based solely on available experimental data. Understandably, this same spirit of observational approach based on experimental data also applies to our present studies. Recent trends of development have been more focused on the localized micro-/meso-scale observations and theoretical foundations. This has been achieved with an increasing emphasis on homogenization (averaging) procedures which are able to provide links to global continuum models that contain only the salient properties of materials by a proper selection of representative volumes and damage parameters, according to Krajcinovic and Mastilovic (1995) and Krajcinovic (1996). As an example, this may be shown in Figure 3.115, by re-plotting Figure 3.110, focusing on the change of the effective modulus from initial Young's modulus, as a result of kinetics dominated by micro-crack growth instabilities.

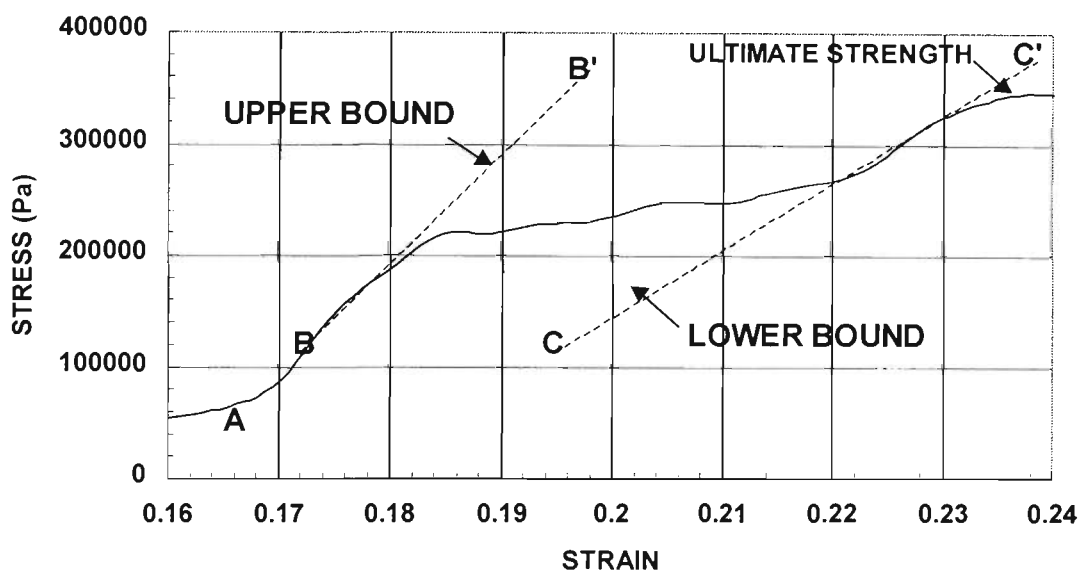


Figure 3.115 Dynamic stress-strain relationship of market-fresh Golden Delicious apple tissues from laser-based test under a strain rate of 133/second showing instabilities as a result of abrupt change (at B) as well as continuous switching (between BC') of 'unsaturated' stress-strain curve to domains of inferior toughness. (Run GD-10a-4) (10 cm drop)

A new global parameter,  $S$ , is required here for the micro- to macro-cracking transition analysis.  $S$  is often called the overall compliance tensor of materials. The reason for incorporating  $S$  into the analysis is that precise information related to the details of the micro-cracking pattern is usually unknown. The situation is usually complicated by a rather random disposition of energy barriers and domains of reduced toughness in produce materials, for instance, the pit fields on the parenchyma cell walls shown in Figure 3.108. By choosing a representative damage parameter which

homogenizes the ensemble of micro-defects (for instance, the modified Lemaitre damage parameter,  $D_m$ , together with  $\mathbf{S}$ , which is considered just sufficient to capture the salient properties of the random medium, the link between local and global pictures is established.

Actually, this overall (effective) compliance tensor,  $\mathbf{S}$ , is precisely the outcome of this specified demand for linking. A global model, then, based on the overall compliance tensor  $\mathbf{S}$  can be established for a solid material weakened by an ensemble of micro-defects. Sumarac and Krajcinovic (1989) and Krajcinovic (1996) gave the full derivation of the compliance,  $\mathbf{S}$ . For plane stress, the non-vanishing components of  $\mathbf{S}$ , now denoted by a scalar  $S$ , are  $S_{11}$  and  $S_{22}$ . Formally, the scalar  $S$  here is actually  $S_{ijmn}$ , the fourth order compliance of  $\mathbf{S}$ . We also have the more familiar expression of:

$$\sigma_{ij} = C_{ijmn} \varepsilon_{mn} \quad (3-17)$$

where  $C_{ijmn}$  is the fourth order stiffness of Cartesian tensor  $\mathbf{C}$ , and  $m, n = 1 \text{ or } 2$ . The compliance and stiffness tensors are related by  $\mathbf{S} = \mathbf{C}^{-1}$ . Then:

$$\varepsilon_{ij} = S_{ijmn} \sigma_{mn} \quad (3-18)$$

The distribution of the micro-cracks can be defined as isotropic when the micro-cracks are uniformly distributed with respect to orientation. In other words, the micro-crack density is identical in planes of all possible orientations. Under this assumption, the concentration of the micro-cracks is so dilute that the behaviour of each crack is not influenced by other cracks, according to Krajcinovic and Sumarac (1987). The constitutive equation, using the Lemaitre damage parameter,  $\omega$ , can be expressed as, according to Ortiz (1985):

$$S = S_{11} = S_{22} = E_o / (1 + \omega_o) \quad \text{and} \quad S = S_{11} = S_{22} = E / (1 + \omega) \quad (3-19)$$

where  $E_o$  and  $\omega_o$  are Young's modulus and original (virgin) Lemaitre damage parameter,  $E$  the effective modulus, and  $\omega$  the Lemaitre damage parameter. This can be explained by showing the compliance tensor,  $\mathbf{S}$ , by a simplified matrix form (with the presence of micro-cracks) as follows:

$$\mathbf{S} = [\mathcal{S}] = \begin{bmatrix} S_{11} & S_{12} & S_{16} \\ S_{12} & S_{22} & S_{26} \\ S_{16} & S_{26} & S_{66} \end{bmatrix} \quad (3-20)$$

Here the non-vanishing components of the matrix attributable to the micro-cracks are:

$$S_{11} = S_{22} \quad \text{and} \quad S_{66} = 2S_{11} \quad (3-21)$$

It should be noted that in the case of intensive compressive loading (under Mode II fracture) with frictional sliding between crack surfaces, as expected for the impact bruising conditions of horticultural produce in general, the symmetry of the compliance matrix of Equation (3-20) may break down, and it is possible that some components in the matrix become zero, see Nemat-Nasser and Hori (1993).

Following the argument of Ortiz (1985) on micro-cracking instabilities as shown in the initial unloading stress-strain curve, the question of whether the curve can saturate in the manner shown in Figure 3.116 may not be satisfactorily answered simply on the basis of global continuum models. Here the random pattern of micro-cracking instabilities will switch an unsaturated curve to a domain of reduced toughness, and the process will repeat. The weak domains may be due to a spot with higher density of micro-cracks, or natural pit fields on the parenchyma cell walls. Some micro-cracks become unstable and switch the curve before a full saturation of the 'original' curve can be realized. In Figure 5.39, the Young's modulus,  $E_o$  (upper bound  $B-B'$ ) can be represented by the expression  $(1+\omega_o)S$ , and subsequent curves by  $(1+\omega_n)S$  where  $n$  ( $= 1, 2, 3\dots$ etc.) is an integer. The slope of  $(1+\omega_n)S$  leading to ultimate strength will be the lower bound  $C-C'$ .

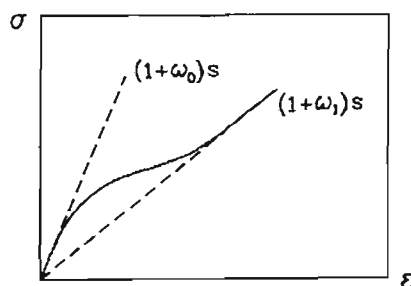


Figure 3.116 Schematic diagram of stress-strain curve showing the random selection of path toward weaker domains under micro-cracking instabilities.  $\omega_o$  and  $\omega_l$  are original (virgin) and effective Lemaître damage parameter, respectively. From Ortiz (1985)

By repeating the laser-based Run GD-10a-4 on Golden Delicious apple specimen as shown in Figures 3.110, 3.111 and 3.115 with Granny Smith apple as Run G-10a-1 at the same strain rate of 133/second, the dynamic stress-strain relationship for Granny Smith is shown on Figure 3.117. Owing to the crisper characteristic of Granny Smith, there is substantially more meso-cracking beyond the bio-yield point, at 12.5% strain in Figure 3.117, leading to the first meso-crack peak at 14% of strain. However, this primary meso-crack was arrested. The curve then follows slope  $D-D'$  which is comparable (parallel) to  $C-C'$ , indicating evidence of shear banding. The specimen reaches its ultimate strength at 25% strain, before continuing on a softening process. It is emphasized here

that the first peak at 14% strain is not due to macro-scale fracturing. One example of macro-scale fracturing is shown in Figure 3.118.

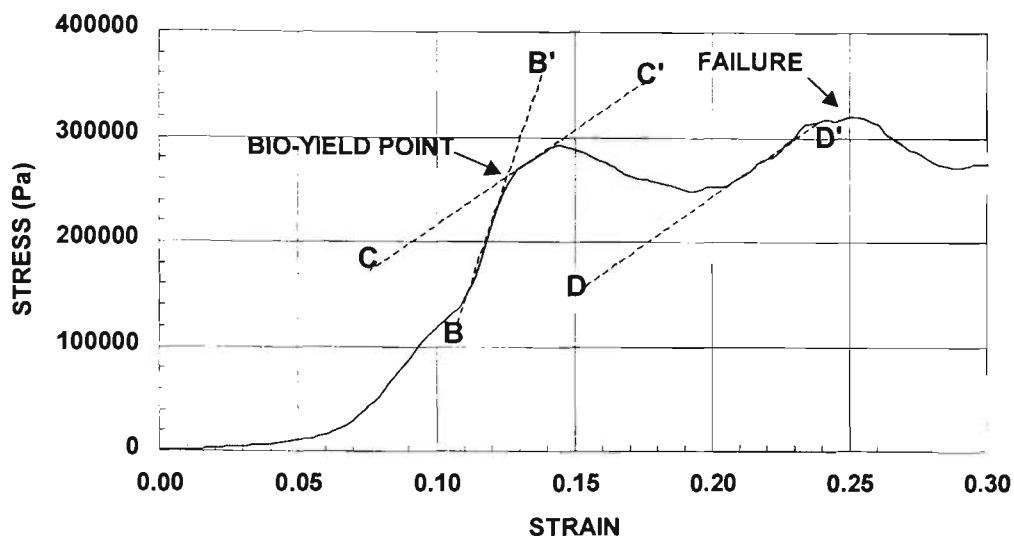


Figure 3.117 Dynamic stress-strain relationship of market-fresh Granny Smith apple tissues from laser-based test under a strain rate of 133 /second showing instabilities as a result of an abrupt switching of stress-strain curve at the bio-yield point. Slopes C-C' and D-D' are comparable, indicating substantially more meso-cracking activities and less micro-cracking instabilities than equivalent Golden Delicious apple specimens in Figure 3.115. (Run G-10a-1)(10 cm drop)

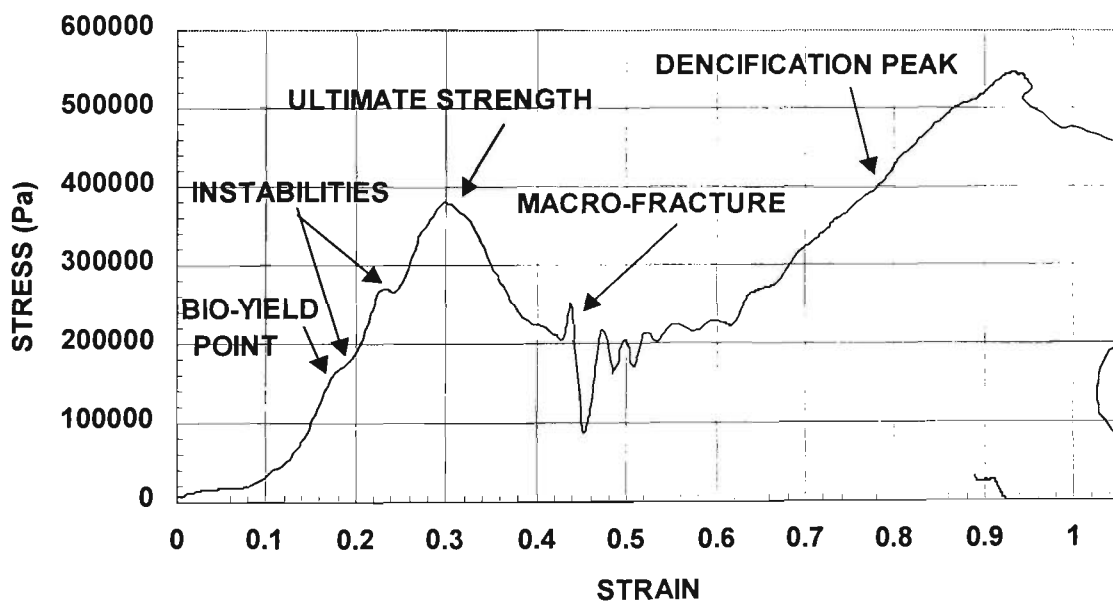


Figure 3.118 Dynamic stress-strain relationship of market-fresh Golden Delicious apple tissues from laser-based test under a strain rate of 150 /second showing micro- and meso-scale instabilities and macro-fracturing at 44% of strain. (Run GD-15-2a)(15 cm drop)

#### 3.7.4 Meso-Cracking and Macro-Cracking Characteristics

Macrocrack-growth, being the primary cause of fracture, can either be a slow or a fast crack growth process. A slow-crack growth process is dominated by the formation of micro- and meso-crack instabilities before reaching the ultimate strength of the material, and thereafter the propagation of meso-/macro-cracks in the post-critical domain. On the other hand, a process with fast-crack growth is characterized by the formation of a single primary crack as a result of the saturation of propagating meso-cracks leading to catastrophic failure. Some materials fail predominantly under the strain softening process with slow-crack growth, while others fail under catastrophic fracturing, and/or buckling/bifurcation in case of thin shell structures and corrugated fibreboard materials. While both slow and fast crack growth processes are propagating in nature, macro-cracks can be illustrated by a sharp fall of the stress-strain curve, see Figure 3.118. On the other hand, a relatively flat stress-strain plateau and the presence of strain softening shows the dominance by the transitional meso-cracks. Both are expected to exist during the post-critical cracking domain. This is not to be confused with the global fracturing process such as the case for eggplant as shown in Figure 3.46. Fracturing processes in the pre-peak domain can be shear-banding induced.

The strain softening process, as described in Section 2.2.4.2, is primarily the result of gradual failure in materials dominated by slow-crack growth. One of the most common examples of this type of failure process is the crack-growth phenomenon of concrete structures. It is also the predominant process for many fruits and vegetables, either with crisp textures such as apples and pears, or those with moderately crisp such as eggplants, and even some with soft textures like kiwifruits, persimmons, and tomatoes. For produce with very soft textures and high Poisson's ratios, plastic deformation and strain rates play a more significant role in the dynamic response than damage instabilities, as has been seen for the case of deformation in banana flesh. Crisp produce like apples, nashi and pear appear to fail predominantly with macro-cracks, see Figure 3.119. They are usually characterized by a complicated post-critical strain softening process such as that shown in Figure 3.110. In that particular case, the plateau of the dynamic response curve is dominated by propagating meso-cracks that hover around the onset of macro-crack saturation.



Figure 3.119 Macro-crack in cylindrical shape Golden Delicious apple specimen of 10 mm in initial thickness after impact by a steel impactor from laser-based test. Strain rate around 135/second

Using the experimental data obtained from the laser-based impact test set-up as illustrated in Figure 3.120, it shows that, in general, the appearance of macro-fractures clearly depends on the final level of strain, see Figure 3.121, and, for soft produce, the applied strain rates as well. For crisp produce, the dynamic responses of these materials with highly complex post-failure behaviours strongly suggest that the dynamic deformation of crisp produce is fairly independent of the applied strain rates.

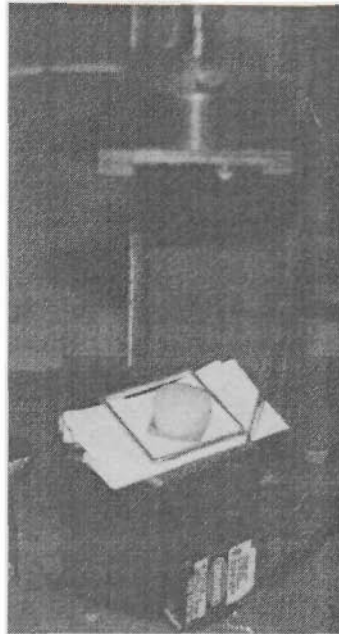


Figure 3.120 Arrangement for laser-based impact testing of cylindrical Golden Delicious apple specimen, showing a 900-gm strike weight above the specimen and an aluminium square guard (one of a series of four with fixed strain values of 0.20, 0.35, 0.50 and 0.75) around the specimen.

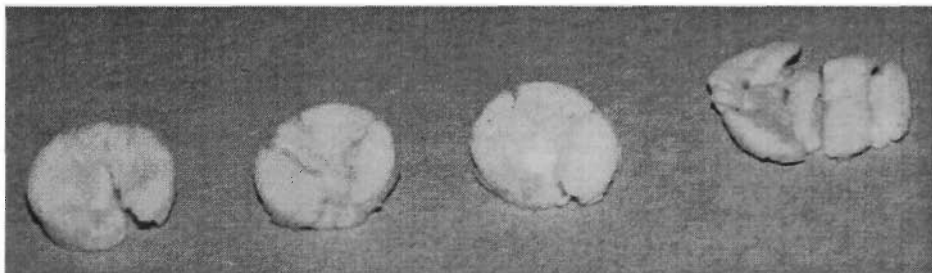


Figure 3.121 Crack growth characteristics as shown in fractures of Golden Delicious specimens as a result of final strain values of (from left) 20%, 35%, 50% and 75%.  
(Controlled by square guards of same sizes but various heights)

Some materials fail under both the slow-crack and the fast-crack modes, depending on the loading conditions and instabilities. Based on results from laser-based tests, fruits that fall into this category include papaya and pawpaw, as shown in Figure 3.122. Like apples and pears, their post-failure modes may include macro- and meso-cracks. But unlike apples and pears, their post-failure modes are unstable, with a high tendency of switching to macro-crack saturation, as shown in Figure 3.123. They may also remain in meso-crack mode throughout the softening process, as shown in Figure 3.124.

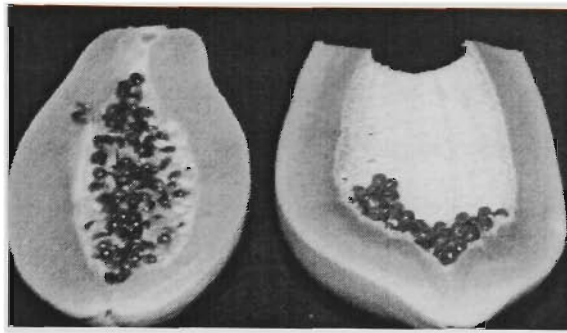


Figure 3.122 Cross-sections of papaya (left) and pawpaw (right). (They are texturally similar except that the taste of pawpaw is normally more bitter than papaya.)

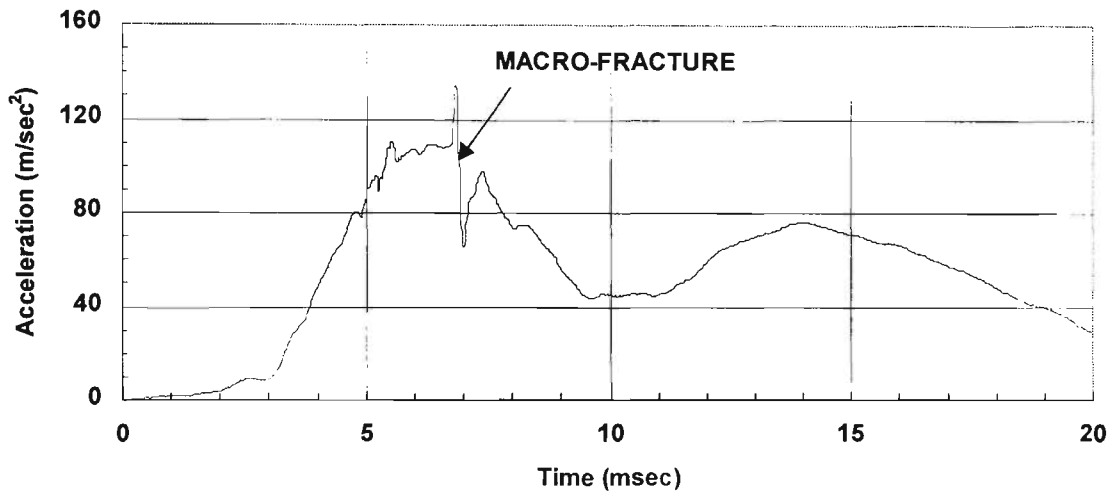


Figure 3.123 Time-history of acceleration of pawpaw specimen with a 0.9 kg strike weight from 5 cm height under laser-based test indicating tendency of fracturing with macro-crack saturation, with final crushing of fractured pieces as shown by a second densification peak. (Run PW-05-m1).

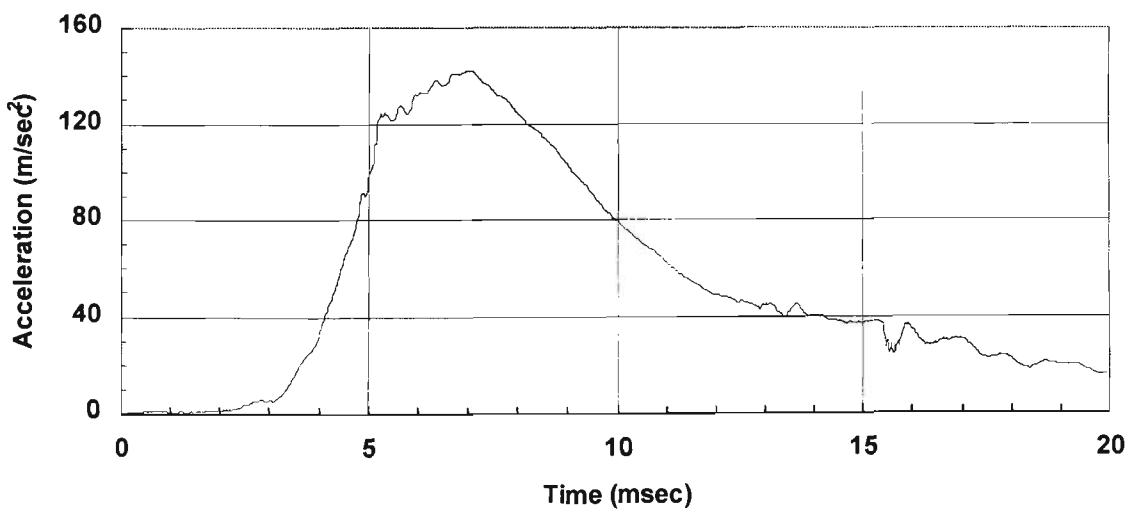


Figure 3.124 Time-history of acceleration for a pawpaw specimen made from same fruit and under similar test conditions as that in Figure 3.123 showing dominating post-failure softening tendency but without macro-fracturing. Second peak is absent in this case. (Run PW-05-m3).

Examples of non-horticultural materials that fail under both modes can be drawn from silicone-silicone carbide (a kind of rate-sensitive ceramic) at high temperature (in this case 1500<sup>0</sup>C) under different strain rates of loading. This results in different levels of thermal activation energy to initiate micro-crack growth, according to Kritz (1983), cited in Grathwohl (1989).

Let us focus on a more valid picture of material brittleness and damage at the meso-crack propagating mode and the onset of macro-cracking, based on the strain energy density damage theory proposed by Sih (1973) and Sih and MacDonald (1974). For most of the developed fracture mechanics theories, one of their primary applications seems to be in the design of structures that can avoid brittle fracture whenever possible. Brittle fractures are sudden and unstable, while ductile fractures such as strain softening are more stable. At the interface between meso-cracks and macro-cracks, whether a crack will saturate into a macro-fracture is highly sensitive to their size effects. It is only since the 1980's that research workers, primarily in concrete studies, started to place more effort into explaining the size effects on crack growth. The strain energy density approach was certainly developed along this line.

Let us study the results from a 3-point quasi-static bending test on concrete beams of various structural sizes but exactly the same material properties and structural shape. In this last regard, the ratio of their dimensions is exactly the same. The results would show that the mechanical behaviour of the beams decidedly changes from 'very brittle' to 'very ductile', when the beam size changes from large to small, as shown in Figure 3.125. For the large beam, we can look at the stress distribution as a global phenomenon, with the stress concentrated only at the first major crack formed; whereas for the small beam, it represents a local phenomenon because the stress distribution affects the entire specimen due to its limited size.

The strain energy density damage theory can be successfully applied to problems to account for the size-scale transition from plastic failure to brittle fracture. For instance, tensile tests were performed on two rectangular mild steel specimens with exactly the same ratio of body sizes and of the same material. One of the specimens is many times bigger than the other one. From the stress-strain schematic diagram as shown in Figure 3.126, it is clear that the bigger specimen behaves in a more brittle fashion than the small specimen, although the material content in both specimens is exactly the same. Thus, the true meaning of the terms such as brittleness and ductility would not be sufficient, *per se*, for a complete explanation if we only focus on the stress-strain behaviours of materials. This is because other factors like loading conditions and micro-structural conditions also play an important role in shaping the stress-strain curves.

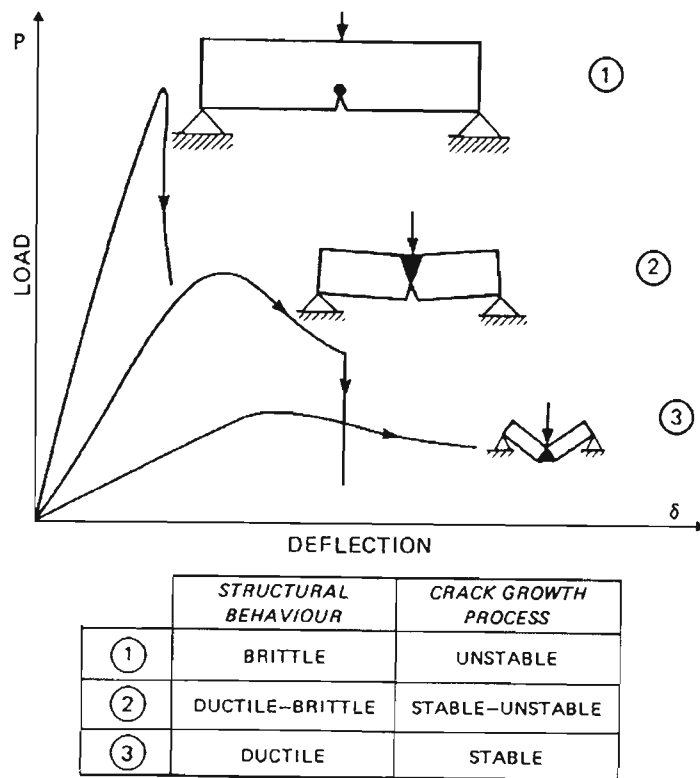


Figure 3.125 Size-scale transition from brittle fracture to ductile (plastic) failure. From Carpinteri and Bocca (1988).

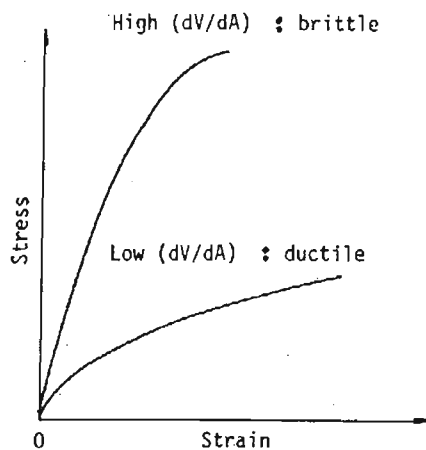


Figure 3.126 Stress-strain characteristic curves of two AISI-316 mild steel specimens of exactly the same ratio of body dimensions: one is many times bigger than the other is. The larger one behaves in more brittle fashion than the smaller one, although they are of the same material. From Sih (1987).

Some of the micro-structural conditions include defects and micro-/meso-scale crack formation and propagation, and, most significantly, the meso- and macro-crack interactions. Sometimes the terminology can be confusing. If the material fractures under cyclic loading (a term frequently used by civil engineers), we can refer to it as fatigue (for material scientist). If it fractures under static loading with chemically active substances present, it is known as stress corrosion (cracking). Sometimes the data from different experimental sets can be misleading, and indeed not

compatible. For instance, when analyzing the dynamic stress-strain curves, one may wonder whether the strain-rates of deformation would be the sole self-sufficient factor for comparing results from different laser-based drop test runs. This can be illustrated by three impact test results of market-fresh Golden Delicious apple specimens. These three tests were performed under the similar testing conditions. The only difference is the strike weights, which are 135.75, 495.38 and 900.81 grams, and the resulting dynamic stress-strain curves are shown in Figures 3.127, 3.128, and 3.129, respectively.

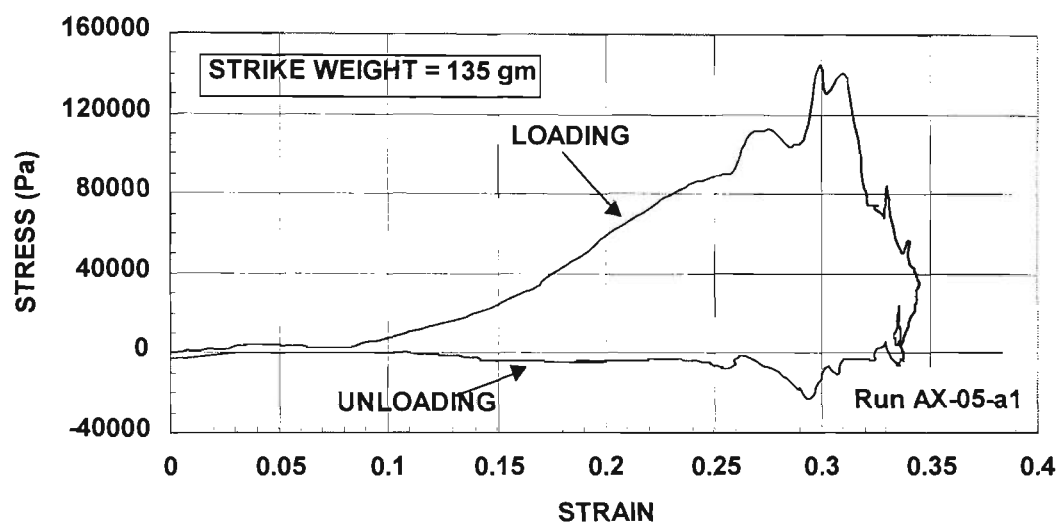


Figure 3.127 Dynamic stress-strain relationship of market-fresh Golden Delicious apple specimen with laser-based test under a strain rate of 89/sec. and 5 cm drop. (Run AX-05-a1).

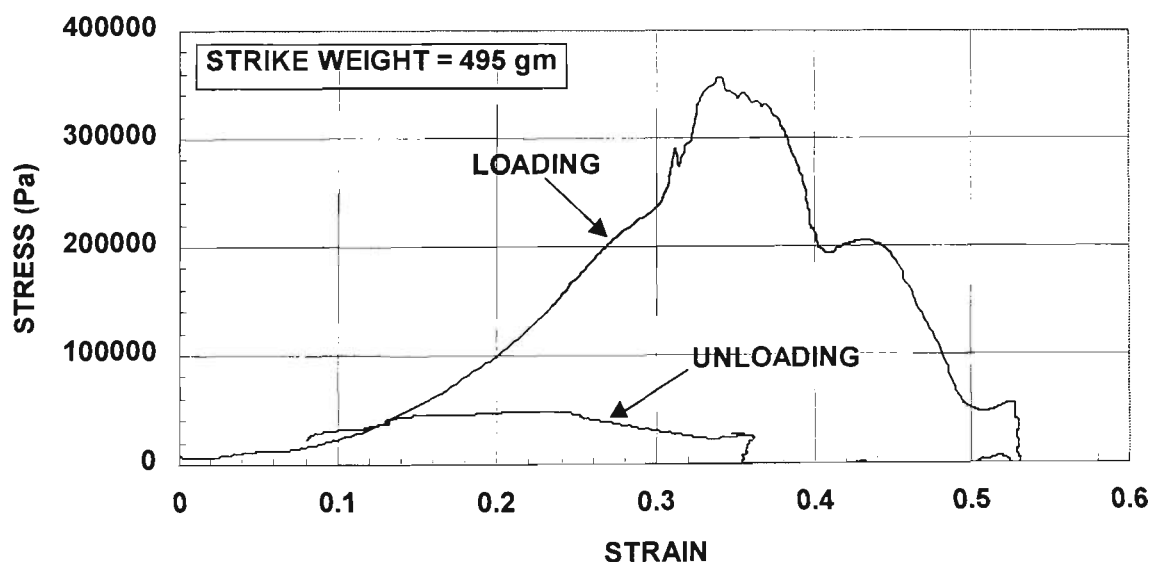


Figure 3.128 Dynamic stress-strain relationship of market-fresh Golden Delicious apple specimen with laser-based test under a strain rate of 100/sec. and 5 cm drop. (Run APP-05-b).

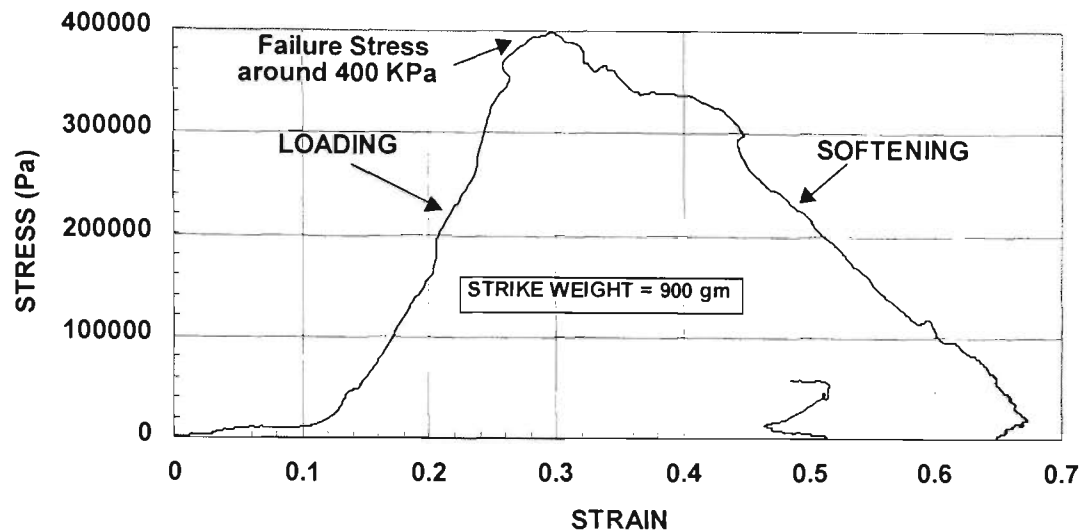


Figure 3.129 Dynamic stress-strain relationship of market-fresh Golden Delicious apple specimen with laser-based test under a strain rate of 91/sec. and 5 cm drop.(Run GD-05-a2).

From these three curves, substantial deviation of dynamic characteristics can be identified when, all other factors being equal, different strike weights were used. Only the curve with the 135-gram strike weight shows no permanent material strain. The peak stress in this case reached only 0.14 MPa, which is far below the expected failure stress of fresh Golden Delicious apple at about 0.35 to 0.40 MPa. Here the damage shown as pre-peak instabilities seems isolated and does not seem to produce any permanent irreversible strain. The extent of damage can be directly correlated with the extent of strain softening. The last test under a 0.9-kg strike weight shows substantial damage, due to the fact that the specimen in this case absorbed more energy per unit volume (sometimes called strain energy density, or the total area under a stress-strain curve) than other specimens.

In order to contain the total absorbed energy, the dynamic response curves can shoot high up to create sharp and sizable areas under the stress-strain curve. However, if the material fails on the uploading curve at certain stress level due to its limited strength, the likely possibility is to let the material be damaged by propagating meso-cracking. If this occurs, the strain energy density will be substantially increased, as shown by the spreading out the area under the dynamic curve with a sizable plateau followed by strain softening. Alternatively, a primary crack or fracture that also acts as an energy sink will occur.

Referring back to Figure 3.126, if we assume that the smaller specimen has the dimensions of  $a$ ,  $b$  and  $c$ , its volume-to-area ratio becomes  $(0.5abc)/(ab+bc+ca)$ . If the larger specimen has the dimensions of  $6a$ ,  $6b$  and  $6c$ , the volume-to-area ratio ( $dV/dA$ ) becomes  $3abc/(ab+bc+ca)$  which is 6 times larger

than that of the smaller one. As the specimen becomes bigger, this ratio ( $dV/dA$ ) will tend to increase as well. Since the larger specimen has a higher energy storage capacity than the smaller one, the energy release rate,  $G$ , will differ between the two different-sized specimens, a fundamental aspect of the size-effects. Here, the energy release rate,  $G$ , is in the sense of Griffith-Irwin energy balance fracture theories, Griffith (1921) and Irwin (1957), denoting the energy rate required to form new cracked surfaces.

In other words, the damage in these two specimens will also differ under the same energies released but different energy release rates,  $G$ . This shows why measured quantities such as total energies or stresses will often be quite sensitive to specimen size-effects and loading conditions. In Figures 3.127, 3.128 and 3.129, the energy release rate would be the highest for the case with the heaviest strike weight, at 0.9 kg, as shown in Figure 3.129. Also, there is a high tendency to damage the tissues in a way so as to maximize the area under the curve and at the same time to prevent macro-cracking. This can be achieved by strain softening. The most optimized form of strain softening is reached when a straight line with negative slope,  $-h$ , is formed, denoting the maximum area achievable under the curve, see Figures 3.118 and 3.129. Under this condition, the material state is unstable, with extreme tendency to form macro-scale cracking, as can be seen in Figures 3.118 and 3.130 for fresh Golden Delicious apple.

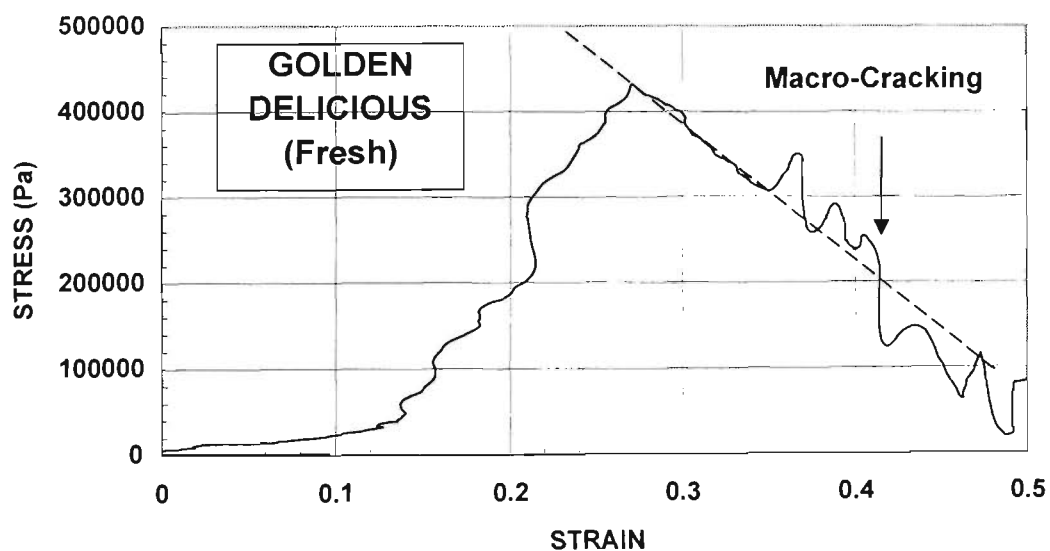


Figure 3.130 Dynamic stress-strain relationship of market-fresh Golden Delicious apple tissues from laser-based test under a strain rate of 156/sec. at 25 cm drop showing micro- and meso-scale instabilities and macro-fracturing at 41% of strain. (Run SGA-1a-2).

One interesting aspect is that they seem to fracture at comparable levels of strain at about 40% to 45%. The above approach denotes that cracks will not proceed if  $G \leq G_R$ , where  $G_R$  is the critical value of  $G$  (often called crack growth resistance).  $G_R$  is often referred to as the critical strain energy release

rate,  $G_C$ . The three modes of macro-crack propagation include: (a) Mode I with opening (common in tensile loading), (b) Mode II with sliding (common in compressive loading), and (c) Mode III with tearing.

It has been a common belief that the more brittle the material under fracturing process is, the smaller the plastic zone will be. In some extremely brittle materials like inorganic glass, the plastic zone is negligible in size, and their fracture toughness,  $K$ , will always be critical ( $K_C$ ), Sakai and Bradt (1993). For quasi-brittle and other materials with failure response such as strain softening, the formation of cracks is influenced by a localization of deformation in the form of a frontal (fracture) process zone (FPZ), Figure 3.131. In the case of produce, the formation of micro-cracks (free surface) initiates when fibrillar slippage instabilities start to occur within the cell-wall structure.

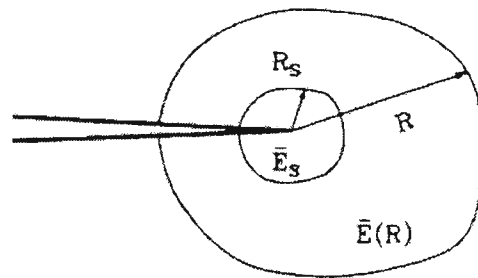


Figure 3.131 Schematic diagram showing a fracture process zone (FPZ) of radius  $R$  with corresponding effective modulus,  $\bar{E}(R)$  of the material matrix far-field from the crack tip, encircling the much smaller plastic zone of radius  $R_s$  with effective modulus  $\bar{E}_s$ .

Figure 3.131 only shows a Mode I fracture (for the purpose of illustration). In Mode II compression cases, common in produce under loading, the volume of a micro-crack can possibly be negligible, but the free surface area will be non-zero, in the form of a slit, with two rough crack surfaces sliding against each other.

As shown in Figure 3.116, the micro-crack density can reach a saturation limit at which the stresses cannot be increased. At this micro-/macro-scale interaction, the effective modulus will eventually switch to the critical value,  $\bar{E}_s$ . At the point of micro-crack saturation, propagating meso-/macro-cracking initiates, with the propagating tip embedded within a very small plastic saturated zone of radius  $R_s$ . Budiansky (1983) and Budiansky *et al* (1983) found that the crack tip region appears to be shielded in a much larger process zone with radius  $R$ , degraded modulus,  $\bar{E}(R)$  and an ‘effective’ stress intensity factor,  $K$ , for strain softening materials. According to Sakai and Bradt (1988) and Bui (1994),

this type of crack-tip shielding through microscopic processes is related to micro-crack formation that occur far-field within the FPZ, in the crack-face friction sliding region, as well as behind the propagating crack-tip in the following wake region, see Figure 3.131. Following the derivation and calculation of Budiansky *et al.* (1983) and assuming that the Poisson's ratio,  $\nu$ , equals to 0.33 as expected for undisturbed apple tissues and other produce with crisp textures, the expressions for fracture toughness,  $K_C$ , is::

$$K_C = K \left[ 1 + \left( k_1 - \frac{5}{8} \right) \delta_1 + \left( k_2 + \frac{3}{4} \right) \delta_2 \right] \quad (3-22)$$

where

$$\delta_1 = \frac{1}{1-\nu} \left[ \frac{\mu}{\bar{\mu}} - 1 \right] \quad \text{and} \quad \delta_2 = \frac{1}{1-\nu} \left[ \bar{\nu} \frac{\mu}{\bar{\mu}} - 1 \right] \quad (3-23)$$

and

$$k_1 = \frac{1}{32\pi} \int_0^\pi (11 \cos \theta + 8 \cos 2\theta - 3 \cos 3\theta) \ln [R(\theta)] d\theta \quad (3-24a)$$

$$k_2 = \frac{1}{2\pi} \int_0^\pi (\cos \theta + \cos 2\theta) \ln [R(\theta)] d\theta \quad (3-24b)$$

and  $\mu$  and  $\bar{\mu}$  are the material shear modulus and damage material shear modulus, respectively,  $\theta$  is the angle between the crack plane and the direction of applied loading, and  $\nu$  and  $\bar{\nu}$  are the Poisson's ratio and damage Poisson's ratio, respectively.

The damaged Poisson's ratio,  $\bar{\nu}$ , can be estimated, according to Chen (1989), by:

$$C_d = \frac{45}{16} \frac{(\nu - \bar{\nu})(2 - \bar{\nu})}{(1 - \bar{\nu}^2)[10\nu - \nu(1 + 3\nu)]} \quad (3-25)$$

where  $C_d$  is the crack density parameter which is related to the Budiansky-O'Connell damage parameter,  $D$ , by:

$$D = \frac{16}{9} \frac{(1 - \bar{\nu}^2)}{(1 - 2\nu)} C_d \quad (3-26)$$

If the Poisson's ratio,  $\nu$ , equals 0.33,  $\delta_1 = 1.99 \omega$ ,  $\delta_2 = -0.095 \omega$ ,  $k_1 = 3/16$ , and  $k_2 = -0.25$ . It follows that the ratio  $K_C/K$  of the macro-crack surrounded by the FPZ can be further expressed as:

$$\frac{K_C}{K} = 1 - \frac{2(35 - 11\nu + 32\nu^2 - 12\nu^3)}{45(2 - \nu)} \omega \quad (3-27)$$

For  $\nu = 0.33$ , the ratio can be further simplified to:

$$\frac{K_C}{K} = 1 - \alpha\omega \quad (3-28)$$

where  $\alpha$  is the shielding coefficient ranging from 0.919 to 2.92, according to Hutchinson (1987), and  $\omega$  the damage parameter. When  $\nu$  equals 0.33, the corresponding value of  $\alpha$  is 0.919.

From Equation (2-9) the ratio of moduli can be written as  $\bar{E}(R)/E_0 = 1 - \omega$ , such that:

$$\frac{K_C}{K} = 1 - \alpha \left( 1 - \frac{\bar{E}(R)}{E_0} \right) \quad (3-29)$$

For  $\nu$  equals to 0.33,  $\alpha$  is very close to unity. Then (3-29) becomes:

$$\frac{K_C}{K} = \left( \frac{\bar{E}(R)}{E_0} \right) \quad (3-30)$$

According to this relationship, it is clear those materials under the effect of damage in the FPZ under a softening process is directly related to changes in effective modulus. More significantly, Equation (3-30) establishes a direct relationship and link between the micro-scale parameters  $K_C$  and  $K$  and macro-scale parameters  $\bar{E}(R)$  and  $E_0$ .

Referring to the Poisson's ratios for crisp textures such as Golden Delicious apple established by DMA tests in Section 3.5, we recall that  $\nu$  varies from 0.30 to 0.405. Earlier results by Garrett (1970) based on sonic pulse velocity passing through Rome Beauty apple specimens during impact show that  $\nu$  is around 0.30 to 0.32. With such values for  $\nu$ , it is possible that Equation (3-30) can be applied to the cracking conditions of crisp textures such as apples and pears. Questions may arise as to what would happen if  $\nu$  is much higher than the values established from experiments, say, at 0.45. Based on Equation (3-27), the shielding coefficient,  $\alpha$ , is equal to 1.016. By substituting this value into Equation (3-29), it becomes Equation (3-30) again. If we try a value of 0.5 for  $\nu$ , the shielding coefficient,  $\alpha$ , is equal to 1.067, and Equation (3-30) still applies. In other words, Equation (3-30) applies to crisp textures as well as very soft textures. The implication is that, for soft produce textures, they seem to prefer other form of energy dissipation processes with higher priority than cracking, notably heat diffusion, not because of the applicability of Equation (3-30). It is clear that cracking as shown in Equation (3-30) as an option of energy dissipation competes on equal grounds with other forms of energy dissipation for soft produce, but the cracking option is seemingly not given the first priority.

Let us focus on micro-crack propagation, taking into account the viscous effects, by considering the influential Norton and Hoff visco-elasto-plastic law:

$$\varepsilon = C_1\sigma + B_1\sigma_e^{m-1}S \quad \text{with } (m \geq 3) \quad (3-31)$$

where  $S (= S_{ij})$  is the deviatoric stress,

$$S = \sigma - (tr \sigma) I/3 \quad \text{and} \quad \sigma_e^2 = 3(S_{ij} S_{ij})/2, \quad \text{and}$$

$m$  is a material power exponent determined from experiments.

The symbol  $(tr \sigma)$  means trace of  $\sigma$  which is equivalent to  $\sigma_{ii}$ , and  $\sigma_e$  is the equivalent stress.  $I$  is called

the identity tensor where:

$$I = \begin{bmatrix} 1 & 0 & 0 \\ 0 & 1 & 0 \\ 0 & 0 & 1 \end{bmatrix}.$$

Far from the crack tip, viscous effects can be neglected. Hence Equation (3-31) reduced to a dominant linear elastic behaviour  $\dot{\epsilon} = C_1 \sigma$ . However, if a viscous process zone is present, as for the cases with the softening processes, the second term of (3-31) is no longer negligible. Recently, significant theoretical development based on (3-31) has been achieved by Kachanov (1978), and further expanded by Hui and Riedel (1981) as:

$$\psi(r, \phi) = \left( \frac{V_{crack}}{\gamma \mu} \right)^{1/(m-1)} r^{(m-2)/(m-1)} f(\phi) \quad (3-32)$$

where  $\psi$  is the Airy function related to  $\partial \psi / \partial t = -V_{crack} \partial \psi / \partial x$  along the  $x$  (cracking) direction,

$\gamma = (2 \mu B_1)^{3(m-1)/2}$ ,  $r = \dot{\epsilon}^{-2/3}$  ( $\dot{\epsilon}$  is the global strain rate) and  $f(\phi)$  is an angular function determined uniquely by the solution of a nonlinear third order differential equation in  $0 < \phi < \pi$ .

When  $\phi = 0$ , the amplitude,  $u$ , of the solution, which is related to the Airy function, is solely dependent on, and determined by, using the crack velocity,  $V_{crack}$ .

This result is significant in that the crack tip under softening processes seems to oscillate (with an amplitude  $u$ ), further reinforcing the observations by Ortiz (1985), see Figures 3.115 and 3.116, with the 'unsaturated' micro-crack path switching toward weaker domains. This phenomenon was recently confirmed experimentally by Parton, Parton and Boriskovsky (1990). They used a high-speed camera with a capacity of 62,500 films per second for the study of crack growth in Plexiglas, that is, polymethylmethacrylate (PMMA), a plastic that deforms with softening process. Their results indicate significant oscillations of crack tip velocities. Evidence of the presence of shear waves was also captured by the camera.

Perhaps the most significant aspect of the work by Hui and Riedel (1981), apart from the theoretical evidence of the direct relationship between crack velocity,  $V_{crack}$  and the amplitude of the created pulse,  $u$ , is the final applicable form of Equation (3-29), which was solved by Bui (1994) and can be expressed as:

$$\frac{\partial u}{\partial t} - 6u \frac{\partial u}{\partial x} + \frac{\partial^3 u}{\partial x^3} = 0 \quad (3-33)$$

Equation (3-33) is a Korteweg de Vries equation that is the fundamental form for solitons, or nonlinear solitary wave pulses. The velocity of these solitons,  $V_{soliton}$ , can be solved from (3-29), according to Bui (1994), as:

$$V_{soliton} = -2u \cosh^2 \frac{\sqrt{V_{soliton}}(x - V_{soliton} - x_0)}{2} \quad (3-34)$$

where  $x_0$  and  $x$  are the original and present location of the crack, respectively.

Bui (1994) concluded that the existence of solitons is the true criterion of viscous fracture process. In other words, during the damage process of micro-crack instabilities, solitary wave pulses, possibly in the form of solitary shear bands, are expected to exist as a result of viscous cracking. Examples of solitary shear bands include Luders bands and Le Chatelier bands. This form of shear waves (or bands) originated from crack tips is not to confuse with shear banding that originated from plastic deformation. If, for instance, the consequence of each fibril slippage in produce cell walls generates a soliton, say Soliton A, and it is followed immediately by another one, say Soliton B, generated as a result of another slippage, Figure 3.132. If the latter one has a faster speed, Soliton B will eventually catch up with Soliton A. The coupled soliton will have a large and destructive amplitude that may further damage the material matrix at the spot of the coupling, see Remoissenet (1994). This can be illustrated by Figure 3.133 in a sequence of wave propagation.

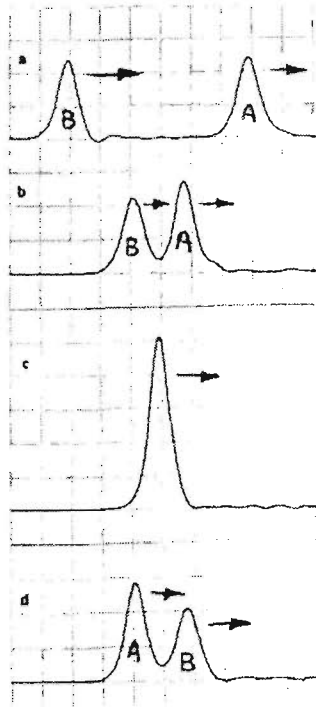


Figure 3.132 Traveling sequence of two solitons at different speeds with instant coupling.

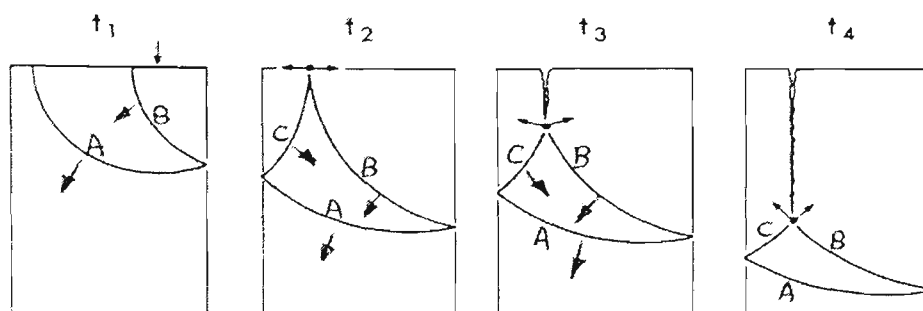


Figure 3.133 Sequence of Wave A propagation from time  $t_1$  to  $t_4$  as a result of an impulse applied asymmetrically giving rise to a compressive pulse. The specimen failed not because of the direct blow (Wave A) but the coupling of Waves B and C. From Zukas *et al.* (1992).

The coupling of the reflected waves B and C from the boundaries can, at the right conditions, probably tear the material specimen apart. As a result, the coupling of isolated solitary wave pulses generated during the formation of individual micro-cracks may form transient wave pulses momentarily with large and destructive displacements that can promote the joining-up and propagation of micro-cracks, forming meso-cracks.

Produce with crisp textures does not seem to be influenced by plastic deformation during the pre-peak domain with work-hardening processes. Instead, the formation of micro-cracks and the transition of micro-cracks into meso-cracks dominate cracking in crisp tissues. When the ultimate strength or, more precisely, the critical rupture stress,  $\sigma_c$ , is reached, they continue to deform in most cases, following a more or less horizontal peak fracture line before undergoing softening, see, for instance, Figure 3.110. The value of  $\sigma_c$  seems to be invariant of strain-rates, as shown in Figure 3.50. This indicates that  $\sigma_c$  could possibly be heavily influenced by some material parameters of the produce, for instance, the shear modulus of the cement bonding among the fibrils of cell-walls, or is itself a unique material parameter of the produce which is invariant of strain rates. Figure 3.134 perhaps can illustrate this.

This phenomenon was initially observed and reported by Ludwik (1909). As has been discussed earlier in this section, it is known that some parameters like specimen sizes can alter the 'brittleness' of materials under dynamic loading. Now, with a fixed size under consideration, other factors such as increasing strain-rates and decreasing temperatures also tend to promote brittle fracture of a normally ductile material.

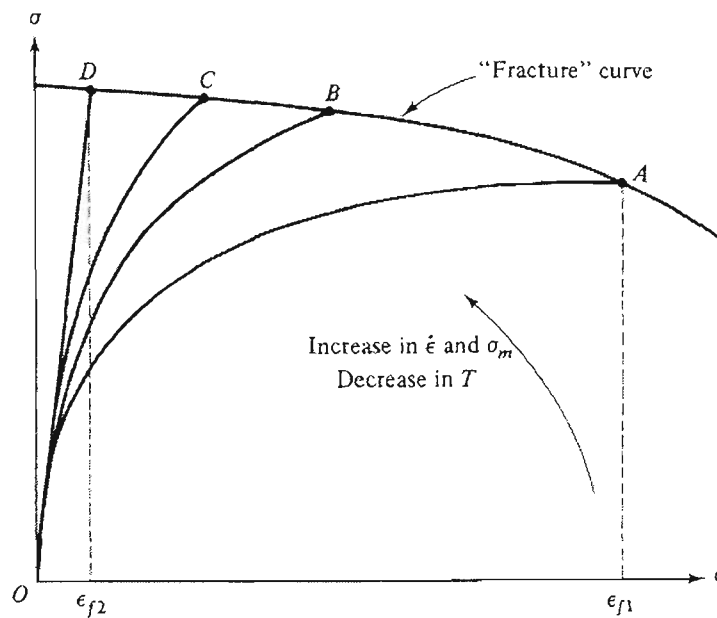


Figure 3.134 Influence of parameters that tend to promote brittle fracture of a normally ductile material. From Caddell (1980).

In Figure 3.134, let us imagine that a fracture curve exists for the material under loading and the stress-strain curve intersects the imaginary fracture curve at a critical rupture stress,  $\sigma_c$ . Under conditions indicated by curve OA, fracture would occur after a large amount of energy was consumed. This indicates that the material undergoes a 'ductile' fracture (sometimes called viscous fracture), with relatively high strain energy density, as shown by the area under the  $\sigma$ - $\epsilon$  curve. This critical rupture stress,  $\sigma_c$ , also corresponds to a high rupture strain of  $\epsilon_f$ . On the other hand, testing the same material under the same test parameters but with higher strain rates will possibly raise the  $\sigma$ - $\epsilon$  curve to OB or even OD. At OD, the total energy required to fracture the material is substantially reduced, as indicated by the much reduced strain energy density when compared with the curve OA. It indicates a relatively 'brittle' fracture. Materials that deform with OA curve indicate a typical elastic-plastic or viscoelastic-plastic deformation.

Now if the  $\sigma$ - $\epsilon$  curve of the material is 'prematurely' truncated by the imaginary fracture curve, this is similar to the case for Golden Delicious apple as shown in Figure 3.110. Here, the initial dynamic responses of the apple behave elastically, or crisp, but 'plastically' (in the form of a horizontal plateau) when a certain critical failure stress is reached. This may explain the rate-independent tendency during the deformation of the apple specimens. Once the material is saturated with micro-cracks, the critical state is reached at  $\sigma_c$ . Meso-cracks that propagates would form a plateau or initiate softening.

In the post-peak domain, the material will undergo further damage processes with softening. Thus, produce with crisp textures like apple does not actually follow an elastic/viscoelastic-plastic deformation as has been generally accepted as the norm of deformation. Rather, the ‘plastic’ plateau is actually the imaginary fracture curve as a direct result of meso-cracking process. Within the pre-peak domain of crisp produce, the dynamic characteristics seem only heavily affected by material instabilities, rather than plastic deformation.

Summing it up, we recall that there are two modes of crack growth, including fast-crack growth, denoting ‘brittle’ cracking for materials, and slow-crack growth, denoting ‘ductile’ or viscous cracking for materials which undergoes softening. We take notice of some crisp horticultural materials such as apple which exhibit both modes. We note the inadequacy of dynamic material characterization solely based on the dynamic stress-strain responses, and the improved elaboration in terms of the strain energy density, as well as the energy release rate,  $G$ , if meso-cracking is involved. This is attributed to the ability of produce textures:

- (i) to maximize their capacity in the containment of kinetic energy of loading by optimizing the area under the stress-strain curve, and
- (ii) to control the softening in such a way that the best possible path of meso-cracking can be achieved, as denoted by the negative slope of softening in the form of a straight line.

On the crack tip characteristics for brittle cracks, plastic crack zones, and the fracture process zone (FPZ) in produce textures that undergo a softening process, we explored the works of Budiansky (1983), Budiansky *et al.* (1983), and Hutchinson (1987), a crucial link between the micro-scale and macro-scale instabilities can be established, based on the micro-scale fracture toughness ( $K_C$ ) and stress intensity factor ( $K$ ), and the macro-scale Young’s modulus ( $E_o$ ) and the effective modulus ( $\bar{E}$ ) within the FPZ. We note that this crucial link applies to crisp produce as well as very soft produce with high Poisson’s ratio.

Based on the works by Kachanov (1978) and Hui and Riedel (1981), we note that the pulse generated at a macro-crack tip can oscillate, which is experimentally observed by Paton and Boriskovsky (1990) and is in line with the observations by Ortiz (1985). Further significant work by Bui (1994) shows that under viscous cracking, the pulse disturbances are solitons responsible for initiating the meso-cracking process, strongly suggesting that they are in fact the Luders and Le Chatelier shear band precursors, which are solitons.

### 3.7.5 *Dynamic Effective Modulus of Horticultural Materials*

#### 3.7.5.1 Introduction

So far we have attempted to clarify bruise damage due to the two fundamentally different phenomena, namely, plastic deformation and plastic instabilities in Section 3.6 as well as instabilities due to damage in Section 3.7. We have introduced the effective modulus as an effective indicator of the state of materials damage by studying and to identifying the damage characteristic produce such as debonding, matrix cracking, and global fracturing.

Under dynamic loading, the interface characteristics between the material matrix and its reinforced-fibres becomes more significant as the loading becomes heavier. These characteristics will affect the overall dynamic mechanical properties of the materials. For horticultural produce such as apples, the situation is even more complex due to their unique material structure of numerous water-based sap-containing cells with sophisticated multi-layered fibrillar-reinforced composite cell-walls that actually act as contact surfaces linking up one another by a natural cement called pectic substance. Depending on the dynamic states of the apple tissues, they may fail upon loading by fracturing through the cell walls or shearing through the pectic cement. In this last regard, the instability mode is basically pre-peak serrated shear jumps. It can also appear as a failure mode with well-developed perfectly-plastic characteristics such as nashi, see Figures 3.57 and 3.58, dominated by cell debonding.

A method of damage evaluation under truly dynamic conditions, based on the strain energy density approach, is presented here, after having been proven to be effective in applying to natural composite materials under laser-based impact tests, as reported by Ip *et al.* (1998). The method has also been proven to be effective to a wide range of materials that undergo softening. Examples include human teeth, apple flesh, polystyrene foam, and corrugated fibreboard, and others. This method of dynamic material damage evaluation uses the instantaneous potential of the strain energy density,  $W_{Di}$ , of test materials when stress-strain relationships can be accurately established using the high quality and reliable strain data acquired with a laser displacement sensor. This technique was used to analyze the dynamic characteristics, particularly the effective modulus, using produce materials as examples, including cylindrical apple specimens, based on their dynamic response to impact under different test conditions. The strain energy density approach that we adopted is not new. It was developed to analyze fracture material behaviour. We have made use of the fact that the ratio of the dynamic stress,  $\sigma$ , to  $W_{Di}$  is dimensionless, providing a means to accurately quantifying the gradual damage against their corresponding strains. In general, the dynamic responses of produce

materials are, as expected, very different from those of quasi-static tests. Under quasi-static uniaxial testing conditions with cyclic loading, it is possible to generate cyclic loops for the evaluation of material damage by an estimation of the effective modulus based on the loops. This is not possible under dynamic conditions.

In light of the short duration during a transient event such as impact, to be able to quantify accurately the instantaneous damage of materials in terms of its state of stress or strain cannot be achieved by direct measurements. Attempts have been made to apply an approach based on the strain energy density of the material for an accurate estimation of the effective modulus and the corresponding damage parameter of some softening produce materials under impact conditions. Here we will use laser-based impact test results of Granny Smith apple specimens to illustrate the effectiveness of this method.

### 3.7.5.2 Application of the Strain Energy Density Method

The dynamic stress-strain curves were selected from two runs with 10-cm drop height and a strike weight of 0.9 kg are illustrated in Figures 3.135 and 3.136:

- (i) Run G-10-a1 (Market-fresh Granny Smith apple specimens)
- (ii) Run OG-10-a1 (Granny Smith apple specimens that had been under cold storage for 8 months at 4.5°C and 100%RH).

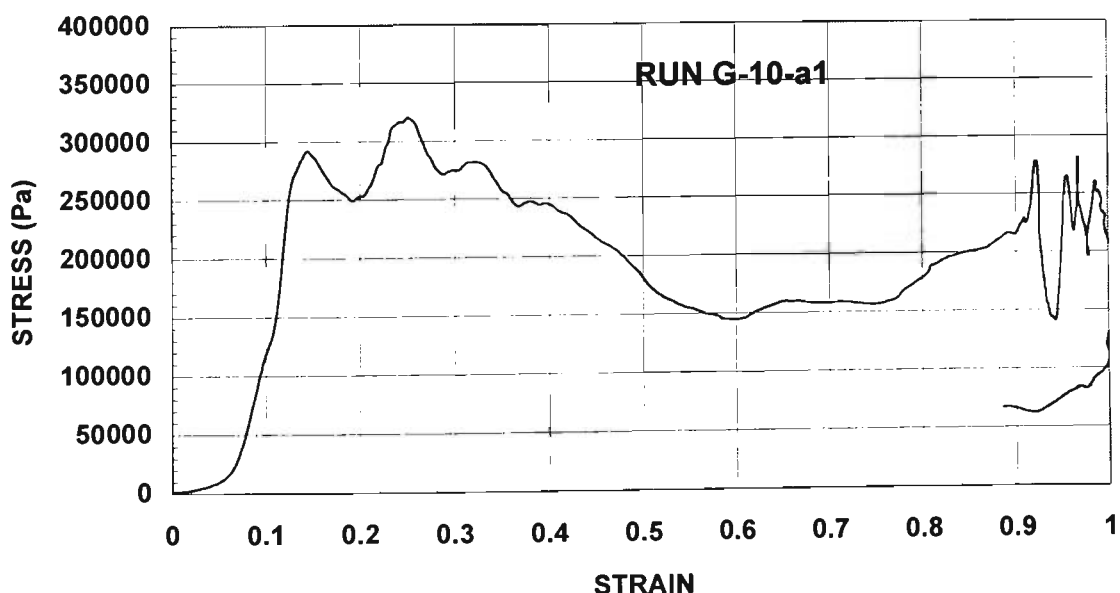


Figure 3.135 Dynamic stress-strain relationship of market-fresh Golden Delicious apple tissue under a laser-based test at 10 cm drop with strain rate of 133/sec. and strike weight of 0.9 kg. (Run G-10a-1)

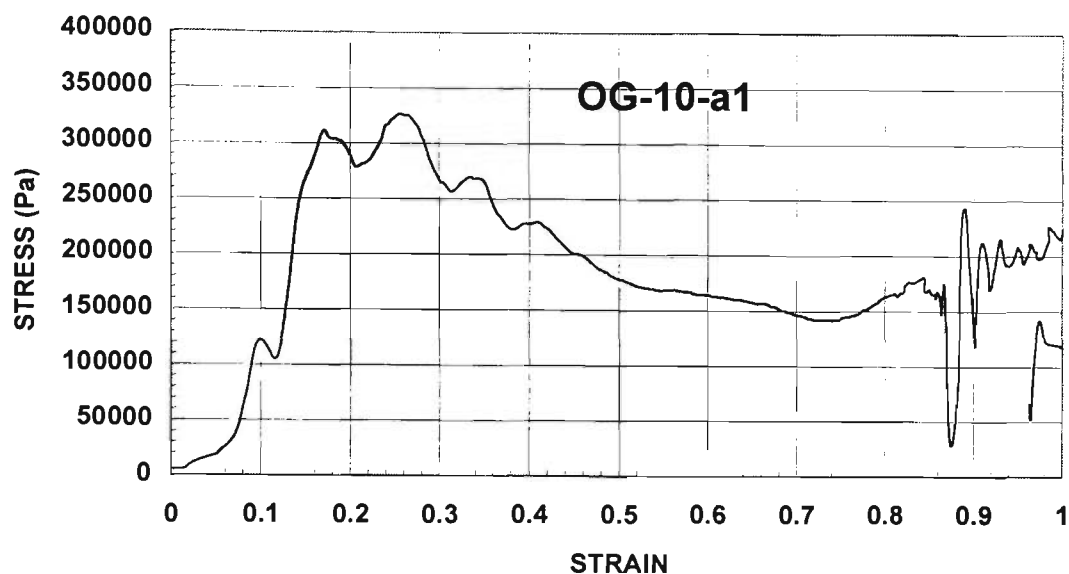


Figure 3.136 Dynamic stress-strain relationship of 8-month aged Granny Smith apple specimen using a laser-based test at 10 cm drop with strain rate of 120/sec. and strike weight of 0.9 kg. (Run OG-10a-1)

A time history of the deformation or strain for Run G-10a-1 for fresh Granny Smith apple is illustrated in Figure 3.137 as captured by the laser displacement sensor. Impact occurred at 4.00 ms into the run when the platen hit the specimen from a drop height of 10 cm. The strain rate can be estimated from the slope of the initial deformation (dotted line) which is 133/second and 120/second for Run G-10a-1 and Run OG-10a-1, respectively.

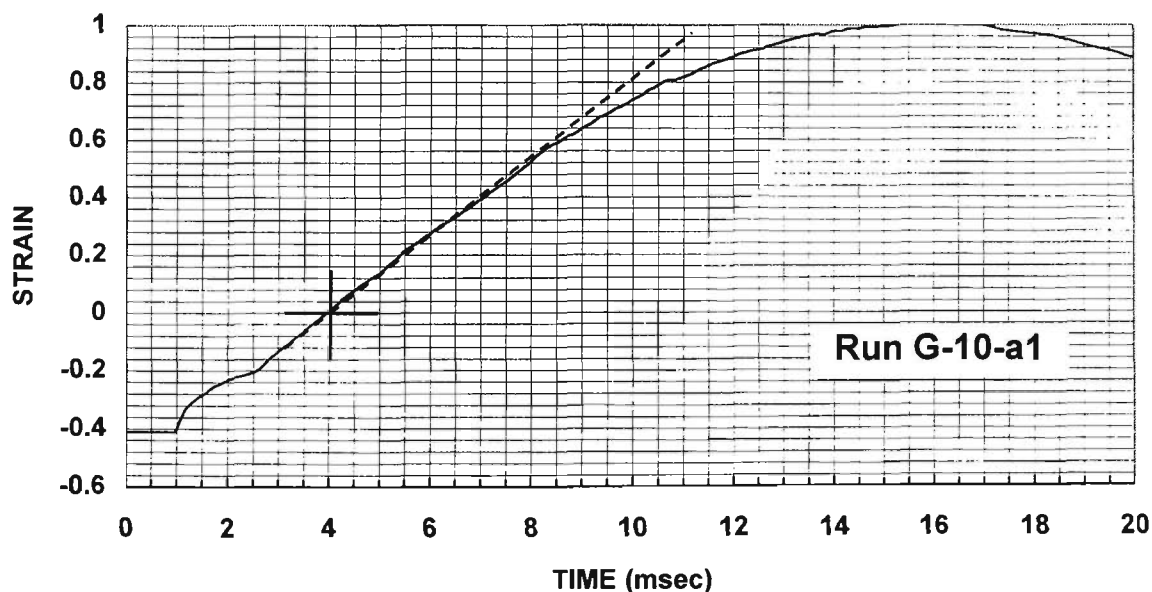


Figure 3.137 Time history of impact deformation on fresh Granny Smith apple specimen with strain rate of 133/sec.

It is interesting to note that, in both runs, a few peaks were present in Figures 3.135 and 3.136, denoting the initiation of meso-cracking. These peaks could well be used in the dynamic evaluation of the instantaneous effective modulus of the material, in a way not much different from the cyclic loops under quasi-static tests were used. The next step requires a good evaluation of the Young's modulus, identified by re-plotting Figure 3.135 as Figure 3.138.

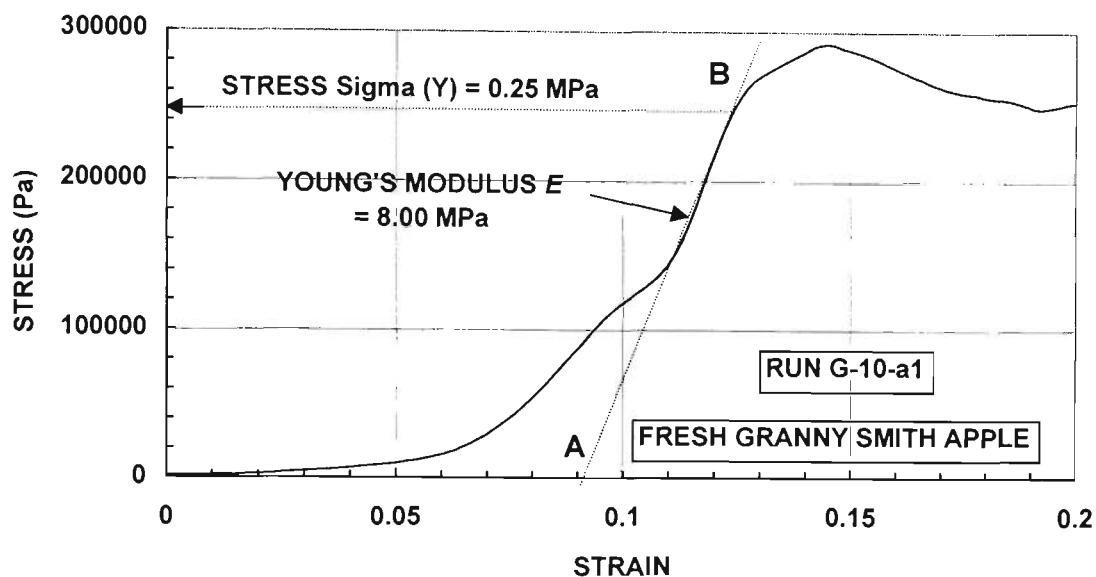


Figure 3.138 Dynamic stress-strain relationship of Run G-10-a1 showing initial deformation and Young's modulus of fresh Granny Smith apple.

A close-up look at the dynamic stress-strain curve as shown in Figure 3.138 shows that the Young's modulus is around 8.00 MPa, obtained by measuring the initial highest slope, AB, with the material deformed under a strain-rate of 133 /second. The estimation of modulus value should be repeated for other runs (normally five runs for each drop height and strike weight) to ensure the estimated values are comparable among one another.

The rapid exchanges of energy in the form of instantaneous work done to the tissues of the specimen provide useful and complete information to the status of bruise damage that is originated both from plastic deformation and damage. Then, let us propose to express the experimental instantaneous data of dynamic force and displacement in terms of the instantaneous applied stress and strain energy density,  $W_{Di}$ , that is associated with the deformation of the test specimen. This representation may provide a more meaningful expression as far as the effective modulus is concerned. Here, the instantaneous strain energy density,  $W_{Di}$ , at any moment on the stress-strain curve has the sense of the strain energy density 'potential' which accounts for the instantaneous strain energy the unit volume of the material can be able to take at that moment, as an energy potential. The strain energy density,  $W_{Di}$ , can be expressed by the product of its instantaneous stress

and strain per unit volume. This product is analogous to the true work per unit volume under a rigidly-elastic/perfectly-plastic deformation condition.

By plotting the actual data this way, one is able to fully account for the instantaneous dynamic characteristics of materials including the state of damage. This is possible because one can express the work-done per unit volume, that is, strain energy density, as a potential, as there has been no other convenient method to measure the energy loss due to material damage such as cracking.

Let us use the experimental results from Run G-10-a1 by plotting the dynamic stress against the instantaneous strain energy density,  $W_{Di}$ . This is illustrated in Figure 3.139. In Figure 3.139, let us join all the tips of the failure peaks to the point of origin. The peaks can be called Peaks A, B, C and D as shown. Then, by measuring the slopes of OA, OB, OC and OD, their dynamic effective moduli, with corresponding stresses at Peaks A, B, C, and D as well as their corresponding strains, can be calculated. This can be done as follows.

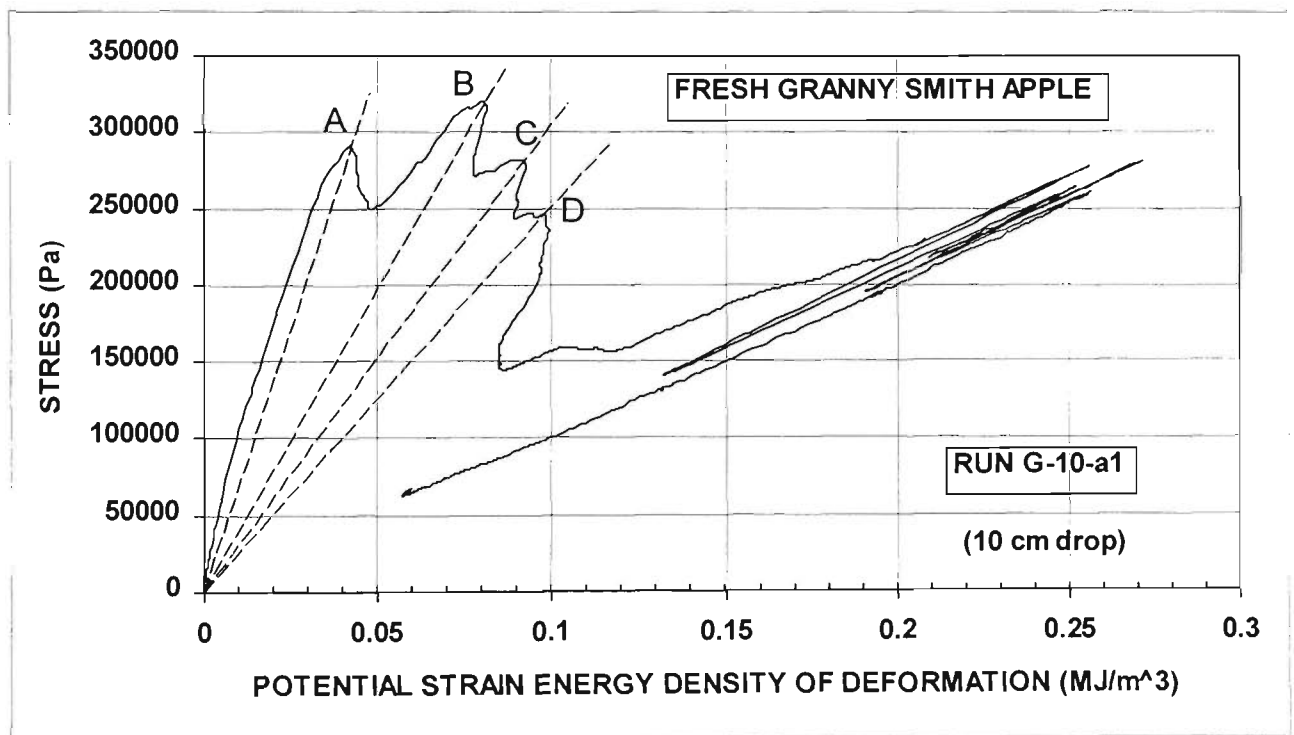


Figure 3.139 Material damage indicator: relationship between dynamic stress and strain energy density potential during dynamic deformation. (Run G-10-a1).

The Young's modulus has been established as 8.00 MPa from Figure 3.138. From the same figure, the yield strength,  $\sigma_Y$ , of the material at point B is 0.25 MPa. Following this, let us calculate the effective modulus that corresponds to Peaks A, B, C and D in Figure 3.139. Let us focus on Peak A by re-plotting Figure 3.139 as Figure 3.140. In Figure 3.140, any slope joining the origin to any point on the curve is unitless, a fact which can be fully exploited as a measure of true representation of the effective

modulus. Then, by marking the yield strength,  $\sigma_Y$ , on the curve and its corresponding potential of strain energy density,  $W_{Di}(Y)$  in Figure 3.140, the first slope (OY), representing the Young's modulus, can be established.

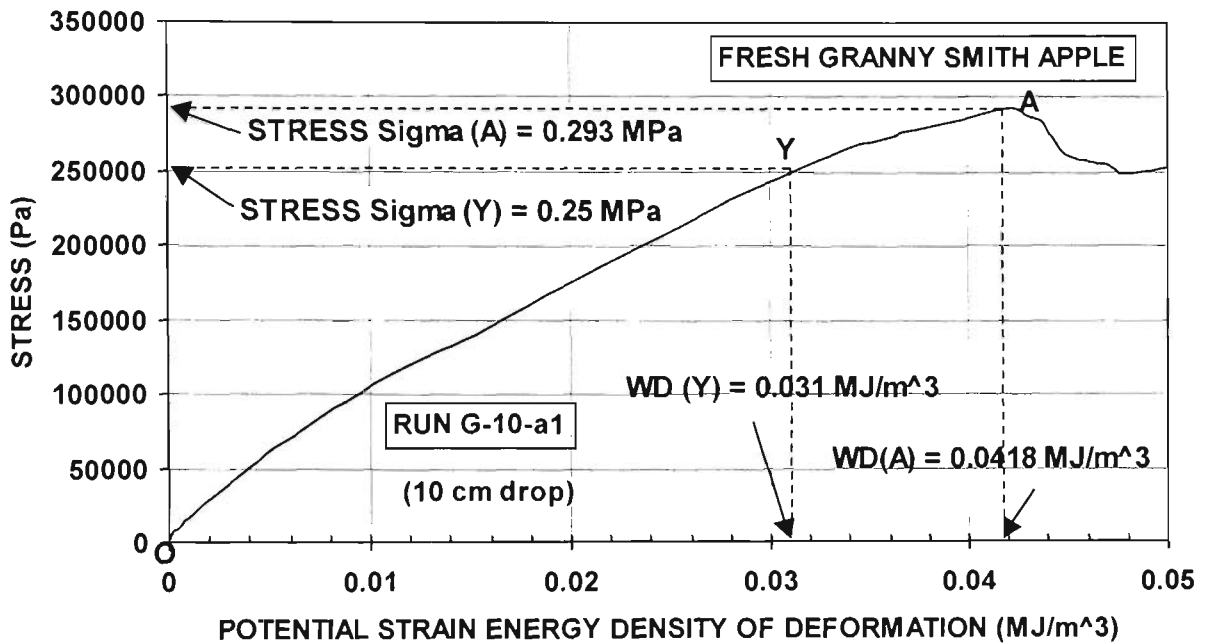


Figure 3.140 Direct estimation of the instantaneous effective modulus,  $E$ , of fresh Granny Smith apple specimen under a strain rate of 133/sec. using the relationship between dynamic stress and the potential of strain energy density,  $W_{Di}$ .

Subsequent slopes of OA, OB, OC and OD can be established by joining the point of origin to the peaks at A, B, C, and D. Corresponding values of the dynamic stress and the potential strain energy density,  $W_{Di}$ , at A, B, C and D can also be measured. For instance, at Peak A in Figure 3.140, the corresponding dynamic stress,  $\sigma_A$ , and  $W_{Di}(A)$  are 0.293 MPa and 0.0418 MJ/m<sup>3</sup>, respectively. It is obvious that, at Peak A, the effective modulus,  $E_A$ , can be established using Equation (3-35), according to Ip *et al.* (1998), as:

$$E_A = E_0 \left( \frac{\text{Slope}(OA)}{\text{Slope}(OY)} \right) = E_0 \frac{\left( \frac{\sigma_A}{W_{Di}(A)} \right)}{\left( \frac{\sigma_Y}{W_{Di}(Y)} \right)} = 8 \frac{\left( \frac{0.293}{0.0418} \right)}{\left( \frac{0.25}{0.031} \right)} = 6.95 \text{ MPa} \quad (3-35)$$

where  $W_{Di}(Y)$  and  $W_{Di}(A)$  are the potential strain energy densities at Y and A, respectively,  $\sigma_Y$  and  $\sigma_A$  are the dynamic stresses at yield point and A, respectively, and  $E_0$  and  $E$  are the Young's modulus (8 MPa) and the effective modulus, respectively.

Similarly, the effective modulus and strain levels at other points of B, C and D can also be established, as shown in Table 3-10.

Table 3-10 Strain values and corresponding effective modulus for Run G-10-a1 fresh Granny Smith apple specimen under 10 cm drop.

Strain	Effective Modulus (MPa)
0	8.00
0.125	8.00
0.145 (Point A)	6.95
0.250 (Point B)	3.97
0.330 (Point C)	3.00
0.400 (Point D)	2.48

Now, referring back to Figure 3.135 for the corresponding strain values under each peak, a direct relationship between the effective modulus and their corresponding strains can be established and shown in Figure 3.141 for fresh Granny Smith apple under transient deformation with progressing damage process.

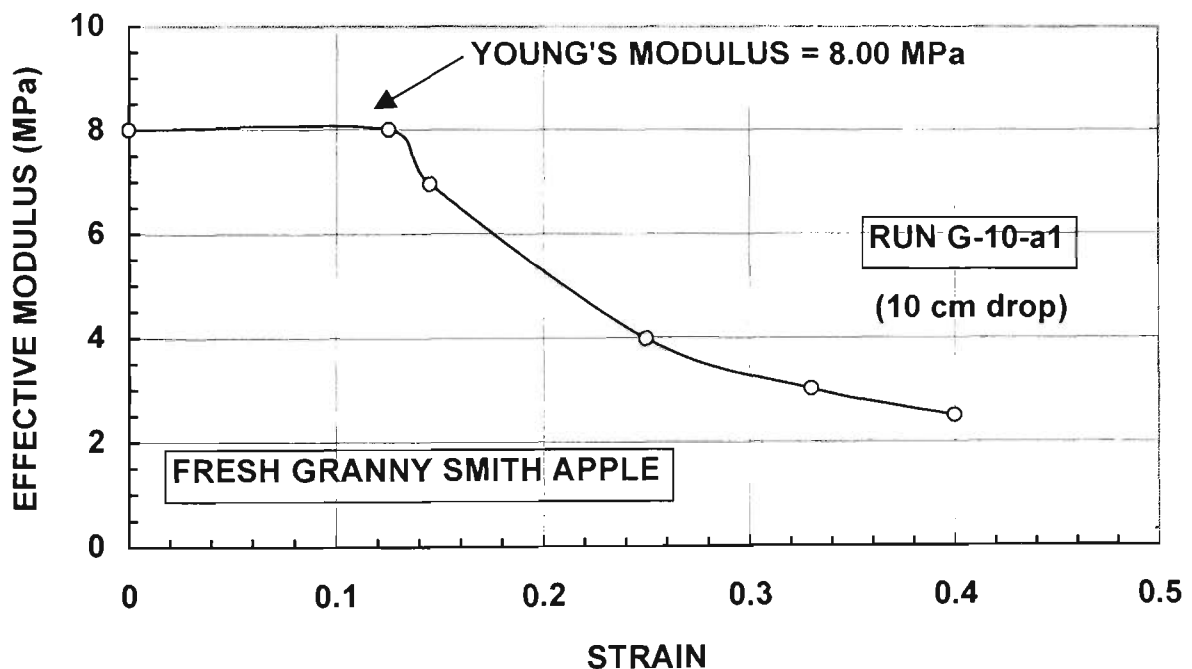


Figure 3.141 Relationship of strain and effective modulus of fresh Granny Smith apple under dynamic deformation with a strain rate of 133/sec.

Based on Figure 3.141, an accurate estimation of the dynamic effective modulus using the gradual reduction of the slope as a result of damage can be realized. The process can be repeated for 8-month aged Granny Smith apple by plotting the dynamic stress and strain energy density potential curve as shown in Figure 3.142.

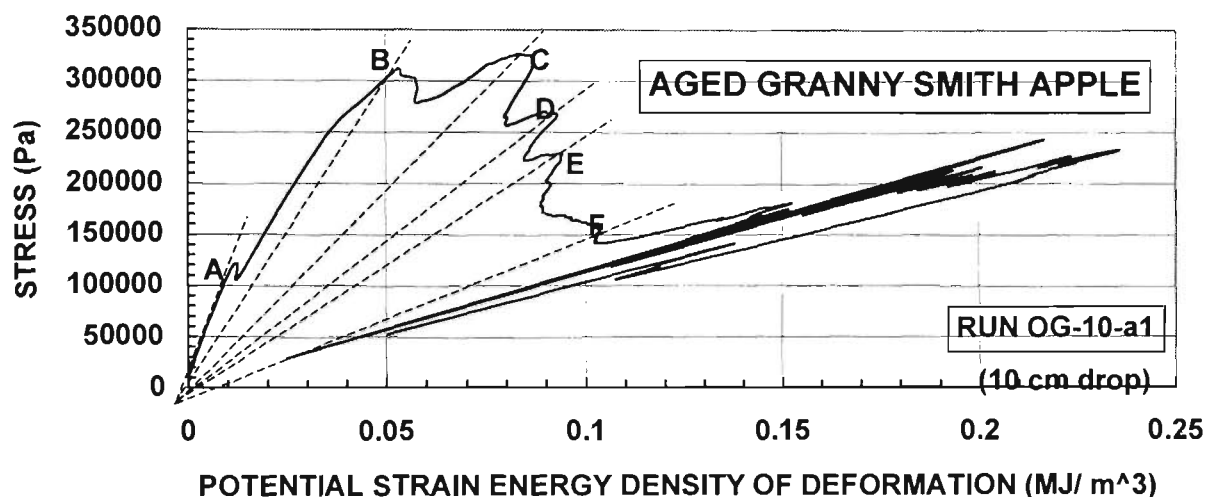


Figure 3.142 Material damage indicator: relationship between dynamic stress and strain energy density potential during dynamic deformation. (Run OG-10-a1).

Using Equation (3-35), the strain values and corresponding effective modulus for Run OG-10-a1 8-month aged Granny Smith apple specimen under 10 cm drop can be established and shown in Table 3-11. For comparison, the data in Table 3-11 were incorporated into Figure 3.141, as shown in Figure 3.143.

Table 3-11 Strain values and corresponding effective modulus for Run OG-10-a1 8-month aged Granny Smith apple specimen under 10 cm drop.

Strain	Effective Modulus (MPa)
0	4.00
0.09	4.00
0.100 (Point A)	3.42
0.170 (Point B)	1.95
0.255 (Point C)	1.31
0.350 (Point D)	1.00
0.410 (Point E)	0.85
0.665 (Point F)	0.52

From Figure 3.143, by comparing the two  $E$ - $\epsilon$  curves, it is clear that the dynamic damage processes of the fresh and 8-month aged Granny Smith apple specimens are comparable, by examining the trends of the two curves. A long cold storage period did not seem to have altered the means and magnitudes of dynamic processes such as fibrillar breakage and debonding. The Young's modulus was markedly reduced after the 8-month storage, however, from 8.00 MPa to 4.00 MPa.

Obviously, the so-called 'bio-yield point' as shown at Point A in Figure 3.143 for the aged Granny Smith apple specimen can be shown here as nothing more than the initial damage as registered by the  $\sigma$  versus  $W_{Di}$  curve. With this new approach, we can comfortably accommodate situations with more complex dynamic failure mechanisms in produce materials, biomaterials and packaging cushions such as the closed-knitted polystyrene foam cell structures.

From the many strain energy density potential plots we did on produce materials, and other materials such as packaging foams and corrugated fibre-boards, and biomaterials like human molar teeth, it is significant to note that each material seems to have a unique curve shape like a fingerprint, suggesting that very specific and invariant failure modes are always associated with each material.

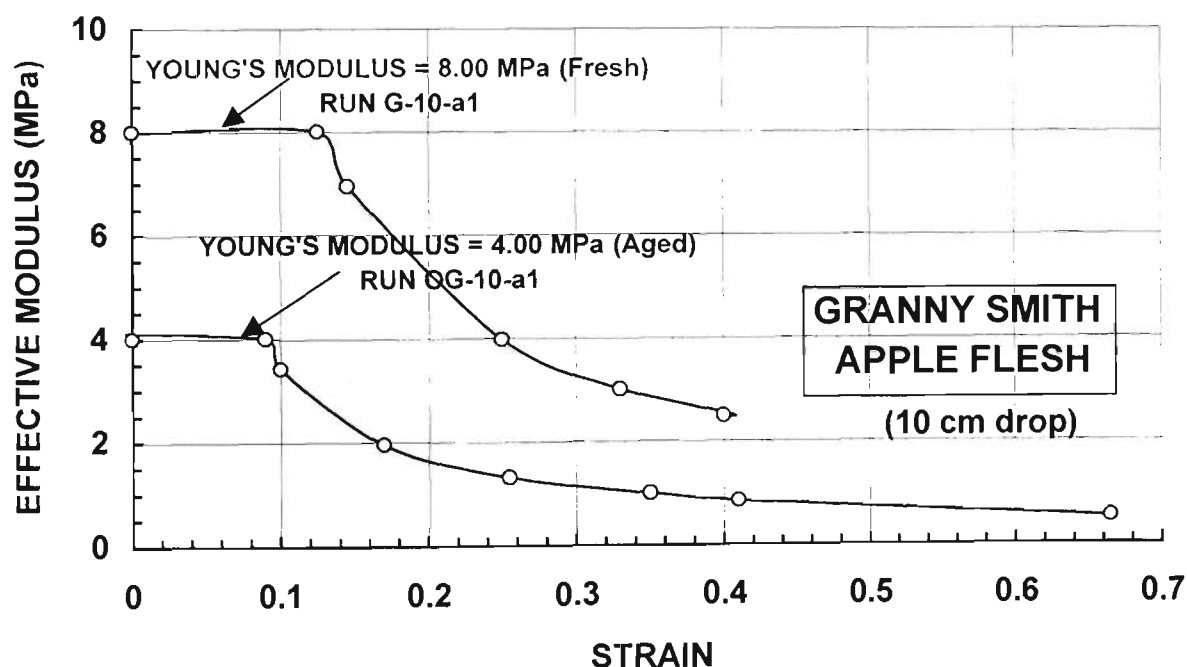


Figure 3.143 Relationship of strain and effective modulus of fresh and 8-month aged Granny Smith apple under dynamic deformation.

### 3.7.6 Bio-Yield Point and S-shaped Sigmoidal Curve in Dynamic Response of Produce and their Relationship with Fibrillar Slippage

Studies of test results from quasi-static deformation of some fruit specimens such as apple in the 1960's indicated the possible existence of a unique yield-point called 'bio-yield point' by earlier workers, see, for instance, Fletcher *et al.* (1965). This yield point appears on the stress-strain curve as a small peak prior to the ultimate failure. Workers have noticed that for some other produce, including peaches and potatoes, no peaks were formed, but only a distinct change in the slope of the force-deformation curve, of which earlier workers also defined as the bio-yield point.

Referring to laser-based test results, for the case of apple deformation as shown in Figure 3.144, the bio-yield point occurs at a stress and strain of 210 kPa and 18.5%, respectively. If these are compared with those in Figure 3.110, the bio-yield point seems to occur at exactly the same stress and strain levels, prompting workers to conclude that the bio-yield point is indeed a material parameter. However, this conclusion will be premature without comparing these figures with Figure 3.51. We recall from Figure 3.51 that produce textures could suffer no fibrillar slippage in their pre-peak domain. Thus, the bio-yield point is nothing more than just pre-peak instabilities. It is certainly not a material parameter in the sense of plastic yield-points in materials.

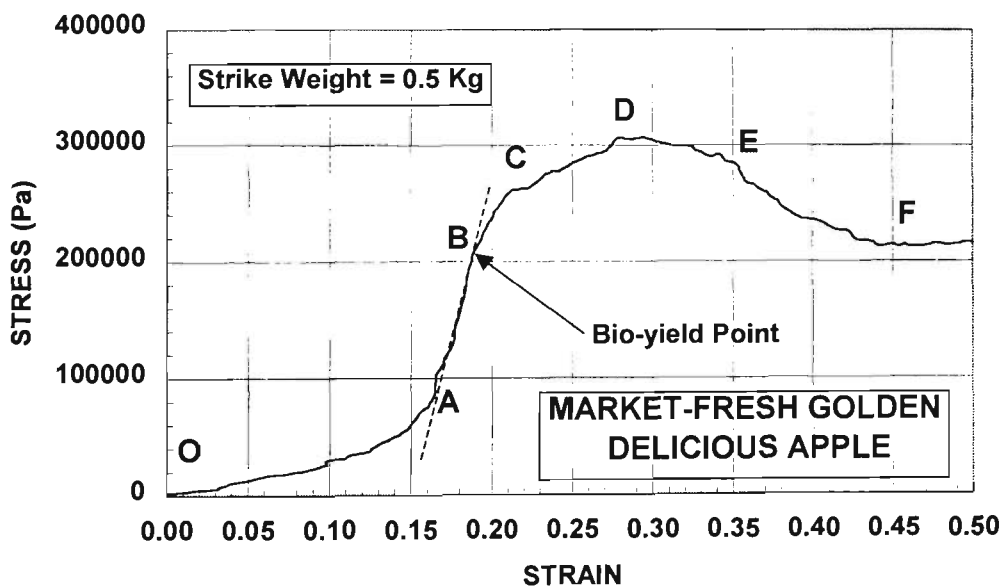


Figure 3.144 Dynamic stress-strain relationship of market-fresh Golden Delicious apple tissues under a strain rate of 170 /sec. with 25 cm drop. (Run SGA-0a-2).

There have not been many debates among research workers on a more precise definition of the bio-yield point for agricultural produce. We recall that it was proposed some 35 years ago, now

more or less generally accepted by a large community of agricultural workers. The proposal followed observations on quasi-static deformation of fruits and vegetable tissues that seem to support the existence of a bio-yield point before the ultimate strength is reached, see Fletcher *et al.* (1965). This point tends to disappear when a critical strain rate is reached. In other words, this bio-yield point seems to be rate sensitive, see Miles and Rehkugler (1973).

Using laser-based stress-strain data of papaya specimens under a strike weight of 0.9 kg, it is noted that the bio-yield point increases slightly from 65 kPa (Figure 3.145) to 85 kPa (Figure 3.45) when the strain rate increases from 88 /second to 127 /second. Immediately after the bio-yield point, both figures show a degraded effective modulus, implying that the bio-yield point is actually the direct consequence of fibrillar slippage, which in turn causes micro-cracking damage with resulting decrease in effective modulus. This can be seen by the change in the stress-strain slopes from A-B to C-D in both Figures. Once again, this is not to be confused with shear banding which usually suffers no change in the effective modulus, showing distinct parallel stress-strain slopes in the pre-peak domain, as indicated in both Figures 3.45 and 3.145. The Young's modulus remains unchanged at around 5.8 MPa in both Figures.

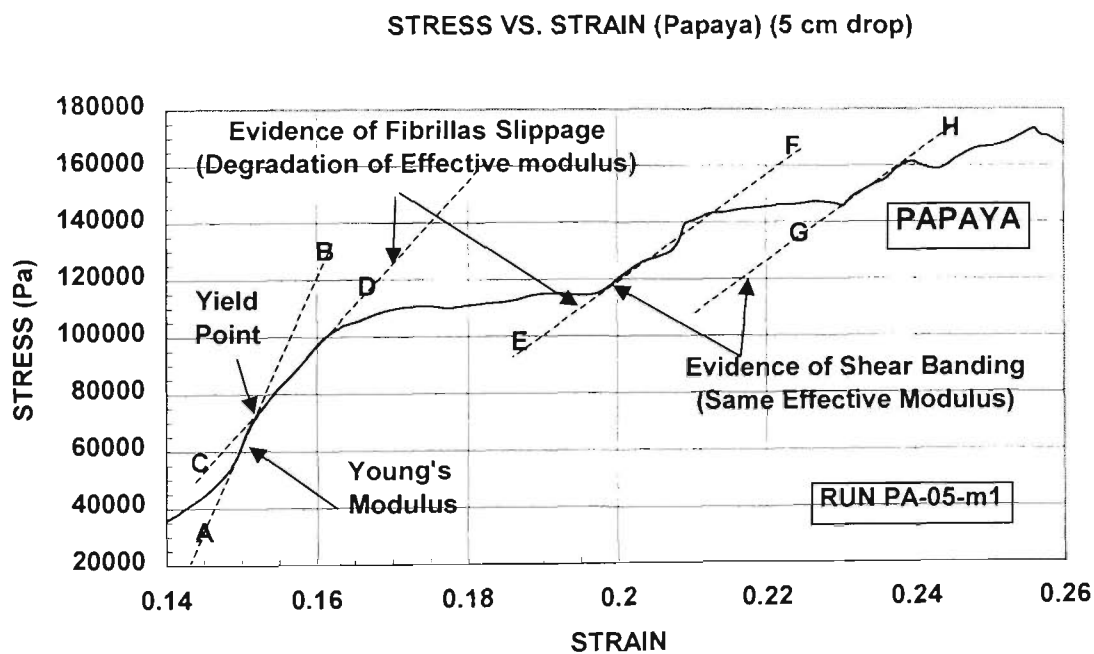


Figure 3.145 Laser-based stress-strain curve of papaya highlighting the evidence of fibrillar slippage and shear banding activities after bio-yield point in Run PA-05-m1 with drop height of 5 cm and strain rate of 88 /sec.

This is comparable to the bio-yield points of Golden Delicious apple specimens as shown in Figures 3.110 and 3.144 under dynamic strain rates of 133 /second and 170 /second, respectively. Both Golden Delicious specimens first yielded at 210 kPa, followed by progressive damage of fibrillar slip

mechanism. It strongly suggests that the bio-yield point actually denotes the first yield of the material as the fibrils start to slip past each other, something not unlike the debonding of fibres in composite materials under dynamic loading. Instabilities play a predominant role in the interfacial behaviour. The interactions at the multiplicity of interfaces of micro-fibrils/fibrils between the different structural levels of molecules (cellulose), cell walls and macro-fibrils are dynamically affected by such factors as orientation and shape, the numbers of fibre layers, as well as mineral and water contents. The micro-scale conditions are usually complex. So, in the end, it is hardly conceivable that the bio-yield point can be a uniquely and invariant material parameter.

For the case of dynamic deformation of potato specimen, Figure 3.146, under a strain rate of 142/sec., the bio-yield point B is registered at 0.2 MPa. This follows a long ‘toe’ section denoted by ‘OA’. This is a distinct characteristic of potato cells, Figure 2.21, which can allow substantial stretching by absorbing an enormous amount of strain energy upon initial loading, up to 22% of strain with negligible level of applied stress. The dynamic stress-strain response ‘OABCD’ and beyond looks like a S-shaped curve and is usually recognized as such by the bio-materials science workers, see also Figures 3.23 and 3.24 for the case of banana flesh deformation.

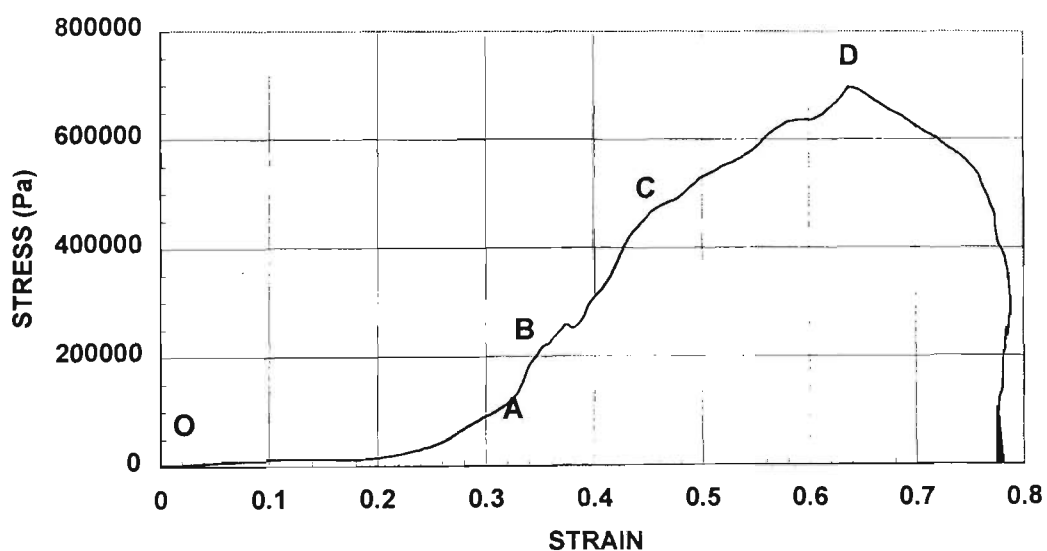


Figure 3.146 Laser-based dynamic stress-strain relationships of potato specimen under a strike weight of 0.9 kg with strain rate of 142/sec. (Run PT-10-m1).

Besides, there should be no direct relationships between the ‘toe’ length of OA and the amount of intercellular spaces of produce tissues. In other words, the ‘size’ of the ‘toe’ length is not due to the total volume size of the intercellular spaces of the produce tissues. This fact is clearly illustrated by the potato tissue here. The size of the intercellular spaces inside potato tissues is

notoriously small, usually less than 1% of the total volume, comparing to, for instance, Golden Delicious apple with more than 20% of total volume as intercellular spaces, see Figures 3.110 and 3.144. At A-B (denoting Young's modulus and the occurrence of the elastic precursor wave front) in Figure 3.146, the fibrils are straightened out, with notable damage due to fibrillar slippage to C as evident by a change in the effective modulus from A-B to B-C. It follows a lower slope C-D, denoting another switch of effective modulus, towards the ultimate strength at D.

Let us focus on the presence or absence of the S-shape feature based on laser-based dynamic stress-strain response from various produce. It is possible to classify produce into four distinct types according to their dynamic characteristics, as far as their resemblance to an S-shaped curve is concerned:

- (1) The softest fruits such as kiwifruit and persimmon do not exhibit S-shaped curves, see, for instance, Figures 3.29 and 3.30. This produce can dissipate dynamic loading by a coupled process of plastic working-hardening and heat diffusion.
- (2) Some fruits exhibit sharp S-shape curves, with short 'toes' which end at a strain of 5% to 10% for papaya and nashi and to 10% for William pear.
- (3) Some S-shape curves of produce are sensitive to strain rates of deformation. For fresh Granny Smith apple, the 'toe' extends to about 10% of strain under a strain rate of 93 /sec., but the 'toe' disappears when the strain rate is raised to 140/sec. In the case of potato, a slight decrease of strain rate from 155/sec. to 142/sec. extends the 'toe' from 8% to 30%.
- (4) The 'toes' of some produce can easily stretch to about 15% to 20% of strain, and are quite stable, that is, insensitive to strain rate changes. Examples are pawpaw, tomato, eggplant, Golden Delicious apple, and banana flesh.

The S-shaped curves play a significant role in minimizing damage to biological materials, including horticultural produce. Most show highly deformable textures and, at initial low stress levels, extensive elongation, some many times greater than those of traditional engineering materials and metals. Although the stress levels along the 'toe' of biological materials may stay low, the stored strain energies, or energies absorbed during the initial deformation, could be a lot higher than those in common engineering materials under comparable strains. As mentioned in Atkins and Mai (1985), Jeronimidis and Gordon first discovered in 1974 that the helical filaments of the cellulose microfibrils in wood cells, fibrils and structural fibres that make up the cell walls, if stretched, can achieve up to 20% of longitudinal extensions. So, an S-shaped stress-strain curve becomes a possibility when the tissue is under initial loading.

On the other hand, the expected S-shape curve would not be affected by the volume size of intercellular spaces in the produce tissues, as mentioned earlier. Produce with a low level of intercellular spaces, such as nashi tissues with about 4% intercellular spaces and potato tissues with less than 1%, do not necessarily imply that they will only stretch with short 'toes'. The OA toes of potato, Figure 3.146, and nashi, Figure 3.147, extend to 22% of (large) strain and 9% of (medium) strain, respectively. Here, as mentioned earlier, the intercellular spaces within produce tissues do not actually contribute to the size of the S-shape 'toe' length. Rather, air spaces allow for a reorientation of cells during compression. If the void volume is relatively large, such as apples, the Poisson's ratio should remain low at around 0.32 to 0.35, according to Chappell and Hamann (1968). But if the void volume is low, such as potatoes, very little total volume reduction can occur and the Poisson's ratio approaches 0.5, see Finney and Hall (1967).

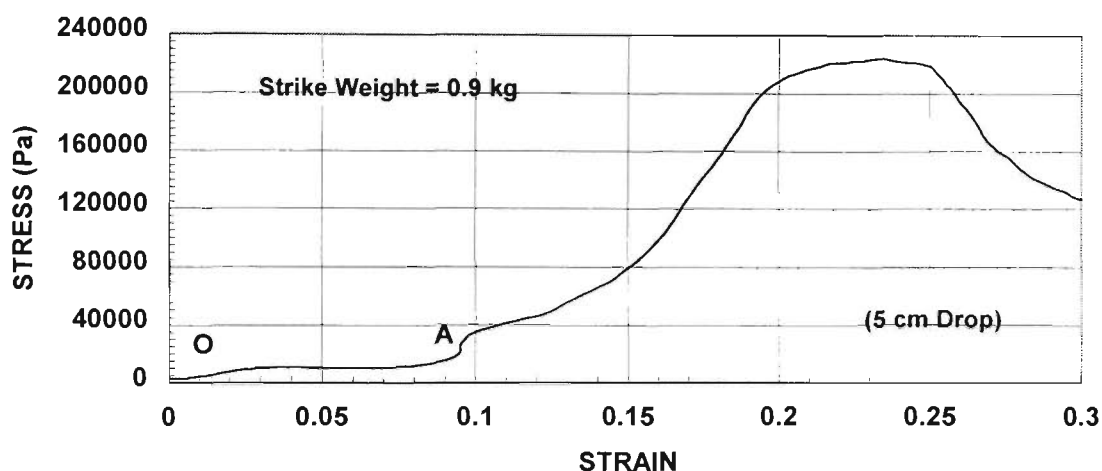


Figure 3.147 Laser-based dynamic stress-strain relationship for market-fresh nashi tissue under a strain rate of 90/sec. (Run N-05-X2a).

The characteristic S-shape curve of produce also plays a crucial role in fracture mechanism. This almost-horizontal curve is not unlike the surface tension of a liquid, with very low shear modulus in the initial strain. If there are cracks within the produce, there is virtually no communication of strain energies between parts of the stressed body and it is difficult to feed energy into existing cracks or potential crack sites. Within this strain range the material does not tear. Actually, difficult-to-tear biological materials do not possess very high works of fracture, with the maximum of only about  $10 \text{ kJ/m}^2$ , according to Atkins and Mai (1985).

Summing it up, we note that the initiation of fracture mechanisms such as fibrillar slippage in produce should not be solely based on the amount of work of fracture. It also based on the characteristic shapes of the dynamic stress-strain curves, particularly the initial S-shaped 'toe' section of each produce under specific forcing conditions. Also, the so-called bio-yield point at the end of the S-shaped curve is by and large the consequence of molecular slippage instabilities of the produce cell walls when the micro-fibrils are fully stretched.

One interesting aspect of instabilities commonly found in the uploading dynamic stress-strain curves of horticultural produce deformation is the serrated (staircase-like) feature. This kind of 'plastic burst (jumps)' is significant and is associated with the plastic failure of the pectic cement that bonds adjacent cells together. Examples are numerous, and can be observed in crisp produce such as Golden Delicious apples (Figures 3.148) and nashi (Figure 3.52) commonly associated with high drop heights, as well as softer fruits like pawpaw (Figure 3.149).

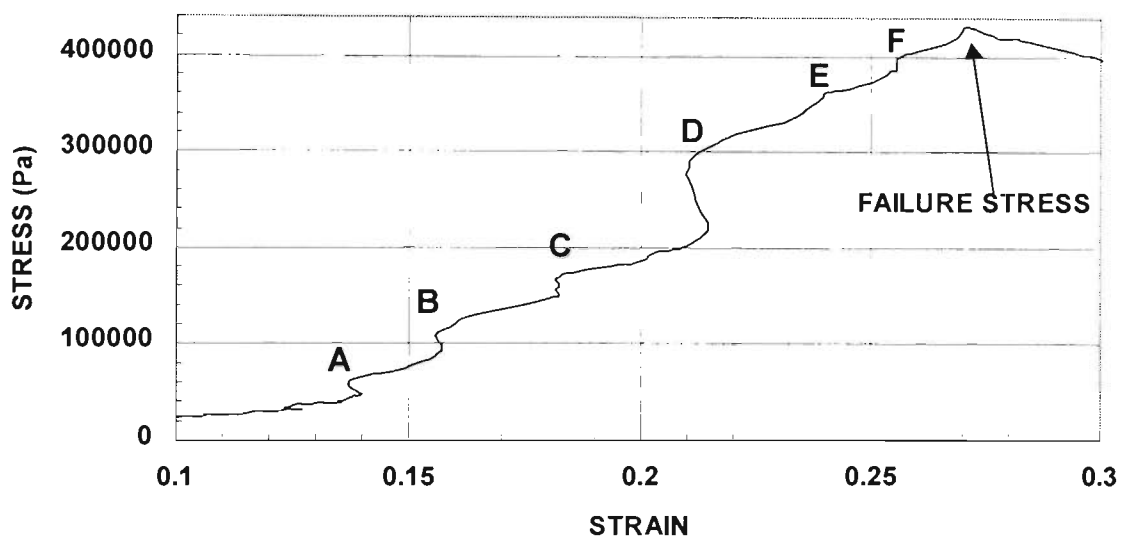


Figure 3.148 Dynamic stress-strain relationship of market-fresh Golden Delicious apple tissues under a strain rate of 156/sec. showing staircase instabilities. (Run SGA-a1-a2) (25 cm drop)

Let us remind ourselves that horticultural materials under deformation are faced with different options or paths leading to instabilities or plastic/viscoplastic deformation. These paths compete with each other to obtain the first priority of being chosen, depending on the physical state of the materials. The physical states of the materials and the paths are inter-related and may be illustrated and summarized in Figure 3.150. Referring to Figures 3.88 and 3.150, we know that the material will be under plastic or viscoplastic deformation by following the Hugoniot curve. We recall

the existence of an imaginary hydrostat curve that originates from the origin and curves upward, as shown in Figure 3.88.

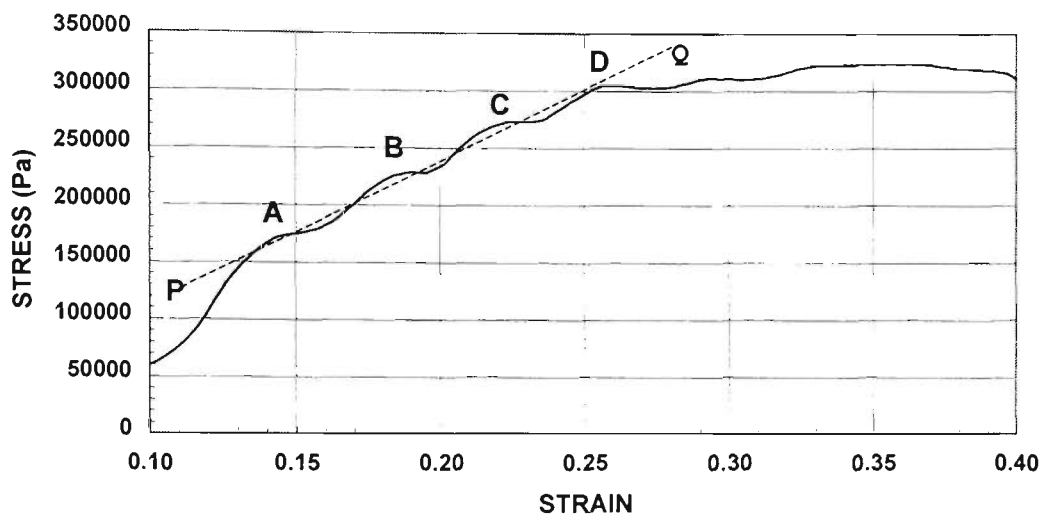


Figure 3.149 Dynamic stress-strain relationship of market-fresh medium-ripe pawpaw tissues under a strain rate of 113/sec. showing staircase instabilities. (Run PW-10-m1)(10 cm drop)

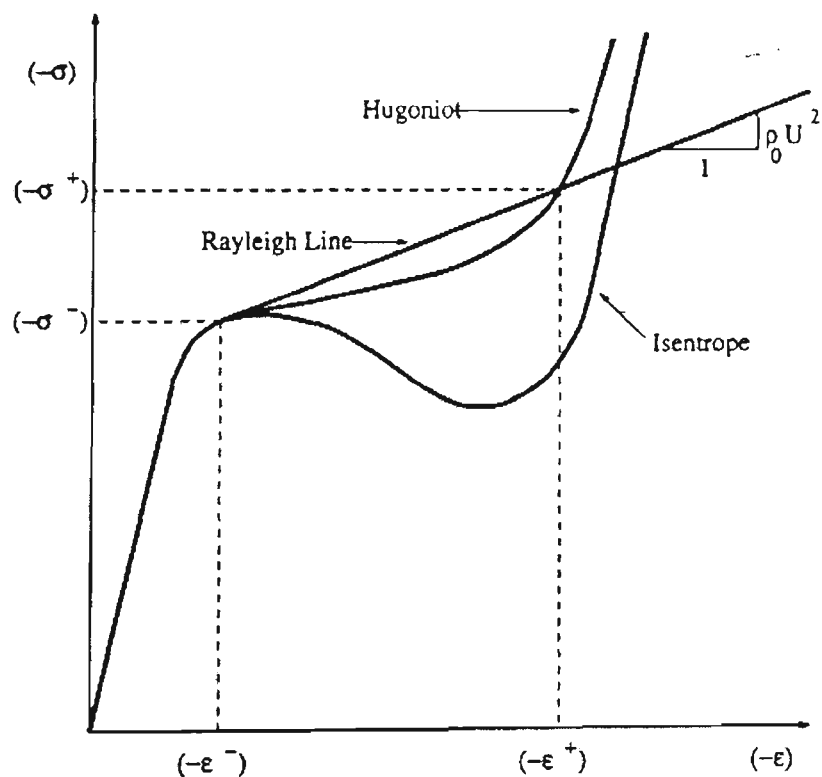


Figure 3.150 Hugoniot stress-strain curve of uniaxial compression of glassy material under subsonic and supersonic crushing speeds. From Clifton (1993).

If both the Hugoniot and the hydrostat curves are parallel, the material is liquid-like, denoting perfectly-plastic conditions. If the slope of the Hugoniot curve is lower than the hydrostat curve, we have a plastic work-hardening situation. If the slope of the Hugoniot curve is higher, the material is in viscoplastic state. If the material follows the Rayleigh line, its structural integrity is completely broken down, denoting viscous flow. However, if the material attempts to follow the isentrope curve, see Figure 2.70, the elaboration on Pages 92 and 93 in this thesis, and Pages 464-469 in Ogden (1984), this could not be possible. This is because this path is only valid under the condition that negligible heat dissipation is involved during the material deformation. The most likely outcome will be a plastic burst, or jump, shown as a horizontal jump from the left peak in Figure 3.150 intersecting the isentrope curve on the right. This jump denotes the substantial slippage in strain in the serrated features.

### 3.8 SUMMARY

This chapter presents the dynamic characterization of horticultural produce based on instrumented impact tests and DMA tests. Two new methods were presented. One is the laser-based test for the measurement of dynamic stress-strain response curves for different produce. The other is the establishment of a relationship between bruise volumes,  $BV$ , and their corresponding duration of impact,  $\tau$ , using an approach based on regular whole-fruit drop tests coupled with shock tests conducted on a package fragility shock tester. A relationship of between  $BV$  and  $\tau$  is important in the design of package protection requirements of the produce.

A new precision and direct displacement measuring method based on laser-displacement sensing using the optical triangulation principle was presented in this Chapter. The reliability of the laser-based instrumented set-up allows high sampling frequency that enhances the analysis of the bruising processes during the uploading cycle of the material deformation with precision. We conclude that this measuring technique is applicable to a broad spectrum of materials that undergo softening processes. Based on data obtained from the laser-based technique, we found that:

- (i) The laser-based measurement technique demonstrated that the horticultural materials tested do not deform in a random fashion, but in a consistent and reproducible manner.

- (ii) Soft produce such as banana flesh exhibits weak structural integrity in such extreme form that its initial material modulus is extremely small and is difficult to trace. It is very rate-sensitive and virtually flows upon the slightest applied stress above the 'toe' section of an S-shaped curve with completely different paths of deformation, implying a typical viscoplastic material.
- (iii) Soft produce flesh like banana is protected by fibrous skin in a sacrificial manner. The flesh will be below its yield point when the fibrous skin fails.
- (iv) Soft fruit such as kiwifruit and persimmon exhibit perfectly-plastic liquid-like deformation characteristics. Damage in the form of softening is found in persimmon, whereas plastic or perfectly-plastic deformation rather than damage occurs in kiwifruit. Both fruits exhibit small but distinct Young's moduli.
- (v) Soft produce such as tomatoes are weak in structural integrity, but possess strong and resilient cells that are able to withstand high strain levels without failure. Under high rate of loading, they deform plastically that precedes the occurrence of a Rayleigh line in its stress-strain curve, as a result of energy dissipation in the form of heat.
- (vi) Soft produce such as papaya and eggplant exhibit consistency in the unloading dynamic response curves, including plastic deformation as well as in instabilities, Figures 3.45 and 3.46. This implies that the material instabilities were as a result of plastic deformation, in the form of shear banding.
- (vii) Soft produce tends to exert self-protection in minimizing the extent of bruise damage by the containment and dissipation of impact energy in the form of heat. Soft produce tends to deform under plastic deformation, often with the complete absence of any pre-peak instability.
- (viii) Moderately crisp produce such as eggplant deform with characteristics that are present in both the soft and crisp produce. Pawpaw possesses pre-peak fibrillar slippage characteristics as clearly shown by the gradual degradation of the effective modulus. Pawpaw also exhibits strong viscoplastic deformation characteristics when the strain rate is increased. This also seems to apply to potato.
- (ix) Produce with crisp and moderately crisp textures tends to deform with pre-peak instabilities. Basically two major categories of pre-peak instabilities may be recognized:
  - those instabilities in produce that do not cause the degradation to the effective modulus
  - those instabilities in produce which cause degradation of the effective modulus. This phenomenon is evident by micro-crack damage in the form of fibrillar slippage on the produce cell walls.

- (x) If the produce textures are crisp, they tend to protect themselves in minimizing bruising by instabilities (damage) such as pre-peak cracking. Significant amounts of impact energy can be absorbed in the formation of these cracks, thus limiting the size of bruise.
- (xi) Crisp produce such as apples, pears and nashi deform predominantly with pre-peak damage. They are rate-independent and have a distinct critical stress level that seems substantially changed when aged.
- (xii) Natural skins, regardless of the small thickness, exhibit strong protective ability in apple and nashi.
- (xiii) DMA tests show that Golden Delicious apple specimens behave in both a viscoelastic and Maxwell liquid manner.
- (xiv) Based on the developed shock test method, a protection design relationship can be established to correlate, in terms of true free-fall drop heights, the bruise volumes of produce and duration of impact as experienced by the produce.
- (xv) Based on IFA tests, the impact duration seems to be insensitive to change of drop heights, but begins to increase when the drop height is lower than the damage threshold.
- (xvi) The restitution coefficients,  $e$ , obtained from drops of whole-fruit such as Golden Delicious apple shows gradual decrease from  $e = 0.7$  at the damage threshold due to material damping.
- (xvii) Analysis of a typical shock pulse from a 5-cm impact on whole-fruit Golden Delicious apple indicates the presence of an acceleration wave immediately after first impact on the rigid surface.

We have applied the results of Chu (1962) to solid-like and liquid-like extreme cases in this study, and have explained, during impact conditions, how soft produce can be ‘immunized’ from the destructive propagating wave fronts that are the main causes of widespread bruise damage. The reasons for this are a direct consequence of the damping of the elastic precursor wave front and the diffusion of the main plastic wave front associated with the work hardening process to heat disturbance.

Shear bands tend to occur in horticultural materials that are soft at the pre-critical domain, but in crisp produce at the post-critical domain. Examples of shear bands as shown in our test results of papaya, potato and apple have been provided. It was noted that shear banding does not alter the material modulus, compared to other damage-based instabilities that result in the degradation of the effective modulus. There is evidently negligible change in the effective modulus of the material before and after the occurrence of shear banding.

This chapter also serves to analyze the instabilities of various scales in produce under dynamic loading. The pre-peak instabilities can be classified into two main categories: namely shear banding induced by plastic deformation, as has been discussed in Section 3.6, and fibrillar slippage associated with micro-crack damage. Both types of instabilities will eventually result in propagating meso-cracking or global-scale fracturing.

Fibrillar slippage occurs in produce with lower Poisson's ratio, such as apples and pears. The limited flexibility of these crisp produce textures to deform or bulge under loading prompts the produce to crack or fracture rather than to deform plastically. But, it is not uncommon to observe a change of textures from crisp to soft when produce such as nashi undergoing extreme strain rates of deformation, or mangoes undergoing a ripening process. Fibrillar slippage, which occurs in most produce with crisp texture, signifies a micro-scale phenomenon with the micro-fibrils on the cell walls of produce slipping passed one another when the cell wall surface is under loading. The most distinctive outcome of fibrillar slippage is an immediate degradation of the effective modulus. Being a form of instability, fibrillar slippage can occur at random.

The first occurrence of either form of instability, be it shear banding or fibrillar slippage, occurs at the first abrupt change of the stress-strain slope which has been termed the bio-yield point of the material. Based on numerous laser-based test results of crisp produce, such as apple, nashi and Williams pear that are dominated by fibrillar slippage instabilities, we conclude that bio-yield point is a direct consequence of micro-crack damage, rather than that of shear banding. Also, bio-yield point cannot be considered as a material parameter as long as it is deemed as instability.

Regarding the S-shape 'toe' section commonly observed in dynamic stress-strain curves for produce, we conclude that there is no direct relationship between the S-shape section and the intercellular space in produce. The conclusion is based on laser-based test data on potato specimens that shows prominent S-shape section of up to 25% strain, as compared to the notoriously small intercellular space in potato tissues (usually less than 1% volume). The S-shape feature can be explained by the loosening or uncoiling of the helical filaments of the cellulose micro-fibrils, first discovered by Jeronimidis and Gordon in 1974. The feature plays a significant role in minimizing bruise damage extensively elongating at the initially stress levels, so that the stress level can stay low, with a negligible amount of energy absorbed. From our results, we observed that the softer the produce materials, the less prominent the S-shape feature becomes. For the extremely soft produce such as persimmon, the S-shape feature is absent. The S-shape curve is also insensitive to strain rate in some produce such as apples, but can be extremely rate sensitive in other produce such as potatoes.

Regarding the micro-to-meso-cracking transitions, we followed the theoretical basis developed by Ortiz (1985). He pointed out that the unloading stress-strain curves under transition should be a random process in terms of path selection always towards the weakest domains in the material. If stronger barriers encircle micro-cracks, the micro-cracks can be arrested and isolated. If a path of weaker strength or inferior toughness is opened, the crack will propagate under the meso-scale, with minimum rise in stress level. A sequence of this nature can result in a serrated stress-strain curve, as observed in numerous of crisp produce textures in our test data and which we attribute to significant strain slippage with meso-scale or plastic burst (jumps). This is distinctively different from the micro-scale fibrillar slippage. Macro-cracking (softening) processes initiate if the primary meso-cracks begin to join together.

Regarding meso-scale, macro-cracking and fracturing, our data show that crisp produce such as apple and pears fail predominantly under meso-scale cracking and/or global-scale macro-cracking under dynamic loading. For other softer produce such as banana, kiwifruit and tomato, plastic deformation (and thus strain rate) plays a more significant role. The first appearance of macro-fractures depends heavily on the level of strain, and, for soft produce, the strain rate as well. Still other produce such as pawpaw tends to fail under both modes, depending on the loading conditions and instabilities. In other words, produce such as pawpaw is sensitive to size effects. It may result in a macro-fracture if, at the interface of meso-cracks and macro-cracks, the cracking is 'brittle'. Or, it can undergo a slow cracking (softening) process if the nature of cracking is more 'ductile'. The true nature of macro-cracking depends on the energy absorbed per unit volume of the produce material (so-called strain energy density,  $D$ ). If the amount of impact energy exceeds  $D$  (which is a material parameter), or the maximum amount of energy the material is capable to handle, a macro-crack will occur to contain the damage energies. We illustrated in Equation (3-30) that materials affected by damage in the fracture process zone and under a softening process are directly related to the change of scales in their effective modulus (from micro-scale to macro-scale).

For the case of produce with crisp textures such as apples, their stress-strain curves will be 'prematurely' truncated, with the occurrence of meso-cracking and macro-softening, if their maximum allowable strain energy density is exceeded. The fact that their characteristic stress-strain curves are all 'truncated prematurely' prompts us to conclude that this is the primary reason for the rate-independence of Golden Delicious apples. The cracking phenomenon is a possible mechanism that effectively contains damage energy in crisp as well as to soft and very soft produce.

The laser-based impact testing technique was used to analyze the dynamic response characteristics of produce. In particular, the dynamic effective modulus of fresh and 8-month aged Granny Smith apple specimens were established. The failure modes between aged and fresh specimens were compared. In general, the dynamic response of materials and their associated failure modes can be identified using this technique.

# CHAPTER 4

## CONCLUSIONS

The conclusions of this study are:

1. That the primary mechanisms identified as causing bruising in horticultural materials are:
  - (i) plastic deformation, leading to the critical stage of shear banding instabilities or perfectly-plastic deformation;
    - (ii) viscoplastic deformation;
    - (iii) pre-critical instabilities that may include one or more of the following: micro-scale fibrillar slippage, debonding between cell walls or plastic jumps associated with serrated features. These instabilities cause the degradation of the effective modulus of the materials, leading to the critical (peak) meso-cracking transitional stage that lead to the post-critical processes of either:
      - (a) macro-cracking (strain softening) or
      - (b) macro-scale fracturing. For some crisp produce, macro-scale fracturing can occur during strain softening if the constant ‘critical softening coefficient’ is reached.
2. Produce with soft textures tends to bruise under plastic or viscoplastic deformation.
3. Soft produce under high rates of loading tends to self-minimize the extent of bruising by:
  - (i) the initiation of shear banding instabilities, or

- (ii) heat diffusion that accompanies the decay and disappearance of the wave pulses.
4. Produce with crisp textures tends to bruise under the following instabilities:  
micro-scale fibrillar slippage, cell-to-cell debonding, plastic jumps associated with serrated features and meso-cracking (in the form of prematurely ‘truncated’ dynamic stress-strain curves).
5. Crisp produce tends to self-minimize the extent of bruising and to contain the kinetic energy by the initiation of the following activities:
- (i) pre-critical instabilities of
    - (a) micro-scale fibrillar slippage; or
    - (b) cell-to-cell debonding;These activities serve to maximize the micro-crack density to saturation, and thus delay the joining-up of micro-cracks.
  - (ii) critical meso-cracking transitional activity leads to post-critical softening, as indicated by prematurely ‘truncated’ dynamic stress-strain curves. This activity serves to enhance the energy containment ability of the produce textures to achieve maximum attainable strain without macro-fracturing. This is achieved by maximizing the kinetic energy per unit volume that the textures can withstand before the highest value of strain softening modulus is reached. Beyond this state the textures are unstable and the occurrence of macro-fracturing is possible.
6. The bio-yield point was identified as the first occurrence of micro-scale fibrillar slippage. This applied to both soft and crisp produce. In the case of soft produce, the bio-yield point occurred at extremely low levels of stress. The bio-yield point cannot occur in viscoplastic produce tissues.

## REFERENCES

- Abeles, F.B. and Takeda, F. Cellulose activity and ethylene in ripening strawberry and apple fruits, *Scient. Hort.* (42) 269-275 (1990).
- Aifantis, E.C. On the microstructural origin of certain inelastic models, *Trans. ASME, J. Eng. Mater. Tech.* (106) 326-334 (1984).
- Akyurt, M., Zachariah, G.L. and Haugh, C.G. Constitutive relations for plant materials, *Trans. ASAE* (15) 766-769 (1972).
- Alfrey, T. Mechanical behavior of high polymers, 581 pages, Interscience Publishers (1948).
- Andrews, E.H. Fracture, Mechanical properties of biological materials, J.F.V. Vincent and J.D. Currey (edit.) 13-35, Cambridge Uni. Press (1980).
- Ashby, M.F. and Jones, D.R.H. Engineering materials: Vol.1, 2<sup>nd</sup> edtn., 306 pages, Pergamon (1996).
- Atkins, A.G. and Mai, Y-W. Elastic and plastic fracture: metals, polymers, ceramics, composites, biological materials, 817 pages, Ellis Horwood (1985).
- Bacic, A., Harris, P.J. and Stone, B.A. Structure and function of plant cell walls, The biochemistry of plants-A comprehensive treatise, J. Preiss (edit.) 297-372, Academic Press (1988).
- Bai, Y., Cheng, C. and Yu, S. *Acta Mechanica Sinica* (2) 1-16 (1986).
- Bazant, Z.P. Instability, ductility and size effect in strain-softening concrete, *J. Engng. Mech., ASCE* (103) 331-344 (1976).
- Bazant, Z.P., Belytschko, T.B. and Chang, T.P. Continuum theory for strain-softening, *J. Engng. Mech., ASCE* (110) 1666-1692 (1984).
- Bedford, A. and Drumheller, D.S. Introduction to elastic wave propagation, 297 pages, John Wiley (1994).
- Bell, J.F. and Stein, A. The incremental loading wave in the pre-stressed fields, *J. Mechanique* (1) 395-412 (1962).
- Ben-Arie, R., Kislev, N. and Frenkel, C. Ultrastructural changes in the cell walls of ripening apple and pear fruit, *Plant Physiology* (64) 197-202 (1979).
- Berry, D.S. A note on stress pulses in viscoelastic rods, *Phil. Mag.* (3) 100-102 (1958a).
- Berry, D.S. Stress propagation in viscoelastic bodies, *J. Mech. Phys. Solids* (6) 177-185 (1958b).
- Bieniawski, Z.T. Deformational behavior of fractured rock under multiaxial compression, Structures, solid mechanics and engineering materials, 589-598, M. Teeni (edit.) John Wiley (1971).
- Biggs, T. Nashi finds market niche, *Good Fruit & Vegetables* (4) 14-19, May (1993).
- Biggs, T. More apples, new markets aim of giant orchard, *Good Fruit & Vegetables* (5) 9-14, May (1994).

- Biggs, T. Mango production set to increase, *Good Fruit & Vegetables* (6) 10-14, March (1995a).
- Biggs, T. Grower group takes on study: apples, *Good Fruit & Vegetables* (6) 56, Oct. (1995b).
- Bittner, D.R., Manbeck, H.B. and Mohsenin, N.N. A method of evaluating cushioning materials used in mechanical harvesting and handling of fruits and vegetables, *Trans. ASAE* (10) 711-714 (1967).
- Blahovec, J., Patocka, K. and Paprstein, F. Inelasticity and bruising of cherries, *J. Texture Stud.* (27) 391-401 (1996).
- Bland, D.R. Application of the one-sided Fourier transform to the stress analysis of linear viscoelastic materials, Proc. Conf. on properties of materials at high rates of strain, Institution of Mechanical Engineers, London, 156-163, IMechE (1957).
- Bland, D.R. On shock structure in a solid, *J. Inst. Maths. Applics.* (1) 56-75 (1965).
- Bleich, H.H. and Nelson, I. Plane waves in an elastic-plastic half space due to combined surface pressure and shear, *Trans. ASME, J. Appl. Mech.* (33) 149-158 (1966).
- Bodner, S.R. and Kosky, H. Stress wave propagation in lead, Proc. 3<sup>rd</sup> U.S. Congress Applied Mech., R.M. Haythornthwaite (edit.) 495-501, ASME (1958).
- Bourne, N.C. Studies on punch testing of apples, *Food Tech.* (19) 113-115 (1965).
- Bourne, N.C. Texture of temperate fruits, *J. Texture Stud.* (10) 25-44 (1979).
- Bourne, N.C. Texture evaluation of horticultural crops, *HortSci.* (15) 7-13 (1980).
- Brett, C.T. and Waldron, K.W. Physiology and biochemistry of plant cell walls, 255 pages, Chapman and Hall (1996).
- Brinson, H.F. and Gupta, D. A. The strain-rate behavior of ductile polymers, *Exp. Mech.* (15) 458-463 (1975).
- Brooks, R.O. Generating specified shock pulses, *J. Env. Sci.* (21) 28-33 (1967).
- Brusewitz, G.H. and Bartsch, J.A. Impact parameters related to post harvest bruising of apples, *Trans. ASAE* (32) 953-957 (1989).
- Buckingham, T. Lifespan extends pear season, *Good Fruit & Vegetable* (6) 14 (1995).
- Budiansky, B. and O'Connell, R.J. Elastic moduli of a cracked solid, *Int. J. Solids Struct.* (12) 81-97 (1976).
- Budiansky, B. Micromechanics, *Comp. & Struct.* (16) 3-12 (1983).
- Budiansky, B., Hutchinson, J.W. and Lambropoulos, A.G. Continuum theory of dilatant transformation toughening in ceramics, *Int. J. Solids Struct.* (19) 337-355 (1983).
- Bui, H.D. Inverse problems in the mechanics of materials: an introduction, 204 pages, CRC Press (1994).

- Caddell, R.M. Deformation and fracture of solids, 307 pages, Prentice-Hall (1980).
- Canberra Horticultural Task Force. Strategies for growth in Australian horticulture, 118 pages, Australian Federal Government Reports (1994).
- Carpinteri, A. and Bocca, P. Transferability of small specimen data to full-size structural components: Chapter 8, Composite material response: Constitutive relations and damage mechanisms, G.C. Sih, G.F. Smith, I.H. Marshall and J.J. Wu (edit.) 111-131, Elsevier (1988).
- Chadwick, P. Thermoelasticity: The dynamical theory, Progress in solid mechanics: Vol.1, I.N. Sneddon & R. Hill (edit.) 263-328, North-Holland (1960).
- Chadwick, P. and Powdrill, B. Application of the Laplace transform method to wave motions involving strong discontinuities, *Proc. Cam. Phil. Soc.* (60) 313-324 (1960).
- Chappell, T.W. and Hamann, D.D. Poisson's ratio and Young's modulus for apple flesh under compressive loading, *Trans. ASAE* (11) 608-610, 612 (1968).
- Chen. E.P. Dynamic brittle fracture analysis based on continuum damage mechanics, Fracture mechanics: perspectives and directions (Twentieth Symposium), ASTM STP 1020, R.P. Wei and R.P. Gangloff (edit.) 447-458, ASTM (1989).
- Chen, P.J. Thermodynamic effects in wave propagation, Course and Lectures No. 72, Int'l Centre for Mech. Sci. Series, 1-33, Springer-Verlag (1971).
- Chen, P., Ruiz, M., Lu, F. and Kader, A.A. Study of impact and compression damage on Asian pears, *Trans. ASAE* (30) 1193-1197 (1987).
- Chen, P. and Yazdani, R. Prediction of apple bruising due to impact on different surfaces, *Trans. ASAE* (34) 956-961 (1991).
- Chen, S.M. Engineering analysis of viscoelastic response of fruits to impacts, 291 pages, PhD thesis, U. California, Davis (1985).
- Chen, W.F. and Saleeb, A.F. Constitutive equations for engineering materials, Vol.1: Elasticity and modelling, 580 pages, John Wiley (1982).
- Cheresh, M.C. and McMichael, S. Instrumented impact test data interpretation, Instrumented impact testing of plastics and composite materials, S.L. Kessler, G.C. Adams, S.B. Driscoll and D.R. Ireland (edit.) 9-23, ASTM (1987).
- Christensen, R.M. Theory of Viscoelasticity, 364 pages, Academic Press (1982).
- Chu, B.T. Stress waves in isotropic linear viscoelastic materials, *J. Mecanique* (1) 439-462 (1962).
- Chu, C.F. and Peleg, M. The compressive behaviour of solid food specimens with small height to diameter ratios, *J. Texture Stud.* (16) 451-464 (1985).
- Chuma, Y., Shiga, T. and Iwamoto, M. Mechanical properties of Satsuma orange as related to the design of a container for bulk transportation, *J. Texture Stud.* (9) 461-479 (1978).

- Clifton, R.J. An analysis of combined longitudinal and torsional plastic waves in a thin-walled tube, Proc. 5<sup>th</sup> U.S. National Cong. of Appl. Mech., 465-480, ASME (1966).
- Clifton, R.J. Elastic-plastic boundaries in combined longitudinal and torsional plastic wave propagation, *Trans. ASME, J. Appl. Mech.* (35) 782-786 (1968).
- Clifton, R.J. and Ting, T.C.T. The elastic-plastic boundary in one-dimensional wave propagation, *Trans. ASME, J. Appl. Mech.* (35) 812-814 (1968).
- Clifton, R.J. Analysis of failure waves in glasses, *Appl. Mech. Rev.* (46) No.12, Pt 1, 540-546 (1993).
- Coleman, B.D., Gurtin, M.E. and Herrera, R. Waves in materials with memory, Part I: The velocity of one-dimensional shock and acceleration waves, *Arch. Rat. Mech. Anal.* (19) 1-19 (1965).
- Coleman, B.D. and Gurtin, M.E. Waves in materials with memory, Part II: On the growth and decay of one-dimensional acceleration waves, *Arch. Rat. Mech. Anal.* (19) 239-265 (1965).
- Coleman, B.D., Greenberg, J.M. and Gurtin, M.E. Waves in materials with memory, Part V: On the amplitude of acceleration waves and mild discontinuities, *Arch. Rat. Mech. Anal.* (22) 333-354 (1966).
- Collins, R. Marketing studies help persimmons export success, *Good Fruit & Vegetables* (5) 45, May (1994).
- Coombe, B.G. Distribution of solutes within the developing grape berry in relation to its morphology, *Amer. J. Ecology & Viticulture* (38) 127-129 (1987).
- Cost, Thomas L. and Dagen, James D. Characterization of bulk cushion materials under impact loads using viscoelastic theory, *Shock & Vibration Bull.* (47) 189-196 (1977).
- Cristescu, N. On some dynamical problems of the theory of plasticity, PhD dissertation, University of Bucharest (1955).
- Cristescu, N. On the propagation of elastic-plastic waves for combined stresses, *PMM* (23) 1605-1612 (1959).
- Cristescu, N. European contributions to dynamic loading and plastic waves, Plasticity: Proc. 2<sup>nd</sup> Symp. Naval Structural Mechanics, E.H. Lee & P.S. Symonds (edit.) 385-442, Pergamon (1960).
- Dafermos, C.M. On the existence and the asymptotic stability of solutions of the equations of linear thermoelasticity, *Arch. Rat. Mech. Anal.* (29) 241-271 (1968).
- Davies, R.M. Stress waves in solids, Surveys in mechanics, G.K. Batchelor and R.M. Davies (edit.) 64-138, Cambridge U. Press (1956).
- Davis, B. Horticulture exports offer food for thought, *The Australian*, February 28 issue (1996).
- De Borst, R. and Muhlhaus, H.B. Gradient-dependent plasticity: formulation and algorithmic aspects, *Int. J. Num. Meth. Eng.* (35) 521-539 (1992).
- De Borst, R., Pamin, J. and Sluys, L.J. Computational issues in gradient plasticity: Ch. 6, Continuum models for materials with microstructure, H.B. Muhlhaus (edit.) 159-200, John Wiley (1995)

- Diehl, K.C., Hamann, D.D. and Whitfield, J.K. Structural failure in selected raw fruits and vegetables, *J. Texture Stud.* (10) 371-400 (1979).
- Diener, R.G., Elliott, K.C., Nesselroad, P.E., Ingle, M., Adams, R.E. and Blizzard, S.H. Bruise energy of peaches and apples, *Trans. ASAE* (22) 287-290 (1979).
- Dilley, D.R. Chapter 8: Enzymes, The biochemistry of fruits and their products: Vol.1, A.C. Hulme (edit.) 179-207, Academic Press (1970).
- Dillon, O.W. A nonlinear thermoelasticity theory, *J. Mech. Phys. Solids* (10) 123-131 (1962).
- Dillon, O.W. Coupled thermoplasticity, *J. Mech. Phys. Solids* (11) 21-33 (1963).
- Dillon, O.W. Waves in bars of mechanically unstable materials, *Trans. ASME, J. Appl. Mech.* (33) 267-274 (1966).
- Dillon, O.W. and Tauchert, T.R. The experimental technique for observing the temperatures due to the coupled thermoelastic effect, *Int. J. Solids Struct.* (2) 385-391 (1966).
- Dillon, O.W. A thermodynamic basis of plasticity, *Acta Mech.* (3) 182-195 (1967).
- Dillon, O.W. Plastic deformation waves and heat generated near the yield point of annealed aluminum, Mechanical behavior of materials under dynamic loads, U.S. Lindholm (edit.) 21-60, Springer-Verlag (1968).
- Domeney, T. Variable weather affects cherry crops, *Good Fruit & Vegetables* (5) 10 (1994).
- Dowling, N.E. Mechanical behavior of materials, 773 pages, Prentice-Hall (1993).
- Duckworth, R.B. Fruit and vegetables, 306 pages, Pergamon (1966).
- Duxbury, P.M. Breakdown of diluted and hierarchical systems, Statistical models for the fracture of disordered media, H.J. Herrmann and S. Roux (edit.) 189-228 (1990) Elsevier.
- Duxbury, P.M. and Kim, S.G. Scaling theory of elasticity and fracture in disordered networks, *M. R. S. Symp. Proc.* (207) 179-185 (1991).
- Dyson, A. Approximate calculations of Hertzian compressive stresses and contact dimensions, *J. Mech. Engng. Sci.* (7) 224-227 (1965).
- Esau, K. Plant anatomy, 767 pages, 2<sup>nd</sup> edtn., John Wiley (1965).
- Ferry, J.D. Viscoelastic properties of polymers, 641 pages, 3<sup>rd</sup> edtn., John Wiley (1980).
- Findley, W.N., Lai, J.S. and Onaran, K. Creep and relaxation of nonlinear viscoelastic materials, P.91, Dover (1989).
- Finney, E.E. Defining and measuring attributes of texture in fruits and vegetables, *Agric. Engng.* (50) 462-465 (1969).
- Finney, E.E. and Hall, C.W. Elastic properties of potatoes, *Trans. ASAE* (10) 4-8 (1967).

- Finney, E.E. and Massie, D.R. Instrumentation for testing the response of fruits to mechanical impact, *Trans. ASAE* (18) 1184-1187, 1192 (1975).
- Fletcher, S.W. The mechanical behaviours of processed apples, *Trans. ASAE* (14) 14-17, 19 (1971).
- Fletcher, S.W., Mohsenin, N.N., Hammerle, J.R. and Tukey, L.D. Mechanical behavior of selected fruits and vegetables under fast rates of loading, *Trans. ASAE* (8) 324-326, 331 (1965).
- Fluck, R.C. and Ahmed, E.M. Impact testing of fruits and vegetables, *Trans. ASAE* (16) 660-666 (1973).
- Fowler, Bryce L. Interactive processing of complex modulus data, Dynamic elastic modulus measurements in materials, ASTM STP 1045, A. Wolfenden (edit.) 208-217, ASTM (1990).
- Fridley, R.B. Texture firmness and strength, Proc. tomato quality workshop, U.C. Davis, 35-40, July 12-15 (1976).
- Fridley, R.B. and Adrian, P.A. Mechanical properties of peaches, pears, apricots and apples, *Trans. ASAE* (9) 135-138, 142 (1966).
- Fry, S.C. Analysis of cross-links in the growing cell walls of higher plants, Plant fibers, H.F. Linskens and J.F. Jackson (edit.) 12-36, Springer-Verlag (1989).
- Fung, Y.C. Bioviscoelastic solids: Ch. 7, Biomechanics: mechanical properties of living tissues, 568 pages, Springer-Verlag (1993).
- Garrett, R.E. Velocity of propagation of mechanical disturbances in apples, PhD thesis, Cornell University, 131 pages (1970).
- Garrett, R.E. and Furry, R.B. Velocity of sonic pulses in apples, *Trans. ASAE* (15) 770-774 (1972).
- Gere, J.M. and Timoshenko, S.P. Mechanics of materials, 762 pages, PWS Engineering (1984).
- Giddings, T.H. and Staehelin, L.A. Microtubule-mediated microfibril deposition: a reexamination of the hypothesis, The cytoskeletal basis of plant growth and form, C. Lloyd (edit.) 85-99, Academic Press (1991).
- Gill, P.S., Lear, J.D. and Leckenby, J.N. Recent developments in polymer characterization by dynamic mechanical analysis, *Polymer Testing* (4) 131-138 (1984).
- Glenn, G.M. and Poovaiah, B.W. Calcium-mediated postharvest changes in texture and cell wall structure and composition in Golden Delicious apples, *J. Amer. Soc. Hort. Sci.* (115) 962-968 (1990).
- Goel, R.P. and Malvern, L.E. Elastic-plastic plane waves with combined compressive and two shear stresses in a half space, *Trans. ASME, J. Appl. Mech.* (38) 895-898 (1971).
- Gordon, J.E. Structures, 395 pages, Penguin Books (1978).
- Grathwohl, G. Current testing methods – a critical assessment, Mechanical testing of engineering ceramics at high temperatures, B.F. Dyson, R.D. Lohr and R. Morrell (edit.) 31-50, Elsevier (1989).

- Griffith, A.A. The phenomena of rupture and flow in solids, *Phil. Trans. Soc. Lond. A* (221) 163-198 (1921).
- Gross, B. Mathematical structure of the theories of viscoelasticity, Hermann (1953).
- Hadamard, J. Lecons sur la propagation des ondes (Chapter 6) Hermann et Cie (1903).
- Haddad, Y.M. On the theory of the viscoelastic solid, *Res Mechanica* (25) 225-259 (1988).
- Haddad, Y.M. Viscoelasticity of engineering materials, 378 pages, Chapman and Hall (1995).
- Hamann, D.D. Dynamic mechanical properties of apple fruit flesh, *Trans. ASAE* (12) 170-174 (1969).
- Hammerle, J.R. and Mohsenin, N.N. Some dynamic aspects of fruit impacting hard and soft materials, *Trans. ASAE* (9) 484-488 (1966).
- Hammerle, J.R. and McClure, W.F. The determination of Poisson's ratio by compression tests of cylindrical specimens, *J. Texture Stud.* (2) 31-49 (1971).
- Hanagud, S. Finite amplitude spherical waves in a locking-relaxing solid, Proc. 5<sup>th</sup> U.S. National Congress in Applied Mechanics, 63-77, ASME (1966).
- Hanke, G. Applying optical measurement techniques, *Sensor Review* (10) 30-34 (1990).
- Hashin, Z. Analysis of composite materials: a survey, *Trans. ASME, J. Appl. Mech.* (50) 481-505 (1983).
- Higgins, R.A. The properties of engineering materials, 495 pages (1994) Industrial Press.
- Hill, R. Acceleration waves in solids, *J. Mech. Phys. Solids* (10) 1-16 (1962).
- Hill, R. The essential structure of constitutive laws for metal composites and polycrystals, *J. Mech. Phys. Solids* (15) 79-95 (1967).
- Hiller, S. and Jeronimidis, G. Fracture in potato tuber parenchyma, *J. Mater. Sci.* (31) 2779-2796 (1996).
- Hodge, J.A. The excitation and propagation of elastic waves, 226 pages, Cambridge U. Press (1980).
- Holt, J.E. and Schoorl, D. Bruising and energy dissipation in apples, *J. Texture Stud.* (7) 421-432 (1977).
- Holt, J.E., Schoorl, D. and Lucas, C. Prediction of bruising in impacted multilayered apple packs, *Trans. ASAE* (24) 242-247 (1981).
- Holt, J.E. and Schoorl, D. Mechanics of failures in fruits and vegetables, *J. Texture Stud.* (13) 83-97 (1982a).
- Holt, J.E. and Schoorl, D. Strawberry bruising and energy dissipation, *J. Texture Stud.* (13) 349-357 (1982b).
- Holt, J.E. and Schoorl, D. Fracture in potatoes and apples, *J. Mat. Sci.* (18) 2017-2028 (1983).

- Holt, J.E. and Schoorl, D. Mechanical properties and texture of stored apples, *J. Texture Stud.* (15) 377-394 (1984).
- Horsfield, B.C., Fridley, R.B. and Claypool, L.L. Application of the theory of elasticity to the design of fruit harvesting and handling equipment for minimum bruising, *Trans. ASAE* (24) 746-750 (1972).
- Hudson, J.A., Brown, E.T. and Fairhurst, C. Shape of the complete stress-strain curve for rock, Stability of rock slopes, Proc. 13<sup>th</sup> Symp. Rock Mechanics, E.J. Cording (edit.) 773-795, Uni. Illinois Urbana Press (1971).
- Huelin, F.E. and Gallop, R.A. Studies in the natural coating of apples: I. Preparation and properties of fractions, *Aust. J. Sci. Res.* (B4) 526-543 (1951).
- Hui, C.Y. and Riedel, H. The asymptotic stress and strain field near the tip of a growing crack under creep conditions, *Int. J. Fracture* (17) 409-425 (1981).
- Hult, J. Effect of voids on creep rate and strength, Damage mechanics and continuum modeling, N. Stubbs and D. Krajcinovic (edit.) 13-24, ASCE (1985).
- Hult, J. Engineering damage mechanics – past and present, Applied solid mechanics: Vol. 2, A.S. Tooth and J. Spence (edit.) 245-276, Elsevier (1988).
- Humbert, W.G. and Hanlon, R.G. Package engineering, 528 pages, McGraw-Hill (1962).
- Hung, Y.C. and Prussia, S.E. Effect of maturity and storage time on the bruise susceptibility of peaches, *Trans. ASAE* (32) 1377-1382 (1989).
- Hunter, S.C. Energy absorbed by elastic waves during impact, *J. Mech. Phys. Solids* (5) 162-171 (1957).
- Hunter, S.C. The Hertz problem for a rigid spherical indenter and a viscoelastic half-space, *J. Mech. Phys. Solids* (8) 219-234 (1960a).
- Hunter, S.C. Viscoelastic waves: Ch. 1, Progress in solid mechanics: Vol.1, I.N. Sneddon and R. Hill (edit.) 1-57, North-Holland (1960b).
- Hutchinson, J.W. Crack tip shielding by micro-cracking in brittle solids, *Acta metall.* (35) 1605-1619 (1987).
- Hyde, G.M. and Mathew, R. Potato impact damage threshold. *ASAE Paper No.* 92-1514, ASAE (1992).
- Hyde, G.M. Impact properties of agricultural commodities, (Internet Homepage) <http://www.wsu.edu:8080/~gmhyde/ImpactProperties.html>, Washington State Uni. (1997).
- Ilyushin, A.A. and Lensky, V.S. Strength of materials, 442 pages, Pergamon (1967).
- Imou, K., Morishima, H., Seo, Y. and Sawada, T. Studies on firmness measurement of fruit by impact force, *J. Jap. Soc. Agric. Mach.* (55) 67-74 (1993).

- Ip, T.D., Leonart, G. and Marcondes, J. Bruise volume measurements of apple using drop tests and shock testers for packaging, Proc. 1<sup>st</sup> Australasian Postharvest Horticultural Conf., 247-252, Melbourne, Australia (1995).
- Ip, T.D., He, J. and Wendlandt, B.C. Evaluation of impact dynamics of viscoplastic materials with laser displacement sensor, Proc. Int. Conf. Experimental Mechanics: Advances and Applications, SPIE Vol. 2921, Singapore, F.S. Chau and C.T. Lim (edit.) 616-621, International Society for Optical Engineering (1996a).
- Ip, T.D., Tobias, B. and He, J. The energy absorption and dissipation processes during impact of viscoplastic materials, Proc. 41<sup>st</sup> International SAMPE Symp., Anaheim, California, 778-784, SAMPE (1996b).
- Ip, T.D., Tobias, B., He, J. and Liu, T. Cyclic deformation behaviours of some non-wood natural fibre-reinforced composites, Mechanics of structures and materials, R.H. Grzebieta, R. Al-Mahaidi and J.L. Wilson (edit.) 69-74, A.A. Balkema (1997).
- Ip, T.D., Sek, M. and He, J. Estimation of the dynamic effective modulus of rice-hull fibre-reinforced composites under impact loading, Proc. 5<sup>th</sup> Int. Conf. Composite Eng., D. Hui (edit.), Las Vegas, July 5-11 (1998).
- Irwin, G.R. Analysis of stresses and strains near the end of a crack traversing a plate, *Trans. ASME, J. Appl. Mech.* (24) 361-364 (1957).
- Ito, S. The persimmon: Ch. 8, The biochemistry of fruits and their products: Vol. 2, A.C. Hulme (edit.) 281-301, Academic Press (1971).
- Jackson, A.P., Vincent, J.F.V. and Turner, R.M. The mechanical design of nacre, *Proc. R. Soc. B* (234) 415-440 (1988).
- Jarimopas, B., Sarig, Y., Peiper, U.M. and Manor, G. Instrumentation for measuring the response of apples subjected to impact loading, *Computers & Electronics in Agriculture* (5) 255-260 (1990).
- Javis, M.C., Hall, M.A., Threlfall, D.R. and Friend, J. The polysaccharide structure of potato cell walls: chemical fractionation, *Planta* (152) 93-100 (1981).
- Jarvis, M.C. Structure and properties of pectin gels in plant cell walls, *Plant Cell & Environ.* (7) 153-164 (1984).
- Jeronimidis, G. The fracture behaviour of wood and the relations between toughness and morphology, *Proc. R. Soc. B* (208) 447-460 (1980).
- Jeronimidis, G. Mechanical and fracture properties of cellular and fibrous materials, Feeding and the texture of food, J.F.V. Vincent and P.J. Lillford (edit.) 1-17, Cambridge U. Press (1991).
- Ji, Z. and Leu, M.C. Design of optical triangulation devices, *Optics & Laser Technology* (21) 335-338 (1989).
- Jindal, V.K. and Mohsenin, N.N. Analysis of a simple pendulum impacting device for determining dynamic strength of selected food materials, *Trans. ASAE* (19) 766-770 (1976).
- Jobling, J. Maturity decides postharvest quality, *Good Fruit & Vegetables* (3) No.12, 36 (1993)

- Johnson, A.F. Pulse propagation in heat-conducting elastic materials, *J. Mech. Phys. Solids* (23) 55-75 (1975).
- Kachanov, L.M. On creep rupture time, *Izv. Acad. Nauk. SSSR, Otd. Techn. Nauk.* (8) 26-31 (1958).
- Kachanov, L.M. Crack growth under creep conditions, *Izv. An SSR Mekhanika Tverdogo Tela* (9) 57-59 (1978).
- Kantor, Y. and Bergman, D.J. Improved rigorous bounds on the effective elastic moduli of a composite material, *J. Mech. Phys. Solids* (32) 41-62 (1984).
- Kastelic, J., Galeski, A. and Baer, E. The multicomposite structure of tendon, *J. Conn. Tis. Res.* (6) 11-23 (1978).
- Khan, A.A. and Vincent, J.F.V. Anisotropy of apple parenchyma, *J. Sci. Food Agric.* (52) 455-466 (1990).
- Khan, A.A. and Vincent, J.F.V. Anisotropy in the fracture properties of apple flesh as investigated by crack-opening tests, *J. Mater. Sci.* (28) 45-51 (1993).
- Klein, J.D. Relationship of harvest date, storage conditions, and fruit characteristics to bruise susceptibility of apple, *J. Amer. Soc. Hort. Sci.* (112) 113-118 (1987).
- Kohn, R.V. Recent progress in the mathematical modeling of composite materials, Composite material response: constitutive relations and damage mechanics, G.C. Sih, G.F. Smith, I.H. Marshall and J.J. Wu (edit.) 155-177, Elsevier (1988).
- Kornhauser, M. Prediction and evaluation of sensitivity to transient accelerations, *Trans. ASME, J. Appl. Mec.* (21) 371-380 (1954).
- Kosky, H. The propagation of stress pulses in viscoelastic solids, *Phil. Mag.* (8) 693-710 (1956).
- Kosky, H. Viscoelastic waves, Proc. int'l symp. stress wave propagation in materials, N. Davids (edit.) 59-90, Interscience (1960).
- Kosky, H. Stress waves in solids, 213 pages, Dover (1963).
- Krajcinovic, D. Continuum damage mechanics revisited: basic concepts and definitions, *Trans. ASME, J. Appl. Mech.* (52) 829-834 (1985).
- Krajcinovic, D. Damage mechanics, 761 pages, North-Holland (1996).
- Krajcinovic, D. and Sumarac, D. Micromechanics of the damage processes, Continuum damage mechanics theory and applications, D. Krajcinovic and J. Lemaitre (edit.) 135-194, Springer-Verlag (1987).
- Krajcinovic, D. and Mastilovic, S. Some fundamental issues of damage mechanics, *Mech. Mater.* (21) 217-230 (1995).
- Kriz, K. Einfluss der Mikrostruktur auf die langsame Ribausbreitung und mechanische Eigenschaften von heissgepresstem Siliziumnitrid zwischen Raumtemperatur und 1500°C. Dissertation Univers., University of Erlangen (1983).

- Kupradze, V.D., Gegelia, T.G., Basheleishvili, M.O. and Burchuladze, T.V. Three-dimensional problems of the mathematical theory of elasticity and thermoelasticity, 929 pages, North-Holland (1979).
- Lapsley, K.G., Escher, F.E. and Hoehn, E. The cellular structure of selected apple varieties, *Food Structure* (11) 339-349 (1992).
- Lee, E.H. A boundary value problem in the theory of plastic wave propagation, *Quart. Appl. Math.* (10) 335-346 (1953).
- Lee, E.H. Viscoelastic stress analysis, Structural mechanics, J.N. Goodier (edit.) 456-482, Pergamon (1960).
- Lee, E.H. and Kanter, I. Wave propagation in finite rods of viscoelastic materials, *J. Appl. Phys.* (24) 1115-1122 (1953).
- Lemaitre, J. and Chaboche, J.L. Aspect phenomenologique de la rupture par endommagement, *J. Mech. Applique* (2) 317-365 (1978).
- Lemaitre, J. and Chaboche, J.L. Mechanics of solid materials, 556 pages (1990) CUP.
- Lensky, V.S. Dynamic diagram of wave propagation for linear work-hardening materials, *PMM* (13) 165-169 (1949).
- Lensky, V.S. The construction of a dynamical tension-compression diagram based on the wave propagation theory, Proc. Conf. Properties of Materials at High Rates of Strain, 173-176, IMechE (1957).
- Lethersich, W. The rheological properties of dielectric polymers, *Brit. J. Appl. Phys.* (1) 294-301 (1950).
- Li, F., Twede, D. and Goff, J.W. Method for deriving the correlation between free fall and shock machine drop height, *Packaging Tech. & Sci.* (6) 139-146 (1993).
- Li, Y.S. and Duxbury, P.M. From moduli scaling to breakdown scaling: a moment spectrum analysis, *Physical Review* (B40) 4889-4897 (1989).
- Lichtensteiger, M.J. Impact analysis of viscoelastic spheres, fruits and vegetables with rigid, plane surfaces, PhD thesis, 210 pages, Ohio State University (1982).
- Lichtensteiger, M.J., Holmes, R.G., Hamdy, M.Y. and Blaisdell, J.L. Impact parameters of spherical viscoelastic objects and tomatoes, *Trans. ASAE* (31) 595-602 (1988).
- Lick, W. Wave propagation: Ch. 15, Handbook of applied mathematics, C.E. Pearson (edit.) 815-877, Van Nostrand Reinhold (1983).
- Lifshitz, J.M. and Kosky, H. Some experiments on anelastic rebound, *J. Mech. Phys. Solids* (12) 35-43 (1964).
- Lighthill, J. Viscosity effects in sound waves of finite amplitude, Surveys in mechanics, G. K. Batchelor and R.M. Davies (edit.) 250-351, Cambridge U. Press (1956).

- Lockhart, J.A. Cell extension, Plant biochemistry, J. Bonner (edit.) 826-849, Academic Press (1965).
- Love, A.E.H. A treatise on the mathematical theory of elasticity, 643 pages, Dover (1954).
- Luan, J.M. On the direct confirmation of Hertz contact pressure distribution during viscoelastic impact, PhD thesis, 219 pages, Department of Agricultural Engineering, North Carolina State University (1990).
- Lubarda, V. and Krajcinovic, D. Damage tensors and the crack density distribution, *Int. J. Solids & Structures* (30) 2859-2877 (1993).
- Lubin, G. and Winans, R.R. Preliminary studies on a drop ball impact machine, *ASTM Bull.* (128) 13-18 (1944).
- Ludwik, P. Elemente der Technologischen Mechanik, Springer-Verlag (1909).
- Malvern, L.E. The propagation of longitudinal waves of plastic deformation in a bar of material exhibiting a strain-rate effect, *Trans. ASME, J. Appl. Mech.* (18) 203-208 (1951).
- Mandel, J. Stability conditions and Drucker's postulate, Rheology and soil mechanics, Proc. 1964 IUTAM Symp., J. Kravtchenko and P.M. Sirleys (edit.) 58-68, Springer-Verlag (1966).
- Mandel, J. Director vectors and constitutive equations for plastic and visco-plastic media, Problems of plasticity, A. Sawczuk (edit.) 135-143, Noordhoff (1974).
- Manor, A.N. Critical analysis of the mechanics of fruit damage under impact conditions, 180 pages, PhD Thesis, Pennsylvania State University (1978).
- Marcondes, J. and Ip, T.D. Impact load distribution on the surface of a programmable free fall shock machine, Internal Report No. 94-Gasnorm2, Centre of Packaging Research & Technology, Victoria U. of Technology, Melbourne, 18 pages (1994).
- Matsuoka, S. Nonlinear viscoelastic stress-strain relationships in polymeric solids, Failure of plastics, W. Brostow and R.D. Corneliussen (edit.) 24-59, Hanser Publishers (1986).
- Matsuoka, S. Relaxation phenomena in polymers, 322 pages, Hanser Publishers (1992).
- McCann, M.C. and Roberts, K. Architecture of the primary cell wall, The cytoskeletal basis of plant growth and form, C. Lloyd (edit.) 109-129, Academic Press (1991).
- McGlasson, W.B. The ethylene factor: Ch. 16, The biochemistry of fruits and their products: Vol. 1, A.C. Hulme (edit.) 475-519, Academic Press (1970).
- Meyers, M.A. Dynamic behavior of materials, 668 pages, John Wiley (1994).
- Miles, J. A., Fridley, R.B. and Lorenzen, C. Strength characteristics of tomatoes subjected to quasi-static loading, *Trans. ASAE* (12) 627-630 (1969).
- Miles, J.A. and Rehkugler, K. A failure criterion for apple flesh, *Trans. ASAE* (16) 1148-1153 (1973).
- Mindlin, R.D. Dynamics of package cushioning, *Bell System Tech. J.* (24) 353-461 (1945).

- Mishnaevsky, L.L. Probabilistic model for the failure of composites under dynamic loading, Impact and dynamic fracture of polymers and composites, J.G. Williams and A. Pavan (edit.) 443-451, Mechanical Engineering Publ. (1995).
- Mohsenin, N.N. Application of engineering techniques to evaluation of texture of solid food materials, *J. Texture Stud.* (1) 133-154 (1970).
- Mohsenin, N.N. Physical properties of plant and animal materials, 891 pages, Gordon & Breach (1986).
- Mohsenin, N.N. and Goehlich, H. Techniques for determination of mechanical properties of fruits and vegetables as related to design and development of harvesting and processing machinery, *J. Agric. Engng. Res.* (7) 300-315 (1962).
- Mohsenin, N.N., Goehlich, H. and Tukey, L.D. Mechanical behaviour of apple fruits as related to bruising, *Proc. Amer. Soc. Hort. Sci.* (81) 67-77 (1962).
- Mok, C.H. and Duffy, J. The dynamic stress-strain relation of metals as determined from impact tests with a hard ball, *Int. J. Mech. Sci.* (7) 355-371 (1965).
- Muhlhaus, H.B. and Aifantis, E.C. A variational principle for gradient plasticity, *Int. J. Solids Struct.* (28) 845-858 (1991).
- Muller, J.T. Transients in mechanical systems, *Bell System Tech. J.* (27) 657-683 (1948).
- Munoz, J. and Sherman, P. Dynamic viscoelastic properties of some commercial salad dressings, *J. Texture Stud.* (21) 411-426 (1990).
- Mustin, G.S. Theory and practice of cushion design, 332 pages, Shock & Vibration Information Center, U.S. Dept. Defense (1968).
- Nahir, D., Schmilovitch, Z. and Ronen, B. Tomato grading by impact force response, *ASAE Paper No.* 86-3028 (1986).
- National Research Council of U.S. National Academy of Sciences. Mathematical research in materials science, Committee on the Mathematical Sciences applied to Materials Science, Board on Mathematical Sciences, Washington, D.C., 129 pages, National Academy Press (1993).
- Nelson, C.W. and Mohsenin, N.N. Maximum allowable static and dynamic loads and effect of temperature for mechanical injury in apples, *J. Agric. Engng. Res.* (13) 317-329 (1968).
- Nemat-Nasser, S. and Hori, H. Micromechanics: overall properties of heterogeneous materials, 687 pages, North-Holland (1993).
- Noble, R. The relation between impact and internal bruising in potato tubers, *J. Agric. Engng. Res.* (32) 111-121 (1985).
- Nolle, A.W. J. Acoustic determination of the physical constants of rubber-like materials, *J. Acoust. Soc. Amer.* (19) 194-201 (1947).
- O'Brien, M, Singh, R.P. and Garrett, R.E. The effect of bruising on dried fruit quality, *Trans. ASAE* (27) 274-277 (1984).

- Ogden, R.W. Non-linear elastic deformation, 532 pages, Ellis Horwood (1984).
- Oleson, M.W. Integration and double integration: a practical technique, *Shock & Vibration Bull.* (35) Pt-4 (1966).
- O'Loughlin, J.B. The bruising of fruit during transport and storage, Proc. 4<sup>th</sup> Australian fruit & vegetable storage research conference (1964).
- Opara, L.U., Studman, C.J. and Banks, N.H. Fruit skin splitting and cracking, *Hort Reviews* (19) 217-262 (1997).
- Ortiz, M. A constitutive theory for the inelastic behaviour of concrete, *Mech. Mater.* (4) 67-93 (1985).
- Pacifico, R.E. Errors in computing displacements from transient acceleration signals, *J. Soc. Env. Engng.* (85) 3-7, 16 (1981).
- Pan, N. and Postle, R. Probabilistic mechanics of hybrid composites, Mechanics of plastics and plastic composites, MD-Vol. 68 / AMD-Vol. 215, M.C. Boyce (edit.) 71-78, ASME (1995).
- Pang, W., Studman, C.J., and Ward, G.T. Bruising damage in apple-to-apple impact, *J. Agric. Engng. Res.* (52) 229-240 (1992).
- Parton, V.Z. and Boriskovsky, V.G. Dynamic fracture mechanics Vol.2: Propagating cracks, revised edit., 393 pages, Hemisphere (1990).
- Peggie, I.D. Technical problems in the retail marketing of fruits and vegetables, Proc. 5<sup>th</sup> Australian fruit & vegetable storage research conference, 142-150 (1968).
- Perkin-Elmer Corp. User manual: 7 series/ Unix dynamic mechanical analyzer (1995).
- Peterlin, A. Mechanical and transport properties of drawn semi-crystalline polymers, The strength and stiffness of polymers, A.E. Zachariades and R.S. Porter (edit.) 97-127, Marcel Dekker (1983).
- Petrell, R.J., Mohsenin, N.N. and Wallner, S. Dynamic mechanical properties of the apple cortex in relation to sample location and ripening, *J. Texture Stud.* (10) 217-229 (1980).
- Pitt, R.E. Models for the rheology and statistical strength of uniformly stressed vegetative tissue, *Trans. ASAE* (25) 1776-1784 (1982).
- Rabotnov, Y.N. Creep problems of structural members, 822 pages, North-Holland (1969).
- Rakhmatulin, K.A. On the propagation of elastic-plastic waves owing to combined loading, *PMM* (22) 1079-1088 (1958).
- Rao, V.N.M., Hamann, D.D. and Purcell, A.E. Dynamic structural properties of sweet potato, *Trans. ASAE* (19) 771-774 (1976).
- Read, H.E. and Hegemier, G.A. Strain softening of rock, soil and concrete – a review article, *Mech. Mater.* (3) 271-294 (1984).

- Reeve, R.M. Histological investigations of texture in apples, *Food Res.* (18) 604-616 (1953).
- Reiner, M. Advanced rheology, P.208, H.K. Lewis & Co. (1971).
- Remoissenet, M. Waves called solitons: concepts and experiments, 236 pages, Springer-Verlag (1994).
- Rice, J.R. Continuum mechanics and thermodynamics of plasticity in relation to microscale deformation mechanisms, Constitutive equations in plasticity, A.S. Argon (edit.) 23-79, MIT Press (1975).
- Rigbi, Z. The value of Poisson's ratio of viscoelastic materials, *Appl. Polymer Symp.* (5) 1-8 (1967).
- Rodriguez, L., Ruiz, M and de Felipe, M.R. Differences in the structural response of Granny Smith apples under mechanical impact and compression, *J. Texture Stud.* (21) 155-164 (1990).
- Roland, J.C. and Vian, B. The wall of the growing plant cell-wall: it's three dimensional organization, *Int. Review Cytol.* (61) 129-166 (1979).
- Rumsey, T.R. and Fridley, R.B. A method for the determining the shear relaxation function of agricultural materials, *Trans. ASAE* (20) 386-389, 392 (1977).
- Sakai, M. and Bradt, R.C. R-curve behavior of polycrystalline graphite: microcracking and grain bridging in the wake region, *J. Am Ceram. Soc.* (71) 609-616 (1988).
- Sakai, M. and Bradt, R.C. Fracture toughness testing of brittle materials, *Int. Mater. Rev.* (38) 53-78 (1993).
- Schoorl, D. and Holt, J.E. Bruise resistance measurements in apples, *J. Texture Stud.* (11) 389-394 (1980).
- Schreyer, H.L. and Chen, Z. 1-D softening with localization, *Trans. ASME, J. Appl. Mech.* (53) 791-797 (1986).
- Schueller, J.K. and Wall, T.M.P. Impact of fruit on flexible beams to sense modulus of elasticity, *Exp. Mech.* (31) 118-121 (1991).
- Schulte, N.L., Brown, G.K. and Timm, E.J. Apple impact damage thresholds, *Appl. Eng. Agr.* (8) 55-60 (1992).
- Schulte, N.L., Timm, E.J. and Brown, G.K. Redhaven peach impact damage thresholds, *HortSci.* (29) 1052-1055 (1994).
- Schwer, L.E. A viscoplastic augmentation of the smooth cap model, Computer Methods & Advances in Geomechanics, H.J. Siriwardane & M.M. Zaman (edit.) 671-676, Balkema (1994).
- Scott Blair, G.W. Introduction to biorheology, 215 pages, Elsevier (1974).
- Sharma, M.G. and Mohsenin, N.N. Mechanics of deformation of a fruit subjected to hydrostatic pressure, *J. Agric. Engng Res.* (15) 65-74 (1970).
- Sharpe, W.N. The Portevin-Le Chatelier effect in aluminum single crystals and polycrystals, *J. Mech. Phy. Solids* (14) 187-202 (1966).

- Sih, G.C. Some basic problems in fracture mechanics and new concepts, *Engng. Fracture Mech.* (5) 365-377 (1973).
- Sih, G.C. Role of fracture mechanics in modern technology, plenary lecture, Role of fracture mechanics in modern technology, G.C. Sih, H. Nisitani and T. Ishihara (edit.), 3-23, Elsevier (1987).
- Sih, G.C. Microstructure and damage dependence of advanced composite material behaviour, Composite material response: constitutive relations and damage mechanisms, G.C. Sih, G.F. Smith, I.H. Marshall and J.J. Wu (edit.) 1-23, Elsevier (1988).
- Sih, G.C. and MacDonald, B. Fracture mechanics applied to engineering problems – strain energy density fracture criterion, *Engng. Fracture Mech.* (6) 361-386 (1974).
- Sips, R. Propagation phenomena in elastic-viscous media, *J. Polym. Sci.* (6) 285-293 (1951).
- Sips, R. General theory of deformation of viscoelastic substances, *J. Polym. Sci.* (7) 191-205 (1951).
- Siyami, S., Brown, G.K., Burgess, G.J., Gerrish, J.B., Tennes, B.R., Burton, C.L. and Zapp, R.H. Apple impact bruise prediction models, *Trans. ASAE* (31) 1038-1046 (1988).
- Slazas, P.A. Non-contact optical displacement sensing, *Sensor Review* (16) 33-37 (1996).
- Sluys, L.J., Bolck, J. and de Borst, R. Wave propagation and localisation in viscoplastic media, Computational plasticity, Proc. COMPLAS /III, Barcelona, Spain, D.R.J. Owen, E. Onate and E. Hinton (edit.), 539-550, Pineridge (1992).
- Sluys, L.J., Cauvern, M. and de Borst, R. Discretization influence in strain-softening problems, *Engng. Comput.* (12) 209-228 (1995).
- Smith, K.R. A scanning electron microscopy study of the surface of pickling cucumber fruit, MSc thesis, North Carolina State University (1978).
- Sober, S.S., Zapp, H.R. and Brown, G.K. Simulated packaging line impacts for apple bruise prediction, *Trans. ASAE* (33) 415-418 (1990).
- Sokolovskii, V.V. The propagation of elastic-viscoplastic waves in bars, *PMM* (12) 261-280 (1948).
- Sondergaard, R., Chaney, K. and Brennen, C.E. Measurements of solid spheres bouncing off flat plates, *Trans. ASME, J. Appl. Mech.* (57) 694-699 (1990).
- Soper, W.G. and Dove, R.C. Similitude in package cushioning, *Trans ASME, J. Appl. Mech.*, (29) 262-266 (1962).
- Spencer, M. Fruit ripening: Ch. 30, Plant biochemistry, J. Bonner (edit.), 793-825, Academic Press (1965).
- Stachurski, Z.H. Engineering science of polymeric materials, 217 pages, Royal Australian Chemical Institute (1987).
- Staker, M.R. The relation between adiabatic shear instability strain and material properties, *Acta Met.* (29) 683-689 (1981).

- Studman, C.J. Model of fruit bruising, Proc. 1<sup>st</sup> Australasian Postharvest Horticulture Conf., 241-246 (1995a).
- Studman, C.J. Private communication, Dept. of Agricultural Engng., Masey University (1995b).
- Studman, C.J. and Banks, N. Indenter shape effects in the impact bruising of apples and nashi, Proc. 4<sup>th</sup> Int. Conf. On Physical Properties of Agric. Materials, Rostock, Germany, Paper A-14 (1989a).
- Studman, C.J. and Banks, N. The measurement of bruise susceptibility in apples and nashi, Conf. Proc. Int. Symp. Agric. Engng: Vol. 3, Beijing, China, 31-36 (1989b).
- Sumarac, D. and Krajcinovic, D. A mesomechanical model for brittle deformation processes: Part II, Trans. ASME, J. Appl. Mech. (56) 57-62 (1989).
- Suole, James. Agriculture handbook No.98, University of Florida (1956).
- Swegle, J.W. and Grady, D.E. Shock viscosity and the prediction of shock wave rise times, J. Appl. Phys. (58) 692-701 (1985).
- Swords, K.M.M. and Staehelin, L.A. Analysis of extensin structure in plant cell walls, Plant fibers, H.F. Linskens and J.F. Jackson (edit.) 219-233, Springer-Verlag (1989).
- Szczesniak, A.S. Classification of textural characteristics, J. Food Sci. (28) 385-389 (1963).
- Szczesniak, A.S and Kleyn, D.H. Consumer awareness of texture and other food attributes, Food Tech. (17) 74-77 (1963).
- Taylor, J.E. Exotics, Biochemistry of fruit ripening, G.B. Seymour, J.E. Taylor and G.A. Tucker (edit.) 151-187, Chapman & Hall (1993).
- Thomas, T.Y. The decay of waves in elastic solids, J. Math. & Mech. (6) 759-768 (1957).
- Thomas, T.Y. Plastic flow and fracture in solids, 267 pages, Academic Press (1961).
- Tillett, J.P.A. A study of the impact on spheres of plates, Proc. Phys. Soc. (B67) 677-688 (1954).
- Ting, T.C.T. On the initial slope of elastic-plastic boundaries in combined longitudinal and torsional wave propagation, Trans. ASME, J. Appl. Mech. (36) 303-211 (1969).
- Ting, T.C.T. Elastic-plastic boundaries in the propagation of plane and cylindrical waves of combined stress, Quart. Appl. Math. (47) 441-449 (1970).
- Ting, T.C.T. The initiation of combined stress waves in a thin-walled tube due to impact loadings, Int. J. Solids Structures (8) 269-293 (1972).
- Ting, T.C.T. A unified theory on elastic-plastic wave propagation of combined stress, Foundations of plasticity, A. Sawczuk (edit.) 301-316, Noordhoff (1973).
- Ting, T.C.T. Nonlinear effects on the propagation of discontinuities of all orders in viscoelastic media, Mechanics of viscoelastic media and bodies, IUTAM Symp., Gothenburg, Sweden (1974), J. Hult (edit.) 84-95, Springer-Verlag (1975).

- Ting, T.C.T. and Nan, N. Plane waves due to combined compressive and shear stresses in a half-space, *Trans. ASME, J. Appl. Mech.* (36) 189-197 (1969).
- Tobolsky, A.V. Stress relaxation studies of the viscoelastic properties of polymers, Rheology: theory and applications, Vol.2, F.R. Eirich (edit.) 63-81, Academic Press (1958).
- Truesdell, C. and Noll, W. The nonlinear theories of mechanics, Encyclopedia of Physics, Vol. 3/3, S. Flugge (edit.) Springer Verlag (1965).
- Tucker, G.A. Introduction: Ch. 1, Biochemistry of fruit ripening, G.B. Seymour, J.E. Taylor and G.A. Tucker (edit.) 1-51, Chapman & Hall (1993).
- Vamos-Vigyazo, L. Polyphenol oxidase and peroxides in fruits and vegetables, *CRC Reviews in Food Science & Nutrition* (14) 49-127 (1981).
- Van der Burg, J. Drop test picks out best peas for soggy soils, *New Scientist* (137) 20 (1993).
- Van Mier, J.G.M., Schlangen, E. and Vervuurt, A. Lattice type fracture models for concrete: Ch. 10, Continuum models for materials with microstructures, H.B. Muhlhaus (edit.) 341-377, John Wiley (1995).
- Vergano, P.J. and Testin, R.F. Distinguishing among bruises in peaches caused by impact, vibration and compression, *J. Food Quality* (14) 285-298 (1991).
- Vincent, J.F.V. Locust oviposition: stress softening of the extensible intersegmental membranes, *Proc. R. Soc. Lond. B* (188) 189-201 (1975).
- Vincent, J.F.V. The mechanical design of grass, *J. Mater. Sci.* (17) 856-860 (1982).
- Vincent, J.F.V. Fracture properties of plants, *Adv. Bot. Res.* (17) 235-287 (1990).
- Vincent, J.F.V. Texture of plants and fruits, Feeding and the texture of food, J.F.V. Vincent & P.J. Lillford (edit.) 19-33, CUP (1991a).
- Vincent, J.F.V. Structural biomaterials, 244 pages, Princeton University Press (1991b).
- Vincent, J.F.V. Plants: Ch. 8, Biomechanics - materials: a practical approach, J.F.V. Vincent (edit.) 165-191, Oxford Uni. Press (1992).
- Vladimirov, V.S. Wave propagation: Ch. 14, Equations of mathematical physics, 464 pages, Mir Publishers (1984).
- Ward, I.M. Mechanical properties of solid polymers, 475 pages, John Wiley (1990).
- Whitham, G.B. Linear and nonlinear waves, 636 pages, Wiley-Interscience (1974).
- Whorlow, R.W. Rheological techniques, 2<sup>nd</sup> edtn, 460 pages, Ellis Horwood (1992).
- Wills, R.B.H., Lee, T.H., Graham, D., McGlasson, W.B. & Hall, E.G. Postharvest: an introduction to the physiology and handling of fruit and vegetables, 166 pages, AVI Publishing (1981).

- Wright, F.S. and Splinter, W.E. Mechanical behavior of sweet potatoes under slow loading and impact loading, *Trans. ASAE* (11) 765-770 (1968).
- Wu, F.H. and Reund, L.B. Deformation trapping due to thermoplastic instability in one-dimensional wave propagation, *J. Mech. Phys. Solids* (32) 119-132 (1984).
- Wyskida, R.M. and McDaniel, D.M. Modeling of cushioning systems, 323 pages, Gordon & Breach (1980).
- Yang, W.H. The contact problem for viscoelastic bodies, *Trans. ASME, J. Appli. Mech.* (33) 395-401 (1966).
- Yang, Y.M. Analysis of the mechanics of deformation of a fruit under a rigid die with spherical end, 112 pages, PhD thesis in Agric. Engng., Penn. State Uni. (1973).
- Yang, Y.M. and Mohsenin, N. Analysis of the mechanics of the fruit pressure tester, *J. Texture Stud.* (5) 213-238 (1974).
- Zener, C.M. The intrinsic inelasticity of large plates, *Phy. Rev.* (59) 669-673 (1941).
- Zener, C.M. Elasticity and anelasticity of metals, 170 pages, Chicago U. Press (1948).
- Zener, C.M. and Hollomon, J.H. Effect of strain rate upon plastic flow of steel, *J. Appl. Phys.* (15) 22-32 (1944).
- Zhang, X., Stone, M.L., Chen, D., Maness, N.O. and Brusewitz, G.H. Peach firmness determination by puncture resistance, drop test, and sonic impulse, *Trans. ASAE* (37) 495-500 (1994).
- Zoerb, G.C. and Hall, C.W. Some mechanical and rheological properties of grains, *J. Agric. Engng. Res.* (5) 83-93 (1960).
- Zukas, J.A., Furlong, J.R. and Segletes, S.B. Hydrocodes support visualization of shock-wave phenomena, *Computers in Physics* (6) 146-154 (1992).

# Appendix A

## DROP TEST RESULTS OF RUN ST-21-B

The drop test results of Run ST-21-B comprise peak acceleration, velocity change and duration of impact. These data are presented in the following tables. The data of peak acceleration and velocity change are raw data that need to be processed according to the sensitivity of the data acquisition and the load-cell coefficient. Sample calculations of this processing work will be presented in Appendix B. For this run, the Kyowa 2 kN load-cell was used in drop heights of 20 cm down to 7.5 cm, and the Sangamo 100 N load-cell was used for drop heights of 5 cm down to 0.5 cm. The sensitivity levels are 3 milli-volts per  $g$  (3 mv/g) and 8 mv/g for the Kyowa and the Sangamo load-cell, respectively. The calibrated load-cell coefficients are 3.285 mv/N and 89.772 mv/N for the Kyowa and the Sangamo load-cell, respectively. Each apple was used for a single drop only.

Table A-1 Raw Data of Peak Acceleration,  $g_{max}$ , at various Drop Heights.  $g_{max}$  is expressed in numbers of  $g$ , the gravitational acceleration.

Drop Height (cm)	Peak Acceleration, $g_{max}$			
	Drop 1	Drop 2	Drop 3	Drop 4
20.0	168.5	173.8	170.1	173.8
17.5	157.2	163.5	162.5	175.3
15.0	173.6	171.5	165.4	173.6
12.5	148.5	160.1	157.0	157.5
10.0	147.6	144.0	128.1	139.3
7.5	134.6	126.3	131.6	116.6
5.0	912.1	959.4	963.2	925.4
4.0	835.9	855.1	849.4	815.8
3.0	647.1	653.7	633.4	636.1
2.0	511.2	572.8	520.7	535.5
1.5	393.5	421.0	572.7	452.2
1.0	337.1	307.4	333.0	327.0
0.5	129.1*	-	-	-

(\*Only one drop was performed with a drop height of 0.5 cm)

Table A-2 Raw Data of Velocity Change at various Drop Heights

Drop Height (cm)	Velocity Change, $\Delta V$ (m/sec.)			
	Drop 1	Drop 2	Drop 3	Drop 4
20.0	4.1	4.1	4.2	4.3
17.5	4.0	4.1	4.2	4.2
15.0	4.1	4.0	4.1	4.1
12.5	3.7	3.8	3.9	3.9
10.0	3.6	3.5	3.4	3.6
7.5	3.2	3.1	3.2	3.2
5.0	2.8	2.8	2.8	2.9
4.0	2.6	2.5	2.5	2.5
3.0	2.1	2.1	2.1	2.1
2.0	1.8	1.9	1.7	1.8
1.5	1.2	1.3	1.6	1.6
1.0	1.3	1.2	1.3	1.2
0.5	0.6	-	-	-

Table A-3 Results of Duration of Impact at various Drop Heights

Drop Height (cm)	Duration of Impact, $\tau$ (milliseconds or ms)			
	Drop 1	Drop 2	Drop 3	Drop 4
20.0	4.2	4.2	4.4	4.2
17.5	4.4	4.4	4.4	4.2
15.0	4.1	4.1	4.4	4.1
12.5	4.4	4.1	4.3	4.3
10.0	4.1	4.0	4.5	4.4
7.5	4.1	4.1	4.1	4.8
5.0	5.1	4.9	5.0	5.3
4.0	5.2	5.0	5.1	5.3
3.0	5.4	5.2	5.7	5.5
2.0	6.1	5.6	5.6	5.8
1.5	5.2	5.3	4.6	5.9
1.0	6.5	6.9	6.4	6.0
0.5	7.5	-	-	-

## Appendix B

### SAMPLE CALCULATIONS OF PEAK ACCELERATION, VELOCITY CHANGE AND COEFFICIENT OF RESTITUTION (RUN ST-21-B)

Referring back to the raw data of peak acceleration,  $g_{\max}$ , and velocity change,  $\Delta V$ , in Appendix A, the actual results of peak acceleration and velocity change can be calculated by taking into account the sensitivity levels of the data acquisition and calibrated load-cell coefficients. As an example, let us take the raw data from Drop 1 of the 20-cm drop height for  $g_{\max}$  and  $\Delta V$ , which are 168.5g and 4.1 ms, respectively. The sensitivity level and the load-cell coefficient are 3 mv/g and 3.285 mv/N, respectively. It follows that the peak load associated with the peak acceleration is:

$$168.5g \left( \frac{3mv/g}{3.285mv/N} \right) = 153.88 N.$$

The weight of the apple for this drop is 130.37 grams. It follows that the actual  $g_{\max}$  experienced by the apple is:

$$\frac{153.88N}{(0.13037kg)(9.81m/sec^2)} = 120.3 g.$$

The actual  $\Delta V$  is:

$$\left[ \frac{4.1m/sec}{(0.13037kg)(9.81m/sec^2)} \right] \left( \frac{3mv/g}{3.285mv/N} \right) = 2.928 m/sec.$$

The impact velocity,  $V_1$ , for a 20-cm drop is:

$$\sqrt{2gh} = \sqrt{2(9.81)(0.2)} = 1.981 m/sec.$$

The corresponding rebound velocity,  $V_2$ , is:

$$\Delta V - V_1 = (2.928 - 1.981) m/sec. \text{ or } 0.947 m/sec.$$

It follows that, for Drop 1, the coefficient of restitution,  $e$ , is:

$$\frac{V_2}{V_1} = \frac{0.947}{1.981} = 0.478.$$

Table B-1 Corrected Results of Peak Acceleration,  $g_{\max}$ , at various Drop Heights.  $g_{\max}$  is expressed in numbers of  $g$ , the gravitational acceleration.

Drop Height (cm)	Peak Acceleration, $g_{\max}$			
	Drop 1	Drop 2	Drop 3	Drop 4
20.0	120.3	123.9	120.5	122.1
17.5	109.6	110.7	109.8	118.3
15.0	116.8	114.8	110.7	116.2
12.5	99.2	105.6	102.5	102.7
10.0	96.0	93.6	82.4	89.6
7.5	86.4	80.9	83.0	72.7
5.0	55.4	58.1	57.8	55.5
4.0	50.0	51.1	50.7	48.5
3.0	38.4	38.8	37.5	37.3
2.0	29.6	33.0	29.8	30.5
1.5	27.9	29.5	32.4	25.4
1.0	18.9	17.0	18.4	17.9
0.5	10.7*	-	-	-

(\*Only one drop was performed with a drop height of 0.5 cm)

Table B-2 Corrected Results of Velocity Change at various Drop Heights

Drop Height (cm)	Velocity Change, $\Delta V$ (m/sec.)			
	Drop 1	Drop 2	Drop 3	Drop 4
20.0	2.93	2.92	2.98	3.02
17.5	2.79	2.78	2.84	2.83
15.0	2.76	2.68	2.74	2.74
12.5	2.47	2.51	2.55	2.54
10.0	2.34	2.28	2.19	2.32
7.5	2.05	1.99	2.02	1.99
5.0	1.68	1.68	1.68	1.72
4.0	1.54	1.49	1.51	1.50
3.0	1.26	1.24	1.28	1.25
2.0	1.07	1.07	0.98	1.04
1.5	0.88	0.93	0.90	0.88
1.0	0.72	0.69	0.69	0.63
0.5	0.46	-	-	-

Table B-3 Averaged Results of Duration of Impact, Peak Acceleration, Velocity Change and Coefficient of Restitution at various Drop Heights

<b>Drop Height (cm)</b>	<b>Duration of Impact (ms)</b>	<b>Peak Acceleration (g)</b>	<b>Velocity Change (m/sec.)</b>	<b>Impact Velocity (m/sec.)</b>	<b>Rebound Velocity (m/sec.)</b>	<b>Coefficient of Restitution</b>
20.0	4.25	121.7	2.96	1.98	0.98	0.50
17.5	4.35	112.1	2.81	1.85	0.96	0.52
15.0	4.18	114.6	2.73	1.72	1.02	0.59
12.5	4.28	102.5	2.52	1.57	0.95	0.61
10.0	4.25	90.4	2.28	1.40	0.88	0.63
7.5	4.28	80.8	2.01	1.21	0.80	0.66
5.0	5.08	56.7	1.69	0.99	0.70	0.71
4.0	5.15	50.1	1.51	0.89	0.62	0.70
3.0	5.45	38.0	1.26	0.77	0.49	0.64
2.0	5.78	30.7	1.04	0.63	0.41	0.66
1.5	5.25	28.8	0.90	0.54	0.36	0.66
1.0	6.45	18.1	0.68	0.44	0.24	0.54
0.5	7.20	10.7	0.46	0.31	0.15	0.47





